

# INL REPORT

INL/EXT-18-44453-Rev001

Unlimited Release

Printed May 2020

## Pronghorn Theory Manual

April J. Novak  
Sebastian Schunert  
Robert W. Carlsen  
Paolo Balestra  
David Andrs  
Joe Kelly  
Rachel N. Slaybaugh  
Richard C. Martineau

Prepared by  
Idaho National Laboratory  
Idaho Falls, Idaho 83415

The Idaho National Laboratory is a multiprogram laboratory operated by Battelle Energy Alliance for the United States Department of Energy under DOE Idaho Operations Office. Contract DE-AC07-05ID14517.

Approved for public release; further dissemination unlimited.



Issued by the Idaho National Laboratory, operated for the United States Department of Energy by Battelle Energy Alliance.

**NOTICE:** This report was prepared as an account of work sponsored by an agency of the United States Government. Neither the United States Government, nor any agency thereof, nor any of their employees, nor any of their contractors, subcontractors, or their employees, make any warranty, express or implied, or assume any legal liability or responsibility for the accuracy, completeness, or usefulness of any information, apparatus, product, or process disclosed, or represent that its use would not infringe privately owned rights. Reference herein to any specific commercial product, process, or service by trade name, trademark, manufacturer, or otherwise, does not necessarily constitute or imply its endorsement, recommendation, or favoring by the United States Government, any agency thereof, or any of their contractors or subcontractors. The views and opinions expressed herein do not necessarily state or reflect those of the United States Government, any agency thereof, or any of their contractors.

Printed in the United States of America. This report has been reproduced directly from the best available copy.



## Pronghorn Theory Manual

A.J. Novak<sup>\*</sup>, S. Schunert<sup>†</sup>, R. W. Carlsen<sup>†</sup>, P. Balestra<sup>†</sup>, D. Andrs<sup>†</sup>,  
J. Kelly<sup>×</sup>, R.N. Slaybaugh<sup>\*</sup>, R.C. Martineau<sup>†</sup>, and H.D. Gougar<sup>†</sup>

<sup>\*</sup> University of California, Berkeley  
3115 Etcheverry Hall  
Berkeley, CA 94708

<sup>†</sup> Idaho National Laboratory  
Idaho Falls, ID 83402

<sup>×</sup> Nuclear Regulatory Commission  
Rockville, MD 20852

# Contents

<b>1</b>	<b>Introduction</b>	<b>9</b>
<b>2</b>	<b>Physical Models</b>	<b>10</b>
2.1	Preliminary Considerations	13
2.2	The Mass Equation	13
2.3	The Momentum Equation	14
2.4	The Fluid Energy Equation	20
2.5	The Friction-Dominated Model	27
2.6	The Solid Energy Equation	27
2.7	The Interior Solid Energy Equation	28
2.7.1	One-Equation Model	28
2.7.2	Heat Source Decomposition	29
2.8	Stabilization and Preconditioning of the Fluid Conservation Equations	33
2.8.1	Streamline-Upwind Petrov-Galerkin Stabilization	34
2.8.2	Low-Mach Preconditioning	36
2.9	Nondimensionalization of the Governing Equations	38
2.10	Summary of Physical Models	40
2.10.1	The Compressible Navier-Stokes Model	41
2.10.2	The Compressible Euler Model	42
2.10.3	The Compressible Friction-Dominated Model	43
2.10.4	The Mesoscale and Microscale Models	44
<b>3</b>	<b>Interface Kernels</b>	<b>45</b>
3.1	Conductive Heat Transfer	45
3.2	Pressure Loss	45
3.3	Radiative Heat Transfer	45
<b>4</b>	<b>Boundary Conditions</b>	<b>46</b>
4.1	Conditions Imposed by Conservation	46
4.2	Additional Conditions Required for Closure	47
4.2.1	The Fluid Mass Equation	49
4.2.2	The Fluid Momentum Equation	50
4.2.3	The Fluid Energy Equation	52
4.2.4	The Solid Energy Equation	53
4.2.5	Heat Flux Boundary Conditions	53
<b>5</b>	<b>Bed Geometry</b>	<b>55</b>
5.1	Porosity	55
5.1.1	One-Dimensional Distributions	58
5.1.2	Multidimensional Distributions	60
5.2	Hydraulic Diameter	62
5.3	Coordination Number	62
<b>6</b>	<b>Friction Factors</b>	<b>65</b>
6.1	Pebble Bed Correlations	67
6.1.1	Ergun Model	68
6.1.2	Fand Piecewise Linear Model	68
6.1.3	KTA Model	68
6.1.4	Eisfeld and Schnitzlein Model	68
6.2	Pipe Flow Correlations	69
6.2.1	Churchill Model	69

<b>7</b>	<b>Brinkman Viscosity</b> .....	<b>70</b>
7.1	Multiplier Model .....	70
<b>8</b>	<b>Heat Transfer Coefficients</b> .....	<b>71</b>
8.1	Interphase Heat Transfer Coefficients .....	71
8.1.1	Gnielinski Model .....	72
8.1.2	Gunn Model .....	73
8.1.3	KTA Model .....	73
8.1.4	Petrovic Model .....	73
8.1.5	Wakao Model .....	73
8.2	Wall-to-Fluid Heat Transfer Coefficient .....	74
8.2.1	Achenbach Model .....	74
8.2.2	Yagi and Wakao Model .....	74
<b>9</b>	<b>Effective Solid Thermal Conductivity</b> .....	<b>75</b>
9.1	Pebble-to-Pebble Radiation .....	79
9.1.1	Breitbach and Barthels Model .....	80
9.1.2	Kunii and Smith Model .....	80
9.1.3	Singh and Kaviany Model .....	81
9.1.4	Tsotsas Model .....	81
9.1.5	Vortmeyer Model .....	81
9.1.6	Wakao and Kato Model .....	82
9.1.7	Zehner, Bauer, and Schlünder Model .....	82
9.2	Multiphase Conduction .....	83
9.2.1	Volume Average Model .....	84
9.2.2	Deissler and Eian Model .....	84
9.2.3	Hsu 2-D Cylinder Array Model .....	85
9.2.4	Hsu 3-D Cube Array Model .....	85
9.2.5	Krupiczka Model .....	85
9.2.6	Kunii and Smith Model .....	85
9.2.7	Zehner, Bauer, and Schlünder Model .....	86
9.3	Pebble-to-Pebble Contact Conduction .....	86
9.3.1	Chan and Tien Model .....	87
9.3.2	Hsu Model .....	87
9.3.3	Hsu 2-D Sphere Array Model .....	88
9.3.4	Hsu 3-D Cube Array Model .....	88
9.3.5	Zehner, Bauer, and Schlünder Model .....	89
<b>10</b>	<b>Effective Fluid Thermal Conductivity</b> .....	<b>90</b>
10.1	Zero Dispersion Model .....	90
10.2	Linear Peclet Model .....	90
<b>11</b>	<b>Fluid Equations of State</b> .....	<b>92</b>
<b>12</b>	<b>Solid Equations of State</b> .....	<b>93</b>
12.1	Aluminum Oxide .....	93
12.2	Composite Mixture .....	93
12.3	Fire Brick .....	93
12.4	Function Dependence .....	94
12.5	Electric Graphite .....	94
12.6	Matrix Graphite .....	94
12.7	Porous Graphite .....	95
12.8	Pyrolytic Graphite .....	95
12.9	Silicon Carbide .....	95
12.10	Stainless Steel 316 .....	96

12.11 Uranium Dioxide .....	96
<b>13 Heterogeneous Solid Properties .....</b>	<b>97</b>
13.1 Arbitrary Component Numbers .....	98
13.1.1 Parallel .....	98
13.1.2 Series .....	99
13.2 Binary Systems .....	99
13.2.1 Chiew and Glandt .....	99
13.2.2 Lewis and Nielsen .....	99
13.2.3 Maxwell .....	100
<b>14 The Finite Element Method .....</b>	<b>101</b>
14.1 Weighted Residual Methods and the Galerkin Method .....	101
14.2 The Finite Element Method .....	102
14.2.1 The Weak Form .....	103
14.2.2 Shape and Test Functions .....	104
14.2.3 Software Implementation Considerations .....	104
14.2.4 Time Stepping .....	106
<b>15 Stabilization Methods .....</b>	<b>108</b>
15.1 An Example: The 1-D Convection-Diffusion Equation .....	108
15.2 Upwinding and Petrov-Galerkin Methods .....	111
15.3 Streamline-Upwind Petrov-Galerkin Stabilization .....	114
15.3.1 An Ideal Gas Example .....	114
15.3.2 The Stabilizing Effect .....	116
15.3.3 Calculation of the Stabilization Parameter $\tau_{SUPG}$ .....	116
15.4 SUPG Stabilization of the Navier-Stokes, Euler, and Friction-Dominated Models .....	118
<b>16 Solution of Nonlinear Equations .....</b>	<b>120</b>
16.1 Iterative Solution of Linear Equations .....	121
16.1.1 Matrix Splitting Methods .....	123
16.1.2 The Steepest Descent Method .....	124
16.1.3 The Conjugate Gradient Method .....	125
16.1.4 The Arnoldi Iteration .....	127
16.1.5 The GMRES Method .....	128
16.2 Jacobian Calculations .....	130
16.3 Preconditioning .....	130
<b>17 Mathematical Definitions and Concepts .....</b>	<b>132</b>
<b>18 Notation .....</b>	<b>138</b>
18.1 Superscripts and Overbars .....	144
<b>19 Appendix .....</b>	<b>145</b>
19.1 Mathematical Properties of Averages .....	145
19.2 Spatial Homogenization of the Conservation Equations .....	149
19.2.1 The Mass Equation .....	149
19.2.2 The Momentum Equation .....	150
19.2.3 The Energy Equation .....	153
19.3 Mathematical Structure of Advection and Diffusion Equations .....	156
19.4 Ideal Gas Inviscid Flux Jacobian Matrices .....	159
<b>References .....</b>	<b>160</b>

## Acronyms

<b>AD</b>	Automatic Differentiation
<b>BC</b>	Boundary Condition
<b>BCC</b>	Body Centered Cubic
<b>BE</b>	Backward Euler
<b>CD</b>	Conjugate Directions
<b>CFD</b>	Computational Fluid Dynamics
<b>CFP</b>	Coated Fuel Particle
<b>CG</b>	Conjugate Gradient
<b>CPU</b>	Central Processing Unit
<b>CVD</b>	Chemical Vapor Deposition
<b>DEM</b>	Discrete Element Method
<b>DG</b>	Discontinuous Galerkin
<b>EOS</b>	Equation of State
<b>FCC</b>	Face Centered Cubic
<b>FCM</b>	Fully Ceramic Microencapsulated
<b>FD</b>	Finite Difference
<b>FE</b>	Finite Element
<b>FEM</b>	Finite Element Method
<b>FLiBe</b>	LiF-BeF <sub>2</sub>
<b>GLS</b>	Galerkin Least Squares
<b>GMRES</b>	Generalized Minimal Residuals
<b>HCP</b>	Hexagonal Close Packing
<b>HEU</b>	High Enriched Uranium
<b>HSD</b>	Heat Source Decomposition
<b>HTGR</b>	High Temperature Gas Reactor
<b>JFNK</b>	Jacobian-Free Newton Krylov
<b>KTA</b>	Kerntechnischer Ausschuss
<b>LEU</b>	Low Enriched Uranium
<b>LHS</b>	left-hand-side

<b>LOCA</b>	Loss of Coolant Accident
<b>LTE</b>	Local Thermal Equilibrium
<b>LWR</b>	Light Water Reactor
<b>MFP</b>	Mean Free Path
<b>MOL</b>	Method of Lines
<b>MOOSE</b>	Multiphysics Object-Oriented Simulation Environment
<b>ODE</b>	Ordinary Differential Equation
<b>OEM</b>	One Equation Model
<b>PARFUME</b>	PARticle FUEl ModEl
<b>PBR</b>	Pebble Bed Reactor
<b>PBWR</b>	Pebble Bed Water Reactor
<b>PDE</b>	Partial Differential Equation
<b>PDF</b>	Probability Density Function
<b>PETSc</b>	Portable, Extensible Toolkit for Scientific Computation
<b>RANS</b>	Reynolds Averaged Navier Stokes
<b>REV</b>	Representative Elementary Volume
<b>RHS</b>	right-hand-side
<b>SBTL</b>	Spline-Based Table Lookup
<b>SC</b>	Simple Cubic
<b>SD</b>	Steepest Descent
<b>SND</b>	Symmetric Negative Definite
<b>SPD</b>	Symmetric Positive Definite
<b>SUPG</b>	Streamline Upwind Petrov-Galerkin
<b>T/H</b>	Thermal-Hydraulic
<b>TRISO</b>	TRistructural ISOtropic
<b>ZBS</b>	Zehner, Bauer, and Schlünder

# 1 Introduction

This manual is intended to provide a thorough description of the governing equations; the relations used for material, heat transfer, and fluid flow parameters; and the numerical method utilized in Pronghorn. Detailed derivations of the governing equations are given, beginning from first principles in order to be as explicit as possible about assumptions made along the way and guide any future methods extensions. Additional explanatory or tangential information that is not required for detailed understanding of the governing equations used in Pronghorn is shown in gray boxes in the text. The convention used in this document is to represent all class names (or file names) in typewriter font. The most up-to-date theory manual can be found in `doc/manual`.

Knowledge of the assumptions made in the governing equations is crucial to the correct use of any code. The table below collects the most important of these assumptions to serve as a concise reference for categories of simulations for which Pronghorn may give erroneous results. Other assumptions that are standard in the computational fluids community are detailed in the text, but are not included in the table below because they constitute assumptions made in virtually all choices of fluids simulation tools.

Table 1: Summary of major assumptions made in the governing equations in Pronghorn.

Assumptions made	Do not use Pronghorn if modeling:
No isolated voids	Non-connected voids of fluid
Single-phase flow	Multi-phase flow
All fluxes are differentiable	Shock waves or discontinuities
The only body force is gravity	Electromagnetic fluids
Fluid is Newtonian	Certain oils or fluids with internal structure
Zero viscous dissipation	Strong shock waves
Fluid is pure	Chemically-reacting flows
Local thermodynamic equilibrium	Strong shock waves
Negligible viscous heating of fluid	Large deformations in the fluid, $Br/Pe \gg 1$
Solid velocity is zero	Moving solid phase
Porosity independent of time	Moving solid phase

This document is organized as follows. In Section 2, the governing equations used in Pronghorn are derived and discussed. These equations rely on closure relationships that are discussed in Sections 11-12. Sections 3-4 summarize the class names used to specify equation models and Boundary Conditions (BCs). Methods used to stabilize the governing equations are discussed in Section 15. The numerical method used is discussed in Sections 14 and 16. Finally, important mathematical definitions and notation are given in Sections 17 and 18.

Finally, the SI unit system is used throughout; these units are listed in Table 2. Unless otherwise noted, all models are given in terms of these units.

Table 2: Set of units assumed in Pronghorn.

Quantity	Unit
molar mass	kg/mol
pressure	Pa
temperature	K
weight	kg
distance	m
time	s

## 2 Physical Models

Many man-made and natural systems exhibit wide ranges in temporal and/or spatial scales such that the use of models applicable to the “smallest common denominator” scale to uniformly represent all length scales are computationally impractical. Examples of such systems include Earth’s climate, drugs targeting cancer cell growth, and Pebble Bed Reactors (PBRs). Multiscale analysis is based on decomposing a complex system into a number of important temporal and spatial length scales, each described by different models that are aggregated together in an intelligent manner to obtain a representative solution for the relevant physical phenomena on all length scales at significantly reduced computational cost relative to fine-scale modeling of all scales. Pronghorn is a multiscale Thermal-Hydraulic (T/H) application intended for application to PBRs. As such, most of the discussion in this manual is posed in terms of PBRs, but the multiscale concepts presented are applicable to many other systems.

PBRs are naturally described in terms of three length scales — 1) the macroscale, defined over the entire reactor core which encompasses the pebble bed and reflectors; 2) the mesoscale, defined over a single fuel pebble; and 3) the microscale, defined over a single fuel particle. Fig. 1 depicts these three length scales for the pebble bed region. For typical PBR bed dimensions, the mesoscale is approximately 20 times smaller than the macroscale and the microscale is approximately 20000 times smaller than the mesoscale.

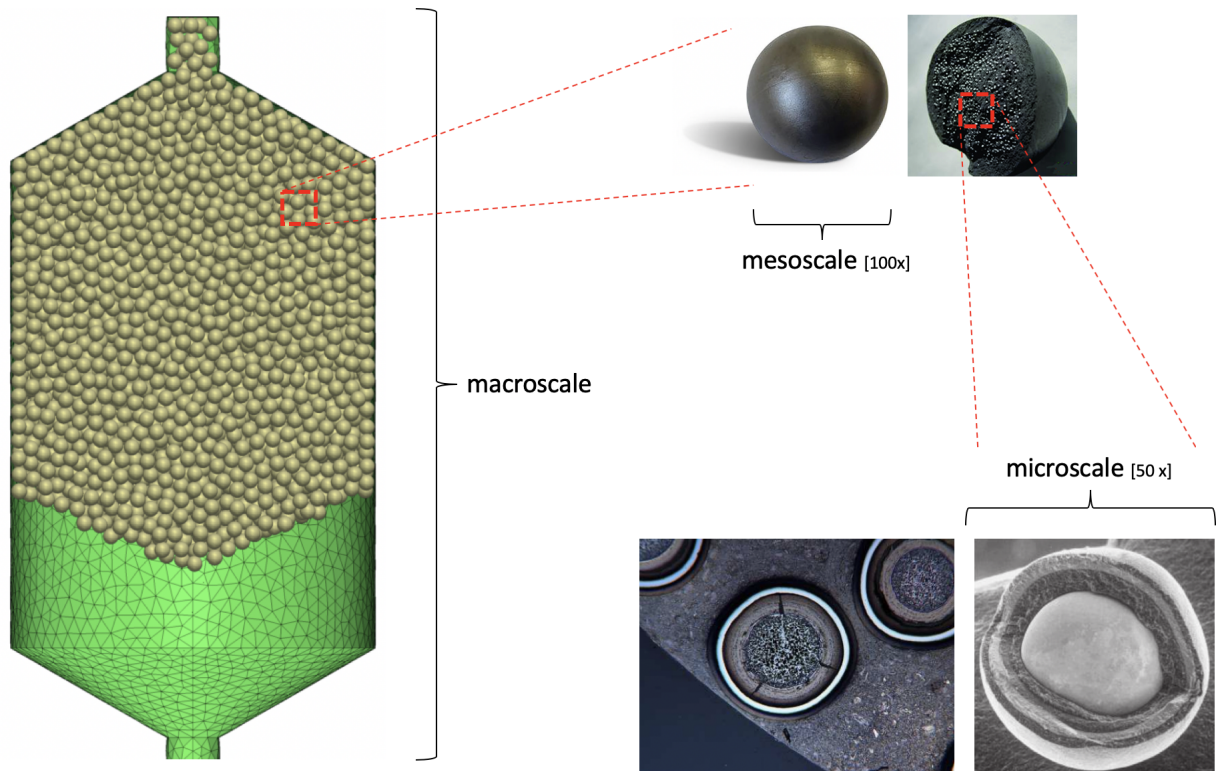


Figure 1: Decomposition of a PBR into three length scales [1–5].

By assuming fine length scales are periodic with respect to coarse length scales, BCs from the coarser-length solution are applied to finer-scale models to obtain representative thermal solutions for all length scales. This section describes Pronghorn’s multiscale modeling approach in terms of the three length scales shown in Fig. 1.

The macroscale length scale characterizes the two-phase mixture of fluid coolant with solid pebbles and reflector blocks. On a spatial scale on the order of the pore size between pebbles or the gap size between reflector blocks, the flow characteristics are highly irregular. Turbulent intensities along pipe centerlines are commonly on the order of 5%,

while experiments in pebble lattices show turbulent intensities as high as 50% in void centers [6].

However, on a scale encompassing small groups of pebbles or blocks, averaged flow properties are regular and predictable. Fluid flow and heat transfer through a two-phase mixture of fluid and solid phases, such as pebbles and coolant, is governed by the Navier-Stokes equations with conjugate heat transfer between the phases. Spatial homogenization of these governing equations over a length scale larger than the characteristic pore size captures physical phenomena that vary on the macroscale at the expense of only considering averaged fine-scale physics through model closures. Spatial homogenization over multiple phases is often referred to as the “porous media” method due to its connections to Henry Darcy’s study of water flow through sand in Dijon, France [7].

A porous media in general refers to a solid matrix with interconnected voids filled with gas and/or liquid. A diverse set of systems have been modeled as porous media, ranging from the flow of subterranean water through permeable rock to conductive heat flow through composite materials [8]. Within the nuclear engineering field, porous media models are commonly applied to flow and heat transfer in tube-in-shell heat exchangers [9], quenched corium heaps [10, 11], tritium breeder blankets in fusion reactors [12–14], and pin-fueled fission reactors [15]. For application to PBRs, the solid matrix is interpreted as the stacked reflector blocks and randomly heaped pebbles, while the interconnected voids correspond to the interstices between pebbles and blocks and the machined flow channels within blocks. The solid phase in a porous media is often referred to the “particles;” to avoid confusion with the particles within PBR fuels, “pebbles” is used to refer to the solid phase on the macroscale, while “particles” is used to refer to the Coated Fuel Particles (CFPs).

Sections 2.2-2.6 present the derivation of the spatially homogenized Navier-Stokes equations with solid conjugate heat transfer. Together with a set of closures described in Sections 11-12 that approximate the effect of local fluid flow and heat transfer on the macroscale and capture phase material properties, the porous media equations are used to describe the macroscale in PBRs. Future implementation of closures applicable to other systems will extend Pronghorn’s application space.

Spatial averaging eliminates the need to explicitly resolve the individual solid and fluid phases, resulting in many orders of magnitude reduction in mesh complexity and element count. Trillions of elements would be required to fully resolve all pebble surfaces in a PBR [16]. Further, the macroscale effects of turbulence are considered in closures rather than through Partial Differential Equations (PDEs) for turbulent viscosity needed to close Reynolds Averaged Navier Stokes (RANS) models. Together, these simplifications result in many orders of magnitude reduction in computational cost required to predict flow and heat transfer locally-averaged over groups of pebbles and reflector blocks in PBRs. Even if significant computing resources were available, it is challenging to generate meshes near pebble contact points without significant skew [17, 18]. Many Computational Fluid Dynamics (CFD) simulations use the “near miss” technique, where the pebble diameter is set to some percentage, around 99%, of its nominal value [18–23], which distorts the porosity used in closure models [17]. Finally, even if computational cost and mesh generation were both non-issues, the precise knowledge of the geometry is unknown, and some form of averaging over multiple Discrete Element Method (DEM) simulations would be required.

There are several important limitations of the homogenization approach with regards to predicting key safety metrics such as maximum fuel temperature that should be acknowledged. Because porous media models are based on spatial averaging, all local flow and heat transfer effects are only retained in an average sense. The distribution of temperature on the solid surface of individual pebbles and blocks is unknown. Resolved CFD simulations of pebbles show that surface temperatures are tens to hundreds of degrees higher, depending on the flow conditions, at stagnation points and near the low-flow recirculation regions behind pebbles than near thin, main-flow aligned, gaps [16, 20, 21, 23–27]. This surface temperature distribution affects the maximum fuel temperature, but the macroscale model is restricted to predicting the mesoscale and microscale temperatures based on a surface-uniform solid temperature, and hence will underpredict the true maximum fuel temperature. CFD simulations of fluid flow around pebbles with the CFPs resolved within each pebble are required to estimate the extent to which a uniform pebble surface temperature underpredicts the true maximum fuel temperature.

Chemical reactions are frequently strong functions of temperature. In addition to underpredicting the true maximum fuel temperature, the homogenization of the pebble surface temperature will underpredict the variation in chemical reaction rates over the surface of a pebble. Fig. 2 shows a graphite pebble, originally spherical in shape, with

significant and nonuniform oxidation that can only be captured in an average sense with a porous media model.

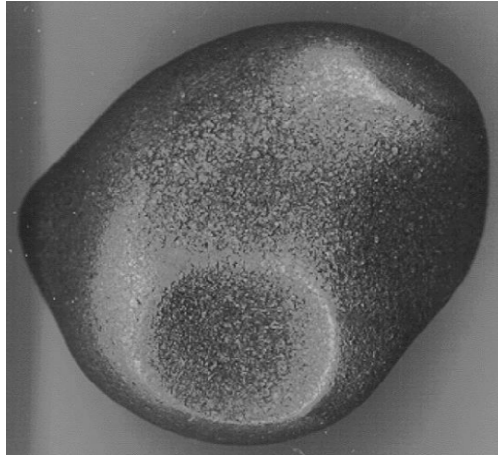


Figure 2: Corroded graphite pebble, originally spherical in shape, with nonuniform oxidation damage from the KFA Veluna experiment [28].

Some of these limitations of homogenized models could be partially overcome by coupling Pronghorn with a turbulence-resolved CFD code. Bulk simulation results from Pronghorn could be used as BCs on CFD closure generation simulations that feed back more accurate correlations into Pronghorn. For example, CFD simulations of pebbles show a strong dependence of heat transfer and drag on the assumed pebble packing [21,23,27,29], which would justify the use of CFD models to refine correlations based only on bulk bed properties. Future efforts will involve multi-scale analysis with Pronghorn and detailed CFD.

While there is not exact correspondence between the average of a detailed CFD simulation and a porous media simulation, provided appropriate error bounds are assumed for the porous media predictions, porous media models can be used for engineering-scale thermal design. Further, provided the neutron migration length is larger than the porous media averaging length, the use of a porous media T/H solution for temperature feedback in neutronics simulations is an acceptable simplification of the fluid flow and heat transfer [1, 30].

The majority of homogenization method development is performed in the chemical, geological, and mechanical engineering fields. Example application areas include analysis of groundwater flow and chemical reactions in complicated composite materials. Several common assumptions from these fields do not apply to reactor simulations, such as

- Thermal equilibrium between the fluid and solid phases; a non-equilibrium model is essential to capture convective heat transfer. Even in the absence of heat sources in either phase, the different thermal properties of the phases may yield different temperatures near boundaries [18, 31–33]. Thermal equilibrium is the default assumption in some commercial CFD porous media packages [34].
- Creeping flow; Pronghorn includes a model based on this assumption, but has additional models that better represent advective flows.
- Constant porosity; porosity variation near walls is essential to capturing flow channeling in reactor applications.
- Small pebble diameters, typically less than 1 mm, which may have important implications on pore turbulence in the larger-diameter pebble beds in reactor applications [25].
- Incompressible flow; most PBRs are characterized by core temperature changes on the order of hundreds of °C, making incompressibility and Boussinesq-type approximations invalid [35].

Sections 2.2-2.6 derive the macroscale model using the averaging theorems in Section 19.1 and Section 2.7 presents the mesoscale and microscale models. A summary of the governing equations is given in Section 2.10. This section defers all detailed discussion of the closure relationships to later sections.

## 2.1 Preliminary Considerations

The derivation of the conservation equations relies on the continuum approximation. As long as the flow length scale is much larger than the length scale on which atoms/molecules in the fluid exchange momentum, the fluid can be treated as a continuum. A fluid particle is defined as having a size intermediate to the flow and momentum exchange length scales, and consists of a group of atoms/molecules.

The validity of the continuum approximation can be quantified by the Knudsen number

$$Kn = \frac{\lambda_{\text{mfp}}}{L}, \quad (2.1)$$

where  $\lambda_{\text{mfp}}$  is the Mean Free Path (MFP) on which particles exchange momentum and  $L$  is the flow length scale. For gases at atmospheric pressure,  $\lambda_{\text{mfp}} \approx 10^{-8}$  m. At high pressure reactor conditions, the MFP is even smaller, so the continuum approximation is valid for gases, and hence liquids, in Pronghorn's intended application space.

This separation of scale is necessary to identify scaling arguments for fluid forces. There are two general types of forces experienced by a fluid particle —

1. External forces, or body forces, act on all molecules in the body. These forces vary slowly over a fluid particle such that the force is proportional to the particle volume.
2. Internal forces, or surface forces, are exerted on a fluid particle by the surrounding fluid. These forces are proportional to the surface area of the particle because the fluid particle is large relative to the length scale on which momentum is exchanged.

The derivation of the governing equations for conservation of mass, momentum, and energy from first principles leads to the inclusion of terms that are often dropped in reactor applications because certain physics are insignificant. The ability to neglect terms in the governing equations depends on the relative ratio of one physical phenomenon to another. It will be noted when terms are neglected, and representative values for dimensionless numbers characterizing these phenomena for different reactor designs are presented in Section 2.9 to justify these simplifications.

## 2.2 The Mass Equation

Because mass is conserved, the rate of change of the mass within an arbitrary volume  $\mathcal{V}$  consisting of a system must be zero, because a system is defined such that its boundaries are closed to mass flow,

$$\frac{d}{dt} \int_{\mathcal{V}(t)} \rho d\mathcal{V} = 0, \quad (2.2)$$

where  $\rho$  is the density and  $d(\cdot)/dt$  represents the material derivative of  $(\cdot)$  as defined in Eq. (17.1). Taking the time derivative of an integral whose bounds depend on time requires the use of the general transport theorem,

$$\frac{d}{dt} \int_{\mathcal{V}(t)} \rho d\mathcal{V} \equiv \int_{\mathcal{V}(t)} \frac{\partial \rho}{\partial t} d\mathcal{V} + \int_{S(t)} \rho \vec{w} \cdot \hat{n} dS, \quad (2.3)$$

where  $\vec{w}$  is the velocity of the surface  $S$  bounding the volume with unit normal vector  $\hat{n}$ . The surface velocity is equal to the fluid velocity if  $S$  is a material surface. Applying Eq. (2.3) to a material volume converts the system perspective to a control volume perspective,

$$\int_{\mathcal{V}(t)} \frac{\partial \rho}{\partial t} d\mathcal{V} + \int_{S(t)} \rho \vec{V} \cdot \hat{n} dS = 0, \quad (2.4)$$

where  $\vec{V}$  is the velocity of the fluid. The divergence theorem will frequently be used to transform a surface integral into a volume integral, which implicitly assumes that the integrand of the surface integral is differentiable. For shock waves or discontinuities near surfaces, fluxes may not be differentiable, and the divergence theorem does not apply. Further, expressing fluxes in volumetric terms introduces numerical errors in their representation that may cause violation of basic conservation principles [36]. Nevertheless, it is assumed that all fluxes are continuous such that the divergence theorem can be used. Applying the divergence theorem to Eq. (2.4) gives

$$\frac{\partial \rho}{\partial t} + \nabla \cdot (\rho \vec{V}) = 0, \quad (2.5)$$

Eq. (2.5) is often referred to as the ‘‘continuity’’ equation. The spatially homogenized version of Eq. (2.5) is derived in Section 19.2.1,

$$\frac{\partial (\epsilon \langle \rho_f \rangle^f)}{\partial t} + \nabla \cdot (\epsilon \langle \rho_f \rangle^f \langle \vec{V}_f \rangle^f) = 0. \quad (2.6)$$

Written in Pronghorn’s notation, Eq. (2.6) becomes

$$\frac{\partial (\epsilon \rho_f)}{\partial t} + \nabla \cdot (\epsilon \rho_f \vec{V}) = 0, \quad (2.7)$$

where  $\rho_f$  represents the intrinsic phase average of the fluid density and  $\vec{V}$  the intrinsic phase average of the fluid velocity.

## 2.3 The Momentum Equation

The conservation of momentum equation is derived beginning from a general treatment of a balance of linear momentum for an arbitrary continuum,

$$\frac{d}{dt} \int_{\mathcal{V}(t)} \rho V_i d\mathcal{V} = \int_{\mathcal{V}(t)} \rho b_i d\mathcal{V} + \int_{S(t)} \sigma_{ij} n_j dS, \quad (2.8)$$

where  $\sigma$  is the stress tensor, or the proportionality between the stress vector  $\vec{f}$  and the unit normal for an arbitrary volume with coordinate axes  $\vec{e}_j$  for  $j = 1 \cdots n_{sd}$ ,

$$\begin{aligned} f_i(\hat{n}) &= f_i(\vec{e}_j) n_j \\ &= \sigma_{ij} n_j. \end{aligned} \quad (2.9)$$

In Eq. (2.8),  $\vec{b}$  is the body force vector. For systems in which gravity is the only body force,  $\vec{b}$  equals  $\vec{g}$ , the gravity vector. The surface integral in Eq. (2.8) is converted to a volume integral using the divergence theorem,

$$\frac{d}{dt} \int_{\mathcal{V}(t)} \rho V_i d\mathcal{V} = \int_{\mathcal{V}(t)} \rho b_i d\mathcal{V} + \int_{\mathcal{V}(t)} \frac{\partial \sigma_{ij}}{\partial x_j} d\mathcal{V} . \quad (2.10)$$

Eq. (2.3) cannot be directly applied to the integral on the left-hand-side (LHS) of Eq. (2.10) because the integrand consists of a product. First, split this integral into a finite series of  $N$  elements,

$$\frac{d}{dt} \int_{\mathcal{V}(t)} \rho V_i d\mathcal{V} \equiv \frac{d}{dt} \sum_{k=1}^N V_{i,k} (\rho_k d\mathcal{V}_k) . \quad (2.11)$$

Because the mass  $\rho d\mathcal{V}$  of each element is constant due to mass conservation in a system whose boundaries are closed to mass flow, the time differentiation can be moved inside the summation to act only on the velocity. Extending this argument to the continuous form in Eq. (2.10),

$$\rho \frac{dV_i}{dt} = \rho b_i + \frac{\partial \sigma_{ij}}{\partial x_j} . \quad (2.12)$$

Eq. (2.12), often called the Cauchy equation, represents a balance of linear momentum for an arbitrary continuum. The only assumption is that mass is conserved in that continuum. In its most general form the stress tensor contains nine unknowns. Conservation of angular momentum shows that the stress tensor is symmetric if the only moments on the fluid particle are due to the resultant body and surface forces. As in virtually all applications, symmetry of the stress tensor is assumed here to reduce nine unknowns to six.

A constitutive relation is required for  $\sigma$ . The kinematics of deformation are useful in obtaining an intuitive understanding of this constitutive relation. The motion of a material element can be decomposed into three contributions — 1) translation, 2) rigid rotation, and 3) stretching. Consider two points in a fluid that are sufficiently close such that their separation  $\vec{\delta r}$  can be approximated by a one-term Taylor series,

$$\begin{aligned} V_i(\vec{r} + \vec{\delta r}, t) - V_i(\vec{r}, t) &= \frac{d}{dt} (\delta r_i) \\ &\approx \delta r_j \frac{\partial V_i}{\partial x_j} . \end{aligned} \quad (2.13)$$

The  $\approx$  symbol is replaced by  $=$  for the remainder of this discussion. Translation of a fluid particle is simply related to the magnitude of the velocity — the other two components require more explanation. Any tensor can be written as the sum of symmetric and antisymmetric parts. Applying this to the velocity gradient tensor gives

$$\frac{\partial V_i}{\partial x_j} = \underbrace{\frac{1}{2} \left( \frac{\partial V_i}{\partial x_j} + \frac{\partial V_j}{\partial x_i} \right)}_{\text{symmetric}} + \underbrace{\frac{1}{2} \left( \frac{\partial V_i}{\partial x_j} - \frac{\partial V_j}{\partial x_i} \right)}_{\text{antisymmetric}} , \quad (2.14)$$

where the symmetric and antisymmetric components are defined as

$$e_{ij} \equiv \frac{1}{2} \left( \frac{\partial V_i}{\partial x_j} + \frac{\partial V_j}{\partial x_i} \right) , \quad (2.15)$$

$$\xi_{ij} \equiv \frac{1}{2} \left( \frac{\partial V_i}{\partial x_j} - \frac{\partial V_j}{\partial x_i} \right) . \quad (2.16)$$

Within the applicability of a one-term Taylor series, setting  $e_{ij} = 0$  for all  $i$  and  $j$  to isolate the effect of  $\xi$  shows that  $\xi$  represents rigid rotation of the fluid particle. To determine the angular velocity characterizing this rigid rotation, Eq. (2.16) can be equivalently written as

$$\xi_{ij} = -\frac{1}{2}\epsilon_{ijk}\omega_k, \quad (2.17)$$

where  $\vec{\omega}$  is the vorticity,

$$\vec{\omega} \equiv \nabla \times \vec{V}, \quad (2.18)$$

and  $\epsilon_{ijk}$  is the permutation tensor defined in Eq. (17.13). Therefore, the angular velocity of the rigid rotation is  $\vec{\omega}/2$ . Because the symmetric component must be associated with stretching, the vorticity can also be interpreted as twice the instantaneous angular velocity of a material line element that is originally aligned along one of the eigenvectors of  $e$  (in which case  $e$  does not contribute anything to the angular velocity).

Within the limits of the one-term Taylor series,  $e$  represents stretching of the fluid particle along the eigenvectors, or principal axes, of  $e$ . The rates of this stretching, or principal strain rates, are given by the eigenvalues corresponding to the eigenvectors.  $e$  is often referred to as the “deformation tensor.” Because  $e$  is a  $3 \times 3$  symmetric, real, tensor, these eigenvectors are unique, real, and mutually orthogonal. When both  $e$  and  $\xi$  are nonzero (a material line not parallel to one of the principal axes of  $e$ ), the fluid particle is both stretched and rotated. The diagonal components of  $e$  represent stretching, while the off-diagonal components represent rotation of eigenvectors relative to another eigenvector (as opposed to  $\xi$  representing instantaneous rotation).

From Eq. (2.15), the trace of the deformation tensor is equal to the divergence of velocity,

$$\text{Tr}(e) = \nabla \cdot \vec{V}. \quad (2.19)$$

For a small volume, the time rate of change of the volume is approximately equal to the velocity of the surface dotted with the unit normal,

$$\begin{aligned} \frac{dV}{dt} &\approx \int_{S(t)} \vec{V} \cdot \hat{n} dS \\ &= \int_{V(t)} \nabla \cdot \vec{V} dV. \end{aligned} \quad (2.20)$$

If  $\nabla \cdot \vec{V}$  can be taken as constant over the small volume, then  $\nabla \cdot \vec{V}$  can be interpreted as the fractional rate of increase of an infinitesimal volume,

$$\frac{1}{V} \frac{dV}{dt} \approx \nabla \cdot \vec{V}. \quad (2.21)$$

Knowing that  $\nabla \cdot \vec{V}$  represents a volume expansion, the motion at a point described by Eq. (2.13) can be separated into 1) an isotropic radial expansion (characterized by  $\nabla \cdot \vec{V}$ ), 2) a volume-preserving motion obtained by subtracting off the volume change from  $e_{ij}$ , and 3) a rigid rotation,

$$\begin{aligned}
V_i(\vec{r} + \vec{\delta r}, t) - V_i(\vec{r}, t) &= \delta r_j \frac{\partial V_i}{\partial x_j} \\
&= \delta r_j e_{ij} - \frac{1}{2} \delta r_j \epsilon_{ijk} \omega_k \\
&= \underbrace{\frac{1}{3} \delta r_i \nabla \cdot \vec{V}}_{\text{radial expansion}} + \underbrace{\delta r_j \left( e_{ij} - \frac{1}{3} \nabla \cdot \vec{V} \delta_{ij} \right)}_{\text{constant-volume motion}} - \underbrace{\frac{1}{2} \delta r_j \epsilon_{ijk} \omega_k}_{\text{rigid rotation}},
\end{aligned} \tag{2.22}$$

where  $\delta_{ij}$  is the Kronecker delta defined in Eq. (17.14). A factor of  $1/3$  appears to cancel the 3 that results from summation over  $i$  and  $j$  in  $\delta_{ij}$ . The Navier-Stokes equations assume a Newtonian fluid constitutive relationship for  $\sigma$ ; this model assumes that  $\sigma$  is a linear, isotropic, function of the deformation tensor  $e$ . Because  $\xi$  causes a rigid rotation, but no deformation, there is no contribution in the stress tensor due to  $\xi$ . For simple fluids, the Newtonian approximation is an excellent assumption over a wide range of strain rates, but for molecules consisting of long chains of atoms, or with suspended solid particles, shearing the fluid breaks down an internal structure that can align the molecules such that the shear stress is not a linear function of the velocity gradient. The constitutive relationship for a Newtonian fluid is, in its most general form,

$$\sigma_{ij} = -P\delta_{ij} + c_{ijkl}e_{kl}, \tag{2.23}$$

where  $P$  is the thermodynamic pressure determined from an equation of state and  $c$  is a fourth-order tensor. The first term on the right-hand-side (RHS) represents isotropic shear stresses due to pressure forces, a requirement to match hydrostatic observations.

In order to reduce the 81 components of  $c$  to a fewer number of unique parameters, isotropy of the stress is assumed. If the axes of a rectangular prism of fluid are aligned with the eigenvectors of  $e$ , then the fluid element will not rotate, but will experience a stretching along the eigenvectors of  $e$ . For an isotropic fluid, the stresses on the faces of that prism should be purely normal — if this were not the case, then the fluid would have a preferred direction of deformation, an anisotropic feature. In order to show that selecting axes along the principal axes of  $e$  for an isotropic fluid produces a diagonal  $e$  (since a diagonal  $e$  means that there are only normal stresses inducing stretching, and no shear stresses inducing rotation), it must be required that when the principal axes of  $\sigma$  coincide with the principal axes of  $e$ ,  $\sigma$  is diagonal (no shear stresses).

This requirement gives  $c_{12kl} = 0$  for all  $k$  and  $l$ . Physically, this means that the same stress rate in different coordinate frames does not give rise to different shear stresses. This reduces the 81 components of  $c_{ijkl}$  to nine. Isotropy also requires that  $c_{1122} = c_{1133}$ , since rotation of axes by  $90^\circ$  should not change the fluid response. With these requirements, the constitutive relationship for a Newtonian fluid is

$$\sigma_{ij} = -P\delta_{ij} + 2\mu e_{ij} + \lambda \nabla \cdot \vec{V} \delta_{ij}, \tag{2.24}$$

where  $\mu$  is the dynamic viscosity and  $\lambda$  is the second coefficient of viscosity. By investigating the form of  $\sigma_{11}$ ,  $2\mu = c_{1111} - c_{1122}$  and  $\lambda = c_{1122}$ ; hence,  $\mu$  and  $\lambda$  just represent combinations of the entries of the  $c$  tensor. For Newtonian fluids,  $\mu$  is only a function of pressure and temperature, while for non-Newtonian fluids, there is a nonlinear relationship between  $\mu$  and pressure, temperature, and the rate of shearing strain (assuming that the Newtonian constitutive law is still used).

Interpreting the significance of each of the terms in Eq. (2.24) is simpler if the contribution associated with volume change is subtracted to show similarity to Eq. (2.22),

$$\sigma_{ij} = -P\delta_{ij} + \underbrace{2\mu \left( e_{ij} - \frac{1}{3} \nabla \cdot \vec{V} \delta_{ij} \right)}_{\text{volume-preserving deformation}} + \underbrace{\left( \lambda + \frac{2\mu}{3} \right) \nabla \cdot \vec{V} \delta_{ij}}_{\text{volume dissipative term}}. \tag{2.25}$$

The deviatoric stress tensor  $\tau$ , also known as the viscous shear stress tensor, represents volume-preserving deformation,

$$\tau_{ij} \equiv \mu \left( \frac{\partial V_i}{\partial x_j} + \frac{\partial V_j}{\partial x_i} \right) - \frac{2\mu}{3} \nabla \cdot \vec{V} \delta_{ij} . \quad (2.26)$$

Due to competing effects of volume change and isochoric deformation, measuring  $\lambda$  is difficult. The Navier-Stokes equations are therefore usually posed in terms of  $\mu$  and  $\zeta$ , the bulk viscosity,

$$\zeta \equiv \lambda + \frac{2\mu}{3} . \quad (2.27)$$

The bulk viscosity is only important for highly compressible fluids (very high temperatures and pressures) [36]. In compression or expansion, internal processes act to restore thermodynamic equilibrium. These restoration processes usually act very quickly such that they almost exactly coincide with the change in volume of the fluid particle. However, if there is a significant discrepancy between the attainment of thermal equilibrium and the change in volume, then  $\zeta$  may be much larger than  $\mu$ , and cannot be neglected.

The term proportional to  $\zeta$  in Eq. (2.25) is often referred to as the viscous dissipation term. This term is only present if  $\nabla \cdot \vec{V} \neq 0$ , and hence is zero for incompressible fluids. In situations with significantly nonzero  $\nabla \cdot \vec{V}$ , the physics are often so different that an entirely different constitutive equation should be used. Substituting Eq. (2.25) into Eq. (2.12) gives the Navier-Stokes equations, where Eq. (2.15) is used to insert the definition of  $e$  and Eq. (2.27) for the definition of  $\zeta$ ,

$$\begin{aligned} \rho \frac{dV_i}{dt} &= \rho b_i + \frac{\partial}{\partial x_j} \left\{ -P \delta_{ij} + 2\mu \left[ \frac{1}{2} \left( \frac{\partial V_i}{\partial x_j} + \frac{\partial V_j}{\partial x_i} \right) - \frac{1}{3} \nabla \cdot \vec{V} \delta_{ij} \right] + \zeta \nabla \cdot \vec{V} \delta_{ij} \right\} \\ &= \rho b_i - \nabla P + \nabla \cdot \left\{ \mu \left[ \nabla V_i + (\nabla V_i)^T \right] - \frac{2\mu}{3} \nabla \cdot \vec{V} \mathbf{I} \right\} + \nabla \cdot (\zeta \nabla \cdot \vec{V}) . \end{aligned} \quad (2.28)$$

The volume dissipative term is commonly neglected by setting  $\lambda = -2\mu/3$ , i.e. setting  $\zeta = 0$  [37]. This gives the conservation of momentum equation most commonly used,

$$\frac{\partial(\rho \vec{V})}{\partial t} + \nabla \cdot (\rho \vec{V} \vec{V}) = \rho \vec{b} - \nabla P + \nabla \cdot \tau , \quad (2.29)$$

where  $\vec{V} \vec{V}$  is short-hand notation for  $\vec{V} \otimes \vec{V} = V_i V_j$ , which represents an outer product of  $\vec{V}$  with itself. Many equivalent forms of Eq. (2.29) can be derived through manipulations of mechanical and thermodynamic relations. The Crocco-Vazsonyi and Bernoulli forms are derived here for later use in specifying stagnation BCs. By expressing  $\partial V_i / \partial x_j$  in terms of  $e_{ij}$  and  $\xi_{ij}$ , and taking the inner product with  $V_j$ , gives

$$V_j \frac{\partial V_i}{\partial x_j} = \nabla \cdot \left( \frac{1}{2} V_j V_j \right) + \vec{\omega} \times \vec{V} . \quad (2.30)$$

Inserting the above result and the enthalpy differential defined in Eq. (2.57) into Eq. (2.29) gives the Crocco-Vazsonyi form of the Navier-Stokes equations,

$$\frac{\partial \vec{V}}{\partial t} + \nabla \cdot \left( \frac{1}{2} V^2 + h + gz \right) - T \nabla s - \vec{V} \times \vec{\omega} - \frac{1}{\rho} \nabla \cdot \tau = 0 , \quad (2.31)$$

where  $\vec{b}$  was replaced by  $\vec{g}$ , the gravitational acceleration vector. The gravitational acceleration vector was then moved inside the gradient by assuming that  $\vec{g} = -g\vec{e}_z$  such that  $\nabla(gz) = g\vec{e}_z$ . In addition,  $h$  is the enthalpy defined in Eq. (2.45) and  $s$  is entropy. Eq. (2.31) reveals that steady flow will be rotational in a stationary reference frame unless the flow is isentropic, frictionless, isoenergetic (term in parentheses is constant), and the inlet BC is irrotational. The Bernoulli equation can be derived from Eq. (2.31) using two different approximations. If the flow is isentropic, steady, irrotational, and frictionless,

$$\nabla \left( \frac{1}{2}V^2 + h + gz \right) = 0. \quad (2.32)$$

Eq. (2.32) applies *anywhere* in the flow field. The second approach for deriving the Bernoulli equation takes the scalar product of Eq. (2.31) with velocity to obtain a form of the equation that only applies along a streamline in isentropic, steady, and frictionless flow,

$$\vec{V} \cdot \nabla \left( \frac{1}{2}V^2 + h + gz \right) = 0. \quad (2.33)$$

Eq. (2.33) does not require the irrotational assumption made in Eq. (2.32), but does require application along a streamline. It is also frequently assumed in the Bernoulli equation that the flow is incompressible, in which case  $e = e(\rho, s)$  is constant, and  $h$  can be replaced by  $P/\rho$ .

The incompressible form of Eq. (2.28) is derived by expanding all terms and setting  $\nabla \cdot \vec{V} = 0$ , giving

$$\rho \frac{d\vec{V}}{dt} = \rho \vec{b} - \nabla P + \nabla \cdot (\mu \nabla \vec{V}) \quad (2.34)$$

For constant viscosity, the Laplace operator  $\nabla \cdot \nabla(\cdot)$  represents isotropic diffusion. Assuming  $\vec{b} = \vec{g}$ , Eq. (2.34) is sometimes written without the gravitational term by bundling gravity into the pressure term. Assume that gravity is equal  $\vec{g} = g\vec{e}_z$  and introduce a reduced pressure  $P'$ :

$$P' = P + \rho gz \quad (2.35)$$

Then, as long as  $\rho$  is uniform (incompressible flow), the gravitational term in Eq. (2.34) can be represented as follows:

$$\begin{aligned} \rho \vec{g} &\rightarrow \rho g \vec{e}_z \\ &\rightarrow \nabla(\rho gz) \end{aligned} \quad (2.36)$$

Then, gravity can be bundled in with the pressure term in Eq. (2.34):

$$\rho \frac{d\vec{V}}{dt} = -\nabla P' + \nabla \cdot \tau \quad (2.37)$$

If there are no free surfaces in the domain, then pressure will not appear as a BC, and within the constraints of incompressible flow, gravity does not impact the solution.

By nondimensionalization arguments, the Navier-Stokes equations will only provide a good representation of fluid momentum conservation if both the normalized velocity and surface force, or drag, are dependent only on the scaled spatial and time scales and the Reynolds number  $Re$ . This is often referred to as ‘‘Reynolds number similarity.’’

The spatially homogenized version of Eqs. (2.29) is derived in Section 19.2.2,

$$\frac{\partial(\varepsilon\langle\rho_f\rangle^f\langle\vec{V}_f\rangle^f)}{\partial t} + \nabla \cdot \left[ \varepsilon\langle\rho_f\rangle^f\langle\vec{V}_f\rangle^f\langle\vec{V}_f\rangle^f \right] = -W\langle\rho_f\rangle^f\langle\vec{V}_f\rangle^f + \varepsilon\nabla\langle P_f\rangle^f + \nabla \cdot \left[ \tilde{\mu}\nabla\langle\vec{V}_f\rangle^f \right] + \varepsilon\langle\rho_f\rangle^f\vec{b}, \quad (2.38)$$

where the viscous term in Eq. (19.42) is represented as the sum of a distributed loss friction term that captures the  $\varepsilon\langle\mu_f\rangle\mathcal{A}(\mathbf{I} + \mathcal{E})^{-1}$  and  $\varepsilon\langle\mu_f\rangle\mathcal{B}(\mathbf{I} + \mathcal{E})^{-1}$  terms, with each of these terms represented as vectors instead of tensors. The sum of these two terms (with  $\mathcal{A}$  divided by  $\langle\rho_f\rangle^f$  to obtain the proper units) is denoted as  $W$ .  $W$  represents a combined Darcy and Forchheimer friction factor. A distributed loss friction model is usually sufficient to capture the important physics in Eq. (19.42) because the length over which the deviatoric stress acts is on the order of several pore diameters [38].

However, an optional Brinkman-type viscous stress term may also be included to allow no-slip BCs to be applied and interactions between advective and diffusive fluxes to be considered. Brinkman's model expresses the viscous stress term in Eq. (19.42) as the sum the Darcy and Forchheimer drag plus a velocity laplacian with effective viscosity  $\tilde{\mu}$ , models for which are discussed in Section 7 [39–41]. Brinkman's model does not have the same validation basis as either Darcy's or Forchheimer's drag terms, and is generally thought to only be applicable for  $\varepsilon > 0.8$ . At low porosities, the solid matrix impedes direct transfer of momentum due to viscous forces and the majority of stresses are communicated via pressure [39]. Some authors staunchly defend Brinkman's hypothesis, however [42]. This Brinkman model is therefore available as a modeling option that should be used with caution for low-Reynolds number flows; at the high-Reynolds numbers typical of most nuclear applications, the additional viscous stress term is often negligibly small anyways.

Therefore, writing Eq. (2.39) in Pronghorn's notation gives

$$\frac{\partial(\varepsilon\rho_f\vec{V})}{\partial t} + \nabla \cdot (\varepsilon\rho_f\vec{V}\vec{V}) = -W\rho_f\vec{V} + \varepsilon\nabla P + \nabla \cdot (\tilde{\mu}\nabla\vec{V}) + \varepsilon\rho_f\vec{g}. \quad (2.39)$$

In Pronghorn's notation,  $\rho_f$  represents the intrinsic phase average of the fluid density,  $\vec{V}$  the intrinsic phase average of the fluid velocity, and  $P$  the intrinsic phase average of the pressure. For creeping flows, the total derivative of momentum may optionally be neglected to give the friction-dominated model described in Section 2.5.

## 2.4 The Fluid Energy Equation

This section presents two derivations of the conservation of energy equation. The first is an equation for total energy conservation and the second is an equation for thermal energy conservation. Both are derived in order to provide background needed for the friction-dominated model described in Section 2.5. The first law of thermodynamics relates the rate of change of energy in a volume to the rate of heat and work. The total energy is the sum of internal energy and kinetic energy. The internal energy per unit mass,  $e$ , represents the potential energy due to bond stretching plus the mean kinetic energy of molecules when moving in a frame of reference moving with the center of mass velocity (i.e. vibratory motion). The total energy per unit mass,  $E$ , is then

$$E = e + \frac{1}{2}V_iV_i. \quad (2.40)$$

Conservation of total energy requires a balance between the power supplied by the contact and body forces and the heat addition. This balance is obtained by multiplying all the forces in the momentum balance in Eq. (2.10) by velocity, since power equals force times velocity,

$$\frac{d}{dt} \int_{\mathcal{V}(t)} \rho E d\mathcal{V} = \int_{\mathcal{V}(t)} \rho b_i V_i d\mathcal{V} + \int_{S(t)} V_i \sigma_{ij} n_j dS - \int_{S(t)} q_i n_i dS + \int_{\mathcal{V}(t)} \dot{q} d\mathcal{V}, \quad (2.41)$$

where  $\vec{q}$  is the heat flux vector representing heat flow out of the fluid particle and  $\dot{q}$  is a volumetric heat source. Applying the divergence theorem to Eq. (2.41),

$$\frac{d}{dt} \int_{\mathcal{V}(t)} \rho E d\mathcal{V} = \int_{\mathcal{V}(t)} \rho b_i V_i d\mathcal{V} + \int_{\mathcal{V}(t)} \frac{\partial}{\partial x_j} (V_i \sigma_{ij}) d\mathcal{V} - \int_{\mathcal{V}(t)} \frac{\partial q_j}{\partial x_j} d\mathcal{V} + \int_{\mathcal{V}(t)} \dot{q} d\mathcal{V} . \quad (2.42)$$

By the same argument that was used to bring the time differentiation under the integral in Eq. (2.11), Eq. (2.42) simplifies to

$$\begin{aligned} \rho \frac{dE}{dt} &= \rho \vec{b} \cdot \vec{V} + \frac{\partial}{\partial x_j} (V_i \sigma_{ij}) - \nabla \cdot \vec{q} + \dot{q} \\ &= \rho \vec{b} \cdot \vec{V} + \underbrace{V_i \frac{\partial \sigma_{ij}}{\partial x_j}}_{\text{contact power}} + \underbrace{\sigma_{ij} \frac{\partial V_i}{\partial x_j}}_{\text{deformation power}} - \nabla \cdot \vec{q} + \dot{q} . \end{aligned} \quad (2.43)$$

By inserting the constitutive relation for  $\sigma$  from Eq. (2.25), a form useful for implementation is obtained,

$$\rho \frac{dE}{dt} = \rho \vec{b} \cdot \vec{V} - \nabla \cdot (P\vec{V}) + \nabla \cdot (\tau\vec{V}) - \nabla \cdot \vec{q} + \dot{q} \quad (2.44a)$$

$$\frac{\partial(\rho E)}{\partial t} + \nabla \cdot (\rho H\vec{V}) = \rho \vec{b} \cdot \vec{V} + \nabla \cdot (\tau\vec{V}) - \nabla \cdot \vec{q} + \dot{q} , \quad (2.44b)$$

where volume dissipative terms have been neglected. The enthalpy per unit mass  $h$  and total enthalpy per unit mass  $H$  are defined as

$$h = e + Pv , \quad (2.45)$$

$$H = E + Pv , \quad (2.46)$$

where  $v$  is the specific volume,

$$v \equiv \frac{1}{\rho} . \quad (2.47)$$

Eq. (2.44b) can equivalently be written in terms of  $H$  using Eq. (2.46),

$$\frac{\partial(\rho H)}{\partial t} + \nabla \cdot (\rho H \vec{V}) = \frac{\partial P}{\partial t} + \rho \vec{b} \cdot \vec{V} + \nabla \cdot (\tau \vec{V}) - \nabla \cdot \vec{q} + \dot{q}. \quad (2.48)$$

In flows dominated by thermal effects, rather than kinetic effects,  $E$  is often approximated as  $e$ , in which case  $H$  is equal to  $h$ , and the above equation is written as

$$\frac{\partial(\rho h)}{\partial t} + \nabla \cdot (\rho h \vec{V}) = \frac{\partial P}{\partial t} + \rho \vec{b} \cdot \vec{V} + \nabla \cdot (\tau \vec{V}) - \nabla \cdot \vec{q} + \dot{q}. \quad (2.49)$$

Within this approximation,  $\partial P / \partial t$  is often assumed to be zero. If the flow is incompressible,  $e = C_v T$  because the flow is always at constant volume, and Eq. (2.49) can be written as

$$\rho \frac{\partial(C_v T)}{\partial t} + \rho \vec{V} \cdot \nabla(e + P) = \rho \vec{b} \cdot \vec{V} + \vec{V} \cdot \nabla \tau - \nabla \cdot \vec{q} + \dot{q}, \quad (2.50)$$

where the  $\partial P / \partial t$  term on both sides cancels without the need to assume it is zero and  $C_v$  is defined in Eq. (2.63).

Neglecting the  $\nabla \cdot (\tau \vec{V})$  viscous heating effects and assuming that  $\vec{q} = -k \nabla T$  represents the conduction flux with  $k$  the thermal conductivity, Eq. (2.44) becomes

$$\frac{\partial(\rho E)}{\partial t} + \nabla \cdot (\rho H \vec{V}) - \rho \vec{b} \cdot \vec{V} - \nabla \cdot (k \nabla T) - \dot{q} = 0. \quad (2.51)$$

The derivation of the conservation of thermal energy equation in terms of temperature is more involved than the derivation of Eq. (2.51). Equilibrium thermodynamics is used to relate total energy to entropy, and then entropy to temperature. In order to obtain the entropy equation, derive the mechanical energy component of Eq. (2.43) by taking the scalar product of the Cauchy momentum equation in Eq. (2.12) with velocity,

$$\begin{aligned} \rho b_i V_i + V_i \frac{\partial \sigma_{ij}}{\partial x_j} &= V_i \rho \frac{dV_i}{dt} \\ &= \rho \frac{d}{dt} \left( \frac{1}{2} V_i V_i \right). \end{aligned} \quad (2.52)$$

A balance of internal energy equation is then obtained by subtracting Eq. (2.52) from Eq. (2.43),

$$\rho \frac{de}{dt} = \sigma_{ij} \frac{\partial V_i}{\partial x_j} - \nabla \cdot \vec{q} + \dot{q}. \quad (2.53)$$

If the fluid is incompressible,  $e = C_v T$  because the fluid is at constant volume, and Eq. (2.53) simplifies to

$$\rho \frac{d(C_v T)}{dt} = \tau_{ij} \frac{\partial V_i}{\partial x_j} - \nabla \cdot \vec{q} + \dot{q}. \quad (2.54)$$

In order to obtain equations for temperature and entropy, relations from equilibrium thermodynamics are needed. But, the dissipative terms on the RHS of Eq. (2.43) do not represent equilibrium conditions at all. Hence, *local* thermodynamic equilibrium must be assumed. While in a global sense the system is not in thermodynamic equilibrium, each fluid particle is assumed to be in equilibrium, a valid approximation provided a fluid particle reaches equilibrium with its surroundings quickly. The time scale on which a fluid particle reaches equilibrium with its surroundings can

usually be cast as some multiple of the collision frequency. Provided this time scale is much smaller than the time scale characterizing the problem, local thermodynamic equilibrium can be assumed.

The classification of a system depends on the number of available energy transfer modes. Any system always has at least two modes of energy transfer - work and heat. Simple systems only experience pressure-volume work, and are not subject to work by electromagnetic fields or other means. Hence, there are two ways by which to change the energy of a simple system - by pressure-volume work and by heat transfer. One thermodynamic property is needed to fix the state of a system for each mode of energy transfer, so the state of a simple, pure system can be fixed with two properties. While no fluid is truly pure, a fluid can be approximated as pure as long as 1) the components are well-mixed, 2) there is no significant reaction between the components, and 3) the components do not break apart in the flow. The first law of thermodynamics, for a simple, pure system is

$$de = \delta q + \delta w , \quad (2.55)$$

where  $q$  represents heat addition and  $w$  represents work done on the body.  $\delta$  indicates a path-dependent term. For an internally reversible process,  $\delta q = Tds$ ; because both temperature and entropy are properties, the same expression can also be applied to internally irreversible processes. The only work mode is pressure-volume work, so  $\delta w = -Pdv$ . Inserting these definitions into Eq. (2.55),

$$de = Tds - Pdv . \quad (2.56)$$

Eq. (2.56) is an exact differential, meaning that any form of a differential in  $e$ ,  $s$ , and  $v$  is equivalent to Eq. (2.56). Substituting Eq. (2.45) into Eq. (2.56) gives a differential for enthalpy,

$$dh = Tds + vdP . \quad (2.57)$$

Using Eq. (2.56), the internal energy equation in Eq. (2.53) can be formulated into an equation for entropy conservation,

$$\rho \left( T \frac{ds}{dt} - P \frac{dv}{dt} \right) = \sigma_{ij} \frac{\partial V_i}{\partial x_j} - \nabla \cdot \vec{q} + \dot{q} . \quad (2.58)$$

The second term on the LHS can be related to the velocity using the continuity equation, Eq. (2.5):

$$\begin{aligned} \frac{d}{dt} (\rho^{-1}) &= \frac{-1}{\rho^2} \frac{d\rho}{dt} \\ &= \frac{\nabla \cdot \vec{V}}{\rho} . \end{aligned} \quad (2.59)$$

Inserting Eq. (2.59) into Eq. (2.58) and using the constitutive relation for a Newtonian fluid gives

$$\begin{aligned} \rho T \frac{ds}{dt} - P \nabla \cdot \vec{V} &= \left( -P \delta_{ij} + \tau_{ij} + \zeta \nabla \cdot \vec{V} \delta_{ij} \right) \frac{\partial V_i}{\partial x_j} - \nabla \cdot \vec{q} + \dot{q} \\ \rho T \frac{ds}{dt} &= \tau_{ij} \frac{\partial V_i}{\partial x_j} + \zeta (\nabla \cdot \vec{V})^2 - \nabla \cdot \vec{q} + \dot{q} . \end{aligned} \quad (2.60)$$

Although viscous dissipation effects are neglected in the implementation of the energy equation, they are retained in Eq. (2.60) for illustration purposes in the surrounding discussion. Viscous dissipation effects are neglected in actual

implementation. Eq. (2.60) shows that the flow is nearly isentropic along streamlines for 1) low-viscous-dissipation, 2) minimally compressive (no shock waves), and 3) adiabatic (no heat conduction) flows.

The classical Euler equations are a simplification of the Navier-Stokes equations for inviscid flow with no external heat sources, conductive heating, or gravitational forces. Based on the equations derived previously, several analytical tools can be used to assess numerical errors made in solving the Euler equations. For the steady Euler equations with no external body forces, Eq. (2.51) shows that  $H$  should be constant along streamlines. If the inflow BCs specify a constant  $H$ , then the entire flow field is characterized by a constant  $H$ . Eq. (2.60) shows that for initially continuous flow variations (such that  $\zeta \approx 0$  can be assumed without significant loss of accuracy),  $s$  should also be constant along streamlines. If the inflow BCs specify a constant  $s$ , then the entire flow field is characterized by a constant  $s$ . Therefore, for totally uniform inflow BCs, the classical Euler equations are equivalent to the potential flow equations, and the entire flow field has constant entropy and total enthalpy.

Equilibrium thermodynamics is now used to provide a relationship between entropy, temperature, and pressure; application of the chain rule to a simple, pure fluid gives

$$\frac{ds}{dt} = \left( \frac{\partial s}{\partial T} \right)_P \frac{dT}{dt} + \left( \frac{\partial s}{\partial P} \right)_T \frac{dP}{dt}. \quad (2.61)$$

Specific heats are defined according to the amount of heat required to increase temperature under different conditions,

$$C_p \equiv \left( \frac{\delta q}{\delta T} \right)_P \quad (2.62a)$$

$$= \left( \frac{\partial h}{\partial T} \right)_P \quad (2.62b)$$

$$= T \left( \frac{\partial s}{\partial T} \right)_P, \quad (2.62c)$$

$$C_v \equiv \left( \frac{\delta q}{\delta T} \right)_v \quad (2.63a)$$

$$= \left( \frac{\partial e}{\partial T} \right)_v \quad (2.63b)$$

$$= T \left( \frac{\partial s}{\partial T} \right)_v, \quad (2.63c)$$

where several equivalent forms are obtained using Eqs. (2.56) and (2.57). Hence, the coefficient on the first term on the RHS of Eq. (2.61) is  $C_p/T$ . The second coefficient in Eq. (2.61) can be determined from a Maxwell identity obtained from manipulation of Eq. (2.56) using the principle of exactness,

$$- \left( \frac{\partial s}{\partial P} \right)_T = \left( \frac{\partial v}{\partial T} \right)_P. \quad (2.64)$$

The expansivity, or volumetric coefficient of thermal expansion, is defined as

$$\begin{aligned} \beta &\equiv \frac{1}{v} \left( \frac{\partial v}{\partial T} \right)_P \\ &= -\frac{1}{\rho} \left( \frac{\partial \rho}{\partial T} \right)_P. \end{aligned} \quad (2.65)$$

Combining Eqs. (2.65), (2.64), (2.62), and (2.61) gives

$$\frac{ds}{dt} = \frac{C_p}{T} \frac{dT}{dt} - \beta v \frac{dP}{dt}. \quad (2.66)$$

Substituting Eq. (2.66) into Eq. (2.60), assuming  $\vec{q} = -k\nabla T$ , and including a volumetric heat source  $\dot{q}$  in the same manner as was done in Eq. (2.41) gives a statement of conservation of thermal energy,

$$\rho C_p \frac{dT}{dt} - T\beta \frac{dP}{dt} = \tau_{ij} \frac{\partial V_i}{\partial x_j} + \zeta(\nabla \cdot \vec{V})^2 + \nabla \cdot (k\nabla T) + \dot{q} \quad (2.67)$$

An alternative form of Eq. (2.67) is sometimes seen in the literature. Instead of taking entropy as a function of pressure and temperature as in Eq. (2.61), the entropy could alternatively have been taken as a function of specific volume and temperature,

$$\frac{ds}{dt} = \left( \frac{\partial s}{\partial T} \right)_v \frac{dT}{dt} + \left( \frac{\partial s}{\partial v} \right)_T \frac{dv}{dt}. \quad (2.68)$$

From Eq. (2.63), the first coefficient on the RHS is  $C_v/T$ . The second coefficient can be expanded as

$$\left( \frac{\partial s}{\partial v} \right)_T = \left( \frac{\partial s}{\partial P} \right)_T \left( \frac{\partial P}{\partial v} \right)_T. \quad (2.69)$$

An isothermal bulk modulus is defined as

$$K_T \equiv -v \left( \frac{\partial P}{\partial v} \right)_T. \quad (2.70)$$

From Eqs. (2.64), (2.65), and (2.68),

$$\frac{ds}{dt} = \frac{C_v}{T} \frac{dT}{dt} - \beta K_T \frac{1}{\rho^2} \frac{d\rho}{dt}. \quad (2.71)$$

Then, the entropy equation in Eq. (2.60) becomes

$$\rho C_v \frac{dT}{dt} - \frac{T\beta K_T}{\rho} \frac{d\rho}{dt} = \tau_{ij} \frac{\partial V_i}{\partial x_j} + \zeta(\nabla \cdot \vec{V})^2 - \nabla \cdot \vec{q} + \dot{q}. \quad (2.72)$$

At this point, some authors erroneously conclude that for negligible viscous heating and for incompressible flow, the equation reduces to  $\rho C_v dT/dt = -\nabla \cdot \vec{q}$ . This is incorrect, however, since the condition for incompressible flow is  $\frac{1}{\rho} |d\rho/dt| \ll |\nabla \cdot \vec{V}|$ , and not  $d\rho/dt = 0$ .

The ratio of the viscous heating term to the convective energy transport term scales as  $Ec/Re$ , and based on representative dimensionless numbers provided in Table 3 is on the order of  $10^{-8}$  for reactor conditions, and can therefore be neglected. By neglecting compression work, viscous heating, and volumetric viscous heating, Eq. (2.67) becomes

$$\rho C_p \frac{\partial T}{\partial t} + \rho C_p \vec{V} \cdot \nabla T - \nabla \cdot (k\nabla T) - \dot{q} = 0. \quad (2.73)$$

The spatially homogenized versions of Eqs. (2.51) and (2.73) are derived in Section 19.2.3,

$$\begin{aligned} & \frac{\partial(\varepsilon\langle\rho_f\rangle^f\langle E_f\rangle^f)}{\partial t} + \nabla \cdot \left[ \varepsilon\langle\rho_f\rangle^f\langle H_f\rangle^f\langle\vec{V}_f\rangle^f \right] + \nabla \cdot \left[ \langle\rho_f\rangle^f\langle\hat{H}_f\hat{V}_f\rangle \right] \\ & - \nabla \cdot \left( \varepsilon\langle k_f\rangle^f\nabla\langle T_f\rangle^f \right) + \alpha \left( \langle T_f\rangle^f - \langle T_s\rangle^s \right) - \varepsilon\langle\rho_f\rangle^f\langle\vec{V}_f\rangle^f \cdot \vec{b} - \langle\dot{q}_f\rangle = 0, \end{aligned} \quad (2.74)$$

$$\begin{aligned} & \varepsilon\langle\rho_f\rangle^f\langle C_{p,f}\rangle^f\frac{\partial\langle T_f\rangle^f}{\partial t} + \langle\rho_f\rangle^f\langle C_{p,f}\rangle^f\langle\hat{V}_f\nabla\hat{T}_f\rangle + \varepsilon\langle\rho_f\rangle^f\langle C_{p,f}\rangle^f\langle\vec{V}_f\rangle^f\nabla\langle T_f\rangle^f + \\ & - \nabla \cdot \left( \varepsilon\langle k_f\rangle^f\nabla\langle T_f\rangle^f \right) + \alpha \left( \langle T_f\rangle^f - \langle T_s\rangle^s \right) - \langle\dot{q}_f\rangle = 0, \end{aligned} \quad (2.75)$$

where  $\alpha$  is the convective heat transfer coefficient between the two intrinsic phase averaged temperatures. To obtain the correct units,  $\alpha$  represents the heat transfer coefficient  $h_c$  (which appears in Nusselt number correlations) multiplied by  $a_w$ ,

$$\alpha \equiv a_w h_c, \quad (2.76)$$

where  $a_w$  is the wetted area per unit length,

$$a_w = \lim_{\delta x \rightarrow 0} \frac{\text{wetted area in domain of length } \delta x}{\text{volume of domain of length } \delta x}. \quad (2.77)$$

For beds of spherical pebbles and in the absence of wall effects,  $a_w$  is defined in terms of the solid area and volume, and then multiplied by  $(1 - \varepsilon)$  to reflect the portion of the volume that is solid,

$$\begin{aligned} a_w &= \frac{\pi(d_p/2)^2}{(4/3)\pi(d_p/2)^3}(1 - \varepsilon) \\ &= \frac{6(1 - \varepsilon)}{d_p}, \end{aligned} \quad (2.78)$$

where  $d_p$  is the pebble diameter, though other forms have been suggested [39,43]. Correlations for the Nusselt number  $Nu$ , defined as

$$Nu = \frac{h_c d_p}{k}, \quad (2.79a)$$

$$Nu_h = \frac{h_c D}{k}, \quad (2.79b)$$

where  $D$  is the hydraulic diameter. Closures for  $Nu$  are discussed in Section 8. Eqs. (2.74) and (2.75) still leave one term that requires closure. Thermal energy dispersion arises due to additional mixing caused by the porous media due to 1) changes in flow direction initiated by the solid pebbles, 2) recirculation flows within the pores, and 3) eddy diffusion in turbulence. Assuming a gradient diffusion model,

$$\langle\rho_f\rangle^f\langle C_{p,f}\rangle^f\langle\hat{V}_f\nabla\hat{T}_f\rangle \approx -\nabla \cdot (\tilde{\kappa}_f\nabla\langle T_f\rangle^f), \quad (2.80)$$

where  $\tilde{\kappa}_f$  is a thermal dispersion conductivity, which is in general a second-order tensor [44]. While Eq. (2.80) is shown in terms of the dispersion kernel in Eq. (2.75), a similar interpretation exists for the dispersion kernel in Eq. (2.74). Correlations representing  $k_f + k_d$  are frequently given in the literature as the ‘‘effective fluid thermal conductivity’’  $\kappa_f$ , or

$$\kappa_f \equiv \epsilon k_f + \tilde{\kappa}_f . \quad (2.81)$$

Correlations for  $\kappa_f$  are discussed in Section 10. Eqs. (2.74) and (2.75) written in Pronghorn's notation become

$$\frac{\partial(\epsilon \rho_f E_f)}{\partial t} + \nabla \cdot (\epsilon H_f \rho_f \vec{V}) - \nabla \cdot (\kappa_f \nabla T_f) - \epsilon \rho_f \vec{b} \cdot \vec{V} + \alpha(T_f - T_s) - \dot{q}_f = 0 , \quad (2.82)$$

$$\epsilon \rho_f C_{p,f} \frac{\partial T_f}{\partial t} + \epsilon \rho_f C_{p,f} \vec{V} \cdot \nabla T_f + \nabla \cdot (\kappa_f \nabla T_f) + \alpha(T_f - T_s) - \dot{q}_f = 0 . \quad (2.83)$$

Hence,  $E_f$ ,  $H_f$ ,  $T_f$ ,  $C_{p,f}$ , and  $k_f$  represent the fluid intrinsic average total energy, total enthalpy, temperature, specific heat, and thermal conductivity, respectively.  $\alpha$  represents the extrinsic average convective heat transfer coefficient (which is the same for both the fluid and solid, and hence can also be interpreted as the intrinsic average convective heat transfer coefficient).  $\dot{q}_f$  represents the fluid extrinsic (superficial) heat source.

## 2.5 The Friction-Dominated Model

For slowly-evolving, low Reynolds number flows, momentum conservation can be assumed dominated by friction effects such that changes in pressure are instantaneously reflected as changes in momentum. Under these assumptions, the total derivative of momentum in Eq. (2.39) may be set to zero, giving a pseudo-steady momentum equation,

$$\epsilon \nabla P - \epsilon \rho_f \vec{g} + W \rho_f \vec{V} = 0 . \quad (2.84)$$

Substituting Eq. (2.84) into Eq. (2.7) gives a pressure Poisson equation,

$$\epsilon \frac{\partial \rho_f}{\partial t} + \nabla \cdot \left[ \frac{\epsilon^2}{W} (\rho_f \vec{g} - \nabla P) \right] = 0 . \quad (2.85)$$

For slowly-evolving flows, compression work is usually negligible such that the conservation of internal energy equation in Eq. (2.83) is used.

Eqs. (2.84), (2.85), and (2.83) are referred to as the ‘‘friction-dominated’’ model, and are very similar to the set of equations solved in a number of other PBR porous media codes [41, 45, 46].

## 2.6 The Solid Energy Equation

To obtain the solid energy equation, simply set  $\vec{V} = 0$  in Eq. (2.82) or (2.83) with  $\epsilon$  replaced by  $1 - \epsilon$  to reflect the fraction of the volume that is solid. The assumptions made in the derivation of the solid energy equation are therefore the same as those made in the derivation of the fluid energy equation, except that the solid is assumed stationary. Because properties are often only available for solids in terms of pressure and temperature, the thermal energy conservation equation in Eq. (2.83) is used exclusively for the solid,

$$(1 - \epsilon) \rho_s C_{p,s} \frac{\partial T_s}{\partial t} - \nabla \cdot (\kappa_s \nabla T_s) + \alpha(T_s - T_f) - \dot{q}_s = 0 , \quad (2.86)$$

where  $\kappa_s$  is the effective solid thermal conductivity that represents the effective thermal dispersion in the solid phase,  $\rho_s$  represents the solid intrinsic average density, and  $C_{p,s}$  represents the solid intrinsic average specific heat.  $\dot{q}_s$  represents

the extrinsic (superficial) solid heat source.  $\kappa_s$  captures the combined effects of solid-to-solid radiation, solid-fluid-solid conduction, and solid-to-solid conduction,

$$\kappa_s = \kappa_{\text{radiation}} + \kappa_{\text{fluid conduction}} + \kappa_{\text{solid conduction}} . \quad (2.87)$$

Models for these components of  $\kappa_s$  are given in Section 9.

## 2.7 The Interior Solid Energy Equation

This section describes how approximate temperature solutions are obtained within the interior of the solid phase based on knowledge of the local heat generation rate and the solid surface temperature  $T_s$  obtained from the solution of Eq. (2.86). Models for the interior of the solid phase are essential for assessing material damage limits and estimating temperatures for multiphysics feedback effects [47]. The equations presented in Sections 2.2-2.4 represent spatially homogenized flow and heat transfer on the macroscale, where spatial averaging was performed over a Representative Elementary Volume (REV) intermediate in size to the largest characteristic length and the smallest individual solid characteristic length, such as the pebble diameter for PBR applications.

If the solid phase is homogeneous or consists of multiple homogeneous layers, a multi-region conduction problem may be solved for “representative” solid interior temperature distributions for solid pebbles located throughout the macroscale domain. This simple approach can be used for the homogeneous solids used in the SANA facility [48], the multi-layer loose TRistructural ISotropic (TRISO) particles used in the Pebble Bed Water Reactor (PBWR) [49], and for any homogeneous or region-wise homogeneous solid phase, such as fresh Light Water Reactor (LWR) fuel pins.

The difficulty in solving for representative interior solid phase temperature distributions arises when the solid is extremely heterogeneous. For example, the solid phase in PBRs typically consists of a sphere containing a central core of thousands of CFPs randomly mixed in a matrix material. Each CFP consists of several concentric spherical layers of differing composition. The heat source in the solid phase is localized to the central kernel of each CFP. Assuming the coordinates of the thousands of CFPs within each pebble were known, a very fine mesh would be required to capture the layers on each particle and the surrounding matrix. This level of detail is computationally prohibitive for routine design and analysis, as well as unnecessary for determining only a representative solution field.

Many other solid fuel forms encountered in nuclear applications are heterogeneous. Fully Ceramic Microencapsulated (FCM) fuel consists of conventional TRISO particles dispersed in a silicon carbide matrix and fabricated into cylindrical pellets intended for replacement of  $\text{UO}_2$  pellets in LWR applications or similar graphite matrix fuels in High Temperature Gas Reactors (HTGRs) [50, 51]. For the conversion of test reactors from High Enriched Uranium (HEU) to Low Enriched Uranium (LEU), either the fuel loading or fissile atom density must be increased to retain the same reactor performance. As the size of the reactors are typically fixed, high fissile density dispersion fuels consisting of  $\text{U}_3\text{Si}_2$  or UMo particles in an aluminum matrix have been used [52, 53]. Fast reactor fuel consisting of metallic-coated fissile kernels surrounded by a “matrix” of fuel powder has also been proposed [54].

The remainder of this section discusses methods available in Pronghorn for approximating the interior solid temperature solution for both simple solids, where multi-region conduction is feasible, and very heterogeneous solids. The methods discussed in this section are referred to as “multiscale” treatments because BCs from the macroscale solution are used to simulate periodic lower length scales. It should be noted that all of the methods to be discussed are approximate because the exact location of the macroscale solid phase and heterogeneities in the solid phase, if present, are unknown.

### 2.7.1 One-Equation Model

The simplest model for the interior of the solid phase is the conservation of thermal energy equation,

$$\rho_S C_{p,S} \frac{\partial T_S}{\partial t} - \nabla \cdot (k_S \nabla T_S) - \dot{q}_S = 0, \quad (2.88)$$

where  $\rho_S$  is the solid density,  $C_{p,S}$  is the solid isobaric specific heat capacity,  $k_S$  is the solid thermal conductivity,  $T_S$  is the internal solid temperature, and  $\dot{q}_S$  is the volumetric heat source. The  $S$  subscript indicates that the thermal properties, volumetric heat source, and temperature correspond to the interior of the solid phase, and is distinct from the  $s$  subscript used to denote the intrinsic phase averaged quantities in the macroscale solid energy conservation equations in Eqs. (2.137d), (2.139d), and (2.141d).

For example, if each of the solid pebbles consisted of concentric layers of  $\text{UO}_2$ , helium, and zircaloy, then  $k_S$  might be specified as

$$k_S(r, T_S) = \begin{cases} k_{\text{UO}_2}(T_S) & r \leq r_1 \\ k_{\text{helium}}(T_S) & r_1 < r \leq r_2 \\ k_{\text{zircaloy}}(T_S) & r_2 \leq r < d_p/2, \end{cases} \quad (2.89)$$

where  $k_{\text{UO}_2}$ ,  $k_{\text{helium}}$ , and  $k_{\text{zircaloy}}$  are temperature-dependent thermal conductivity correlations for each layer. The spatial dependence is listed in terms of the radial coordinate due to the uniform surface temperature BC and interpretation of each representative pebble as a sphere with average radius  $d_p/2$ .  $r_1$  indicates the boundary between the  $\text{UO}_2$  and helium regions and  $r_2$  indicates the boundary between the helium and zircaloy regions. Similar piecewise expressions would be used for the heat source and the other properties of the solid.

Eq. (2.88) is referred to here as the One Equation Model (OEM) because a single temperature field is predicted for the solid. No approximation has been made in the application of Eq. (2.88) to homogeneous solids. For heterogeneous solids, no distinction is made between the temperatures characterizing different constituent materials and the locality of the heat source in heterogeneous solids, which will not be accurate for very localized heat sources and/or for quickly-evolving transients [55, 56]. Extension of T/H codes originally developed for homogeneous LWR fuels to heterogeneous fuels frequently use the OEM due to rigidity in software implementation and/or simplicity in Eq. (2.88) [57].

Small variations on the OEM have been proposed and used for nuclear applications. In the ‘‘homogeneous layers’’ technique, a heterogeneous domain may be smeared into distinct material regions while preserving volume fractions, at the expense of potentially drastic changes in thermal resistance that compromise accuracy [58].

## 2.7.2 Heat Source Decomposition

The Heat Source Decomposition (HSD) method is based on concepts of superposition techniques that apply to linear differential equations [59]. A description of the method begins by splitting a heterogeneous heat source  $\dot{q}$  into an average  $\langle \dot{q} \rangle$  and a fluctuation  $\hat{q}$ ,

$$\dot{q} = \langle \dot{q} \rangle + \hat{q}, \quad (2.90)$$

where the average of the fluctuation is zero. Each heat source in Eq. (2.90) is used in a separate conduction equation. The conduction equation based on the average heat source is referred to as the ‘‘mesoscale’’ model,

$$\rho_{\text{meso}} C_{p,\text{meso}} \frac{\partial T_{\text{meso}}}{\partial t} - \nabla \cdot (k_{\text{meso}} \nabla T_{\text{meso}}) - \langle \dot{q} \rangle = 0, \quad (2.91)$$

where the ‘‘meso’’ subscript indicates mesoscale quantities.  $\rho_{\text{meso}}$ ,  $C_{p,\text{meso}}$ , and  $k_{\text{meso}}$  represent the thermal properties of the heterogeneous domain homogenized in space according to various mixing approaches described in Section 13.

The mesoscale temperature  $T_{\text{meso}}$  represents the long-wavelength thermal solution due to the average heat source and average properties.

The conduction equation based on the fluctuating heat source is referred to as the ‘‘microscale’’ model,

$$\rho_{\text{micro}} C_{p,\text{micro}} \frac{\partial T_{\text{micro}}}{\partial t} - \nabla \cdot (k_{\text{micro}} \nabla T_{\text{micro}}) - \hat{q} = 0 , \quad (2.92)$$

where the ‘‘micro’’ subscript indicates microscale quantities.  $\rho_{\text{micro}}$ ,  $C_{p,\text{micro}}$ , and  $k_{\text{micro}}$  represent the thermal properties resolved on the fine scale. The approximate temperature solution in the interior solid domain is the superposition of the two solutions,

$$T(\vec{x}) = T_{\text{meso}}(\vec{x}) + \sum_{i=1}^{n_p} T_{\text{micro},i}(\vec{x}_i) , \quad (2.93)$$

where the summation over the number of particles  $n_p$  indicates that the microscale solution  $T_{\text{micro},i}$  for the  $i$ -th particle is translated to the location  $\vec{x}_i$  corresponding to the center of that particle. If pebble self-shielding effects are neglected such that the heat source in each particle is identical, a microscale model may be constructed for a single particle and translated to each of the  $n_p$  locations. This simplification is assumed in the representation shown in Eq. (2.93), but is not a requirement of the method or implementation in Pronghorn.

The BCs require matching a specified temperature  $\bar{T}$  and heat flux  $\bar{q}$  on the boundary  $\Gamma$ ,

$$(T_{\text{meso}} + T_{\text{micro}})|_{\Gamma} = \bar{T} , \quad (2.94)$$

$$(-k_{\text{meso}} \nabla T_{\text{meso}} \cdot \hat{n} - k_{\text{micro}} \nabla T_{\text{micro}} \cdot \hat{n})|_{\Gamma} = \bar{q} . \quad (2.95)$$

In addition, the microscale solution must have a zero average over the microscale domain in order to represent a zero-average fluctuation on the long-wavelength mesoscale solution. This is enforced by applying a Dirichlet BC on the boundary of the microscale domain such that the average of the microscale solution is zero,

$$T_{\text{micro}}|_{\Gamma} = - \frac{\int T_{\text{micro}} d\Omega}{\int d\Omega} . \quad (2.96)$$

The only fundamental approximations made in the HSD method are that 1) thermal properties are independent of temperature and 2) the long-wavelength thermal behavior is governed by spatially homogenized properties. The latter of these assumptions introduces small differences from fully-resolved simulations, while the former is essential for the heat equation to be linear and solvable by superposition techniques. Some temperature dependence in the material properties can be retained by 1) using different (constant) thermal properties for each pebble according to its position in the macroscale solid temperature field and/or 2) including in the algorithm a material property iteration loop using properties evaluated at an appropriate average of the most recently evaluated multiscale temperature field. In most PBRs, of equal or greater concern is the dependence of thermal properties on burnup. This dependence can be easily accommodated provided the burnup over a pebble can be assumed uniform.

An intuitive grasp of the HSD method can be obtained by considering a example consisting of nine CFPs, each consisting of five material layers, in a matrix material. A reference temperature distribution in this geometry involves solution of the heat conduction equation on the mesh shown in Fig. 3a. This mesh is colored with block numbers to illustrate the regions of different material properties. The reference temperature solution is shown in Fig. 3b along with contours shown as white lines. Dirichlet temperature BCs of 1100°C, 1100°C, and 1150°C are applied on the left, top, and right boundaries, respectively. The bottom boundary is insulated. A uniform heat source per unit volume

of the centermost region of each CFP is set to a constant  $2 \times 10^8 \text{ W/m}^3$ . The contours are tightly packed in the second material layer in each CFP due to its much lower thermal conductivity relative to the other materials.

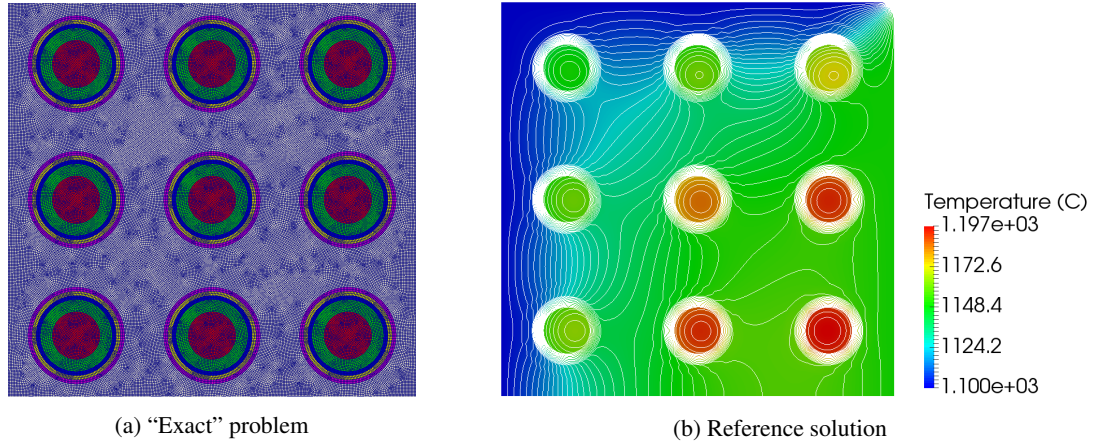


Figure 3: (a) Mesh for a heterogeneous solid consisting of nine CFPs in a matrix material, where each CFP consists of five material layers, and (b) reference heat conduction solution for the mesh shown in (a) with white contour lines.

The HSD involves solution of a mesoscale and microscale problem. The mesoscale domain encompasses the entire heterogeneous domain, but is represented with a relatively coarse mesh. The mesoscale mesh and solution are shown in Fig. 4a and Fig. 4b, respectively. Eq. (13.3) is used for mixing the thermal conductivity of the CFPs and the matrix, while Eq. (13.1) is used for mixing the five layers of the CFPs. The color bar in Fig. 4b is intentionally not the same as in Fig. 3b to reinforce that it is the sum of the mesoscale and microscale solutions that satisfy the imposed Dirichlet BCs.

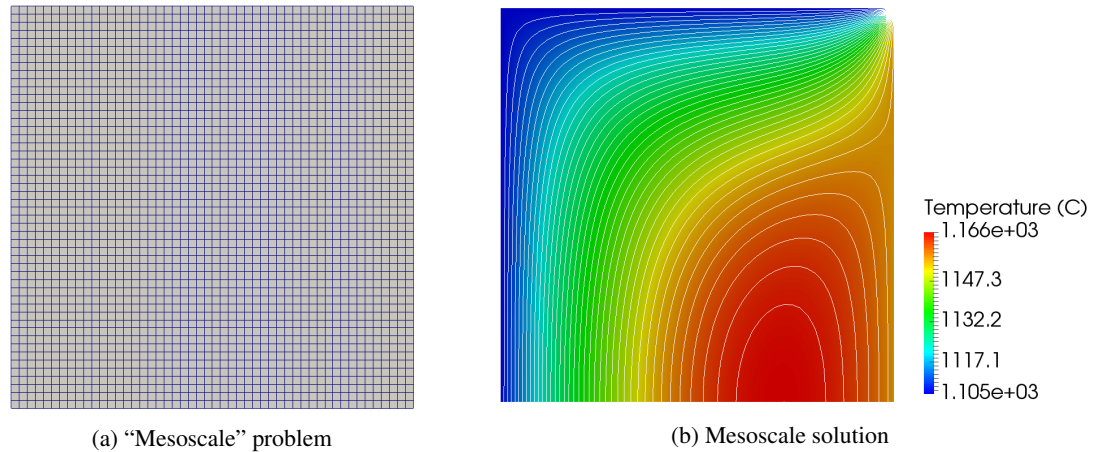


Figure 4: (a) HSD Mesoscale mesh, and (b) mesoscale solution for the mesh shown in (a) with white contour lines.

The microscale domain is a 1-D representation of a single CFP plus a layer of surrounding matrix material scaled to obtain the correct packing fraction. Fig. 5 shows the multiscale solution along a horizontal line passing through the centers of the middle row of particles. The bottom section of Fig. 5 shows the microscale particle solution translated to the locations of each of the three particles. Despite the approximations made in the homogenization of the mesoscale properties, the HSD multiscale model agrees with the reference temperature distribution very well. Though not shown here, the HSD method also predicts temperatures well for transient cases.

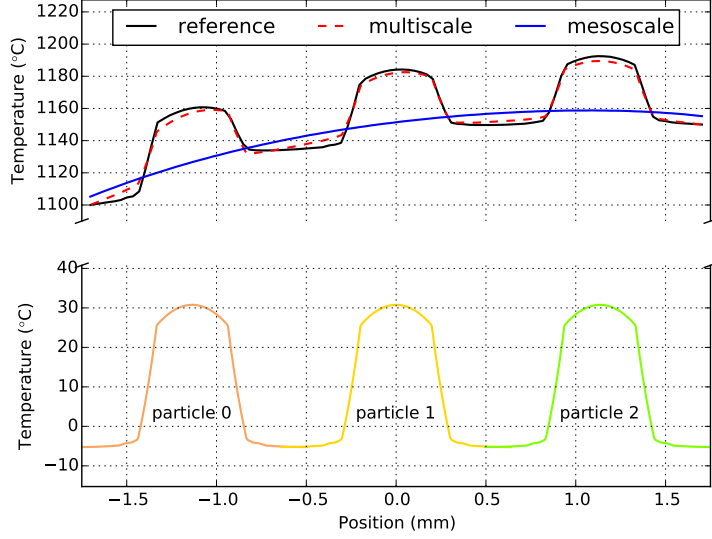


Figure 5: Multiscale, mesoscale, particle, and reference solutions for constant thermal properties and heat source for the geometry shown in Fig. 3.

The example shown in Fig. 5 required knowledge of the location of the CFPs within the matrix in order to plot the multiscale temperature approximation. If the CFP locations are unknown, the HSD method may be used to predict maximum, minimum, and material-wise averaged temperatures, which are often of greater practical use in assessing fuel integrity and neutron transport feedback. With such an approach, it is assumed that the heterogeneities are smaller than the mesoscale domain and that the heterogeneities are randomly dispersed. Then, maximum and minimum temperatures in material  $i$  can be approximated as

$$\max(T_i) \approx \max(T_{\text{meso}}) + \max(T_{\text{micro},i}) , \quad (2.97)$$

$$\min(T_i) \approx \min(T_{\text{meso}}) + \min(T_{\text{micro},i}) . \quad (2.98)$$

In other words, maximum and minimum temperatures are evaluated assuming a microscale domain is situated precisely at the location of the maximum and minimum mesoscale temperatures, respectively. This provides the bounding maximum and minimum temperatures for material  $i$ , and hence the actual maximum and minimum temperatures will be within this range, given the limitations of the mixing methods used for mesoscale material properties.

Further, the average of the temperature in material  $i$  is approximated as

$$\langle T_i \rangle \approx \langle T_{\text{meso}} \rangle + \langle T_{\text{micro},i} \rangle . \quad (2.99)$$

In addition to the assumptions discussed in the context of Eqs. (2.97) and (2.98), Eq. (2.99) assumes that the mesoscale solution varies over a slower scale than the size of the heterogeneities.

The HSD is less accurate in predicting full resolution temperature fields when particles are clustered, since each particle does not have the same “share” of the matrix material in its microscale domain. Such clustering effects may contribute several degrees standard deviation in the peak layer temperatures [60].

## 2.8 Stabilization and Preconditioning of the Fluid Conservation Equations

The previous sections have derived the conservation equations for the fluid and solid phases for a general compressible fluid and a stationary solid. Because the coupling of the fluid and solid energy equations only occurs through the convective heat transfer term, the fluid conservation equations share many similarities with the Navier-Stokes equations with an additional source term in the energy equation. This section introduces preconditioning and stabilization methods that are applied to the spatially homogenized Navier-Stokes equations as extensions of methods originally developed for the non-porous Navier-Stokes equations. This section also describes the small modifications required to the governing equations for solution in axisymmetric coordinates.

To illustrate the similarity between the spatially homogenized equations and the non-porous Navier-Stokes equations, rewrite the system of fluid conservation equations in condensed form as

$$\frac{\partial(\epsilon\vec{U})}{\partial t} + \frac{\partial(\epsilon\vec{F}_i)}{\partial x_i} - \frac{\partial\vec{G}_i}{\partial x_i} + \vec{S} + \vec{Z}_w = \vec{0}, \quad (2.100)$$

where  $\vec{U}$  is the vector of unknowns,

$$\vec{U} = \begin{bmatrix} \rho_f \\ \rho_f V_1 \\ \rho_f V_2 \\ \rho_f V_3 \\ \rho_f E_f \end{bmatrix}; \quad (2.101)$$

$\vec{F}_i$  is the inviscid flux vector in the  $i$ -th dimension,

$$\vec{F}_i = \begin{bmatrix} \rho_f V_i \\ \rho_f V_1 V_i + P\delta_{1i} \\ \rho_f V_2 V_i + P\delta_{2i} \\ \rho_f V_3 V_i + P\delta_{3i} \\ \rho_f V_i H_f \end{bmatrix}, \quad (2.102)$$

which can be written in terms of the entries in  $\vec{U}$  as

$$\vec{F}_i = \begin{bmatrix} U_i \\ \frac{U_1 U_i}{U_0} + P\delta_{1i} \\ \frac{U_2 U_i}{U_0} + P\delta_{2i} \\ \frac{U_3 U_i}{U_0} + P\delta_{3i} \\ U_i H_f \end{bmatrix}; \quad (2.103)$$

$\vec{G}_i$  is the diffusive flux vector in the  $i$ -th dimension,

$$\vec{G}_i = \begin{bmatrix} 0 \\ \tilde{\mu} \frac{\partial V_1}{\partial x_i} \\ \tilde{\mu} \frac{\partial V_2}{\partial x_i} \\ \tilde{\mu} \frac{\partial V_3}{\partial x_i} \\ \kappa_f \frac{\partial T_f}{\partial x_i} \end{bmatrix}; \quad (2.104)$$

$\vec{S}$  is the source vector,

$$\vec{S} = \begin{bmatrix} 0 \\ -\varepsilon\rho_f g_1 + W\rho_f V_1 + P \frac{\partial \varepsilon}{\partial x_1} \\ -\varepsilon\rho_f g_2 + W\rho_f V_2 + P \frac{\partial \varepsilon}{\partial x_2} \\ -\varepsilon\rho_f g_3 + W\rho_f V_3 + P \frac{\partial \varepsilon}{\partial x_3} \\ -\varepsilon\rho_f b_i V_i + \alpha(T_f - T_s) - \dot{q}_f \end{bmatrix}, \quad (2.105)$$

which can be written in terms of the entries in  $\vec{U}$  as

$$\vec{S} = \begin{bmatrix} 0 \\ -\varepsilon U_0 g_1 + W U_1 - P \frac{\partial \varepsilon}{\partial x_1} \\ -\varepsilon U_0 g_2 + W U_2 - P \frac{\partial \varepsilon}{\partial x_2} \\ -\varepsilon U_0 g_3 + W U_3 - P \frac{\partial \varepsilon}{\partial x_3} \\ -\varepsilon g_i U_i + \alpha(T_f - T_s) - \dot{q}_f \end{bmatrix}. \quad (2.106)$$

In Eq. (2.100),  $\vec{Z}_w$  is an additional source term required for solution in axisymmetric coordinates. While the Multi-physics Object-Oriented Simulation Environment (MOOSE) framework defines the correct coordinate system transformations from  $dx dy dz$  to  $2\pi r dr dz$ , the transformation rules for divergences and gradients to cylindrical coordinates,

$$\nabla \cdot \vec{v} \equiv \frac{\partial v_r}{\partial r} + \frac{v_r}{r} + \frac{1}{r} \frac{\partial v_\theta}{\partial \theta} + \frac{\partial v_z}{\partial z}, \quad (2.107)$$

$$\nabla \vec{v} \equiv \begin{bmatrix} \frac{\partial v_r}{\partial r} & \frac{1}{r} \left( \frac{\partial v_r}{\partial \theta} - v_\theta \right) & \frac{\partial v_z}{\partial z} \\ \frac{\partial v_\theta}{\partial r} & \frac{1}{r} \left( \frac{\partial v_\theta}{\partial \theta} + v_r \right) & \frac{\partial v_\theta}{\partial z} \\ \frac{\partial v_z}{\partial z} & \frac{1}{r} \frac{\partial v_z}{\partial \theta} & \frac{\partial v_z}{\partial z} \end{bmatrix}, \quad (2.108)$$

where  $\theta$  is the aximuthal coordinate, require the inclusion of

$$\vec{Z}_w \equiv \begin{bmatrix} 0 \\ -\varepsilon P/r \\ 0 \\ 0 \end{bmatrix}. \quad (2.109)$$

The nonzero term in Eq. (2.109) is shown notationally in the first momentum equation, but in implementation is added to the momentum equation corresponding to the radial direction. Finally, for notational simplicity,  $\varepsilon$  is kept within the time differentiation term in Eq. (2.100) though the actual implementation assumes porosity is independent of time. The  $\varepsilon \nabla P$  term has been reverse integrated by parts as  $\nabla(\varepsilon P) - P \nabla \varepsilon$  such that  $\varepsilon P$  could be moved inside the inviscid flux term.

### 2.8.1 Streamline-Upwind Petrov-Galerkin Stabilization

The previous section reorganized the spatially homogenized fluid conservation equations to draw similarities to the non-porous conservation equations. This section introduces the Streamline Upwind Petrov-Galerkin (SUPG) stabilization applied to the fluid conservation equations that is discussed at much greater length in Section 15. Eq. (2.100) is written in quasi-linear form using the chain rule,

$$\vec{\mathcal{R}} \equiv \frac{\partial(\epsilon \vec{U})}{\partial t} + \epsilon \mathbf{A}_i \frac{\partial \vec{U}}{\partial x_i} + \vec{F}_i \frac{\partial \epsilon}{\partial x_i} - \frac{\partial}{\partial x_i} \left( \mathbf{K}_{ij} \frac{\partial \vec{U}}{\partial x_j} \right) + \vec{S} + \vec{Z}_w, \quad (2.110)$$

where  $\mathbf{A}_i$  are the inviscid flux Jacobian matrices,

$$\mathbf{A}_i \equiv \frac{\partial \vec{F}_i}{\partial \vec{U}}, \quad (2.111)$$

and  $\mathbf{K}_{ij}$  are the diffusive flux Jacobian matrices,

$$\mathbf{K}_{ij} \frac{\partial \vec{U}}{\partial x_j} \equiv \vec{G}_i \quad (2.112)$$

and  $\vec{\mathcal{R}}$  is the quasi-linear strong residual vector.  $\mathbf{A}_i$  requires the partial derivatives of the entries of  $\vec{U}$ ,  $P$ , and  $H_f$  with respect to the entries of  $\vec{U}$ . When represented as components in  $\vec{U}$ , partial derivatives of  $U_i$  with respect to  $U_j$  are

$$\frac{\partial U_i}{\partial U_j} = \delta_{ij}. \quad (2.113)$$

The derivatives of  $H_f$  with respect to the entries in  $\vec{U}$  are

$$\frac{\partial H_f}{\partial \vec{U}} = \frac{1}{\rho_f} \left[ \frac{\partial P}{\partial U_0} - H_f \quad \frac{\partial P}{\partial U_1} \quad \frac{\partial P}{\partial U_2} \quad \frac{\partial P}{\partial U_3} \quad \frac{\partial P}{\partial U_4} + 1 \right]. \quad (2.114)$$

The derivatives of pressure with respect to the entries in  $\vec{U}$  are written in the form of a chain rule as

$$\frac{\partial P}{\partial \vec{U}} = \frac{\partial P}{\partial v_f} \frac{\partial v_f}{\partial \vec{U}} + \frac{\partial P}{\partial e_f} \frac{\partial e_f}{\partial \vec{U}}, \quad (2.115)$$

where  $\partial v_f / \partial \vec{U}$  is given as

$$\frac{\partial v_f}{\partial \vec{U}} = \frac{1}{\rho_f^2} \begin{bmatrix} 1 & 0 & 0 & 0 & 0 \end{bmatrix}, \quad (2.116)$$

and  $\partial e_f / \partial \vec{U}$  is given as

$$\frac{\partial e_f}{\partial \vec{U}} = \frac{1}{\rho_f} \begin{bmatrix} \|\vec{V}\|_2^2 - E_f & -V_1 & -V_2 & -V_3 & 1 \end{bmatrix}. \quad (2.117)$$

With the derivatives of  $\vec{U}$ ,  $P$ , and  $H_f$  with respect to  $\vec{U}$  defined, the inviscid flux Jacobian matrices are

$$\mathbf{A}_i = \begin{bmatrix} 0 & \delta_{1i} & \delta_{2i} & \delta_{3i} & 0 \\ \frac{-U_1 U_i}{U_0^2} + \delta_{1i} \frac{\partial P}{\partial U_0} & \delta_{1i} \left[ \frac{2U_1}{U_0} + \frac{\partial P}{\partial U_1} \right] + \tilde{\delta}_{1i} \frac{U_i}{U_0} & \delta_{2i} \frac{U_1}{U_0} + \delta_{1i} \frac{\partial P}{\partial U_2} & \delta_{3i} \frac{U_1}{U_0} + \delta_{1i} \frac{\partial P}{\partial U_3} & \delta_{1i} \frac{\partial P}{\partial U_4} \\ \frac{-U_2 U_i}{U_0^2} + \delta_{2i} \frac{\partial P}{\partial U_0} & \delta_{1i} \frac{U_2}{U_0} + \delta_{2i} \frac{\partial P}{\partial U_1} & \delta_{2i} \left[ \frac{2U_2}{U_0} + \frac{\partial P}{\partial U_2} \right] + \tilde{\delta}_{2i} \frac{U_i}{U_0} & \delta_{3i} \frac{U_2}{U_0} + \delta_{2i} \frac{\partial P}{\partial U_3} & \delta_{2i} \frac{\partial P}{\partial U_4} \\ \frac{-U_3 U_i}{U_0^2} + \delta_{3i} \frac{\partial P}{\partial U_0} & \delta_{1i} \frac{U_3}{U_0} + \delta_{3i} \frac{\partial P}{\partial U_1} & \delta_{2i} \frac{U_3}{U_0} + \delta_{3i} \frac{\partial P}{\partial U_2} & \delta_{3i} \left[ \frac{2U_3}{U_0} + \frac{\partial P}{\partial U_3} \right] + \tilde{\delta}_{3i} \frac{U_i}{U_0} & \delta_{3i} \frac{\partial P}{\partial U_4} \\ U_i \frac{\partial H_f}{\partial U_0} & U_i \frac{\partial H_f}{\partial U_1} + \delta_{1i} H_f & U_i \frac{\partial H_f}{\partial U_2} + \delta_{2i} H_f & U_i \frac{\partial H_f}{\partial U_3} + \delta_{3i} H_f & U_i \frac{\partial H_f}{\partial U_4} \end{bmatrix}, \quad (2.118)$$

where  $\tilde{\delta}_{ij} \equiv (1 - \delta_{ij})$  is defined for conciseness. Eq. (2.100) is a set of coupled equations for the variables in  $\vec{U}$  as defined in Eq. (2.104), and has the following weak form,

$$\int_{\Omega} \left[ \epsilon \vec{W} \cdot \frac{\partial \vec{U}}{\partial r} + \frac{\partial \vec{W}}{\partial x_i} \cdot (\vec{G}_i - \epsilon \vec{F}_i) + \vec{W} \cdot (\vec{S} + \vec{Z}_w) \right] d\Omega + \int_{\Gamma} (\epsilon \vec{F}_i - \vec{G}_i) \cdot \vec{W} n_i d\Gamma + \underbrace{\int_{\Omega} \epsilon \left\{ \mathbf{A}_i \left[ \tau_{SUPG} (\vec{\mathcal{R}} + \vec{Z}_s) \right] \right\} \cdot \frac{\partial \vec{W}}{\partial x_i} d\Omega}_{\text{SUPG term}} = 0 \quad (2.119)$$

where  $\vec{W}$  is a vector of weight functions and  $\vec{Z}_s$  is an additional term required for solution in axisymmetric coordinates based on the divergence and gradient operators in Eqs. (2.107) and (2.108),

$$\vec{Z}_s \equiv \frac{1}{r} (\epsilon \vec{F}_r - \vec{G}_r) \quad (2.120)$$

where  $r$  subscripts indicate the  $\vec{F}$  and  $\vec{G}$  vectors corresponding to the radial direction. The last term in Eq. (2.119) is the SUPG stabilization term, whose theoretical motivation is deferred to Section 15.

## 2.8.2 Low-Mach Preconditioning

The Navier-Stokes equations must be solved in terms of the three components of velocity (or momentum) and two thermodynamic state variables, such as  $P$  and  $T$  or  $\rho E$  and  $\rho$ . One choice of solution variables will not necessarily be ideal for all flows. This section has up until this point implicitly assumed that the solution variables are the conserved quantities  $\rho_f$ ,  $\rho_f \vec{V}$ , and  $\rho_f E_f$  as shown in Eq. (2.101). For nearly incompressible flows such as molten salts [61], solution of the mass conservation equation for density would require pressure to be obtained from an Equation of State (EOS) that has an extremely small dependence on density, which would result in stiffness and solution contamination [1, 62]. For compressible flows such as most gases, density tends to vary strongly with both pressure and temperature such that the ideal choice of solution variables are the conserved quantities of mass, momentum, and energy [63]. There is no clean dividing line between compressible and incompressible flows. This section describes a low-Mach preconditioner available to solve Eq. (2.100) for the primitive variables of  $P$ ,  $\vec{V}$ , and  $T_f$  that is preferred for nearly-incompressible flows [64].

Eq. (2.100) can be solved for an arbitrary set of variables  $\vec{U}$  by replacing  $\partial \vec{U} / \partial \xi_i$  by  $\mathbf{M} \partial \vec{U} / \partial \xi_i$ , where  $\xi$  is either the spatial or time derivatives and  $\mathbf{M}$  is a matrix representing the partial derivative of the conserved set of variables to the arbitrary set of variables  $\vec{U}$ ,

$$\mathbf{M} \equiv \frac{\partial \vec{U}}{\partial \vec{U}}. \quad (2.121)$$

Inserting Eq. (2.121) and expressing the diffusive terms with the  $\mathbf{K}_{ij}$  notation, Eq. (2.119) becomes

$$\begin{aligned}
& \int_{\Omega} \left[ \boldsymbol{\varepsilon} \mathbf{M} \vec{W} \cdot \frac{\partial \vec{U}}{\partial t} + \frac{\partial \vec{W}}{\partial x_i} \cdot \left( \mathbf{K}_{ij} \mathbf{M} \frac{\partial \vec{U}}{\partial x_j} - \boldsymbol{\varepsilon} \vec{F}_i \right) + \vec{W} \cdot \left( \vec{S} + \vec{Z}_w \right) \right] d\Omega + \\
& \int_{\Gamma} \left( \boldsymbol{\varepsilon} \vec{F}_i - \mathbf{K}_{ij} \mathbf{M} \frac{\partial \vec{U}}{\partial x_j} \right) \cdot \vec{W} n_i d\Gamma + \underbrace{\int_{\Omega} \boldsymbol{\varepsilon} \left\{ \mathbf{A}_i \mathbf{M} \left[ \tau_{SUPG} \left( \vec{R} + \vec{Z}_s \right) \right] \right\}}_{\text{SUPG term}} \cdot \frac{\partial \vec{W}}{\partial x_i} d\Omega = 0.
\end{aligned} \tag{2.122}$$

To solve Eq. (2.100) for an arbitrary set of sufficiently well-posed variables requires determining Eq. (2.121) and forming Eq. (2.122). The Automatic Differentiation (AD) capabilities in Pronghorn permit Jacobians to be calculated automatically for any set of solution variables, which results in a relatively clean implementation of this low-Mach preconditioner. The ability to retain the conservative form the conservation equations permits more accurate predictions of shock structures and the ability to use equal-order interpolation bases that is often absent for fully incompressible flows [63].

For solution in conserved variables,  $\mathbf{M}$  is the identity matrix. For an alternative set of solution variables to be “well-posed” for application to nearly incompressible flows,  $\mathbf{M}$  and  $\mathbf{M}^{-1}$  must be finite in the limit of an incompressible EOS where  $\alpha_T = 0$  and  $\beta = 0$ , where  $\alpha_T$  is the compressibility,

$$\begin{aligned}
\alpha_T &\equiv \frac{1}{\rho} \left( \frac{\partial \rho}{\partial P} \right)_T \\
&= -\frac{1}{v} \left( \frac{\partial v}{\partial P} \right)_T,
\end{aligned} \tag{2.123}$$

and  $\beta$  is the thermal expansion coefficient as defined in Eq. (2.65). Clearly, if density is selected as a solution variable for a nearly incompressible system, entries in the inviscid flux Jacobian matrices defined in Eq. (2.111) for the new system of variables will tend to infinity as  $\alpha_T$  and  $\beta$  tend to zero. This condition would certainly be met for molten salts, with  $\alpha_T$  being on the order of  $10^{-11}$ . In other words, the condition number of the  $\mathbf{A}_i$  gets increasingly large as the system becomes less and less compressible [63].

Both entropy variables and  $P-\vec{V}-T_f$  variables are well-posed in the incompressible limit, and are hence suitable as preconditioning matrices  $\mathbf{M}$  for nearly incompressible flows [63, 65]. However, the matrices involved may still become rank deficient as  $\alpha_T$  and  $\beta$  tend to zero, so the inverses should always be computed analytically. Pronghorn’s low-Mach preconditioner permits solution for the primitive variables

$$\vec{U} = \left[ P \quad V_1 \quad V_2 \quad V_3 \quad T \right]^T, \tag{2.124}$$

which corresponds to  $\mathbf{M}$  and its inverse being

$$\mathbf{M} = \begin{bmatrix} \rho \alpha_T & 0 & 0 & 0 & -\rho \beta \\ \rho \alpha_T V_1 & \rho & 0 & 0 & -\rho \beta V_1 \\ \rho \alpha_T V_2 & 0 & \rho & 0 & -\rho \beta V_2 \\ \rho \alpha_T V_3 & 0 & 0 & \rho & -\rho \beta V_3 \\ \rho \alpha_T H - \beta T & \rho V_1 & \rho V_2 & \rho V_3 & \rho C_p - \rho \beta H \end{bmatrix}, \tag{2.125}$$

$$\mathbf{M}^{-1} = \frac{1}{\rho} \begin{bmatrix} \frac{\rho C_p - \rho \beta H + \rho \beta \|\vec{V}\|_2^2}{\rho \alpha_T C_v} & -\frac{\beta V_1}{\alpha_T C_v} & -\frac{\beta V_2}{\alpha_T C_v} & -\frac{\beta V_3}{\alpha_T C_v} & \frac{\beta}{\alpha_T C_v} \\ -V_1 & 1 & 0 & 0 & 0 \\ -V_2 & 0 & 1 & 0 & 0 \\ -V_3 & 0 & 0 & 1 & 0 \\ \frac{\rho \alpha_T \|\vec{V}\|_2^2 - (\rho \alpha_T H - \beta T)}{\rho \alpha_T C_v} & -\frac{V_1}{C_v} & -\frac{V_2}{C_v} & -\frac{V_3}{C_v} & \frac{1}{C_v} \end{bmatrix}. \quad (2.126)$$

## 2.9 Nondimensionalization of the Governing Equations

This section presents non-dimensionalization of the local momentum and energy conservation equations to justify omission of certain terms for reactor applications. No terms are neglected in the mass conservation equation, so this equation is not considered in the present discussion. Beginning with the momentum conservation equation from Eq. (2.29), repeated here for convenience,

$$\rho \frac{dV_i}{dt} = \rho g_i - \nabla P + \nabla \cdot \left\{ \mu \left[ \nabla V_i + (\nabla V_i)^T \right] - \frac{2\mu}{3} \nabla \cdot \vec{V} \right\},$$

the following non-dimensional quantities are defined,

$$t^+ = \frac{t}{L/V_o}, \quad V^+ = \frac{V_i}{V_o}, \quad P^+ = \frac{P}{\rho_o V_o^2}, \quad x^+ = \frac{x}{L}, \quad g^+ = \frac{g_i}{g_o}. \quad (2.127)$$

Inserting Eq. (2.127) into the 1-D form of Eq. (2.29) and dividing through by the coefficient on the advective term,

$$\frac{dV^+}{dx^+} = \frac{L g_o}{V_o^2} g^+ - \frac{\partial P^+}{\partial x^+} + \frac{1}{Re} \frac{\partial}{\partial x^+} (\diamond), \quad (2.128)$$

where the complicated form of the viscous term is denoted as  $\diamond$  for notational simplicity.  $Re$  is the Reynolds number; for a generic porous medium characterized by two different velocity scales  $v$  and  $V$  and two different length scales  $d_p$  and  $D$ , there are many manners in which the Reynolds number has been defined, such as

$$Re = \frac{\rho v d_p}{\mu} \quad (2.129a)$$

$$Re_h = \frac{\rho V D}{\mu} \quad (2.129b)$$

$$Re_i = \frac{\rho V d_p}{\mu} \quad (2.129c)$$

Non-dimensionalization of the energy conservation equation is performed beginning from Eq. (2.67), repeated here for convenience,

$$\rho C_p \frac{dT}{dt} - T \beta \frac{dP}{dt} = \tau_{ij} \frac{\partial V_i}{\partial x_j} + \nabla \cdot (k \nabla T),$$

where the volume viscous dissipation has already been assumed negligible by setting  $\zeta = 0$  and the volumetric heat source is omitted for the present purpose of scaling analysis. The same non-dimensionalization in Eq. (2.127) is used with the additional scaling

$$T^+ = \frac{T}{\Delta T} . \quad (2.130)$$

Inserting Eqs. (2.127) and (2.130) into the 1-D form of Eq. (2.67) and dividing through by the coefficient on the advective term,

$$\frac{dT^+}{dt^+} - \beta Ec T^+ \frac{dP^+}{dt^+} = \frac{Br}{Pe} (\diamond) - \frac{1}{Pe} \frac{\partial T^{+2}}{\partial x^{+2}} , \quad (2.131)$$

where the complicated form of the viscous power term is denoted as  $\diamond$  for notational simplicity.  $Pe$  is the Peclet number defined as

$$Pe \equiv \frac{VL}{\alpha} , \quad (2.132)$$

where  $\alpha$  is a diffusivity that for the energy equation equals  $k/\rho C_p$  and for the momentum equation equals  $\mu/\rho$ . The diffusivity in Eq. (2.132) is usually taken to be the diffusivity for the fluid energy equation, in which case  $Pe = Re \cdot Pr$ , where  $Pr$  is the Prandtl number

$$Pr \equiv \frac{\mu C_p}{k} . \quad (2.133)$$

$Ec$  is the Eckert number defined as

$$Ec = \frac{V^2}{C_p \Delta T} . \quad (2.134)$$

$Br$  is the Brinkman number, defined as

$$Br = \frac{\mu V^2}{k \Delta T} . \quad (2.135)$$

The  $\rho \vec{b} \cdot \vec{V}$  term in Eq. (2.51) is often approximated as  $\rho \vec{g} \cdot \vec{V}$ , though derivation of the energy conservation equation beginning from the spatially homogenized momentum equation would suggest  $\vec{b} = W \vec{V}$ . To assess the validity of this approximation, normalize the neglected term by the diffusive term,

$$\begin{aligned} \frac{\rho W \vec{V} \cdot \vec{V}}{\nabla \cdot (k \nabla T)} &\approx \frac{150 \mu (V^+)^2 + 1.75 \rho (V^+)^3 d_p}{k \Delta T} \left( \frac{D}{d_p} \right)^2 \\ &= 150 Br \left( \frac{D}{d_p} \right)^2 + 1.75 Re Ec Pr \frac{D}{d_p} \end{aligned} \quad (2.136)$$

where Eq. (6.10) is used for  $W$  for illustration purposes [39]. Several approximations are made in implementation of the momentum and energy conservation equations based on the non-dimensional forms in Eqs. (2.128), (2.131), and (2.136) — it is assumed that 1)  $Br/Pe \ll 1$  such that viscous power term in Eqs. (2.44) and (2.67) is neglected; 2)  $\beta Ec \ll 1$  such that compression work  $dP/dt$  term in Eq. (2.67) is neglected; and 3) Eq. (2.136)  $\ll 1$  such that the distributed friction power is neglected. While  $Re \gg 1$  for virtually all of the intended application space, the Brinkman stress term permits the viscous stress term in the momentum equation to optionally be included.

To justify these assumptions for reactor conditions, Table 3 provides coarse estimates for the dimensionless numbers in Eqs. (2.128), (2.131), and (2.136) for five representative reactor designs. For all of these reactors, viscous heating effects can be neglected because  $Br/Pe$  is on the order of  $10^{-9}$ . There is a larger variation in  $Re$ , but in general  $Re$  is relatively high such that the viscous stress term in the momentum equation can usually be neglected. Thermal energy conduction is included due to the relatively low  $Pe$  observed in liquid metal reactors [66].

Values for Eq. (2.136) vary widely among the reactor types presented, and in general the distributed friction power is of the same order of magnitude as the energy conduction term for gas-cooled PBRs. While the energy conduction term is retained due to its importance for liquid metal coolants, neglecting the distributed friction power is justified for PBRs where the energy conduction term is small.

Table 3: Operating conditions and approximate non-dimensional numbers for representative nuclear reactor designs using a variety of coolants. All material properties are evaluated at the median of the operating temperature range. “—” denotes that Eq. (2.136) is not evaluated for non-pebble bed designs.

	PFBR [67, 68]	THTR [69]	PB-FHR [70]	AP-1000 [71, 72]	Torness AGR [73]
Coolant	sodium	helium	FLiBe	water	CO <sub>2</sub>
Power (MW <sub>th</sub> )	1250	750	236	3400	1623
Fuel	assembly	pebble	pebble	assembly	assembly
Type	pool	loop	loop	loop	loop
$P$ (MPa)	0.1	4.0	0.1	15.5	4.1
Temperature (°C)	397/547	250/750	600/700	279/325	339/639
Flowrate (kg/s)	6385	298	976	13705	4067
Velocity (m/s)	4.8	12.0	0.4	4.8	1.6
$D$ (mm)	5.0	26.0	13.0	11.7	38.0
$\rho$ (kg/m <sup>3</sup> )	840.9	2.5	1999.7	720.2	28.4
$\mu$ (10 <sup>-5</sup> Pa·s)	24.6	3.85	678.08	8.73	3.4
$k$ (W/m·K)	139.0	0.30	1.09	0.56	0.05
$C_p$ (J/kg·K)	1268.1	5195	2416	5534	1157
$Pr$	0.002	0.67	15.0	0.86	0.79
$Br$	$2.7 \times 10^{-7}$	$3.7 \times 10^{-5}$	$9.9 \times 10^{-6}$	$7.8 \times 10^{-5}$	$5.8 \times 10^{-6}$
$Re$	$8.2 \times 10^4$	$2.0 \times 10^4$	$1.5 \times 10^3$	$4.6 \times 10^5$	$5.0 \times 10^4$
$Pe$	$1.8 \times 10^2$	$1.3 \times 10^4$	$2.3 \times 10^4$	$4.0 \times 10^5$	$4.0 \times 10^4$
$Ec$	$1.2 \times 10^{-4}$	$5.5 \times 10^{-5}$	$6.6 \times 10^{-7}$	$9.0 \times 10^{-5}$	$7.4 \times 10^{-6}$
$Br/Pe$	$1.5 \times 10^{-9}$	$2.8 \times 10^{-9}$	$4.3 \times 10^{-10}$	$2.0 \times 10^{-10}$	$1.5 \times 10^{-10}$
$\Delta T/T$	$2.2 \times 10^{-1}$	$9.6 \times 10^{-1}$	$1.1 \times 10^{-1}$	$8.3 \times 10^{-2}$	$4.9 \times 10^{-1}$
Eq. (2.136)	—	$0.6 \times 10^0$	$1.1 \times 10^{-2}$	—	—

Pronghorn solves the compressible flow equations for all flows, which range from nearly-incompressible flows, to thermally-compressible flows typical of molten salts, to fully compressible flows typical of most gases. This capability is important for reactor conditions, where large temperature ranges make Boussinesq-type approximations inaccurate.

## 2.10 Summary of Physical Models

This section has presented the governing conservation equations solved in Pronghorn. Later sections describe in great detail the selection of closure relationships for  $\epsilon$ ,  $\kappa_f$ ,  $\kappa_s$ ,  $W$ ,  $\alpha$ , and  $\tilde{\mu}$  for the macroscale and  $\rho_{\text{meso}}$ ,  $C_{p,\text{meso}}$ , and  $k_{\text{meso}}$  for the mesoscale and microscale. This section provides a summary of the three macroscale models available in Pronghorn —

1. Navier-Stokes model;

2. Euler model; and
3. Friction-dominated model.

All three models are compressible flow models with the same solid energy conservation equation. In addition, all three models may be solved for a number of different sets of variables given the flexible nature of the AD material implementation —

1. Conserved variables with interstitial momentum ( $\rho_f$ ,  $\rho_f \vec{V}$ , and  $\rho_f E_f$ );
2. Primitive variables with interstitial velocity ( $P$ ,  $\vec{V}$ , and  $T_f$ );
3. Primitive variables with superficial velocity ( $P$ ,  $\vec{v}$ , and  $T_f$ );
4. Mixed variables with interstitial momentum ( $P$ ,  $\rho_f \vec{V}$ , and  $T_f$ ) and
5. Mixed variables with superficial momentum ( $P$ ,  $\rho_f \vec{v}$ , and  $T_f$ ).

Using superficial velocity and momentum solution variables results in improved convergence for problems with large spatial gradients in porosity. The Navier-Stokes and Euler models use a SUPG stabilization that cross-stabilizes all equations against one another, while the friction-dominated model only stabilizes the mass and energy equations against one another due to the absence of an advective term in the friction-dominated momentum equation.

The remainder of this section summarizes the three macroscale models and two mesoscale and microscale models in Pronghorn; integrals are shown in general terms for a domain  $\Omega$  with boundary  $\Gamma$ . For brevity, the SUPG stabilization terms are not shown in Sections 2.10.1-2.10.3. It is also understood that  $i = 1, 2, 3$  represents each of the momentum equations. Additional background information regarding construction of the weak forms is available in Section 14.

### 2.10.1 The Compressible Navier-Stokes Model

The strong form of the Navier-Stokes model is

$$\varepsilon \frac{\partial \rho_f}{\partial t} + \nabla \cdot (\varepsilon \rho_f \vec{V}) = 0, \quad (2.137a)$$

$$\varepsilon \frac{\partial (\rho_f \vec{V})}{\partial t} + \nabla \cdot (\varepsilon \rho_f \vec{V} \vec{V}) + \varepsilon \nabla P - \varepsilon \rho_f \vec{g} + W \rho_f \vec{V} - \nabla \cdot (\tilde{\mu} \nabla \vec{V}) = 0, \quad (2.137b)$$

$$\varepsilon \frac{\partial (\rho_f E_f)}{\partial t} + \nabla \cdot (\varepsilon H_f \rho_f \vec{V}) - \nabla \cdot (\kappa_f \nabla T_f) - \varepsilon \rho_f \vec{g} \cdot \vec{V} + \alpha (T_f - T_s) - \dot{q}_f = 0, \quad (2.137c)$$

$$(1 - \varepsilon) \rho_s C_{p,s} \frac{\partial T_s}{\partial t} - \nabla \cdot (\kappa_s \nabla T_s) + \alpha (T_s - T_f) - \dot{q}_s = 0. \quad (2.137d)$$

The weak form of the Navier-Stokes model is

$$\int_{\Omega} \varepsilon \frac{\partial \rho_f}{\partial t} \psi d\Omega - \int_{\Omega} \varepsilon \rho_f \vec{V} \cdot \nabla \psi d\Omega + \int_{\Gamma} \varepsilon \rho_f \vec{V} \cdot \hat{n} \psi d\Gamma = 0, \quad (2.138a)$$

$$\begin{aligned} \int_{\Omega} \left[ \varepsilon \frac{\partial(\rho_f V_i)}{\partial t} - \varepsilon \rho_f g_i + W \rho_f V_i - P \frac{\partial \varepsilon}{\partial x_i} \right] \psi d\Omega - \int_{\Omega} \varepsilon \rho_f V_i \vec{V} \cdot \nabla \psi d\Omega + \\ \int_{\Omega} \left( -\varepsilon P \frac{\partial \psi}{\partial x_i} + \tilde{\mu} \nabla V_i \cdot \nabla \psi \right) d\Omega + \int_{\Gamma} \left( \varepsilon \rho_f V_i \vec{V} \cdot \hat{n} + \varepsilon P n_i - \tilde{\mu} \nabla V_i \cdot \hat{n} \right) \psi d\Gamma = 0, \end{aligned} \quad (2.138b)$$

$$\begin{aligned} \int_{\Omega} \left[ \varepsilon \frac{\partial(\rho_f E_f)}{\partial t} - \varepsilon \rho_f \vec{g} \cdot \vec{V} + \alpha(T_f - T_s) - \dot{q}_f \right] \psi d\Omega - \int_{\Omega} \varepsilon H_f \rho_f \vec{V} \cdot \nabla \psi d\Omega + \\ \int_{\Omega} \kappa_f \nabla T_f \cdot \nabla \psi + \int_{\Gamma} \left( \varepsilon H_f \rho_f \vec{V} \cdot \hat{n} - \kappa_f \nabla T_f \cdot \hat{n} \right) \psi d\Gamma = 0, \end{aligned} \quad (2.138c)$$

$$\int_{\Omega} \left[ (1 - \varepsilon) \rho_s C_{p,s} \frac{\partial T_s}{\partial t} + \alpha(T_s - T_f) - \dot{q}_s \right] \psi d\Omega + \int_{\Omega} \kappa_s \nabla T_s \cdot \nabla \psi d\Omega - \int_{\Gamma} \kappa_s \nabla T_s \cdot \hat{n} \psi d\Gamma = 0, \quad (2.138d)$$

where  $i$  represents each component of the momentum equation.

## 2.10.2 The Compressible Euler Model

The strong form of the Euler model is

$$\varepsilon \frac{\partial \rho_f}{\partial t} + \nabla \cdot (\varepsilon \rho_f \vec{V}) = 0, \quad (2.139a)$$

$$\varepsilon \frac{\partial(\rho_f \vec{V})}{\partial t} + \nabla \cdot (\varepsilon \rho_f \vec{V} \vec{V}) + \varepsilon \nabla P - \varepsilon \rho_f \vec{g} + W \rho_f \vec{V} = 0, \quad (2.139b)$$

$$\varepsilon \frac{\partial(\rho_f E_f)}{\partial t} + \nabla \cdot (\varepsilon H_f \rho_f \vec{V}) - \nabla \cdot (\kappa_f \nabla T_f) - \varepsilon \rho_f \vec{g} \cdot \vec{V} + \alpha(T_f - T_s) - \dot{q}_f = 0, \quad (2.139c)$$

$$(1 - \varepsilon) \rho_s C_{p,s} \frac{\partial T_s}{\partial t} - \nabla \cdot (\kappa_s \nabla T_s) + \alpha(T_s - T_f) - \dot{q}_s = 0, \quad (2.139d)$$

which is the same as Eq. (2.137) except that  $\tilde{\mu}$  is set to zero. The weak form of the Euler model is

$$\int_{\Omega} \varepsilon \frac{\partial \rho_f}{\partial t} \psi d\Omega - \int_{\Omega} \varepsilon \rho_f \vec{V} \cdot \nabla \psi d\Omega + \int_{\Gamma} \varepsilon \rho_f \vec{V} \cdot \hat{n} \psi d\Gamma = 0, \quad (2.140a)$$

$$\int_{\Omega} \left[ \varepsilon \frac{\partial(\rho_f V_i)}{\partial t} - \varepsilon \rho_f g_i + W \rho_f V_i - P \frac{\partial \varepsilon}{\partial x_i} \right] \psi d\Omega - \int_{\Omega} \varepsilon \rho_f V_i \vec{V} \cdot \nabla \psi d\Omega + \int_{\Omega} \left( -\varepsilon P \frac{\partial \psi}{\partial x_i} \right) d\Omega + \int_{\Gamma} \left( \varepsilon \rho_f V_i \vec{V} \cdot \hat{n} + \varepsilon P n_i \right) \psi d\Gamma = 0, \quad (2.140b)$$

$$\int_{\Omega} \left[ \varepsilon \frac{\partial(\rho_f E_f)}{\partial t} - \varepsilon \rho_f \vec{g} \cdot \vec{V} + \alpha(T_f - T_s) - \dot{q}_f \right] \psi d\Omega - \int_{\Omega} \varepsilon H_f \rho_f \vec{V} \cdot \nabla \psi d\Omega + \int_{\Omega} \kappa_f \nabla T_f \cdot \nabla \psi + \int_{\Gamma} \left( \varepsilon H_f \rho_f \vec{V} \cdot \hat{n} - \kappa_f \nabla T_f \cdot \hat{n} \right) \psi d\Gamma = 0, \quad (2.140c)$$

$$\int_{\Omega} \left[ (1 - \varepsilon) \rho_s C_{p,s} \frac{\partial T_s}{\partial t} + \alpha(T_s - T_f) - \dot{q}_s \right] \psi d\Omega + \int_{\Omega} \kappa_s \nabla T_s \cdot \nabla \psi d\Omega - \int_{\Gamma} \kappa_s \nabla T_s \cdot \hat{n} \psi d\Gamma = 0. \quad (2.140d)$$

### 2.10.3 The Compressible Friction-Dominated Model

The strong form of the friction-dominated model is

$$\varepsilon \frac{\partial \rho_f}{\partial t} + \nabla \cdot \left[ \frac{\varepsilon^2}{W} (\rho_f \vec{g} - \nabla P) \right] = 0, \quad (2.141a)$$

$$\varepsilon \nabla P - \varepsilon \rho_f \vec{g} + W \rho_f \vec{V} = 0, \quad (2.141b)$$

$$\varepsilon \rho_f C_{p,f} \frac{\partial T_f}{\partial t} + \varepsilon \rho_f C_{p,f} \vec{V} \cdot \nabla T_f - \nabla \cdot (\kappa_f \nabla T_f) + \alpha(T_f - T_s) - \dot{q}_f = 0, \quad (2.141c)$$

$$(1 - \varepsilon) \rho_s C_{p,s} \frac{\partial T_s}{\partial t} - \nabla \cdot (\kappa_s \nabla T_s) + \alpha(T_s - T_f) - \dot{q}_s = 0. \quad (2.141d)$$

The weak form of the friction-dominated model is

$$\int_{\Omega} \varepsilon \frac{\partial \rho_f}{\partial t} \psi d\Omega - \int_{\Omega} \left[ \frac{\varepsilon^2}{W} (\rho_f \vec{g} - \nabla P) \right] \cdot \nabla \psi d\Omega + \int_{\Gamma} \left[ \frac{\varepsilon^2}{W} (\rho_f \vec{g} - \nabla P) \right] \psi d\Gamma = 0, \quad (2.142a)$$

$$\int_{\Omega} \left[ -\varepsilon \rho_f g_i + W \rho_f V_i - P \frac{\partial \varepsilon}{\partial x_i} \right] \psi d\Omega - \int_{\Omega} \varepsilon P \frac{\partial \psi}{\partial x_i} d\Omega + \int_{\Gamma} \varepsilon P n_i \psi d\Gamma = 0, \quad (2.142b)$$

$$\int_{\Omega} \left( \varepsilon \rho_f C_{p,f} \frac{\partial T_f}{\partial t} + \varepsilon \rho_f C_{p,f} \vec{V} \cdot \nabla T_f + \alpha(T_f - T_s) - \dot{q}_f \right) \psi d\Omega + \int_{\Omega} \kappa_f \nabla T_f \cdot \nabla \psi d\Omega - \int_{\Gamma} \kappa_f \nabla T_f \cdot \hat{n} \psi d\Gamma = 0, \quad (2.142c)$$

$$\int_{\Omega} \left[ (1 - \varepsilon) \rho_s C_{p,s} \frac{\partial T_s}{\partial t} + \alpha(T_s - T_f) - \dot{q}_s \right] \psi d\Omega + \int_{\Omega} \kappa_s \nabla T_s \cdot \nabla \psi d\Omega - \int_{\Gamma} \kappa_s \nabla T_s \cdot \hat{n} \psi d\Gamma = 0. \quad (2.142d)$$

#### 2.10.4 The Mesoscale and Microscale Models

The weak form of the mesoscale and microscale models in Eqs. (2.88), (2.91), and (2.92) is

$$\int_{\Omega} \left[ \rho_j C_{p,j} \frac{\partial T_j}{\partial t} \psi + k_j \nabla T_j \cdot \nabla \psi + Q \psi \right] d\Omega - \int_{\Gamma} k_j \nabla T_j \cdot \hat{n} \psi d\Gamma = 0, \quad (2.143)$$

where  $j = S$  and  $Q = \dot{q}_s$  for Eq. (2.88);  $j = \text{meso}$  and  $Q = \langle \dot{q} \rangle$  for Eq. (2.91); and  $j = \text{micro}$  and  $Q = \hat{q}$  for Eq. (2.92).

### 3 Interface Kernels

Interface kernels are used to apply Neumann-type BCs or other constraints on interior mesh sidesets to link variables defined on two different regions of the mesh. Interface kernels use a Discontinuous Galerkin (DG) formulation to specify a residual contribution from one block to another. For Neumann-type conditions, fluxes described as variable differences, such as is the case for convection and radiation fluxes, are simple to define. A numerical flux function must be used for diffusive fluxes, which have different forms depending on the block adjacent to the sideset due to potentially different diffusion coefficients. The following sections describe the interface kernels available in Pronghorn, which are augmented by many further kernels in the MOOSE heat conduction module.

#### 3.1 Conductive Heat Transfer

To enforce a conductive heat flux between two variables  $T_1$  and  $T_2$ , the heat flux along a shared interface is given as

$$q''_{1 \rightarrow 2} = \frac{1}{2} \left( -k_1 \frac{\partial T_1}{\partial x} \hat{n} - k_2 \frac{\partial T_2}{\partial x} \hat{n} \right), \quad (3.1)$$

where the  $1 \rightarrow 2$  notation indicates that the heat flux is directional from block 1 to block 2.

#### 3.2 Pressure Loss

To enforce a pressure drop between two variables  $P_1$  and  $P_2$ , the jump condition along a shared interface is given as

$$P_1 = P_2 + K \rho_f V_i V_i, \quad (3.2)$$

where  $K$  is a form loss coefficient.

#### 3.3 Radiative Heat Transfer

To enforce a radiative heat transfer between gray bodies, the heat flux along a shared interface is given as

$$q''_{1 \rightarrow 2} = \sigma (T_1^4 - T_2^4) / \left( \frac{1}{\epsilon_{r,1}} + \frac{1}{\epsilon_{r,2}} + 1 \right) \quad (3.3)$$

## 4 Boundary Conditions

This section discusses the BCs for the spatially homogenized conservation equations. Section 4.1 presents a derivation of BCs required from conservation principles, while the following sections describe additional inflow, outflow, wall, and symmetry BCs not strictly required to obey conservation of mass, momentum, and energy.

### 4.1 Conditions Imposed by Conservation

This section presents BCs required from conservation principles for a Newtonian fluid by considering a fluid control volume straddling an interface. This interface moves with velocity  $\vec{V}$ , while the control volume moves relative to the interface with velocity  $\vec{V}'$ ,

$$\vec{V}' = \vec{V} - \vec{V} \cdot \hat{n} . \quad (4.1)$$

If the interface is a material interface, then that interface moves with the fluid velocity  $\vec{V}$  such that the relative velocity between the control volume and the material interface is zero,

$$\vec{V} = \vec{V} \cdot \hat{n} . \quad (4.2)$$

Balancing mass as in Eq. (2.7) over a moving interface, with the positive direction defined pointing from side “1” to side “2” gives

$$\int_{\mathcal{V}} \frac{\partial(\epsilon \rho_f)}{\partial t} d\mathcal{V} = -\epsilon \rho_f \vec{V}' \cdot \hat{n} \Big|_1^2 + \text{mass flow} \parallel \text{to interface} \quad (4.3)$$

In the limit of zero thickness of the control volume in the direction normal to the interface, the volume integral and parallel flow terms are zero, giving

$$\epsilon \rho_f \vec{V}' \cdot \hat{n} \Big|_1^2 = 0 \quad (\text{general interface}) , \quad (4.4a)$$

$$\epsilon \vec{V} \cdot \hat{n} \Big|_1^2 = 0 \quad (\text{material interface}) . \quad (4.4b)$$

Inserting Eq. (4.2) into Eq. (4.4a) for  $\vec{V} = \vec{V}_1$  or  $\vec{V} = \vec{V}_2$  gives Eq. (4.4b). Therefore, mass conservation requires a zero normal velocity on material interfaces; this is often referred to as the “kinematic,” or “no-penetration” BC. Within the Finite Element (FE) discretization, such a term in the mass equation is synonymous with the “natural” BC.

Balancing momentum as in Eq. (2.39) over the same control volume as for the mass equation,

$$\begin{aligned} \int_{\mathcal{V}} \frac{\partial(\epsilon \rho_f V_i')}{\partial t} d\mathcal{V} = & -\epsilon \rho_f V_i' \vec{V}' \cdot \hat{n} \Big|_1^2 + \sigma_{ij} n_j \Big|_1^2 + f_{s,i} + \\ & \int_{\mathcal{V}} (\epsilon \rho_f g_i - W \rho_f V_i) d\mathcal{V} + \text{momentum flow} \parallel \text{to interface} , \end{aligned} \quad (4.5)$$

where  $\vec{f}_s$  represents the resultant surface tension force vector and the stress is retained as  $\sigma$  for conciseness. In the limit of zero thickness of the control volume in the direction normal to the interface, the volume integral and parallel flow terms are zero.

$$\varepsilon \rho_f V_i' \vec{V}' \cdot \hat{n} \Big|_1^2 = \sigma_{ij} n_j \Big|_1^2 + f_{s,i} \quad (\text{general interface}) \quad (4.6a)$$

$$0 = \sigma_{ij} n_j \Big|_1^2 + f_{s,i} \quad (\text{material interface}) \quad (4.6b)$$

Inserting Eq. (4.2) into Eq. (4.4a) for  $\vec{V} = \vec{V}_1$  or  $\vec{V} = \vec{V}_2$  gives Eq. (4.6b). For a free jet, neglecting viscous and surface tension forces in Eq. (4.6) shows that the pressure in the jet everywhere equals atmospheric pressure.

Finally, balancing energy as in Eq. (2.82) over the same control volume as for the mass equation,

$$\int_{\mathcal{V}} \frac{\partial(\varepsilon \rho_f E_f)}{\partial t} d\mathcal{V} = -\varepsilon \rho_f E_f \vec{V}' \cdot \hat{n} \Big|_1^2 - \vec{q} \cdot \hat{n} \Big|_1^2 + \sigma_{ij} n_j V_i' \Big|_1^2 + \int_{\mathcal{V}} \varepsilon \rho_f b_i V_i d\mathcal{V} + \text{energy flow} \parallel \text{to interface} , \quad (4.7)$$

where the stress is retained as  $\sigma$  for conciseness. In the limit of zero thickness of the control volume in the direction normal to the interface, the volume integral and parallel flow terms are zero,

$$\varepsilon \rho_f E_f \vec{V}' \cdot \hat{n} \Big|_1^2 = -\vec{q} \cdot \hat{n} \Big|_1^2 + \sigma_{ij} n_j V_i' \Big|_1^2 \quad (\text{general interface}) \quad (4.8a)$$

$$0 = -\vec{q} \cdot \hat{n} \Big|_1^2 + \sigma_{ij} n_j V_i' \Big|_1^2 \quad (\text{general interface}) \quad (4.8b)$$

$$(4.8c)$$

The important result obtained in this section is that the normal velocity at material interfaces must be zero; for solid walls, this also shows that the advective term in the momentum and energy BCs in Eqs. (4.6) and (4.8), respectively, are zero.

## 4.2 Additional Conditions Required for Closure

Section 4.1 derived the no-penetration conditions required for conservation of mass, momentum, and energy. This section discusses additional BCs required to close the system of equations while forming a well-posed problem. Section 19.3 provides relevant background on the mathematical structure of advection and diffusion kernels. For systems of equations that permit real wave propagation, which include hyperbolic and parabolic equations, a well-posed set of BCs should not impose any conditions in the zone of influence, or regions that affect the solution in other parts of the domain. This will result in certain requirements on the number of BCs that can be set on inflow versus outflow boundaries. BCs must only be imposed on boundaries where the wave speeds in Eq. (19.76) are positive relative to the unit normal of the boundary, or where characteristics enter the domain. For boundaries with negative wave speeds, characteristics propagate out of the domain. Due to the existence of boundary terms in the weak form a “free” BC must be set using the implicit solution fields. On a given boundary, the number of physical BCs is equal to the number of positive wave speeds, while the number of numerical BCs is equal to the number of negative wave speeds.

Conversely, elliptic problems are characterized by complex wave propagation such that the zone of dependence and zone of influence coincide, removing special considerations on specifying BCs on inflow and outflow boundaries. For each elliptic equation, a BC may be specified on each boundary.

Pronghorn contains three different models that are summarized in Section 2.10 — 1) a compressible Navier-Stokes model; 2) a compressible Euler model; and 3) a friction-dominated model. Due to the inclusion of both advective and

diffusive terms in the energy equations for all models, the three equation sets are mixed hyperbolic-parabolic models. Despite this mixed nature, insights to the required BCs can be obtained by considering the conventional form of the Euler equations which neglect the heat conduction term in the energy equation. A purely advective set of conservation equations in a domain with unit inward normals  $\vec{n}$  has eigenvalues  $\vec{V} \cdot \hat{n} - c$ ,  $\vec{V} \cdot \hat{n} + c$ , and  $\vec{V} \cdot \hat{n}$ , the latter occurring once for each spatial dimension [74]. Therefore, on subsonic inlets,  $n_{sd} + 1$  eigenvalues are positive and one eigenvalue is negative such that inflow BCs require specification of  $n_{sd} + 1$  physical conditions and one implicit condition. A well-posed system can be formed by specifying velocity or momentum and temperature, with implicit pressure.

On subsonic outlets,  $n_{sd} + 1$  eigenvalues are negative and one eigenvalue is positive such that outflow BCs require specification of  $n_{sd} + 1$  implicit conditions and one physical condition. A well-posed system is typically formed by imposing pressure on the outflow with implicit mass, momentum, and energy fluxes.

For supersonic inlets, all eigenvalues are positive, necessitating  $n_{sd} + 2$  physical conditions. For supersonic outlets, all eigenvalues are negative, necessitating  $n_{sd} + 2$  implicit conditions.

At solid walls, there is always one positive eigenvalue and one negative eigenvalue. Therefore, one physical BC and one implicit BC must be imposed. The physical BC corresponds to conservation of mass in Eq. (4.4) and requires setting  $\vec{V} \cdot \hat{n} = 0$ . The implicit BC corresponds to slip (for an inviscid flow model) and implicitly-integrated pressure for the momentum equation.

The eigenvalues also have implications on numerical solution techniques. For the time-independent Euler equations, the conservation equations are hybrid hyperbolic-elliptic for subsonic flow but fully hyperbolic for supersonic flow. Exactly at a Mach number of unity, the system of equations is parabolic. The difficulty of constructing numerical methods that perform well over this range in mathematical structure motivates the use of time-dependent equations, which are always of the same mathematical character regardless of Mach number. For this reason, even the simulation of steady states in Pronghorn is performed with pseudo transients to enhance convergence.

There are two general types of BCs available in the FE discretization — a Dirichlet BC, which strongly enforces a value for a variable, and Neumann BCs, which weakly enforce a flux. Neumann-type BCs are additive within the MOOSE framework, allowing some BCs to be split into more than one BC for modularity. In the sections that follow, the available BCs in the fluid mass, momentum, and energy equations and solid energy equation are described. In this discussion,  $i$  subscripts denote known quantities, while a lack of a subscript indicates an implicit value. Functional notation, such as  $\rho_f(P, T_f)$ , indicates the use of the EOS to obtain  $\rho_f$  from  $P$  and  $T_f$ .

For the fluid equations, most simulations can be described in terms of four types of boundaries such that the boundary is the union of the inlet  $\Gamma_{\text{in}}$ , outlet  $\Gamma_{\text{out}}$ , wall  $\Gamma_{\text{wall}}$ , and  $r$ - $z$  symmetry axis  $\Gamma_{r\text{-}z \text{ symmetry}}$ ,

$$\Gamma \equiv \Gamma_{\text{in}} \cup \Gamma_{\text{out}} \cup \Gamma_{\text{wall}} \cup \Gamma_{r\text{-}z \text{ symmetry}} , \quad (4.9)$$

where the intersection of the  $j$ -th term on the RHS of Eq. (4.9) with the  $k$ -th term on the RHS of Eq. (4.9) is the empty set for  $j \neq k$ .

On inlet boundaries, temperature and either velocity or momentum are specified. Velocity and momentum may be specified in an interstitial or superficial basis such that the inlet boundary is the union of boundaries on which the interstitial velocity, superficial velocity, interstitial momentum, and superficial momentum are specified,

$$\begin{aligned} \Gamma_{\text{in}} \equiv & \Gamma_{\text{in, interstitial velocity}} \cup \Gamma_{\text{in, superficial velocity}} \cup \\ & \Gamma_{\text{in, interstitial momentum}} \cup \Gamma_{\text{in, superficial momentum}} , \end{aligned} \quad (4.10)$$

where the intersection of the  $j$ -th term on the RHS of Eq. (4.24) with the  $k$ -th term on the RHS of Eq. (4.24) is the empty set for  $j \neq k$ .

On outlet boundaries, pressure is specified. The wall boundary is the union of the slip and no-slip boundaries,

$$\Gamma_{\text{wall}} \equiv \Gamma_{\text{wall, slip}} \cup \Gamma_{\text{wall, no-slip}} , \quad (4.11)$$

where  $\Gamma_{\text{wall, slip}} \cap \Gamma_{\text{wall, no-slip}} = \emptyset$ . The wall boundary is also the union of the specified temperature and heat flux boundaries,

$$\Gamma_{\text{wall}} \equiv \Gamma_{\text{wall, temperature}} \cup \Gamma_{\text{wall, heat flux}} , \quad (4.12)$$

where  $\Gamma_{\text{wall, temperature}} \cap \Gamma_{\text{wall, heat flux}} = \emptyset$ . The heat flux boundary is understood to consist of a variety of different representations of heat flux, such as conduction, convection, and radiation, which may have a nonzero intersection with one another. The  $r$ - $z$  symmetry boundary is a fully implicit no-penetration boundary.

Sections 4.2.1–4.2.3 describe in further detail the BCs for the fluid conservation equations, while Section 4.2.4 describe the BCs for the solid energy equation.

#### 4.2.1 The Fluid Mass Equation

When solving the mass equation for pressure, the outlet condition is

$$P = P_i \text{ for } \Gamma \in \Gamma_{\text{out}} , \quad (4.13)$$

while the outlet condition for density as the nonlinear variable is a fully-implicit condition with pressure weakly imposed in the momentum BCs,

$$\epsilon \rho_f \vec{V} \cdot \hat{n} = \epsilon \rho_f \vec{V} \cdot \hat{n} \text{ for } \Gamma \in \Gamma_{\text{out}} . \quad (4.14)$$

When pressure is a nonlinear variable, a variation of Eq. (4.13) is also available to apply a hydrostatic pressure distribution relative to a reference coordinate, with an optional form loss proportional to the momentum,

$$P = P_{\text{ref}} + \rho_f |g| (\zeta_{\text{ref}} - \zeta) + K \rho_f \|\vec{V}\|^2 , \quad (4.15)$$

where “ref” indicates the reference coordinate,  $\zeta$  is the position along the axis in which gravity acts with magnitude  $|g|$ , and  $K$  is a form loss coefficient.

The Neumann-type BCs for the advective flux integral for the remaining boundaries are

$$\epsilon \rho_f \vec{V} \cdot \hat{n} = \begin{cases} 0 & \Gamma \in \Gamma_{\text{wall}} \\ 0 & \Gamma \in \Gamma_{r-z \text{ symmetry}} \\ \epsilon \rho_f \vec{V} \cdot \hat{n} & \Gamma \in \Gamma_{\text{in}} \\ \epsilon \rho_f \vec{V}_i \cdot \hat{n} & \Gamma \in \Gamma_{\text{in, interstitial velocity}} \\ \rho_f \vec{v}_i \cdot \hat{n} & \Gamma \in \Gamma_{\text{in, superficial velocity}} \\ \epsilon (\rho_f \vec{V})_i \cdot \hat{n} & \Gamma \in \Gamma_{\text{in, interstitial momentum}} \\ (\rho_f \vec{v})_i \cdot \hat{n} & \Gamma \in \Gamma_{\text{in, superficial momentum}} \end{cases} , \quad (4.16)$$

where the condition on  $\Gamma_{\text{in}}$  indicates that a fully-implicit condition may optionally be used instead of the more specific weak conditions on  $\Gamma_{\text{in, interstitial velocity}}$ ,  $\Gamma_{\text{in, interstitial momentum}}$ ,  $\Gamma_{\text{in, superficial velocity}}$ , and  $\Gamma_{\text{in, superficial momentum}}$ .

For the special case of the ideal gas EOS which has simple isentropic relations that obviate the need for entropy calculations in the fluid properties system, a stagnation inlet BC is available. Because this is a special case that is currently only available for the ideal gas EOS, the stagnation portion of  $\Gamma_{\text{in}}$  is not included in the more general Eq. (4.24). For a specified stagnation temperature  $T_{\text{stag}}$  and pressure  $P_{\text{stag}}$ , the inlet temperature  $T_{\text{in}}$  is

$$T_{\text{in}} = T_{\text{stag}} - \frac{1}{2} \frac{\|\vec{V}\|^2}{C_{p,f}}, \quad (4.17)$$

while the inlet pressure  $P_{\text{in}}$  is

$$P_{\text{in}} = P_{\text{stag}} \frac{T_{\text{stag}}^{-\frac{\gamma}{\gamma-1}}}{T_{\text{in}}}, \quad (4.18)$$

where  $\gamma$  is the specific heat ratio, defined as

$$\gamma \equiv \frac{C_p}{C_v}. \quad (4.19)$$

The stagnation inlet BC for the mass equation is then

$$\varepsilon \rho_f \vec{V} \cdot \hat{n} = \varepsilon \rho_f(P_{\text{in}}, T_{\text{in}}) \vec{V} \cdot \hat{n} \text{ for } \Gamma \in \Gamma_{\text{in,stag}}. \quad (4.20)$$

#### 4.2.2 The Fluid Momentum Equation

The BCs for the fluid momentum equation are described here assuming that the pressure gradient kernel  $\varepsilon \nabla P$  is expressed as  $\nabla(\varepsilon P) - P \nabla \varepsilon$  with the first term integrated by parts to give a pressure contribution on the boundary. If this option is not exercised, then all BCs related to pressure in this section are omitted.

For the momentum conservation equation, a Dirichlet value of velocity or momentum is specified on the inlet. While no boundary term exists in the friction-dominated momentum conservation equation from the advective flux kernel, Dirichlet conditions are still applied on the inlets to strongly enforce the desired inlet condition.

If the nonlinear variable is interstitial velocity, the inlet BC is

$$\vec{V} = \begin{cases} \vec{V}_i & \Gamma \in \Gamma_{\text{in}}, \text{ interstitial velocity} \\ \vec{v}_i / \varepsilon & \Gamma \in \Gamma_{\text{in}}, \text{ superficial velocity} \\ (\rho_f \vec{V})_i / \rho_f(P, T_{f,i}) & \Gamma \in \Gamma_{\text{in}}, \text{ interstitial momentum} \\ (\rho_f \vec{v})_i / [\varepsilon \rho_f(P, T_{f,i})] & \Gamma \in \Gamma_{\text{in}}, \text{ superficial momentum} \end{cases}. \quad (4.21)$$

If the nonlinear variable is superficial velocity, the inlet BC is

$$\vec{v} = \begin{cases} \varepsilon \vec{V}_i & \Gamma \in \Gamma_{\text{in}}, \text{ interstitial velocity} \\ \vec{v}_i & \Gamma \in \Gamma_{\text{in}}, \text{ superficial velocity} \\ \varepsilon (\rho_f \vec{V})_i / \rho_f(P, T_{f,i}) & \Gamma \in \Gamma_{\text{in}}, \text{ interstitial momentum} \\ (\rho_f \vec{v})_i / \rho_f(P, T_{f,i}) & \Gamma \in \Gamma_{\text{in}}, \text{ superficial momentum} \end{cases}. \quad (4.22)$$

If the nonlinear variable is interstitial momentum, the inlet BC is

$$\rho_f \vec{V} = \begin{cases} \rho_f(P, T_{f,i}) \vec{V}_i & \Gamma \in \Gamma_{\text{in, interstitial velocity}} \\ \rho_f(P, T_{f,i}) \vec{v}_i / \varepsilon & \Gamma \in \Gamma_{\text{in, superficial velocity}} \\ (\rho_f \vec{V})_i & \Gamma \in \Gamma_{\text{in, interstitial momentum}} \\ (\rho_f \vec{v})_i / \varepsilon & \Gamma \in \Gamma_{\text{in, superficial momentum}} \end{cases} \quad (4.23)$$

If the nonlinear variable is superficial momentum, the inlet BC is

$$\rho_f \vec{v} = \begin{cases} \varepsilon \rho_f(P, T_{f,i}) \vec{V}_i & \Gamma \in \Gamma_{\text{in, interstitial velocity}} \\ \rho_f(P, T_{f,i}) \vec{v}_i & \Gamma \in \Gamma_{\text{in, superficial velocity}} \\ \varepsilon (\rho_f \vec{V})_i & \Gamma \in \Gamma_{\text{in, interstitial momentum}} \\ (\rho_f \vec{v})_i & \Gamma \in \Gamma_{\text{in, superficial momentum}} \end{cases} \quad (4.24)$$

For no-slip solid walls, additional Dirichlet-type BCs are one of

$$\vec{V} = \vec{0} \text{ for } \Gamma \in \Gamma_{\text{wall, no-slip}} , \quad (4.25a)$$

$$\vec{v} = \vec{0} \text{ for } \Gamma \in \Gamma_{\text{wall, no-slip}} , \quad (4.25b)$$

$$\rho_f \vec{V} = \vec{0} \text{ for } \Gamma \in \Gamma_{\text{wall, no-slip}} , \quad (4.25c)$$

$$\rho_f \vec{v} = \vec{0} \text{ for } \Gamma \in \Gamma_{\text{wall, no-slip}} , \quad (4.25d)$$

depending on the nonlinear solution variable. The Neumann-type BCs for the advective flux integral in the  $j$ -th momentum equation for the remaining boundaries are

$$\varepsilon \rho_f V_j \vec{V} \cdot \hat{n} = \begin{cases} 0 & \Gamma \in \Gamma_{\text{wall, slip}} \\ 0 & \Gamma \in \Gamma_{r-z \text{ symmetry}} \\ \varepsilon \rho_f V_j \vec{V} \cdot \hat{n} & \Gamma \in \Gamma_{\text{out}} \end{cases} \quad (4.26)$$

The Neumann-type BCs for the pressure integral in the  $j$ -th momentum equation for the remaining boundaries are

$$\varepsilon P n_j = \begin{cases} \varepsilon P n_j & \Gamma \in \Gamma_{\text{wall, slip}} \\ \varepsilon P n_j & \Gamma \in \Gamma_{r-z \text{ symmetry}} \\ \varepsilon P_i n_j & \Gamma \in \Gamma_{\text{out}} \end{cases} \quad (4.27)$$

The Neumann-type BCs for the diffusive flux integral in the  $j$ -th momentum equation for the remaining boundaries are

$$-\tilde{\mu} \nabla V_j \cdot \hat{n} = \begin{cases} -\tilde{\mu} \nabla V_j \cdot \hat{n} & \Gamma \in \Gamma_{\text{wall, slip}} \\ 0 & \Gamma \in \Gamma_{r-z \text{ symmetry}} \\ -\tilde{\mu} \nabla V_j \cdot \hat{n} & \Gamma \in \Gamma_{\text{out}} \end{cases} \quad (4.28)$$

For a stagnation inlet, with the ideal gas EOS, the inlet pressure and temperature in Eqs. (4.17) and (4.18) provide the following conditions,

$$\varepsilon \rho_f V_j \vec{V} \cdot \hat{n} = \varepsilon \rho_f (P_{\text{in}}, T_{\text{in}}) V_j \vec{V} \cdot \hat{n} \text{ for } \Gamma \in \Gamma_{\text{in,stag}} , \quad (4.29)$$

$$\varepsilon P n_j = \varepsilon P_{\text{in}} n_j \text{ for } \Gamma \in \Gamma_{\text{in,stag}} . \quad (4.30)$$

### 4.2.3 The Fluid Energy Equation

When solving the fluid energy equation for temperature, a Dirichlet value of temperature may be specified on the inlet and walls,

$$T_f = T_{f,i} \text{ for } \Gamma \in \Gamma_{\text{in}} \cup \Gamma_{\text{wall, temperature}} , \quad (4.31)$$

If the nonlinear variable is total fluid energy, this BC in Dirichlet form is

$$\rho_f E_f = \rho_f (P, T_{f,i}) \left[ e_f(P, T_{f,i}) + \frac{1}{2} \vec{V} \cdot \vec{V} \right] \text{ for } \Gamma \in \Gamma_{\text{in}} \cup \Gamma_{\text{wall, temperature}} . \quad (4.32)$$

Alternatively, a Neumann-type implementation of the same temperature BC is

$$\varepsilon \rho_f H_f \vec{V} \cdot \hat{n} = \varepsilon \left\{ \rho_f (P, T_{f,i}) \left[ e_f(P, T_{f,i}) + \frac{1}{2} \vec{V} \cdot \vec{V} \right] + P \right\} \vec{V} \cdot \hat{n} \text{ for } \Gamma \in \Gamma_{\text{in}} , \quad (4.33)$$

where the wall contribution is no longer present because all walls are no-penetration boundaries.

No advective flux integral appears in the weak form of the friction-dominated model in Eq. (2.142c). The Neumann-type BCs for the advective flux integral in Eqs. (2.138c) and (2.140c) for the remaining boundaries are

$$\varepsilon \rho_f H_f \vec{V} \cdot \hat{n} = \begin{cases} 0 & \Gamma \in \Gamma_{\text{wall}} \\ 0 & \Gamma \in \Gamma_{r-z \text{ symmetry}} \\ \varepsilon \left\{ \rho_f \left[ e_f(P_i, T_f) + \frac{1}{2} \vec{V} \cdot \vec{V} \right] + P_i \right\} \vec{V} \cdot \hat{n} & \Gamma \in \Gamma_{\text{out}} \end{cases} . \quad (4.34)$$

The Neumann-type BCs for the diffusive flux integral for the remaining boundaries are

$$-\kappa_f \nabla T_f \cdot \hat{n} = \begin{cases} \tilde{q} & \Gamma \in \Gamma_{\text{wall, heat flux (generic)}} \\ -k_\infty \nabla T_\infty \cdot \hat{n} & \Gamma \in \Gamma_{\text{wall, heat flux (conduction)}} \\ h_c (T_f - T_\infty) & \Gamma \in \Gamma_{\text{wall, heat flux (convection)}} \\ \varepsilon \sigma (T_f^4 - T_\infty^4) & \Gamma \in \Gamma_{\text{wall, heat flux (radiation)}} \\ 0 & \Gamma \in \Gamma_{r-z \text{ symmetry}} \\ -\kappa_f \nabla T_f \cdot \hat{n} & \Gamma \in \Gamma_{\text{out}} \end{cases} , \quad (4.35)$$

where  $\tilde{q}$  represents a generic heat flux, the  $\infty$  subscripts refer to the domain adjacent to the boundary,  $h_c$  is the convective heat transfer coefficient,  $\varepsilon$  is the surface emissivity, and  $\sigma$  is the Boltzmann constant. Section 4.2.5 describes more specific versions of the wall heat flux condition that also apply to the solid energy equation.

For a stagnation inlet, with the ideal gas EOS, the inlet pressure and temperature in Eqs. (4.17) and (4.18) provide the following conditions,

$$\varepsilon \rho_f H_f \vec{V} \cdot \hat{n} = \varepsilon \left[ \rho_f (P_{\text{in}}, T_{\text{in}}) \left( C_{v,f} T_{\text{in}} + \frac{1}{2} \|\vec{V}\|^2 \right) + P_{\text{in}} \right] \vec{V} \cdot \hat{n} \text{ for } \Gamma \in \Gamma_{\text{in,stag}} , \quad (4.36)$$

$$-\kappa_f \nabla T_f \cdot \hat{n} = -\kappa_f \nabla T_f \cdot \hat{n} \Gamma \in \Gamma_{\text{in,stag}} . \quad (4.37)$$

#### 4.2.4 The Solid Energy Equation

The parabolic character of the solid energy conservation equation permits BCs to be applied on any boundary of the domain; these boundaries are either temperature, heat flux, or  $r$ - $z$  symmetry boundaries, irrespective of whether the boundary represents a fluid inlet, outlet, or wall,

$$\Gamma \equiv \Gamma_{\text{temperature}} \cup \Gamma_{\text{heat flux}} \cup \Gamma_{r\text{-}z \text{ symmetry}} , \quad (4.38)$$

where the intersection of the  $j$ -th term on the RHS of Eq. (4.38) with the  $k$ -th term on the RHS of Eq. (4.38) is the empty set for  $j \neq k$ . A Dirichlet temperature is specified as

$$T_s = T_{s,i} \text{ for } \Gamma \in \Gamma_{\text{temperature}} . \quad (4.39)$$

The Neumann-type BCs for the diffusive flux integral for the remaining boundaries are

$$-\kappa_s \nabla T_s \cdot \hat{n} = \begin{cases} \bar{q} & \Gamma \in \Gamma_{\text{heat flux (generic)}} \\ -k_\infty \nabla T_\infty \cdot \hat{n} & \Gamma \in \Gamma_{\text{heat flux (conduction)}} \\ h_c (T_s - T_\infty) & \Gamma \in \Gamma_{\text{heat flux (convection)}} \\ \varepsilon \sigma (T_s^4 - T_\infty^4) & \Gamma \in \Gamma_{\text{heat flux (radiation)}} \\ 0 & \Gamma \in \Gamma_{r\text{-}z \text{ symmetry}} \end{cases} . \quad (4.40)$$

Section 4.2.5 describes more specific versions of the wall heat flux condition that also apply to the fluid energy equation.

#### 4.2.5 Heat Flux Boundary Conditions

Several more specific heat flux BCs are available that apply to both the fluid and solid energy BCs. First, consider the case where a constant heat flux is applied to the boundary of a two-phase region. The most common approach for applying this type of BC is to only specify that the total heat flux enters both phases, with an additional condition imposed as Local Thermal Equilibrium (LTE),

$$\bar{q} = -\kappa_f \frac{\partial T_f}{\partial x} - \kappa_s \frac{\partial T_s}{\partial x} , \quad (4.41a)$$

$$T_f = T_s , \quad (4.41b)$$

where  $\bar{q}$  is the known heat flux [43, 75]. However, Eq. (4.41b) is unlikely to hold for reactor applications due to the presence of heat sources in the solid phase. Therefore, the approach used in Pronghorn is to split the heat source between the phases according to either the porosity, the thermal conductivity, or the effective thermal conductivity [76],

$$\bar{q}_f = \varepsilon \bar{q}, \quad (4.42a)$$

$$\bar{q}_f = \frac{k_f}{k_f + k_s} \bar{q}, \quad (4.42b)$$

$$\bar{q}_f = \frac{\kappa_f}{\kappa_f + \kappa_s} \bar{q}. \quad (4.42c)$$

The heat flux into the solid phase is then determined as  $\bar{q} - \bar{q}_f$ . The  $\varepsilon$ ,  $k$ , and  $\kappa$  parameters may be computed using local values at the wall or domain-averaged quantities. The best BCs for reactor applications may require trial-and-error investigations, since most investigations have not considered porous media with heat sources in the solid phase or  $\kappa_s$  correlations more complex than  $\kappa_s = (1 - \varepsilon)k_s$  [43, 75–77].

To simplify geometry generation and reduce problem sizes, Pronghorn also includes a thermal resistance BC that approximates the heat flux at a boundary due to a series conduction resistance and a parallel radiation and convection resistance,

$$q'' = \frac{T - T_\infty}{r_{th}}, \quad (4.43)$$

where  $T$  is the value of the temperature on the boundary and  $r_{th}$  is the thermal resistance. The thermal resistance is computed as the series resistance of an arbitrary number of conducting layers in Cartesian slabs of equal cross-sectional area or cylindrical annuli, followed by the parallel resistance of convection and radiation heat transfer to the ambient. This BC eliminates the need to model a series of conduction layers; to obtain parallel resistance and convection heat transfer, without conduction layers, use the convection and radiation BCs instead.

To obtain the correct radiation thermal resistance, an iterative procedure is utilized to compute the temperature on the surface of the conducting layers; only after this surface temperature has been determined is the BC applied. This BC applies a flux at each quadrature point only using information from that quadrature point; in other words, this BC is essentially equivalent to  $n_{qp}$  independent heat transfer paths consisting of series conduction plus parallel radiation and convection. No heat transfer between adjacent quadrature points is considered. For very large conduction layers and boundaries with large tangential thermal gradients, this may give a large underestimation of the heat flux. This BC should not be used for time-dependent simulations, as no heat capacity effects are included, or for cases where there are heat sources in the conducting layers.

## 5 Bed Geometry

This section describes closures for porosity, hydraulic diameter, and coordination number. Important physical phenomena are also described to provide context. All models described in this section apply to beds of uniform diameter spheres; custom implementations by the user are required to accommodate other geometries such as non-spherical pebbles [69, 78, 79] or mixed-diameter sphere beds [80]. A number of other assumptions include —

- Smooth walls without dimpling;
- No intermittent wall crystallization, which can result in relatively low porosities [81];
- Relatively large pebbles; for  $d_p < 100 \mu\text{m}$ , Van der Waals forces become significant [82];
- No in-bed alignment structures such as control rods or guiding plates, which may affect bed structure relatively far from the disruption due to the insignificant diffusion of pebbles from the mean flow streamlines [83];
- Cylindrical walls (when a radial dependence is specified);
- No asymmetric axial configurations, such as converging/diverging conical sections [83];
- Negligible pebble roughness [84]; and
- Flow and/or time dependence [62, 70, 85].

Pebbles move continuously through the core of PBRs in online refueling operation. Depending on the design, pebbles pass between 2 and 10 times through the bed over a period of several years. The velocity of such motions is orders of magnitude smaller than the fluid velocity. Liquid salt-cooled PBRs typically employ fluidized beds, but the kinetic energy of the pebbles is also small [86]. The negligibly small pebble motions during normal operation support the assumption of a time-independent porosity.

All stochastic effects of the bed geometry are assumed represented by the closures in this section. On-the-fly statistical sampling of closures such as coordinate number is not performed. DEM simulations for non-cylindrical geometries or unconventional designs can be performed to reduce the limitations listed above [13, 40, 54, 62, 87]. The remainder of this section describes the available porosity, hydraulic diameter, and coordination number models.

### 5.1 Porosity

The porosity is a function of both height and distance from a wall. This section will discuss these dependencies separately; to employ both dependencies, the correlations would simply need to be multiplied together and scaled appropriately. A brief literature review by Giese et. al and the references cited within provides many examples of better agreement between numerical predictions and experimental data when using a more physically-realistic porosity profile, so care should be taken in selecting the porosity profile [78].

Correlations for  $\epsilon$  have been determined experimentally and numerically in many ways. It is common to use a DEM code to numerically generate a packed bed [54, 83, 88, 89], though it is recognized that porosity and mean coordination number are both sensitive to DEM simulation parameters that may be unknown or poorly-characterized for many systems [84]. Experimentalists may fill a cylinder with spheres, pour in a wax or resin that is allowed to solidify, and then chop the cylinder into pieces for weighing after melting of the wax or resin [79, 80, 90]. Some researchers have also used image analysis, photography [91], radiography [92], and other techniques such as quickly rotating a bed filled with a known amount of liquid and measuring the thickness of the annulus formed by centripetal forces at the edge of the bed [78]. However, there still exists variation amongst correlations given by researchers due to how the bed is initially filled with pebbles. A pebble bed can generally be filled in four different ways, which show progressive decreases in the infinite bed porosity  $\epsilon_\infty$  [93] —

1. Drain fluid from the bed:  $\epsilon_\infty \approx 0.44$ ;
2. Drop spheres individually into the bed and allow them to roll into place:  $\epsilon_\infty \approx 0.395 - 0.4$ ;
3. Pour spheres into the bed:  $\epsilon_\infty \approx 0.375 - 0.391$ ; and
4. Shake down the packed bed by vibration:  $\epsilon_\infty \approx 0.359 - 0.375$ .

Gentler filling methods lead to higher porosities because less pebble motion is induced while filling the bed [88]. For beds of equal-sized spheres, the limits on  $\epsilon$  are 0.2595 for rhombohedral packing and 0.4764 for Simple Cubic (SC) packing.

Most porosity correlations require the specification of the infinite-bed porosity, or the porosity in the center region of the bed if the bed were of very large extent. For medium- and small-sized beds, educated guesses can be made as to this value by using correlations developed from experimental measurements of bed average porosities, though consideration of the bed filling method is also required. Zou et. al correlated experimental data for loose and dense packings of spheres in cylindrical beds of  $d_{\text{bed}}/d_p \geq 3.95$ , giving [94]

$$\epsilon_\infty = \begin{cases} 0.372 + 0.002 \exp\left(15.306 \frac{d_p}{d_{\text{bed}}} - 1\right) & \text{dense packing} \\ 0.400 + 0.010 \exp\left(10.686 \frac{d_p}{d_{\text{bed}}} - 1\right) & \text{loose packing} \end{cases} \quad (5.1)$$

In the limit of  $d_p/d_{\text{bed}} \rightarrow 0$ , Eq. (5.1) agrees well with the limits found by Scott [95]. Mueller provides a different correlation for  $\epsilon_\infty$  using several sources of experimental measurements [92],

$$\epsilon_\infty = 0.365 + 0.22 \frac{d_p}{d_{\text{bed}}} \quad (5.2)$$

Any of Eqs. (5.1), (5.2), or experimental information regarding bed filling method may be used to estimate  $\epsilon_\infty$ .

The radial porosity profile is a damped, oscillatory function of the distance from the wall, reaching a nearly constant porosity within four to five pebble diameters from the wall [78–80, 88–90, 92, 93, 96]. Beyond five pebble diameters from the wall, the deviation from an infinite medium porosity is less than 5% [96]. The porosity is unity at the wall, and reaches a global minimum at about  $d_p/2$  distance from the wall due to sphere alignment [78, 79, 96]. The structure near the wall is similar to a hexagonal-cubic lattice [79] and a Hexagonal Close Packing (HCP) lattice [89]. A parabolic profile is most commonly used to describe the near-wall oscillatory porosity profile [97].

The governing porous media equations generally become stiff and difficult to converge in the near-wall regions where  $\epsilon = 1$  [42] or in very low flow regions where  $\epsilon = 0$  [98]. For this reason, it may help convergence to assume a simpler porosity profile or a non-unity wall porosity to avoid numerical stiffness [88]. Using a non-unity wall porosity can be physically motivated by the apparent decrease in porosity “seen” by the fluid at the walls caused by fluid stagnation points [78, 99, 100] or practically motivated by inherent limitations in closure laws [78]. Most models in Pronghorn have the capability to adjust the wall porosity.

The radial increase in porosity near the walls impacts the friction factors discussed in Section 6, the heat transfer coefficients discussed in Section 8, and the effective thermal conductivities discussed in Sections 9 and 10. The higher porosity results in lower drag coefficients and an axial flow-channeling effect [32, 62, 78, 101], which manifests as higher tritium purging rates in solid tritium breeder blankets in fusion systems [13]. The channeling region extends approximately six pebble diameters into the bed [96]; a large peak occurs within a half pebble diameter of the wall [96, 102]. The larger the pebble diameter, the wider and shallower the velocity peak [32, 42].

Experiments built with half and quarter spheres near boundaries to obtain uniform porosity still observe some flow channeling near walls; this likely occurs due to flow alignment and less mixing of opposing streamlines behind

pebbles [6]. Therefore, the bypass effect is not entirely related to the magnitude of porosity, though porosities near unity are representative of the near-wall regions. Early researchers attempted to reconcile these different effects by using constant porosity models augmented by wall friction factors, to little success [96].

Fig. 6 shows an example of a channeled velocity profile near the wall in a pebble bed for two different Reynolds numbers. The ratio of the peak superficial velocity to the bed-center superficial velocity is in the range of 1.5-10 for most flows [13,101,102]. Because high Reynolds number flow is characterized by better momentum transfer, the width of the velocity peak is larger for high Reynolds number flows; therefore, the impact of assuming a constant porosity is more significant at low Reynolds number [42,97]. The ratio of superficial velocities decreases with Reynolds number, and is in the range of 1.5-4 for  $10 < Re < 1000$  [78,96], asymptotically approaching a constant ratio for large Reynolds numbers [42]. However, some experimental measurements suggest that such general conclusions regarding the effect of Reynolds number and proximity to the wall are highly dependent on the pebble-wall geometry [101]. While less significant, small peaks in temperature have been observed corresponding with peaks in porosity in catalytic bed reactors [103].

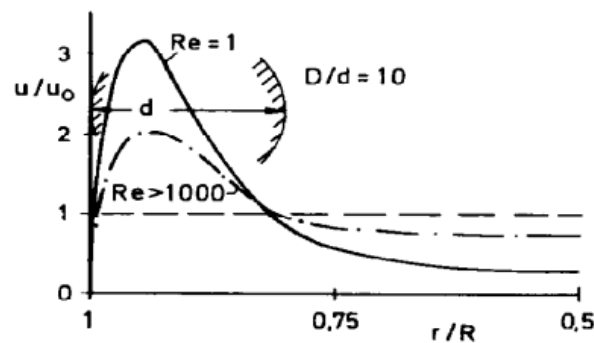


Figure 6: Velocity flow channeling effect at the wall of a pebble bed for two different Reynolds numbers [104]. The figure shows the velocity normalized by the bed-averaged superficial velocity.

The bypass flow-channeling effect results in less effective cooling of the fuel, higher overall temperatures in the bed [31, 40], and a more nonuniform outlet temperature [105]. The bypass flow does produce greater convective cooling of the bounding wall, however, which can help extend component lifetimes.

The porosity profile also impacts the pressure drop; if the high-porosity region constitutes a relatively small portion of the bed, the overall pressure drop may differ by only about 2.5% from the pressure drop obtained assuming a uniform porosity. However, for small diameter beds, the reduction in pressure drop may be significant [40]. The majority of packed beds for nuclear applications are designed with fairly high  $d_{bed}/d_p$  ratios such that such wall effects are minimized; a general criterion  $d_{bed}/d_p > 30$  has been suggested for the use of constant porosity profiles or other distributions that don't explicitly account for the wall effect [96].

If free-slip BCs are imposed on the walls, the vertical velocity field will almost exactly “follow” the porosity profile due to the strong effect on drag [40,42]. If no-slip BCs are applied, the velocity profile is similar to the slip condition, but with peaks shifted slightly further from the wall [13, 78, 103].

While some experimentalists have not observed any significant axial variation in porosity [79] or have only treated axial dependence in a bulk sense [94,95], many DEM simulations, sometimes confirmed by experiments, have shown that the axial porosity profile is a damped oscillatory function of the distance from the bounding wall, while smoothly approaching unity at the free end of the bed [54, 62, 88, 89, 106]. The damping is very similar to the radial damping described previously, with wall effects disappearing within about five pebble diameters of the bounding wall [89]. The axial porosity profile is also impacted by the weight of the pebbles [88], bed filling method [107], and flow profile [1]. All porosity profiles available in Pronghorn can be used to describe either an axial or a radial dependence.

In addition to T/H effects, the radial porosity profile has an important impact on the neutronics of a pebble bed system via its impact on neutron streaming and leakage. Though mostly outside the scope of this document, a brief dis-

cussion may be useful for those directly using the porosity correlations in Pronghorn for coupling to neutron transport physics. A neutronics model may either 1) homogenize the entire bed and use a uniform porosity; 2) use a piecewise constant porosity according to different spatial zones; or 3) explicitly model all pebbles. Due to wall structuring effects, using a piecewise model results in less leakage relative to a uniform model because fuel is located closer to the bed center [108]. However, explicit pebble resolution best captures the net increase in leakage near boundaries, which can affect the multiplication factor by hundreds of pcm relative to a piecewise model [108]. Likewise, accurate prediction of reaction rates requires the use of a spatially-varying porosity [109]. Therefore, a spatially-dependent porosity is preferred for multiphysics coupling to neutron transport.

All correlations in Pronghorn are adapted from the original sources such that the closure can be applied to both annular and cylindrical beds. Correlations developed for cylindrical beds are adjusted such that the distance from the outer wall is replaced by

$$d \equiv \min(R_o - r, r - R_i) . \quad (5.3)$$

For sufficiently large  $R_i$  and  $R_o$ , the radial porosity profile is independent of whether a cylindrical wall is concave or convex such that this approximation is valid [88,90]. Section 5.1.1 describes the available 1-D porosity profiles, which may be customized by setting  $\epsilon_\infty$  and  $\epsilon_{\text{wall}}$  and applied to the radial and/or axial directions. Section 5.1.2 then describes several ad hoc methods for combining multiple 1-D profiles together to approximate the effects of interacting walls in regions such as corners.

### 5.1.1 One-Dimensional Distributions

This section describes the 1-D porosity profiles available in Pronghorn. More generally, any of the `Function` capabilities of MOOSE may be used to create customized profiles.

#### 5.1.1.1 Cohen and Metzner Model

Cohen and Metzner correlated cylindrical bed experimental data for  $7 \leq d_{\text{bed}}/d_p \leq 60$  as [96]

$$\epsilon = \begin{cases} (\epsilon_\infty - \epsilon_{\text{wall}}) 4.5 \left[ \frac{d}{d_p} - \frac{7}{9} \left( \frac{d}{d_p} \right)^2 \right] + \epsilon_{\text{wall}} & \frac{d}{d_p} \leq 0.25 \\ (\epsilon_{\text{wall}} - \epsilon_\infty) 0.3463 e^{\left( -0.4273 \frac{d}{d_p} \right)} \cos \pi \left( 2.4509 \frac{d}{d_p} - 2.2011 \right) + \epsilon_\infty & 0.25 < \frac{d}{d_p} < 8 \\ \epsilon_\infty & 8 < \frac{d}{d_p} \end{cases} . \quad (5.4a)$$

#### 5.1.1.2 Exponential Model

An exponential porosity variation can be interpreted as the porosity profile that would be obtained experimentally if the averaging regions were taken to be larger than about a pebble diameter [88]. An exponential variation has been calculated by several researchers as [42, 88, 110]

$$\epsilon = \epsilon_\infty + (\epsilon_{\text{wall}} - \epsilon_\infty) e^{-N d/d_p} . \quad (5.5)$$

du Toit recommends  $N = 6$ , while others have selected  $N = 2$  or have defined  $N$  based on iterative procedures [88].

### 5.1.1.3 Klerk Model

Klerk correlates an oscillatory porosity distribution as [93]

$$\varepsilon = \begin{cases} 2.14 \left( \frac{d}{d_p} \right)^2 - 2.53 \frac{d}{d_p} + 1 & \frac{d}{d_p} \leq 0.637 \\ \varepsilon_\infty + 0.29e^{-0.6 \frac{d}{d_p}} \cos \left[ 2.3\pi \left( \frac{d}{d_p} - 0.16 \right) \right] + 0.15e^{-0.9 \frac{d}{d_p}} & \frac{d}{d_p} > 0.637 \end{cases} \quad (5.6a)$$

The period of the oscillation is constant because it has not been successfully correlated with the bed to pebble diameter ratio [93]. It is not immediately clear how to manipulate Eq. (5.6a) to obtain an arbitrary wall porosity, so this capability is not present with this model. Eq. (5.6a) is recommended for use by Antwerpen et. al [111].

### 5.1.1.4 Linear Model

The porosity may be expressed as a linear function in terms of the percentage reduction  $\tilde{\chi}$  in the porosity relative to the infinite-medium porosity in the center of the bed,

$$\varepsilon = \frac{2\tilde{\chi}\varepsilon_\infty}{\tilde{H}}(z - z_0) + (1 - \tilde{\chi})\varepsilon_\infty, \quad (5.7)$$

where  $\tilde{H}$  is the radial/axial span of the bed,  $z$  is the radial/axial coordinate, and  $z_0$  is the minimum coordinate of the bed (the bottom of the bed or the inner radius, depending on the profile type). A linear porosity distribution can be used to capture the effects of pebble weight on increasing the porosity at the bottom of the bed.

### 5.1.1.5 Martin Model

Martin correlated cylindrical bed data as an oscillatory function [90,97],

$$\varepsilon = \begin{cases} \varepsilon_{\min} + (\varepsilon_{\text{wall}} - \varepsilon_{\min}) \left( \frac{2d}{d_p} - 1 \right)^2 & \frac{2d}{d_p} - 1 \leq 0 \\ \varepsilon_\infty + (\varepsilon_{\min} - \varepsilon_\infty) \exp \left[ -\frac{1}{4} \left( \frac{2d}{d_p} - 1 \right) \right] \cos \left[ \frac{\pi}{C} \left( \frac{2d}{d_p} - 1 \right) \right] & \frac{2d}{d_p} - 1 > 0 \end{cases} \quad (5.8a)$$

where  $C$  is defined as

$$C \equiv \begin{cases} \sqrt{2/3} & \frac{d_{\text{bed}}}{d_p} = \infty \\ 0.876 & \frac{d_{\text{bed}}}{d_p} = 20.3 \end{cases} \quad (5.9)$$

The minimum porosity for beds of spherical pebbles is often in the range of 0.2 to 0.26 and occurs at approximately  $d_p/2$  [78, 90, 97], though the minimum porosity does decrease slightly with  $d_{\text{bed}}/d_p$  and shifts further from the wall for smaller  $d_{\text{bed}}/d_p$  [90, 97]. This shift can be neglected for  $d_{\text{bed}}/d_p \geq 10$  [96, 97]. Based on recommendations by du Toit,  $\epsilon_{\text{min}}$  is taken as 0.23 and  $C$  as 0.876 for all beds [88].

### 5.1.1.6 Piecewise Model

The porosity may be given as a piecewise constant distribution,

$$\epsilon = \begin{cases} \epsilon_1 & r < r_i \\ \epsilon_2 & r > r_i \end{cases} \quad (5.10)$$

where only two intervals in the radial direction are shown for notational simplicity, but an arbitrary number can be used. The piecewise constant values may be determined as averages throughout an oscillatory porosity profile, for example [97].

### 5.1.1.7 White and Tien Model

White and Tien correlated porosity as [102]

$$\epsilon = \frac{\epsilon_{\text{wall}}}{1 + \frac{\epsilon_{\text{wall}} - \epsilon_{\infty}}{\epsilon_{\infty}} \sqrt{1 - e^{-2d/d_p}}} \quad (5.11)$$

## 5.1.2 Multidimensional Distributions

This section describes methods available for combining the 1-D functions in Section 5.1.1 to approximate the multidimensional effect of interacting walls in regions such as corners. While the 1-D functions in Section 5.1.1 derive from MOOSE's `Function` class, a multidimensional distribution is achieved with classes deriving from MOOSE's `AuxKernel` class.

### 5.1.2.1 Marginal Probability Density Functions

Correlations for porosity are most frequently given in the literature in terms of a radial function, where averaging has been performed over physical experiments or DEM simulations in the axial and azimuthal directions. Sometimes, axial porosity profiles are shown graphically, but these have not yet been correlated. These axial porosity profiles, when normalized by their integral over their entire domain, represent marginal Probability Density Functions (PDFs) of porosity, indicated with tilde overbars,

$$\tilde{\epsilon}(z) \equiv \frac{\int_{R_i}^{R_o} \epsilon(r, z) dr}{R_i - R_o}, \quad (5.12)$$

$$\tilde{\epsilon}(r) \equiv \frac{\int_{Z_i}^{Z_o} \epsilon(r, z) dz}{Z_o - Z_i}, \quad (5.13)$$

where  $R_i$  and  $R_o$  are the inner and outer radii of the bed and  $Z_i$  and  $Z_o$  are the lower and upper axial coordinates of the bed. Eqs. (5.13) and (5.12) represent marginal PDFs because their integral over their domain equals unity and

the value at any point is always within the range  $[0, 1]$  because porosity itself is confined to the same range. Two marginal PDFs can be combined into a single joint PDF provided the marginal PDFs are independent by multiplying the two marginal PDFs. It is assumed that wall effects are small such that multiplying the two marginal PDFs gives, to first-order, the joint PDF. To evaluate the joint porosity at a given location  $(r_i, z_i)$  requires integrating the joint PDF over a small window about  $(r_i, z_i)$ , giving the fraction of the total fluid that resides in the integration window,

$$\text{fraction of total fluid in } (r_i - \Delta r \leq r \leq r_i + \Delta r, z_i - \Delta z \leq z \leq z_i + \Delta z) = \int_{z_i - \Delta z}^{z_i + \Delta z} \int_{r_i - \Delta r}^{r_i + \Delta r} \bar{\epsilon}(r) \bar{\epsilon}(z) dr dz . \quad (5.14)$$

To obtain the porosity at this location, an assumption regarding the average porosity  $\bar{\epsilon}$  over the  $r - z$  plane must be made to multiply the percentage of the total fluid in the region of interest by the total amount of fluid, dividing by the integration volume, to obtain the porosity

$$\epsilon(r_i, z_i) = \underbrace{\int_{z_i - \Delta z}^{z_i + \Delta z} \int_{r_i - \Delta r}^{r_i + \Delta r} \bar{\epsilon}(r) \bar{\epsilon}(z) dr dz}_{\text{fraction of total fluid at } (r_i, z_i)} \underbrace{\bar{\epsilon} \int_{Z_i}^{Z_o} \int_{R_i}^{R_o} dr dz}_{\text{total fluid in domain}} \underbrace{\frac{1}{\int_{z_i - \Delta z}^{z_i + \Delta z} \int_{r_i - \Delta r}^{r_i + \Delta r} dr dz}}_{\text{normalized by local area}} . \quad (5.15)$$

The average porosity  $\bar{\epsilon}$  over the  $r - z$  plane is not usually known, however. Typically, the average porosity over the bed volume is known, and hence iteration must be performed on the imposed average area porosity until the desired average volume porosity is obtained. Currently, this iteration must be performed by hand.

Certain axial and radial porosity profiles will not behave well with this joint construction. For example, if both the axial and radial profiles have a porosity at the wall of unity, then Eq. (5.15) requires that the porosity at the very top of the bed have a radial average of unity. To obtain a radial average of unity with an exponential distribution requires that the entire radial profile shift upwards giving a porosity that exceeds unity, which is non-physical. Therefore, this approach works best when the axial distribution has a much less significant variation than the radial distribution, such as when the axial profile is a linear function representing only the effect of pebble weight, a gradual effect.

### 5.1.2.2 Function Infinite Porosity

As an alternative to the marginal PDF approach described in Section 5.1.2.1, a multidimensional porosity distribution can be obtained by using a variable infinite-medium porosity  $\epsilon_\infty$  that is obtained from an evaluation of an axial porosity distribution. That is, the infinite-medium porosity is no longer constant, but is given by a different porosity distribution. This concept is similar to the inverse porosity weighting method used by Visser, but provides smoother transitions between radial and axial profiles in corners [112].

For example, consider a 2-D  $r-z$  distribution formed as a combination of a 1-D  $r$  profile with a 1-D  $z$  profile. The radial distribution  $\epsilon(r)$  is in general a function of  $\epsilon_\infty$ ,  $\epsilon_{\text{wall}}$ ,  $d_p$ , and the minimum distance  $d_r$  to a radial wall. This dependence may be expressed as

$$\epsilon(r) = f(d_p, d_r, \epsilon_{\text{wall}}, \epsilon_\infty) , \quad (5.16)$$

where  $f$  indicates a radial functional dependence. A 2-D distribution is obtained by replacing the constant  $\epsilon_\infty$  in Eq. (5.16) with a 1-D axial profile, which is itself a function of  $\epsilon_\infty$ ,  $\epsilon_{\text{wall}}$ ,  $d_p$ , and the minimum distance  $d_z$  to an axial wall,

$$\begin{aligned} \epsilon(r, z) &= f(d_p, d_r, \epsilon_{\text{wall}}, \epsilon_\infty(z)) \\ &= f(d_p, d_r, \epsilon_{\text{wall}}, g(d_p, d_z, \epsilon_{\text{wall}}, \epsilon_\infty)) , \end{aligned} \quad (5.17)$$

where  $g$  indicates an axial functional dependence. In other words, the infinite-medium porosity used in the radial dependence is computed based on the assumed axial dependence.

This auxiliary kernel cannot be used with porosity distributions that are not everywhere dependent on the infinite-medium porosity. Likewise, the radial distribution will ignore any functional dependence on the infinite-medium porosity if the radial distribution is independent of such a value, such as for piecewise or constant distributions.

## 5.2 Hydraulic Diameter

The hydraulic diameter is a characteristic length scale defined as

$$D = \frac{4V_f}{a_w \ell}, \quad (5.18)$$

where  $V_f$  is the fluid flow volume,  $a_w$  is the wetted surface area per unit length defined in Eq. (2.77), and  $\ell$  is the length of the volume. Many different definitions of hydraulic diameter have been used in porous media applications. In the absence of wall effects, combining Eqs. (5.18), (2.78), and the representation of the fluid flow volume as  $V_f = \varepsilon V$ , the hydraulic diameter in the bulk of a bed of spherical pebbles is

$$D = \frac{4\varepsilon}{6(1-\varepsilon)} d_p, \quad (5.19)$$

though the factor of  $4/6$  is often neglected. Near the wall as the porosity tends towards unity, Eq. (5.19) tends to infinity. While modifications to Eq. (5.19) have been proposed, none are currently implemented [96, 113].

## 5.3 Coordination Number

The coordination number  $N_c$ , or the number of pebbles contacting a pebble, is another important geometric parameter that affects solid-to-solid contact conduction in  $\kappa_s$ . The coordination number is usually correlated only as a function of porosity such that dependence on packing structure is implicit, which neglects the fact that many different packing structures can result in the same coordination number despite very different porosities [114]. Some coordination number models also do not coincide well with the known coordination numbers for regular lattices, though this is of contested importance due to the engineering emphasis on random beds [107]. There is significant variation in correlations for coordination number, primarily due to whether the model is based on experimental/numerical data or interpolations of coordination numbers for regular packings [29, 85, 111]. These variations may also be caused by the distance over which the pebbles are defined as touching for numerically-generated beds [82], the dropping height and friction factor parameters [84], and whether the wall region was excluded from the measurement [84, 89, 107]. While most models are developed based on numerical simulations, some experiments based on chemical reactions induced at contact points have also been performed [107].

To be stable, a pebble needs at least three contacts. At the wall, one of these contacts can be provided by the wall, so the minimum coordination number is 3 far from the walls and 2 at the walls. The maximum theoretical coordination number is 12, corresponding to an HCP lattice. DEM simulations and experiments suggest a mean coordination number of approximately 6 to 8 in the centers of beds, with a nearly Gaussian PDF with upper and lower bounds approximately  $\pm 4$  from the mean [82, 84, 89, 91, 107]. The average coordination number is lower in the near-wall region. However, due to the HCP structure at bounding walls, the largest coordination numbers can occur in these high porosity regions [89].

Fig. 7 summarizes the available models for coordination number. The original validity ranges are plotted with solid lines, and extensions to cover  $0.23 \leq \varepsilon \leq 1.0$  are shown with dashed lines. Each dot represents an experimental data point and the coordination numbers of SC, Body Centered Cubic (BCC), and Face Centered Cubic (FCC) lattices.

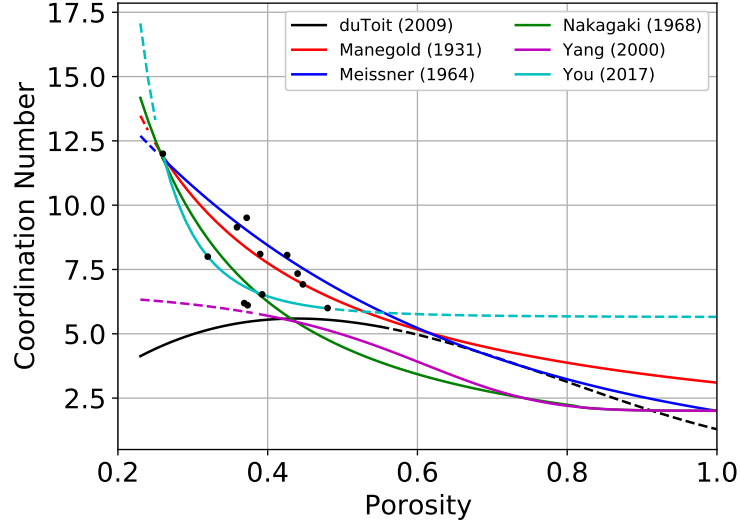


Figure 7: Coordination number correlations as a function of porosity. Solid lines correspond to the original validity ranges, while dashed lines provide extensions over  $0.23 \leq \epsilon \leq 1.0$ . Black dots represent the coordination numbers of SC, BCC, and FCC lattices and experimental or numerical data [91, 107, 115].

du Toit estimates the average coordination number for  $0.2398 \leq \epsilon \leq 0.54$  as [111]

$$N_c = 25.952\epsilon^3 - 62.364\epsilon^2 + 39.724\epsilon - 2.0233 . \quad (5.20)$$

Meissner et. al estimate the average coordination number for  $0.2595 \leq \epsilon \leq 1$  as [114]

$$N_c = 2e^{2.4(1-\epsilon)} . \quad (5.21)$$

Nakagaki and Sunada estimate the average coordination number over an unspecified range in  $\epsilon$  as [111, 116]

$$N_c = \begin{cases} 1.61\epsilon^{-1.48} & \epsilon \leq 0.82 \\ 4.28 \times 10^{-3}\epsilon^{-17.3} + 2 & \epsilon > 0.82 . \end{cases} \quad (5.22)$$

Yang et. al estimate the average coordination number for  $0.39 \leq \epsilon \leq 1$  as [82]

$$N_c = 2.02 \frac{1 + 87.38(1-\epsilon)^4}{1 + 25.81(1-\epsilon)^4} . \quad (5.23)$$

Eqs. (5.20)-(5.23) are coordination number correlations based on fitting experimental and numerical data.

Manegold et. al estimate the average coordination number for  $0.25 \leq \epsilon \leq 1.0$  as [114]

$$N_c = 3.1\epsilon^{-1} . \quad (5.24)$$

You et. al estimate  $N_c$  for  $0.26 \leq \epsilon \leq 0.476$  as [111, 115]

$$N_c = (1.008E - 2)\epsilon^{-4.785} + 5.6480 , \quad (5.25)$$

Eqs. (5.24)-(5.25) are developed assuming that the coordination number can be expressed as a linear combination of coordination numbers associated with regular lattices. The default correlation used in Pronghorn is Eq. (5.21).

## 6 Friction Factors

This section describes closures for the interphase friction factor  $W$ , which is generally correlated in terms of the solid surface roughness, Reynolds number, and geometry. The interpretation of  $W$  differs slightly from conventional definitions of friction factors, though it is referred to as a friction factor here. After describing the friction factor for porous media, the relationship between  $W$  and the friction factor is provided.

If a non-dimensional pressure is defined as  $P^+ = P/(\mu V_o/D)$ , the scaling analysis performed in Section 2.9 shows that at low flowrates, the pressure drop is linearly proportional to velocity,

$$\nabla P \propto \frac{\mu V}{D^2}, \quad (6.1)$$

a viscous effect. The phenomenon represented by Eq. (6.1) is often referred to as “friction drag” or “skin friction.” If the non-dimensional pressure is instead defined as in Eq. (2.127), the scaling analysis performed in Section 2.9 shows that at high flowrates the pressure drop is quadratically proportional to velocity,

$$\nabla P \propto \frac{\rho V^2}{D}, \quad (6.2)$$

an inertial effect. The phenomenon represented by Eq. (6.2) is often referred to as “form drag” or “pressure drag.” The total pressure drop is approximated as the sum of the viscous and kinetic losses,

$$-\nabla P = A \frac{\mu V}{D^2} + B \frac{\rho V^2}{D}, \quad (6.3)$$

where  $A$  and  $B$  are constants of proportionality [117]. A friction factor represents a pressure drop normalized by either the dynamic pressure  $\rho V^2$  or the viscous shear stress  $\mu V/D$ ,

$$-\nabla P \frac{D}{\rho V^2} = A \frac{1}{Re_h} + B, \quad (6.4a)$$

$$-\nabla P \frac{D^2}{\mu V} = \hat{A} + \hat{B} Re_h, \quad (6.4b)$$

where  $\hat{A}$  and  $\hat{B}$  are constants of proportionality. The LHS of each of Eqs. (6.4a) and (6.4b) is a friction factor, each based on different normalizations.

Most friction factor models for porous media are based on the forms in Eq. (6.4), but with different representative length and velocity scales [118]. Replacing  $V$  by  $v/\varepsilon$  according to Eq. (19.29), and  $D$  by Eq. (5.19) without the factor of  $4/6$ , the viscous proportionality in Eq. (6.1) becomes

$$\nabla P \propto \frac{(1-\varepsilon)^2}{\varepsilon^3} \frac{\mu}{d_p^2} v, \quad (6.5)$$

and the inertial proportionality in Eq. (6.2) becomes

$$\nabla P \propto \frac{(1-\varepsilon)}{\varepsilon^3} \frac{\rho_f}{d_p} v^2. \quad (6.6)$$

The friction drag scales as the inverse of the pebble area, while the form drag scales as the inverse of the length of the wake region behind a pebble. Representing the total pressure drop as a combination of Eqs. (6.5) and (6.6) and normalizing by the dynamic pressure  $\rho v^2$  or viscous shear stress  $\mu v/d_p$  gives

$$-\nabla P \frac{\varepsilon^3}{1-\varepsilon} \frac{d_p}{\rho v^2} = A \frac{1-\varepsilon}{Re} + B, \quad (6.7a)$$

$$-\nabla P \frac{\varepsilon^3}{(1-\varepsilon)^2} \frac{d_p^2}{\mu v} = A + B \frac{Re}{1-\varepsilon}. \quad (6.7b)$$

The form in Eq. (6.7a) shows that the friction factor becomes independent of Reynolds number above approximately  $10^3$  to  $10^6$ , while the friction factor scales as  $(1-\varepsilon)/Re$  at low Reynolds numbers [118–120].

The earliest models of porous media considered by Darcy and his contemporaries were based on experiments at very low Reynolds numbers where inertial effects were negligible. Had Darcy's water source not been tied to a hospital's supply, higher flowrates might have enabled him to observe the transition from linear to nonlinear behavior at higher Reynolds numbers [121]. All models available in Pronghorn consider both the linear and inertial drag effects. Note that the kinetic drag is not synonymous with turbulent flow effects — inertial effects such as streamline bending around pebbles and expansion/contraction between pore spaces, which is classically proportional to  $\rho v^2$ , are also present in laminar flows [122, 123].

The spatial homogenization of the momentum conservation equation relates the pressure drop in a porous media to  $W$  as

$$\varepsilon \nabla P = -W \rho_f \vec{V}. \quad (6.8)$$

Rearranging the dynamic pressure scaling in Eq. (6.7a) to match the form in Eq. (6.8) provides the relationship between the friction factor as defined the LHS of Eq. (6.7a) and  $W$ ,

$$W \equiv \underbrace{-\nabla P \frac{\varepsilon^3}{1-\varepsilon} \frac{d_p}{\rho v^2}}_{\text{friction factor}} \frac{(1-\varepsilon) \|\vec{V}\|}{d_p}. \quad (6.9)$$

Therefore,  $W$  is proportional to the friction factor and can be specified in terms of the coefficients  $A$  and  $B$  in Eq. (6.7a). For isotropic media,  $W$  is a scalar. For anisotropic media,  $W$  may be specified as a diagonal tensor with coefficients  $A$  and  $B$  unique for each coordinate direction, with an additional scalar multiplier for each direction. Anisotropic drag models are essential for modeling of porous media with a preferred direction of motion, such as reflector blocks [123] or banks of tubes [124, 125]. The near-wall regions of PBRs are far from isotropic, but a lack of experimental and numerical data for these regions requires the use of isotropic models.

The coefficients  $A$  and  $B$  in any single coordinate direction are usually independent of Reynolds number [117, 118, 126], but there are many experimental and theoretical studies that suggest  $A$  and  $B$  have a dependence on flow regime [38, 121, 122, 127–129]. However, there is no general consensus on how  $A$  and  $B$  might vary with Reynolds number if such a dependence existed. Many researchers report drag reduction in the fully turbulent regime, whereby  $A$  increases and  $B$  decreases [38, 121, 127, 129, 130]. This may be caused by the fluid more efficiently following streamlines; a greater contribution of higher-resistance channels to the overall flow; and/or the inability for a separated boundary layer to grow unbounded, limiting drag.

However, a drag reduction effect at high Reynolds number is not in agreement with trends observed for internal pipe flows. Extrapolating the laminar friction factor on a Moody diagram to higher Reynolds number would predict a lower friction factor than actually observed [128]. These different conclusions regarding the turbulent regime may be reconciled based on whether the transition from laminar to turbulent flow is dominated by viscous or kinetic effects. If

the transition is dominated by kinetic effects, then  $B$  should decrease. If the transition is dominated by viscous effects, which is usually the case for transitions in internal pipe flows,  $B$  should increase [128]. Because porous media consist of many closely-packed bodies, rather than a single body for which the transition is well-known to be dominated by kinetic effects, it is difficult to characterize the transition. Most regime-dependent coefficients exhibit a decrease in  $B$  at high Reynolds number, which suggest that the transition is dominated by kinetic effects.

Other models for the turbulent regime, such as a cubic velocity dependence, have been proposed, but are not supported by theoretical arguments [121, 122, 128].

Section 6.1 provides models for  $W$  applicable to beds of uniform diameter spherical pebbles, while Section 6.2 provides models for pipe flows.

## 6.1 Pebble Bed Correlations

This section describes models for  $W$  applicable to randomly-packed beds of smooth, uniform diameter spheres. Applying these correlations to ordered beds generally results in an overestimation of the pressure drop due to the lower-resistance flow channels through the lattice [23, 29].

All closures in this section are obtained from experimental or numerical evaluations of the pressure drop over a packed bed. As such, the porosity that appears in these models represents the bed-averaged porosity, but is interpreted numerically as the local porosity. This approximation is used frequently in porous media applications [42, 78, 131, 132]. While using the local porosity in place of the bed-averaged porosity does capture the wall bypass effect, drag models correlated based on data exclusive to the near-wall region are required to fully understand the implications of this assumption.

Fig. 8 shows the friction factor as defined in Eq. (6.6) for the available models for  $\epsilon = 0.4$ , along with the experimental data of Avdeev et. al for  $\epsilon = 0.37$  [133]. The Eisfeld correlation in Section 6.1.4 is shown for  $d_p/d_{bed} = 0$ . All correlations predict a friction factor within several percent of the experimental data.

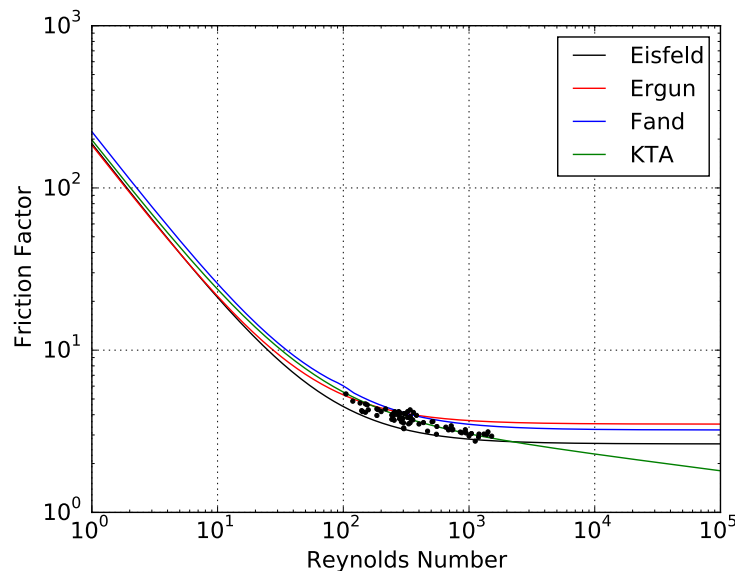


Figure 8: Friction factor correlations as a function of Reynolds number with  $\epsilon = 0.40$  with the experimental data points of Avdeev et. al for  $\epsilon = 0.37$  [133].

### 6.1.1 Ergun Model

The Ergun friction factor correlation sets  $A$  and  $B$  in Eq. (6.7a) as

$$A = 150 , \quad (6.10a)$$

$$B = 1.75 , \quad (6.10b)$$

which correlates well with large experimental data sets [38, 39, 118, 119] and is the most commonly-used model for spherical packed beds [20,31,49,62,87,100,134,135]. Macdonald et. al proposed a minor adjustment with  $A = 180$  and  $B = 1.8$  for smooth pebbles and  $A = 180$  and  $B = 4.0$  for very rough pebbles, though the difference is small [117, 136].

### 6.1.2 Fand Piecewise Linear Model

Fand et. al proposed a variation on the Ergun model that sets different values of  $A$  and  $B$  in Eq. (6.7a) depending on flow regime [127],

$$A = \begin{cases} 182 & 5 < Re < 80 \\ 225 & Re \geq 120 \end{cases} , \quad (6.11a)$$

$$B = \begin{cases} 1.92 & 5 < Re < 80 \\ 1.61 & Re \geq 120 \end{cases} . \quad (6.11b)$$

It is assumed that the range  $0 \leq Re \leq 5$  is described by the same friction factor as the  $5 \leq Re \leq 80$  range and that linear interpolation can be performed between Reynolds numbers of 80 and 120.

### 6.1.3 KTA Model

The Kerntechnischer Ausschuss (KTA) friction factor sets  $A$  and  $B$  in Eq. (6.7a) as [129]

$$A = 160 , \quad (6.12a)$$

$$B = 3 \left( \frac{Re}{1 - \epsilon} \right)^{-0.1} . \quad (6.12b)$$

Eq. (6.12) is valid for  $1 < Re_h < 10^5$ ,  $0.36 < \epsilon < 0.42$ ,  $d_{bed}/d_p$  above a limiting curve provided in the original reference, and the height of the bed being at least five times greater than the pebble diameter. The lower the Reynolds number, the greater the diameter of the bed required to use Eq. (6.12) because the greater mixing at high Reynolds number reduces the magnitude of the bypass flow. For example, for  $Re_h = 1$ , the bed must be roughly 35 pebbles wide. The fluid viscosity is evaluated at the average of the fuel surface temperature and the fluid temperature. Eq. (6.12) is commonly used for the analysis of helium-cooled PBRs [31, 40, 100, 137].

### 6.1.4 Einfeld and Schnitzlein Model

The Einfeld and Schnitzlein friction factor correlation sets  $A$  and  $B$  in Eq. (6.7a) as

$$A = 1 + \frac{2}{3 \frac{d_{\text{bed}}}{d_p} (1 - \varepsilon)}, \quad (6.13a)$$

$$B = \frac{A}{\left[1.15 \left(\frac{d_p}{d_{\text{bed}}}\right)^2 + 0.87\right]^2}, \quad (6.13b)$$

where  $A$  in Eq. (6.13b) is given by Eq. (6.13a) [119]. Eq. (6.13) correlates against a large experimental data set with  $0.01 < Re < 17365$ ,  $1.6 < d_{\text{bed}}/d_p < 250$ , and  $0.33 < \varepsilon < 0.882$ . Important to note is that Eq. (6.13) should only be used for simulations with constant porosity or for 1-D models of packed beds because  $\varepsilon$  represents the bed averaged porosity.

## 6.2 Pipe Flow Correlations

This section describes models for  $W$  applicable to pipe flow. Unlike the correlations presented in Section 6.1, these models should only be used in 1-D domains such that there is only one entry non zero that corresponds to the flow direction. Rather than present these correlations in terms of the  $A$  and  $B$  that appear in Eq. (6.7a), these models are presented for  $W$  directly for simplicity.

### 6.2.1 Churchill Model

Churchill combined several correlations for laminar, transitional, and turbulent flow to obtain a correlation valid for all  $Re$  and relative pipe surface roughness  $\varepsilon_{\text{pipe}}/D$ , giving

$$W = \frac{\varepsilon \|\vec{V}\|_2}{2D} \left[ \left(\frac{8}{Re}\right)^{12} + \frac{1}{(A_c + B_c)^{3/2}} \right]^{1/12}, \quad (6.14)$$

where the factor of  $\varepsilon \|\vec{V}\|_2 / 2D$  appears in order to use this friction factor to represent  $\varepsilon \nabla P$  [138].  $A_c$  and  $B_c$  are defined as

$$A_c = \left\{ 2.457 \ln \left[ \frac{1}{\left(\frac{7}{Re}\right)^{0.9} + 0.27 \frac{\varepsilon_{\text{pipe}}}{D}} \right] \right\}^{16}, \quad (6.15)$$

$$B_c = \left(\frac{37530}{Re}\right)^{16}. \quad (6.16)$$

## 7 Brinkman Viscosity

This section describes closures for the Brinkman viscosity  $\tilde{\mu}$ . There is substantial disagreement on appropriate models for  $\tilde{\mu}$ , which tends to only impact the flow field within about a half pebble diameter of walls [40, 78, 132]. Generally,  $\tilde{\mu}$  increases with  $Re$  due to enhanced mixing, though some solid shapes show no dependence on  $Re$  [78].

### 7.1 Multiplier Model

The simplest model for the effective viscosity is a constant multiplier on the fluid dynamic viscosity,

$$\tilde{\mu} = \epsilon \Upsilon \mu , \tag{7.1}$$

where  $\Upsilon$  is a constant. Auwerda et. al somewhat arbitrarily select  $\Upsilon = 100$  for helium-cooled HTGRs due to a lack of experimental correlations, and varying  $\Upsilon$  by two orders of magnitude showed fairly similar temperature profiles [40, 41].

## 8 Heat Transfer Coefficients

This section describes models for the interphase convective heat transfer coefficient  $\alpha$  and the convective heat transfer coefficient between the porous media and a wall  $\alpha_w$ . All correlations discussed in this section apply to randomly packed beds of smooth, uniform diameter spheres.

### 8.1 Interphase Heat Transfer Coefficients

The interphase heat transfer coefficient  $\alpha$  models heat transfer between the fluid and solid phases, and is generally a function of Reynolds number, Prandtl number, and porosity. Significant scatter exists in both experimental data and correlations for  $Re < 10$ , which may be attributable to the difficulty in measuring pebble surface temperatures in this regime that often necessitates the assumption of an underlying energy conservation equation. When these underlying models account for thermal dispersion in the fluid and/or solid phases, the Nusselt number tends to zero at low Reynolds number [120, 139]. Conversely, other models show a limiting Nusselt number in the range of 1 to 10 at low Reynolds number [140]. At high Reynolds number, thermal dispersion and other heat transfer mechanisms are secondary to convective heat transfer, and the sensitivity of experimental predictions to model selection is weaker. Other potential causes of the scatter at low Reynolds number can be attributed to 1) more significant back-mixing [141, 142]; 2) differences between packed, fluidized, and distended beds [141], though not all researchers have observed such differences [142, 143]; and 3) more sensitive measurements as the Nusselt number becomes less dependent on the Reynolds number [140].

For a single sphere in the limit of  $Re \rightarrow 0$ , the Nusselt number equals 2. Not all correlations satisfy this limit, which can be motivated by the difference between a single sphere and a packing [99]. Combined with model disagreement regarding the proper asymptotic trend at low Reynolds number, the limiting Nusselt number should likely not be the primary reason for selecting a particular interphase heat transfer coefficient correlation, especially when the low Reynolds regime is often of negligible importance to reactor applications.

In a spherical coordinate system, conduction in a constant thermal conductivity fluid surrounding a sphere is described by

$$k \frac{1}{r^2} \frac{\partial}{\partial r} \left( r^2 \frac{\partial T}{\partial r} \right) = 0. \quad (8.1)$$

Solving this equation with the BCs of  $T(R) = T_o$  and  $T(r \rightarrow \infty) = T_\infty$  gives

$$T(r) = \frac{R(T_o - T_\infty)}{r} + T_\infty. \quad (8.2)$$

Matching the heat flux at  $R$  with the convection heat flux gives

$$k \frac{R(T_o - T_\infty)}{R^2} = h(T_o - T_\infty). \quad (8.3)$$

Solving the above for  $hD/k$  gives  $Nu = 2$  for a sphere in stagnant fluid.

The interphase convective heat transfer coefficient is usually larger in the entrance region of a bed due to a thinner boundary layer, but the lack of turbulent wakes from upstream pebbles counteracts this effect, leading to some disagreement as to the correct entrance length behavior [23, 27, 120, 144]. For example,  $\alpha$  has been measured as 100% higher than the bulk value for random beds [27], 20% higher than the bulk value for BCC lattices [23], the same as the bulk value for FCC lattices, and 50% lower than the bulk value for random beds [144].

Fig. 9 shows the available models for  $\alpha$  as a function of Reynolds number for  $\epsilon = 0.40$  and  $Pr = 0.71$  along with the experimental data points of Gupta and Thodos for packed and distended BCC lattices with  $0.444 \leq \epsilon \leq 0.778$  and  $Pr = 0.71$  [145]; Littman et. al [146]; McConnachie and Thodos for packed and distended BCC lattices with

$0.416 \leq \varepsilon \leq 0.778$  and  $Pr = 0.719$  [142]; Petrovic and Thodos for  $0.394 \leq \varepsilon \leq 0.475$  and  $Pr = 0.60$  [139]; and Wilkins and Thodos for  $0.421 \leq \varepsilon \leq 0.640$  for  $Pr = 3.72$  [143]. Despite the relatively large range in Prandtl number and porosity shown in the experimental data shown in Fig. 9, all correlations agree for moderate to large Reynolds numbers. The low Reynolds number data of Littman et. al and Petrovic and Thodos include thermal dispersion corrections, therefore showing a decrease in the Nusselt number to zero as the Reynolds number tends to zero [139, 146].

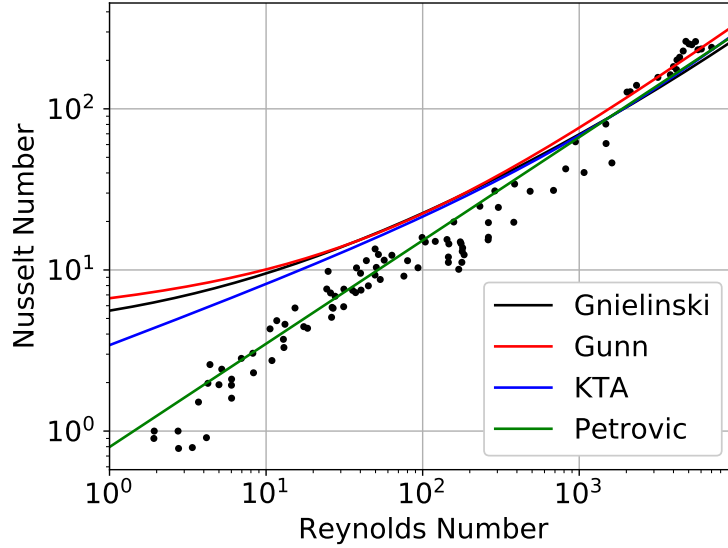


Figure 9: Nusselt number correlations as a function of Reynolds number with  $\varepsilon = 0.40$  and  $Pr = 0.71$  with the experimental data points of Gupta and Thodos for packed and distended BCC lattices with  $0.444 \leq \varepsilon \leq 0.778$  and  $Pr = 0.71$  [145]; Littman et. al [146]; McConnachie and Thodos for packed and distended BCC lattices with  $0.416 \leq \varepsilon \leq 0.778$  and  $Pr = 0.719$  [142]; Petrovic and Thodos for  $0.394 \leq \varepsilon \leq 0.475$  and  $Pr = 0.60$  [139]; and Wilkins and Thodos for  $0.421 \leq \varepsilon \leq 0.640$  for  $Pr = 3.72$  [143].

The remainder of this section presents the models available for  $\alpha$ . These closures have typically been measured for gases and water, and while application to high-Prandtl number fluids such as molten salts is a reasonable approximation, these models should be refined as more refined thermophysical property measurements become available [147].

### 8.1.1 Gnielinski Model

Gnielinski introduced modified length and velocity scales to a correlation originally developed for convective heat transfer from a flat plate to give [120]

$$Nu = [1 + 1.5(1 - \varepsilon)] \left( 2 + \sqrt{Nu_{\text{lam}}^2 + Nu_{\text{turb}}^2} \right), \quad (8.4)$$

where the laminar and turbulent Nusselt numbers,  $Nu_{\text{lam}}$  and  $Nu_{\text{turb}}$ , respectively, are defined as

$$Nu_{\text{lam}} = 0.664 Re_i^{0.5} Pr^{1/3}, \quad (8.5)$$

$$Nu_{\text{turb}} = \frac{0.037 Re_i^{0.8} Pr}{1 + 2.443 Re_i^{-0.1} (Pr^{2/3} - 1)}. \quad (8.6)$$

Eq. (8.4) is valid for  $Re_i \leq 7.7 \times 10^5$ ,  $0.7 \leq Pr \leq 10^4$ , and  $0.26 \leq \epsilon \leq 0.935$  and has been experimentally verified by Achenbach using a single heated sphere in an unheated packing [120]. Eq. (8.4) is commonly used for the analysis of helium-cooled PBRs [31, 40, 100].

### 8.1.2 Gunn Model

Gunn correlated heat and mass transfer data in gas and liquid beds subject to constraints at low and high Reynolds numbers to give [140]

$$Nu = (7 - 10\epsilon + 5\epsilon^2) \left(1 + 0.7Re^{0.2}Pr^{1/3}\right) + (1.33 - 2.4\epsilon + 1.2\epsilon^2) Re^{0.7}Pr^{1/3}. \quad (8.7)$$

Eq. (8.7) is valid for  $0.35 \leq \epsilon \leq 1.0$  and  $Re \leq 10^5$  and has been used for analysis of gas-cooled pebble bed experiments [112].

### 8.1.3 KTA Model

KTA correlated experimental data as [144]

$$Nu = 1.27 \frac{Pr^{1/3}Re^{0.36}}{\epsilon^{1.18}} + 0.033 \frac{Pr^{0.5}Re^{0.86}}{\epsilon^{1.07}}. \quad (8.8)$$

Eq. (8.8) is valid for  $100 \leq Re \leq 10^5$ ,  $0.36 < \epsilon < 0.42$ ,  $Pr = 0.7$ , and a bed height greater than four times the pebble diameter. If plane-averaged values of the porosity and a global value for  $Re$  are used, then the bed diameter must be 20 times greater than the pebble diameter. The viscosity and thermal conductivity of the gas are evaluated at the average of the fluid and solid surface temperatures, both in Eq. (8.8) and in the evaluation of  $\alpha$  in Eq. (2.79a). If a bed entrance can be clearly defined, Eq. (8.8) is halved in the first layer of pebbles at the bed entrance. Eq. (8.8) is widely used for the analysis of helium-cooled PBRs [31, 87, 100, 134, 137].

### 8.1.4 Petrovic Model

Petrovic and Thodos correlated mass transfer data as [139]

$$Nu = 0.357 \frac{Pr^{1/3}}{\epsilon} Re^{0.641}. \quad (8.9)$$

Eq. (8.9) is valid for  $3 \leq Re \leq 230$ . While this range is fairly small, this correlation is available for low Reynolds number systems where the sensitivity of the solution to asymptotic Nusselt number behavior is of interest.

### 8.1.5 Wakao Model

Wakao correlated heat and mass transfer data as [148]

$$Nu = 2 + 1.1Pr^{1/3}Re^{0.6}. \quad (8.10)$$

Eq. (8.10) is valid for  $15 \leq Re \leq 8500$  and  $\varepsilon = 0.4$ . This model is the only Nusselt number correlation that is independent of porosity, so should only be regarded as accurate in an average sense. Despite this limitation, Eq. (8.10) is widely used due to its simplicity [49, 58, 62, 135].

## 8.2 Wall-to-Fluid Heat Transfer Coefficient

The wall-to-fluid heat transfer coefficient  $\alpha_w$  models heat transfer between a porous bed and an adjacent solid wall. The pebbles act to break up an otherwise continuous wall thermal boundary layer such that the boundary layer never becomes fully developed along the wall [149]. The packing structure of pebbles against a wall has a large impact on the convective heat transfer; the heat flux is largest near pebble-wall contact points due to the local flow acceleration and lowest in the recirculation regions behind pebbles and where flow paths join [18]. For turbulent flows, most heat is transferred by the fluid phase to the wall such that wall convection heat transfer can be approximated as a BC on the fluid phase equation [149].

### 8.2.1 Achenbach Model

Correlating mass transfer data, Achenbach gives [120]

$$Nu = \left(1 - \frac{d_p}{d_{\text{bed}}}\right) Re^{0.61} Pr^{1/3} \quad (8.11)$$

which is valid for  $50 < Re < 2 \times 10^4$ .

### 8.2.2 Yagi and Wakao Model

Yagi and Wakao correlate heat and mass transfer experiments as

$$Nu = 0.036 Pr^{1/3} Re^{0.8}, \quad (8.12)$$

where a functional form similar to the Colburn flat plate correlation is rationally based on substitution of the distance along the plate by the sphere diameter [149]. This shortened characteristic length can also be motivated by the continual break-up of the thermal boundary layer due to the solid obstacles.

## 9 Effective Solid Thermal Conductivity

The effective solid thermal conductivity  $\kappa_s$  models thermal dispersion in the solid phase that occurs via three different mechanisms as shown in Eq. (2.87). While all porous media are characterized by the same three heat transfer mechanisms, the discussion in this introductory section uses a bed of spherical pebbles as a pedagogical example.

The three components in  $\kappa_s$  are —

1. Conduction in a pebble and radiation between pebbles across a transparent fluid. This is represented by the blue (“conduction”) and red (“radiation”) lines in Fig. 10, and is denoted as  $\kappa_{\text{radiation}}$ .
2. Conduction in a pebble and conduction in the fluid between pebbles. This is represented by the blue (“conduction”) and green (“conduction”) lines in Fig. 10, and is denoted as  $\kappa_{\text{fluid conduction}}$ .
3. Conduction in a pebble and conduction between pebbles at contact areas. This is represented by the blue (“conduction”) and pink (“contact conduction”) lines in Fig. 10, and is denoted as  $\kappa_{\text{solid conduction}}$ .

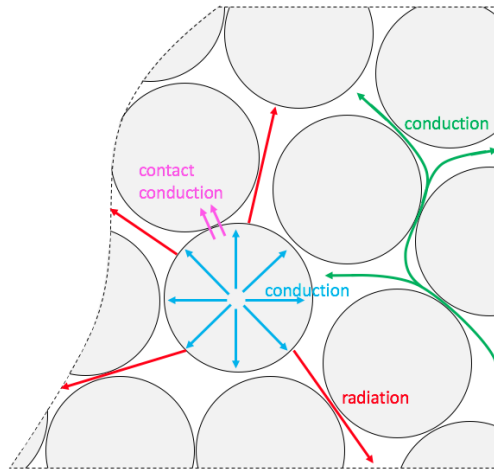


Figure 10: Various heat transfer processes in a pebble bed.

These three heat transfer mechanisms are measured with a stationary, or “stagnant”, fluid to avoid “double-counting” the convection effects represented by kernels in the fluid energy conservation equation. Therefore,  $\kappa_s$  is sometimes referred to as the “stagnant” effective thermal conductivity.

For PBR applications,  $\kappa_s$  represents the primary heat transfer removal mechanisms in Loss of Coolant Accidents (LOCAs) or other conditions where convective cooling capabilities are severely degraded. Maximum temperatures are in some cases very sensitive to the models used for  $\kappa_s$  [31,33]. Contributing to this sensitivity are the relatively high uncertainties reported in many experimental measurements, which may be partially attributable to the sensitivity of contact conduction to corrosion [150], the sensitivity of the thermal conductivity to the oxidation state [151], and/or the presence of small convection currents [152].

Most models for  $\kappa_s$  are only applicable to the bulk region of the bed [111]. In the near-wall region, the high porosity and HCP-like pebble structure motivates the use of a different correlation entirely [40] or a coarse correction factor in the near-wall region. Both modifications are available.

The remainder of this section describe models for the three components of  $\kappa_s$ . Many of these correlations are based on a model developed by Zehner, Bauer, and Schlünder (ZBS), and some general intuition can be gained by first discussing this model. The ZBS model is based on the cylindrical unit cell shown in Fig. 11 that consists of two

regions through which heat transfer occurs in parallel. An inner cylinder of radius unity contains solid and fluid, while a surrounding cylindrical annulus contains fluid.

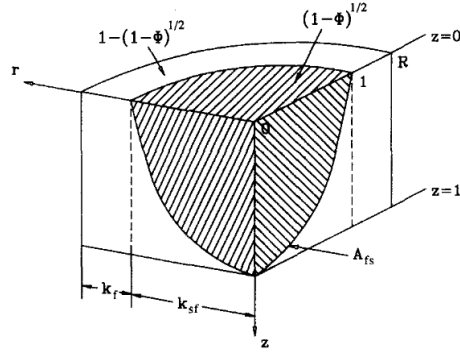


Figure 11: ZBS cylindrical unit cell. For further information on notation, refer to [153].

The ZBS model is based on the analogy between heat and mass transfer. From mass transfer experiments, the diffusivity in a packed bed,  $\mathbb{D}$ , relative to the diffusivity of a fluid-saturated medium,  $\mathbb{D}_f$ , is best fit by [153]

$$\frac{\mathbb{D}}{\mathbb{D}_f} = 1 - \sqrt{1 - \varepsilon}. \quad (9.1)$$

Mass transfer in a packed bed is mathematically equivalent to conduction in a bed with  $k_s = 0$ , so Eq. (9.1) can be equivalently expressed as

$$\lim_{\frac{k_s}{k_f} \rightarrow 0} \frac{\kappa_s}{k_f} = 1 - \sqrt{1 - \varepsilon}. \quad (9.2)$$

If the heat transfer in the center cylinder is assumed to occur in series between the solid and fluid,  $\kappa_s$  can be expressed as the summation of the heat transfer processes occurring in each region [115, 154],

$$\kappa_s = (1 - \sqrt{1 - \varepsilon}) k_f \underbrace{\left( \frac{\varepsilon}{\varepsilon - 1 + 1/\mathcal{K}_D} + \varepsilon \mathcal{K}_R \right)}_{\text{outer cylinder}} + \sqrt{1 - \varepsilon} k_f \underbrace{(\varphi \lambda + (1 - \varphi) \mathcal{K}_{SF})}_{\text{inner cylinder}}, \quad (9.3)$$

$\lambda$  is the solid-to-fluid conductivity ratio, defined as

$$\lambda \equiv \frac{k_s}{k_f}. \quad (9.4)$$

$\mathcal{K}_D$  represents a modified gas thermal conductivity that accounts for the ‘‘Smoluchowski effect,’’ or the reduction in the effective thermal conductivity due to collisions between fluid molecules and solid surfaces when the fluid MFP is on the order of the solid characteristic length.  $\mathcal{K}_D$  is defined as

$$\frac{1}{\mathcal{K}_D} = 1 + \frac{\tilde{\lambda}_{\text{mfp}}}{d_p}, \quad (9.5)$$

where  $\tilde{\lambda}_{\text{mfp}}$  is a modified mean free path [154]. For atmospheric or higher pressures, and pebble sizes on the order of centimeters, a reasonable approximation takes  $\mathcal{K}_D = 1$ . This simplification is assumed throughout.

However, Smoluchowski effects should no longer be neglected once the Knudsen number is larger than approximately  $3 \times 10^{-4}$  to  $7 \times 10^{-4}$  [151, 155]. The fact that Smoluchowski effects are significant even for  $Kn \ll 1$  shows the importance of the contact region to the overall heat transfer. Experimental data for helium, argon, and air at temperatures above 200°C shows that Smoluchowski effects impact the effective thermal conductivity at pressures relevant to nuclear systems such that assuming  $\mathcal{K}_D = 1$  might be a poor approximation [155]. Future investigations are required to fully characterize this effect.

$\mathcal{K}_{SF}$  represents the conduction-radiation and conduction-conduction processes that occur between the solid and fluid phases, and is defined <sup>1</sup> as

$$\mathcal{K}_{SF} = \frac{2}{a} \left\{ \frac{B(\lambda + \mathcal{K}_R - 1)}{a^2 \lambda \mathcal{K}_D} \ln \left[ \frac{\lambda + \mathcal{K}_R}{B [\mathcal{K}_D + (1 - \mathcal{K}_D)(\lambda + \mathcal{K}_R)]} \right] - \frac{B - 1}{a \mathcal{K}_D} + \frac{B + 1}{2B} \left[ \frac{\mathcal{K}_R}{\mathcal{K}_D} - B \left( 1 + \frac{1 - \mathcal{K}_D}{\mathcal{K}_D} \mathcal{K}_R \right) \right] \right\} \quad (9.6)$$

where  $B$  is a shape factor, and is defined as

$$B = C \left( \frac{1 - \varepsilon}{\varepsilon} \right)^m, \quad (9.7)$$

and  $a$  is defined as

$$a = \left[ 1 + \frac{\mathcal{K}_R - B \mathcal{K}_D}{\lambda} \right] \frac{1}{\mathcal{K}_D} - B \left( \frac{1}{\mathcal{K}_D} - 1 \right) \left( 1 + \frac{\mathcal{K}_R}{\lambda} \right). \quad (9.8)$$

Zehner and Schlünder recommend  $C = 1.25$  and  $m = 10/9$  to exactly fit the geometrical constraint on the shape factor  $B$ , though other values have been proposed [153].

$\varphi$  is the contact area fraction, or the fraction of the solid surface area in contact with a neighboring solid.  $\varphi$  is a function of the deformation ratio  $d_c/d_p$ , where  $d_c$  is the diameter of a contact point between two adjacent spheres.

By assuming a linearly elastic contact between two smooth spheres,  $\varphi$  is given as

$$\varphi = \frac{N_c}{4} \left( \frac{d_c}{d_p} \right)^2, \quad (9.9)$$

where  $N_c$  is the coordination number discussed in Section 5.3 [115].

For most systems of practical interest, the deformation ratio is on the order of 0.01 to 0.001 [153]. The deformation ratio may be specified as a fixed value or computed with Hertzian elastic deformation theory as follows [115, 153, 154]. The deformation ratio for contact under a collinear force  $F$  is

$$\frac{d_c}{d_p} = \left( \frac{3}{4} \frac{1 - \nu_p^2}{E} \frac{4F}{d_p^2} \right)^{1/3}, \quad (9.10)$$

<sup>1</sup>Eq. (9.6) unfortunately has a typo as shown in our 2019 journal article [156]. The form in Eq. (9.6) is correct.

where  $\nu_p$  is the Poisson ratio of the solid and  $E$  is the Young's modulus of the solid [115]. Eq. (9.10) is accurate provided  $d_c \ll d_p$ . The force is given in terms of the pressure  $P$  exerted by the pebble weight,

$$F = S_F \frac{P}{N_A}, \quad (9.11)$$

where  $N_A$  is the number of spheres per unit area (in the unit cell) and  $S_F$  is a factor that relates the total force to the vertical component along which gravity acts, since pebbles may contact one another along directions not aligned with the gravitational axis.

Values for  $\epsilon$ ,  $N_A$ ,  $S_F$ , and  $N_L$ , the number of spheres per unit length, for three different regular lattices are given in Table 4.

Table 4: Simple cubic, body-centered cubic, and face-centered cubic lattice packing geometries.

	Simple cubic	Body-centered cubic	Face-centered cubic
$N_A$	$\frac{1}{4R_p^2}$	$\frac{3}{16R_p^2}$	$\frac{1}{2\sqrt{3}R_p^2}$
$N_L$	$\frac{1}{2R_p}$	$\frac{\sqrt{3}}{2R_p}$	$\frac{\sqrt{3}}{2\sqrt{2}R_p}$
$S_F$	1	$\frac{\sqrt{3}}{4}$	$\frac{1}{\sqrt{6}}$
$\epsilon$	0.48	0.32	0.26

The gravitational pressure is approximated here as a function of the gravitational-aligned coordinate  $z$ ,

$$P \approx (1 - \epsilon_\infty) \rho_s \Delta z |g_z|, \quad (9.12)$$

where  $\Delta z$  is the height of pebbles above the  $z$ -plane on which the sphere lies, the factor  $1 - \epsilon_\infty$  approximates the fraction of this region that is solid, and  $|g_z|$  is the magnitude of the gravitational acceleration.

Finally,  $\mathcal{K}_R$  is defined as [154]

$$\mathcal{K}_R = \frac{1}{k_f} 4\sigma \bar{T}^3 d_p F_E, \quad (9.13)$$

where  $\sigma$  is the Stefan-Boltzmann constant,  $\bar{T}$  is the average temperature, and  $F_E$  is the radiation exchange factor. Most experimental measurements of  $\kappa_{\text{radiation}}$  assume LTE, which is not applicable to reactor applications. Therefore, it is not immediately obvious how to calculate  $\bar{T}$  in multiphase systems with very different intrinsic phase temperatures. Following the approach used by Auwerda et. al,  $\bar{T}$  is taken as the local solid temperature [40], though other averaging methods based on black bodies have been proposed [157].

Most experimental data points lie within  $\pm 30\%$  of Eq. (9.3) [154]. Eq. (9.3) is valid for essentially all values of porosity and  $1 < \lambda < 2000$ . This model, with minor variations such as accounting for irradiation-induced changes in material properties, is commonly used for the analysis of helium- and LiF-BeF<sub>2</sub> (FLiBe)-cooled PBRs [31, 62, 100].

The remainder of this section describes models for each of the three components in  $\kappa_s$ . Some are based on the ZBS model described here, while other are more empirical in nature. All models assume a uniform-diameter bed of spheres except the averages for  $\kappa_{\text{fluid conduction}}$  in Eqs. (9.32) and (9.33).

## 9.1 Pebble-to-Pebble Radiation

This section describes models for  $\kappa_{\text{radiation}}$ . In LOCA conditions,  $\kappa_{\text{radiation}}$  is the most significant of the  $\kappa_s$  components due to the high temperatures observed. In HTGRs,  $\kappa_{\text{radiation}}$  may also be the most significant component for any temperature above 300 to 400°C [41, 115]. All models in this section assume the fluid is transparent; this may be a good approximation for gases such as helium and is commonly assumed for liquids as well [158, 159], but should be investigated further for new proposed coolants such as molten salts [27]. Many of the models described here are correlated in terms of a dimensionless solid thermal conductivity  $\Lambda$ , defined as

$$\Lambda \equiv \frac{k_s}{4\sigma T^3 d_p}, \quad (9.14)$$

Fig. 12 shows a normalized  $\kappa_{\text{radiation}}$  as a function of  $\Lambda$  for  $\epsilon = 0.4$  and  $\epsilon_{r,s} = 0.8$ . Also shown is the experimental data of Wakao and Kato, with the fluid conduction component subtracted out using the Krupiczka correlation in Eq. (9.40) and the solid conduction component assumed small [159]. At low and high  $\Lambda$ , plateaus are reached in  $\kappa_{\text{radiation}}$ , with high  $\Lambda$  corresponding to higher  $\kappa_{\text{radiation}}$  due to the bypassing of some radiation resistance [157].

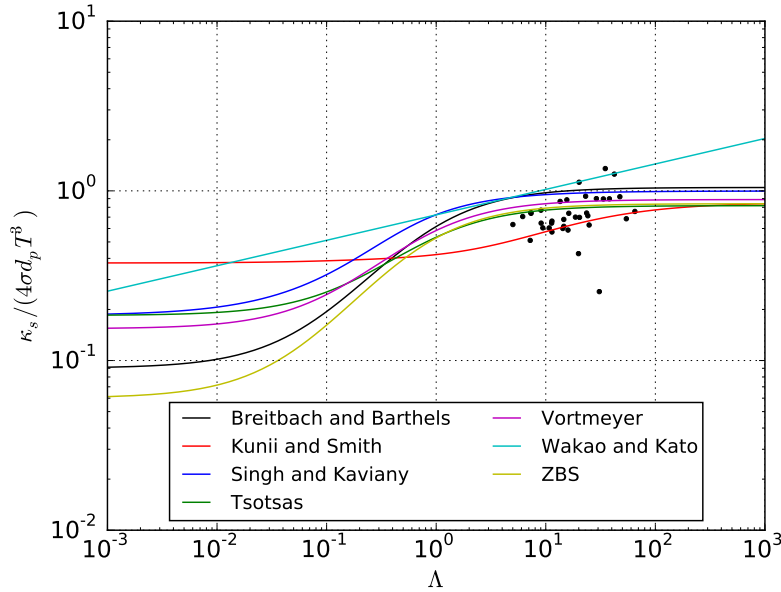


Figure 12: A comparison of a normalized  $\kappa_{\text{radiation}}$  computed by the various correlations as a function of  $\Lambda$  for  $\epsilon = 0.4$  and  $\epsilon_{r,s} = 0.8$ . Also shown is the experimental data of Wakao and Kato, with the fluid conduction component subtracted out using the Krupiczka correlation in Eq. (9.40) and the solid conduction component assumed small [159].

Fig. 13 shows the radiation component as a function of temperature for  $\epsilon = 0.4$ ,  $\epsilon_{r,s} = 0.8$ , and  $\lambda = 100$ .  $\kappa_{\text{radiation}}$  also increases with porosity and pebble diameter, since larger gaps permit greater radiation transfer [115, 158]. Several correlations in this section do not show any explicit porosity dependence, and should be used with caution.

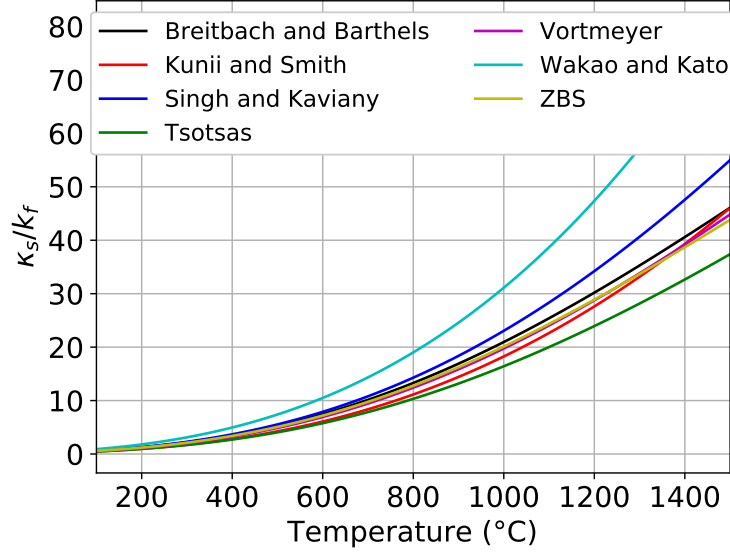


Figure 13: A comparison of  $\kappa_{\text{radiation}}$  computed by the various correlations available in this section as a function of temperature for  $\epsilon = 0.4$ ,  $\epsilon_{r,s} = 0.8$ , and  $\lambda = 100$ .

### 9.1.1 Breitbach and Barthels Model

Breitbach and Barthels derive a corrected version of the ZBS model described in Section 9.1.7 that relaxes the assumption of zero incoming radiation to the unit cell and is more accurate at higher temperatures [160]. Assuming the unit cell base areas are black surfaces, this model gives

$$\kappa_{\text{radiation}} = \left[ \left(1 - \sqrt{1 - \epsilon}\right) \epsilon + \frac{\sqrt{1 - \epsilon}}{2/\epsilon_{r,s} - 1} \frac{B + 1}{B} \frac{1}{1 + \frac{1}{(2/\epsilon_{r,s} - 1)\lambda}} \right] 4\sigma d_p \bar{T}^3. \quad (9.15)$$

Experiments performed with high emittance graphite and low emittance  $\text{ZrO}_2$  spheres at temperatures up to 1000-1500°C illustrate a better agreement of Eq. (9.15) than Eq. (9.31) at low emittance [160]. Eq. (9.15) is commonly used for PBR analysis [87], and is the default radiation model in Pronghorn.

### 9.1.2 Kunii and Smith Model

Kunii and Smith derive a model based on a unit cell consisting of two half-spheres in contact with combinations of parallel and series heat transfer in a geometry similar to the ZBS unit cell. By neglecting the Smoluchowski effect, the radiation component is [158, 161]

$$\kappa_{\text{radiation}} = \epsilon \left( 1 + \frac{C_0 h_{rv}}{k_f} \right) k_f + \frac{C_0 (1 - \epsilon)}{\frac{1}{1/\psi_t + h_{rs}/k_f} + \frac{2}{3\lambda}} k_f - \kappa_{\text{fluid conduction}}, \quad (9.16)$$

where  $\kappa_{\text{fluid conduction}}$  is obtained by setting  $h_{rs}$  and  $h_{rv}$  to zero in the first part of Eq. (9.16) and is given by Eq. (9.41).  $C_0$  is defined empirically as

$$C_0 = \begin{cases} 0.895 & \text{dense packings} \\ 1.0 & \text{loose packings} \end{cases} \quad (9.17)$$

Based on Eq. (5.1), a dense packing is considered to correspond to porosities of 0.372 or smaller, while a loose packing to porosities of 0.409 or higher. Interpolation between these bounds is performed for intermediate porosities to obtain  $C_0$ .  $\psi_t$  is given as a linear interpolation in terms of porosity, with truncation for porosities outside the valid range,

$$\psi_t = \begin{cases} \frac{\frac{1}{3} \left( \frac{\lambda-1}{\lambda} \right)^2}{\ln(0.214\lambda + 0.786) - 0.214 \frac{\lambda-1}{\lambda}} - \frac{2}{3\lambda} & \varepsilon = 0.260 \\ \frac{\frac{1}{8\sqrt{3}} \left( \frac{\lambda-1}{\lambda} \right)^2}{\ln(1.925\lambda - 0.925) - 1.925 \frac{\lambda-1}{\lambda}} - \frac{2}{3\lambda} & \varepsilon = 0.476 \end{cases} \quad (9.18)$$

$h_{rs}$  and  $h_{rv}$  represent radiation heat transfer coefficients in the solid and void regions, respectively, and are given as [111]

$$h_{rs} \equiv \frac{\varepsilon_{r,s}}{2 - \varepsilon_{r,s}} 4\sigma d_p \bar{T}^3, \quad (9.19)$$

$$h_{rv} \equiv \frac{1}{1 + \frac{\varepsilon}{2(1-\varepsilon)} \frac{1-\varepsilon_{r,s}}{\varepsilon_{r,s}}} 4\sigma d_p \bar{T}^3. \quad (9.20)$$

### 9.1.3 Singh and Kaviany Model

Singh and Kaviany combined ray tracing with a Finite Difference (FD) heat conduction solution in a pebble lattice with  $\varepsilon = 0.476$  for diffuse, randomly-displaced, multi-layer beds between two parallel black body emissive plates, giving [157]

$$\kappa_{\text{radiation}} = \left[ 0.5756 \varepsilon_{r,s} \tan^{-1} \left( 1.5353 \frac{\Lambda^{0.8011}}{\varepsilon_{r,s}} \right) + 0.1843 \right] 4\sigma d_p \bar{T}^3. \quad (9.21)$$

### 9.1.4 Tsotsas Model

Tsotsas proposed a modification to the ZBS model that is more applicable in the near-wall region [112],

$$\kappa_{\text{radiation}} = \left( 1 - \sqrt{1-\varepsilon} \right) \frac{\lambda}{\Lambda(2/\varepsilon_{r,s} - 1)} + \sqrt{1-\varepsilon} \frac{\lambda}{\Lambda(2/\varepsilon_{r,s} - 1) + 1}. \quad (9.22)$$

### 9.1.5 Vortmeyer Model

Vortmeyer modeled radiation heat transfer in a system of parallel layers of spheres with temperature variation within each layer to give [160]

$$\kappa_{\text{radiation}} = \left[ \frac{\pi}{6} \frac{\Psi_v}{1-\varepsilon} \frac{1-\tau_v h_v}{1+\tau_v h_v \Psi_v} \right] 4\sigma d_p \bar{T}^3, \quad (9.23)$$

where  $\Psi_v$ ,  $\tau_v$ ,  $h_v$ , and  $\varepsilon'_{r,s}$  are defined as

$$\Psi_v \equiv \frac{1+B_r-R_r}{1-B_r+R_r}, \quad (9.24)$$

$$\tau_v \equiv \frac{1-B_r-R_r}{1+B_r-R_r}, \quad (9.25)$$

$$h_v \equiv \left( 1 - 2 \frac{B_r(0) - B_r}{1 - B_r - R_r} \right) \frac{\varepsilon'_{r,s}}{\frac{12}{\pi} \Lambda(1-\varepsilon) + \varepsilon'_{r,s}}, \quad (9.26)$$

$$\varepsilon'_{r,s} \equiv \frac{\varepsilon_{r,s}}{0.5(1-\varepsilon_{r,s}) + \varepsilon_{r,s}}, \quad (9.27)$$

and  $B_r$  and  $R_r$  are the radiation transmission and reflection numbers, defined as [111]

$$R_r = (1 - B_r)(1 - \varepsilon'_{r,s}), \quad (9.28)$$

$$B_r = \begin{cases} 0.149909 - 0.24791\varepsilon_{r,s} + 0.290799\varepsilon_{r,s}^2 - 0.20081\varepsilon_{r,s}^3 + 0.0651042\varepsilon_{r,s}^4 & \varepsilon = 0.40 \\ 0.179 - 0.24791\varepsilon_{r,s} + 0.290799\varepsilon_{r,s}^2 - 0.20081\varepsilon_{r,s}^3 + 0.0651042\varepsilon_{r,s}^4 & \varepsilon = 0.48 \end{cases}. \quad (9.29)$$

No description is provided for the calculation of  $B_r(0)$  in works that show this correlation, so interpolation is performed between  $B_r(0) = 0.15$  for  $\varepsilon = 0.4$  and  $B_r(0) = 0.18$  for  $\varepsilon = 0.48$  based on graphical data [111, 160]. Interpolation is performed with Eq. (9.29) based on the porosity with truncation if outside the valid porosity range.

### 9.1.6 Wakao and Kato Model

Wakao and Kato model radiation heat transfer in cubic and orthorhombic lattices assuming 1-D heat transfer, a constant radiation heat transfer coefficient over the sphere surfaces, and constant isothermal adjacent surface temperatures, giving [159]

$$\kappa_{\text{radiation}} = \left\{ 0.707\lambda^{1.11} \left[ \frac{2}{k_s(2/\varepsilon_{r,s} - 0.264)} \right]^{0.96} \right\} (4\sigma d_p \bar{T}^3)^{0.96}. \quad (9.30)$$

Eq. (9.30) is valid for  $20 \leq \lambda \leq 1000$  and  $0.395 \leq \varepsilon \leq 0.476$ .

### 9.1.7 Zehner, Bauer, and Schlünder Model

The ZBS model is derived from the unit cell introduced in Fig. 11. The spheres are assumed opaque with grey surfaces and the non-solid parts of the base areas are assumed to have the same emittance as the sphere surfaces; all other surfaces are assumed to be specular reflecting surfaces. It is assumed that the unit cell is closed to radiation heat transfer from neighboring unit cells, giving

$$\kappa_{\text{radiation}} = \left[ \frac{(1 - \sqrt{1 - \epsilon}) \epsilon}{2/\epsilon_{r,s} - 1} + \frac{\sqrt{1 - \epsilon}}{2/\epsilon_{r,s} - 1} \frac{B + 1}{B} \frac{1}{1 + \frac{1}{(2\epsilon_{r,s} - 1)\Lambda}} \right] 4\sigma d_p \bar{T}^3. \quad (9.31)$$

Because no radiation enters from outside the cell, Eq. (9.31) underpredicts  $\kappa_s$  at high temperature [160]. This assumptions made in this model also do not account for solids with low emittance due to the assumption of the pebble's interior having the same emissivity as its surface.

## 9.2 Multiphase Conduction

This section describes models for  $\kappa_{\text{fluid conduction}}$ . The simplest model of conduction heat transfer is a volume average of the fluid and solid thermal conductivities,

$$\kappa_{\text{fluid conduction}} + \kappa_{\text{solid conduction}} = \epsilon k_f + (1 - \epsilon) k_s. \quad (9.32)$$

Eq. (9.32) is equivalent to assuming heat transfer occurs in series between the two phases. Alternatively, parallel heat transfer could be assumed,

$$\kappa_{\text{fluid conduction}} + \kappa_{\text{solid conduction}} = \frac{\epsilon}{k_f} + \frac{1 - \epsilon}{k_s}. \quad (9.33)$$

Both Eqs. (9.32) and (9.33) have been used in simple models [20, 136, 158]. Eqs. (9.32) and (9.33) provide bounds on the actual  $\kappa_{\text{fluid conduction}}$  of the medium. Series heat transfer represents the minimum bound, since all heat must eventually pass through the lower-conducting phase, while parallel heat transfer represents the maximum bound, since the low-conducting phase can be bypassed. Some models use linear combinations of Eqs. (9.32) and (9.33), with a fixed 20% fraction of the heat transfer occurring in series [154].

Fig. 14 shows the available models for  $\kappa_{\text{fluid conduction}}$  as a function of  $\lambda$  for  $\epsilon = 0.4$ ; also shown are the series and parallel heat transfer bounds described by Eqs. (9.32) and (9.33). Experimental data is shown from Prasad et. al, Wakao and Kato, Aichlmayr and Kulacki, Ofuchi and Kunii, Nozad et. al, Swift, and assimilated by Gonzo and Fundamenski and Gierszweski [150–152, 159, 161–164]. The combined porosity range of these data sets is  $0.337 \leq \epsilon \leq 0.476$ , but only data in the range  $0.39 \leq \epsilon \leq 0.41$  is shown. The porosity for the data assimilated by Fundamenski and Gierszweski is not available, and is therefore assumed to be  $\epsilon = 0.4$  [164].

For  $\lambda > 10^3$ , deviation from experimental data occurs due to the neglect of solid contact conduction, though the data of Swift does not reflect this trend, possibly due to different solid contacts [150]. Models including solid contact conduction shown in Fig. 15b show much better agreement with experimental data, and different trends in experimental data are often reconciled when the solid contact component is neglected [164].

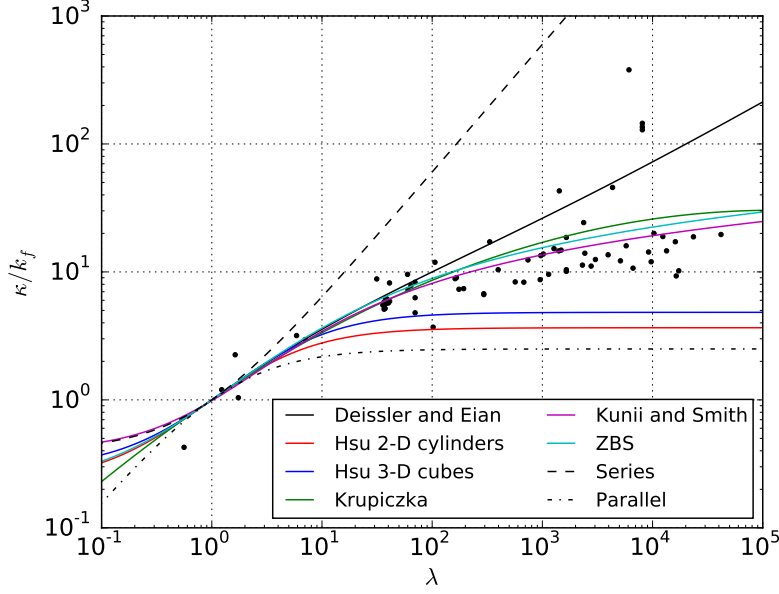


Figure 14: A comparison of  $\kappa_{\text{fluid conduction}}$  computed by the various correlations available in Pronghorn for  $\varepsilon = 0.4$ , along with the theoretical bounds provided by series and parallel heat transfer with Eqs. (9.32) and (9.33). Also shown are experimental data points in the range  $0.39 \leq \varepsilon \leq 0.41$  [150–152, 159, 161–164].

All of the available models lie within the bounds of series and parallel heat transfer. For  $\lambda > 1$ ,  $\kappa_{\text{fluid conduction}}$  decreases with porosity, while for  $\lambda < 1$ ,  $\kappa_{\text{fluid conduction}}$  increases with porosity [153, 165]. The fluid conduction component should satisfy the two following limits,

$$\lim_{\varepsilon \rightarrow 1} \frac{\kappa_{\text{fluid conduction}}}{k_f} = 1, \quad (9.34)$$

$$\lim_{\varepsilon \rightarrow 0} \frac{\kappa_{\text{fluid conduction}}}{k_f} = \lambda. \quad (9.35)$$

All models satisfy Eqs. (9.34) and (9.35) except the Krupiczka model.

### 9.2.1 Volume Average Model

A parallel heat transfer model is given by Eq. (9.32), and is only recommended for non-spherical “pebbles,” such as may be encountered in modeling of reflectors with bypass flow.

### 9.2.2 Deissler and Eian Model

For spheres and cylinders in a 2-D SC lattice, Deissler and Eian derive [155]

$$\kappa_{\text{fluid conduction}} = \begin{cases} \frac{\pi}{2(1/\lambda - 1)^2} [1/\lambda - 1 - \ln(1/\lambda)] k_f + \left(1 - \frac{\pi}{4}\right) k_f & \varepsilon = 0.475 \\ \frac{\pi}{2(1/\lambda - 1)} k_f - \frac{\pi/2 - \arcsin(1/\lambda - 1)}{(1/\lambda - 1)\sqrt{2\lambda - 1}} \lambda k_f & \varepsilon = 0.214 \end{cases}. \quad (9.36)$$

Linear interpolation is performed between  $\varepsilon = 0.214$  and  $\varepsilon = 0.475$ . Linear interpolation is performed for  $\varepsilon < 0.214$  and  $\varepsilon > 0.475$  based on the limits in Eqs. (9.34) and (9.35). For  $\lambda < 0.5$ , the argument of the arcsin in the cylinder correlation is outside the valid domain, so this correlation cannot be used for  $\lambda < 0.5$ .

Eq. (9.36) assumes a regular lattice and that the heat flow lines do not bend. Irregular lattices decrease conductivity, while bending heat flow lines increases conductivity. Assuming these effects cancel one another at high  $\lambda$  may produce a significant underprediction of  $\kappa_{\text{fluid conduction}}$  [164].

### 9.2.3 Hsu 2-D Cylinder Array Model

For a 2-D array of touching square cylinders with series heat transfer through layers of fluid and composite fluid-solid layers, Hsu et. al derive [166]

$$\kappa_{\text{fluid conduction}} = \left(1 - \sqrt{1 - \varepsilon}\right) k_f + \sqrt{1 - \varepsilon} \mathcal{K}_{SF} k_f, \quad (9.37)$$

where  $\mathcal{K}_{SF}$  is given by

$$\mathcal{K}_{SF} = \frac{1}{1 + (1/\lambda - 1) \sqrt{1 - \varepsilon}}, \quad (9.38)$$

instead of Eq. (9.6). Eq. (9.37) shows good agreement with numerical results obtained by Nozad et. al [166].

### 9.2.4 Hsu 3-D Cube Array Model

For a 3-D array of connected cubes and other assumptions similar to those described in Section 9.2.3, Hsu et. al derive [166]

$$\kappa_{\text{fluid conduction}} = \left[1 - (1 - \varepsilon)^{2/3}\right] k_f + \frac{(1 - \varepsilon)^{2/3}}{1 + (1/\lambda - 1)(1 - \varepsilon)^{1/3}} k_f. \quad (9.39)$$

### 9.2.5 Krupiczka Model

Krupiczka numerically solved 2-D heat conduction for a bundle of long cylinders with no temperature drop between the phases and extended the results to a bed of spherical pebbles, giving [163]

$$\kappa_{\text{fluid conduction}} = k_f \lambda^{0.280 - 0.757 \log \varepsilon + 0.057 \log(1/\lambda)}. \quad (9.40)$$

Eq. (9.40) matches experimental results within about 20% for liquid fluids, but does gives poorer predictions for gases [163].

### 9.2.6 Kunii and Smith Model

The fluid conduction component of the Kunii and Smith model in Eq. (9.16) is isolated by setting  $h_{rs}$  and  $h_{rv}$  to zero, giving [158]

$$\kappa_{\text{fluid conduction}} = \varepsilon k_f + (1 - \varepsilon) \frac{C_0}{\Psi_f + \frac{2}{3\lambda}} k_f . \quad (9.41)$$

Eq. (9.41) shows a good agreement with numerical results obtained by Wakao and Kato and with experimental data in intermediate  $\lambda$  ranges [150, 159].

### 9.2.7 Zehner, Bauer, and Schlünder Model

The ZBS model is obtained from Eq. (9.3) by setting  $\mathcal{K}_R = 0$ ,  $\mathcal{K}_D = 1$ , and  $\varphi = 0$  [153, 163, 165],

$$\kappa_{\text{fluid conduction}} = \left(1 - \sqrt{1 - \varepsilon}\right) k_f + \sqrt{1 - \varepsilon} \mathcal{K}_{SF} k_f , \quad (9.42)$$

where  $\mathcal{K}_{SF}$  is given by Eq. (9.6) by setting  $\mathcal{K}_R = 0$  and  $\mathcal{K}_D = 1$ ,

$$\mathcal{K}_{SF} = \frac{2}{1 - B/\lambda} \left[ \frac{B(1 - 1/\lambda)}{(1 - B/\lambda)^2} \ln\left(\frac{\lambda}{B}\right) - \frac{B - 1}{1 - B/\lambda} - \frac{B + 1}{2} \right] . \quad (9.43)$$

The ZBS model has been validated experimentally for  $0.2 \leq \varepsilon \leq 0.44$  [163, 165]. Good agreement with experimental data for intermediate  $\lambda$  has also been observed [150]. This is the default multiphase conduction model in Pronghorn.

## 9.3 Pebble-to-Pebble Contact Conduction

This section describes models for  $\kappa_{\text{solid conduction}}$ . In pebble-to-pebble contact, the contact area, contact roughness, and surface film contamination (especially if the surface is heavily oxidized) all have an impact on this form of conduction heat transfer. The correlations discussed in this section only address the contact area factor, which for spherical pebbles also tends to be the most important, especially for  $\lambda > 10^3$  [153, 165, 167].

Fig. 15a shows all models available for  $\kappa_{\text{solid conduction}}$  with  $\varepsilon = 0.4$  and  $d_c/d_p = 0.1$  for 3-D correlations and  $d_c/d_p = 0.01$  for 2-D correlations. Most of the correlations shown in this section were originally developed to represent both the solid and fluid conduction components; for these correlations, Fig. 15b shows the sum of the solid and fluid conduction components for the same conditions as in Fig. 15a. Experimental data is also shown from Prasad et. al, Wakao and Kato, Aichlmayr and Kulacki, Ofuchi and Kunii, Nozad et. al, Swift, and assimilated by Gonzo and Fundamenski and Gierszewski. The combined porosity range of these data sets is  $0.337 \leq \varepsilon \leq 0.476$ , but only data in the range  $0.39 \leq \varepsilon \leq 0.41$  is shown. The porosity for the data assimilated by Fundamenski and Gierszewski is not available, and is therefore assumed to be  $\varepsilon = 0.4$  [164]. As mentioned in Section 9.2, the data of Swift for  $\lambda > 10^3$  is generally considered to not accurately reflect solid conduction effects [150].

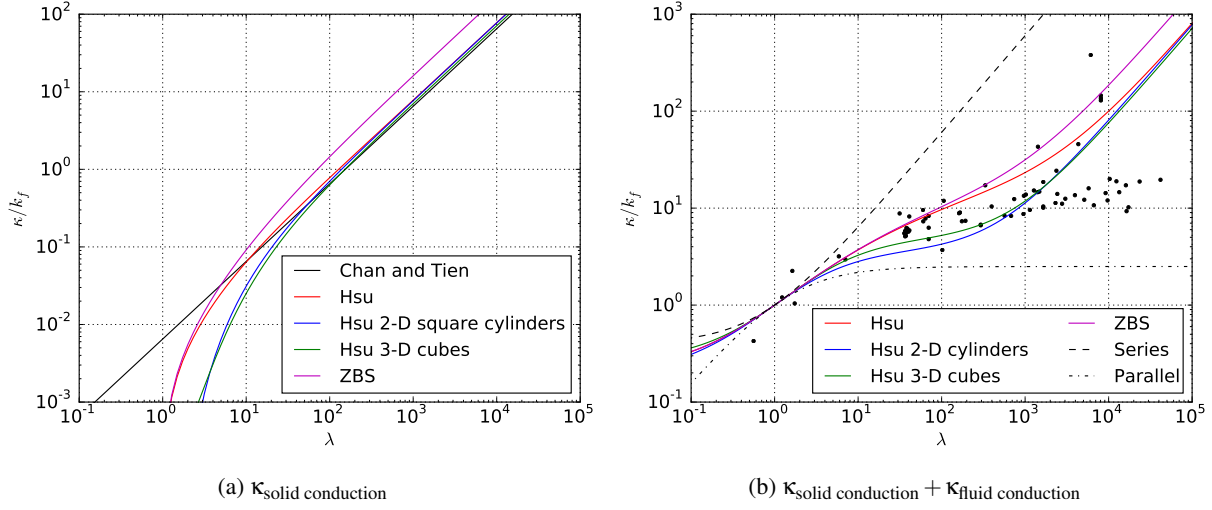


Figure 15: A comparison of (a)  $\kappa_{\text{solid conduction}}$  and (b)  $\kappa_{\text{solid conduction}} + \kappa_{\text{fluid conduction}}$  computed by the various correlations available in this section for  $\varepsilon = 0.4$  and  $d_c/d_p = 0.1$  for 3-D correlations and  $d_c/d_p = 0.01$  for 2-D correlations. Also shown in (b) are experimental data points in the range  $0.39 \leq \varepsilon \leq 0.41$  [150–152, 159, 161–164].

$\kappa_{\text{solid conduction}}$  is sensitive to  $d_c/d_p$  for  $\lambda > 50$ ; increasing  $d_c/d_p$  by an order of magnitude results in approximately an order of magnitude increase in  $\kappa_{\text{solid conduction}}$  [166]. Models of the type given in Eq. (9.10) should be used to estimate  $d_c/d_p$ , though known values may also be provided.

### 9.3.1 Chan and Tien Model

Chan and Tien solve steady-state heat conduction for a single sphere in an isothermal layer of spheres, with heat transfer at areas contacting different layers approximated with a modified thermal resistance. Assuming each sphere contains several contacts of uniform heat flux, with the remainder of the surface insulated, this model gives [167]

$$\kappa_{\text{solid conduction}} = \frac{1}{2 \cdot 0.53} \frac{N_A}{N_L} \left( \frac{d_c}{d_p} \right) d_p \lambda k_f, \quad (9.44)$$

where  $N_L$  is the number of spheres per unit length in the unit cell. Table 4 provides values for  $N_A$ ,  $N_L$ , and  $S_F$  for various regular packings. Interpolation or a nearest-value selection is performed based on the porosity.

### 9.3.2 Hsu Model

Hsu et. al extend the ZBS model to include solid contact conduction, giving [153]

$$\kappa_{\text{solid conduction}} = \frac{2\sqrt{1-\varepsilon} k_f}{\alpha_1} \left\{ \frac{(1-1/\lambda)(1+\alpha)B}{\alpha_1^2} \ln \left[ \frac{(1+\alpha)B}{(1+\alpha)B} \right] - \frac{B+1+2\alpha B}{2(1+\alpha B)^2} - \frac{B-1}{\alpha_1(1+\alpha B)} \right\} + (1-\sqrt{1-\varepsilon})k_f + \lambda\sqrt{1-\varepsilon} \left( \frac{d_c}{d_p} \right)^2 k_f - \kappa_{\text{fluid conduction}} \quad (9.45)$$

where  $\kappa_{\text{fluid conduction}}$  is given by Eq. (9.42);  $\alpha_1$  is defined as

$$\alpha_1 \equiv 1 - \frac{B}{\lambda} + \left(1 - \frac{1}{\lambda}\right) \alpha B ; \quad (9.46)$$

and  $\alpha$  and  $B$  are related by

$$1 + \alpha B = \left[ 1 - \left( \frac{d_c}{d_p} \right)^2 \right]^{-1/2} , \quad (9.47)$$

$$\varepsilon = 1 - \frac{B^2}{(1-B)^6(1+\alpha B)^2} \left\{ B^2 - 4B + 3 + 2(1+\alpha)(1+\alpha B) \ln \left[ \frac{(1+\alpha)B}{1+\alpha B} \right] + \alpha(B-1)(B^2 - 2B - 1) \right\}^2 . \quad (9.48)$$

Eqs. (9.47) and (9.48) are solved in an iterative manner.

### 9.3.3 Hsu 2-D Sphere Array Model

For the 2-D array of touching spheres model described in Section 9.2.3, the solid conduction component is obtained by subtracting the  $\kappa_{\text{fluid conduction}}$  component, giving [166]

$$\kappa_{\text{solid conduction}} = \gamma_a \lambda \frac{d_c}{d_p} k_f + \frac{\gamma_a \left(1 - \frac{d_c}{d_p}\right)}{1 + (1/\lambda - 1) \gamma_a} k_f + \frac{1 - \gamma_a}{1 + (1/\lambda - 1) \gamma_a \frac{d_c}{d_p}} k_f - \kappa_{\text{fluid conduction}} , \quad (9.49)$$

where  $\kappa_{\text{fluid conduction}}$  is given by Eq. (9.37),  $\mathcal{K}_{SF}$  is given by Eq. (9.38), and  $\gamma_a$  is defined as

$$\gamma_a = \frac{-2 \frac{d_c}{d_p} + \sqrt{4 \left( \frac{d_c}{d_p} \right)^2 - 4 \left(1 - 2 \frac{d_c}{d_p}\right) (\varepsilon - 1)}}{2 \left(1 - 2 \frac{d_c}{d_p}\right)} . \quad (9.50)$$

$d_c/d_p$  was originally set to 0.01 in order to fit experimental data [166].

### 9.3.4 Hsu 3-D Cube Array Model

For a 3-D array of touching cubes, the solid conduction component is obtained by subtracting the  $\kappa_{\text{fluid conduction}}$  component, giving [166]

$$\begin{aligned} \kappa_{\text{solid conduction}} = 1 + \gamma_a^2 \left[ \lambda \left( \frac{d_c}{d_p} \right)^2 + 2 \frac{d_c}{d_p} - 1 \right] - 2 \gamma_a \frac{d_c}{d_p} + \frac{\gamma_a^2 \left[ 1 - \left( \frac{d_c}{d_p} \right)^2 \right]}{1 + (1/\lambda - 1) \gamma_a} + \\ \frac{2 \gamma_a \frac{d_c}{d_p} (1 - \gamma_a)}{1 + \gamma_a \frac{d_c}{d_p} (1/\lambda - 1)} - \kappa_{\text{fluid conduction}} , \end{aligned} \quad (9.51)$$

where  $\kappa_{\text{fluid conduction}}$  is given by Eq. (9.39) and  $\gamma_a$  is given by

$$1 - \varepsilon = \left[ 1 - 3 \left( \frac{d_c}{d_p} \right)^2 \right] \gamma_a^3 + 3 \left( \frac{d_c}{d_p} \right)^2 \gamma_a^2 . \quad (9.52)$$

### 9.3.5 Zehner, Bauer, and Schlünder Model

For the ZBS model, the solid conduction component is obtained from Eq. (9.3) by setting  $\mathcal{K}_R = 0$  and subtracting the  $\kappa_{\text{fluid conduction}}$  component, giving [115, 153]

$$\kappa_{\text{solid conduction}} = \sqrt{1 - \varepsilon} k_f \phi (\lambda - \mathcal{K}_{SF}) , \quad (9.53)$$

where  $\mathcal{K}_{SF}$  is given by Eq. (9.43).

## 10 Effective Fluid Thermal Conductivity

The effective fluid thermal conductivity  $\kappa_f$  models thermal dispersion in the fluid phase. Thermal dispersion, also referred to as the “braiding” effect, represents enhancements to convective heat transfer that occur in porous media [32]. The remainder of this section describes available models for  $\kappa_f$ .

### 10.1 Zero Dispersion Model

Most porous media simulations of PBRs neglect thermal dispersion [62, 87], in which case  $\bar{\kappa}_f = 0$  and Eq. (2.81) becomes

$$\kappa_f = \epsilon k_f . \quad (10.1)$$

Neglecting thermal dispersion is a reasonable approximation for high Reynolds numbers [140, 146], but for low Reynolds numbers more sophisticated models should be used [31]. Because thermal dispersion acts to increase the diffusive effects, neglecting thermal dispersion is (thermally) conservative in the sense that peak temperatures are usually higher [31].

### 10.2 Linear Peclet Model

$\kappa_f$  generally increases with Reynolds and Prandtl numbers; the linear Peclet model gives  $\kappa_f$  as [32, 77, 104, 113, 149, 168]

$$\kappa_f = \epsilon k_f + C_0 Pe k_f . \quad (10.2)$$

Eq. (10.2) represents a linear combination of diffusive and convective limits for thermal dispersion [169]. The assumption of superposition is accurate in the limits of low and high Peclet number, but may be inaccurate in the transition regime and for liquids which typically have larger ranges in Prandtl number than gases [170]. And while some experiments suggest difference dependencies for the Reynolds and Prandtl numbers, Eq. (10.2) remains the most common thermal dispersion model [170]. Note that some literature references replace  $\epsilon$  by  $1/\mathcal{J}$ , where  $\mathcal{J}$  is the tortuosity [32, 77].

The proportionality constant  $C_0$  in Eq. (10.2) accounts for the effects of solid shape and packing and is typically determined experimentally as a constant for each of the radial and axial flow directions in cylindrical beds to give a tensorial  $\kappa_f$  [77]. All measurements cited for  $C_0$  in the remainder of this section only apply to beds of uniform-diameter spheres.

While most data used to develop thermal dispersion models is obtained using beds of pebbles with diameters much smaller than seen in PBRs, experiments performed with large pebbles show that existing correlations are applicable to PBR analysis [99, 154].

$C_0$  is typically about five times larger in the axial direction than in the radial direction [170]. For example, Amiri et. al suggest  $C_0 = 0.5$  for the axial component [77], while Yagi and Kunii suggest  $C_0 = 0.11$  for the radial component [168]. Other researchers propose values of similar magnitude [168].

For simplicity and because a relatively weak dependence of flow and heat transfer on the absolute value of  $C_0$  has been observed for reactor conditions, individual radial and axial dependencies are neglected [40]. A default of  $C_0 = 0.11$  is used, which is valid for  $20 < Re < 800$  and  $13.8 < d_{\text{bed}}/d_p < 47.6$  [40, 104, 149, 168].  $C_0$  is smaller in the near-wall region than in the bulk of the bed, and a constant scaling factor may be applied within a specified distance

from the walls that is taken as  $d_p/2$  by default. This scaling factor is often taken as 0.5, though Tsotsas and Schlünder propose a correction dependent on the bed to pebble diameter ratio [104],

$$\frac{1}{2 - \left(1 - 2\frac{d_p}{d_{\text{bed}}}\right)^2} \quad (10.3)$$

## 11 Fluid Equations of State

The fluid isobaric specific heat, thermal conductivity, and viscosity are required to close the conservation of fluid mass, momentum, and energy equations. Depending on the set of solution variables, density, pressure, and temperature in terms of two other state variables are also required. Derivatives of many properties are also needed for the SUPG stabilization.

Both general EOS, such as ideal gas and stiffened gas, as well as custom properties, such as FLiBe and helium, are available in the MOOSE fluid properties module. Table 5 provides a list of a subset of these EOS that are the most likely to be used in PBR applications. Nitrogen and helium properties using the Spline-Based Table Lookup (SBTL) method are also available as submodules. Additional information may be found in the fluid properties module documentation [171].

Table 5: Summary of several fluid property EOS available in MOOSE.

Name	Fluid or EOS
FlibeFluidProperties	FLiBe
FlinakFluidProperties	FLiNaK
HeliumFluidProperties	helium
IdealGasFluidProperties	ideal gas
NitrogenFluidProperties	nitrogen
StiffenedGasFluidProperties	stiffened gas

## 12 Solid Equations of State

The solid isobaric specific heat, thermal conductivity, and density are required to close the conservation of solid energy equation. Depending on the models used for  $\kappa_s$ , the emissivity, Poisson ratio, and Young's modulus are also required. This section describes the available solid EOSs. Table 2 shows the units assumed in this section.

### 12.1 Aluminum Oxide

$\text{Al}_2\text{O}_3$  density, thermal conductivity, and isobaric specific heat capacity are given as [48, 172]

$$\rho_S \text{ (kg/m}^3\text{)} = 3637 , \quad (12.1a)$$

$$k_S \text{ (W/m}\cdot\text{K)} = 743.0066T_S^{-0.69515} , \quad (12.1b)$$

$$C_{p,S} \text{ (J/kg}\cdot\text{K)} = 880 . \quad (12.1c)$$

Eq. (12.1b) is valid for  $293 \text{ K} \leq T_S \leq 1579 \text{ K}$ .

### 12.2 Composite Mixture

Solid properties for a solid composed of  $N$  constituents may be specified in terms of the properties of the individual constituents as

$$\rho_S \text{ (kg/m}^3\text{)} = f(\rho_{S,1} \cdots \rho_{S,N}, \epsilon_{S,1} \cdots \epsilon_{S,N}) , \quad (12.2a)$$

$$k_S \text{ (W/m}\cdot\text{K)} = g(k_{S,1} \cdots k_{S,N}, \epsilon_{S,1} \cdots \epsilon_{S,N}) , \quad (12.2b)$$

$$C_{p,S} \text{ (J/kg}\cdot\text{K)} = h(C_{p,S,1} \cdots C_{p,S,N}, \epsilon_{S,1} \cdots \epsilon_{S,N}) , \quad (12.2c)$$

where  $f$ ,  $g$ , and  $h$  are generic functions of the properties and phase fractions of the  $N$  constituent materials.

Any of the mixing models described in Section 13 may be used for the density, thermal conductivity, and isobaric specific heat capacity.

### 12.3 Fire Brick

Type C-22Z fire brick from BNZ Materials, Inc. density, thermal conductivity, and isobaric specific heat are given as [173, 174]

$$\rho_S \text{ (kg/m}^3\text{)} = 737 , \quad (12.3a)$$

$$k_S \text{ (W/m}\cdot\text{K)} = 1.7285 \times 10^{-4}T_S + 0.12581 , \quad (12.3b)$$

$$C_{p,S} \text{ (J/kg}\cdot\text{K)} = 1050 , \quad (12.3c)$$

where Eq. (12.3b) is obtained with a linear fit to manufacturer data and is valid for  $533 \text{ K} \leq T_S \leq 1366 \text{ K}$ .

## 12.4 Function Dependence

Generic function solid properties may be specified as

$$\rho_S \text{ (kg/m}^3\text{)} = \rho_S(\vec{x}, T_S), \quad (12.4a)$$

$$k_S \text{ (W/m}\cdot\text{K)} = k_S(\vec{x}, T_S), \quad (12.4b)$$

$$C_{p,S} \text{ (J/kg}\cdot\text{K)} = C_{p,S}(\vec{x}, T_S), \quad (12.4c)$$

where  $\rho_S(\vec{x}, T_S)$ ,  $k_S(\vec{x}, T_S)$ , and  $C_{p,S}(\vec{x}, T_S)$  are the specified functions for density, thermal conductivity, and isobaric specific heat capacity, respectively. These functions may be dependent on the spatial coordinate and temperature by parameterizing in the time coordinate  $t$ .

## 12.5 Electric Graphite

Sigri Al 2-500 electric graphite density, thermal conductivity, and isobaric specific heat are given as [48, 175]

$$\rho_S \text{ (kg/m}^3\text{)} = 1673, \quad (12.5a)$$

$$k_S \text{ (W/m}\cdot\text{K)} = (2.5738 \times 10^4) T_S^{-0.86367}, \quad (12.5b)$$

$$C_{p,S} \text{ (J/kg}\cdot\text{K)} = 4184 \left( 0.5421 - 2.4267 \times 10^{-6} T_S - \frac{90.273}{T_S} - \frac{43449}{T_S^2} + \frac{1.5931 \times 10^7}{T_S^3} - \frac{1.4369 \times 10^9}{T_S^4} \right), \quad (12.5c)$$

where Eq. (12.5c) is based on a data for a variety of types of graphite and is used for the Sigri Al 2-500 due to a lack of other data. Eq. (12.5b) is valid for  $373 \text{ K} \leq T_S \leq 1273 \text{ K}$ .

## 12.6 Matrix Graphite

Matrix graphite density, thermal conductivity, and isobaric specific heat capacity are given as [48, 175]

$$\rho_S \text{ (kg/m}^3\text{)} = 1632, \quad (12.6a)$$

$$k_S \text{ (W/m}\cdot\text{K)} = -22.05679 \ln(T_S) + 194.32788, \quad (12.6b)$$

$$C_{p,S} \text{ (J/kg}\cdot\text{K)} = 4184 \left( 0.5421 - 2.4267 \times 10^{-6} T_S - \frac{90.273}{T_S} - \frac{43449}{T_S^2} + \frac{1.5931 \times 10^7}{T_S^3} - \frac{1.4369 \times 10^9}{T_S^4} \right), \quad (12.6c)$$

where Eq. (12.5c) is based on a data for a variety of types of graphite and is used for the matrix graphite due to a lack of other data. Eq. (12.6b) is valid for  $292 \text{ K} \leq T_S \leq 1574 \text{ K}$ .

## 12.7 Porous Graphite

Porous graphite refers to low-density graphite typically used in the buffer layer of TRISO particles. Porous graphite density, thermal conductivity, and isobaric specific heat capacity are given as [5, 58]

$$\rho_S \text{ (kg/m}^3\text{)} = 1000 , \quad (12.7a)$$

$$k_S \text{ (W/m}\cdot\text{K)} = 0.5 , \quad (12.7b)$$

$$C_{p,S} \text{ (J/kg}\cdot\text{K)} = 720 . \quad (12.7c)$$

The dependence of thermal properties on the gas composition within the graphite voids is not considered. The same or slightly different values for  $\rho_S$ ,  $k_S$ , and  $C_{p,S}$  have been measured or used elsewhere [5, 58, 59, 106, 176–179], with the except of large differences in specific heat [58, 178] and thermal conductivity [180].

## 12.8 Pyrolytic Graphite

Pyrolytic graphite is formed by Chemical Vapor Deposition (CVD) and used in the inner and outer graphite layers surrounding the silicon carbide layer in TRISO particles. Pyrolytic graphite density, thermal conductivity, and isobaric specific heat capacity are given as

$$\rho_S \text{ (kg/m}^3\text{)} = 1900 , \quad (12.8a)$$

$$k_S \text{ (W/m}\cdot\text{K)} = 4.0 , \quad (12.8b)$$

$$C_{p,S} \text{ (J/kg}\cdot\text{K)} = 720 . \quad (12.8c)$$

The same or slightly different values for  $\rho_S$ ,  $k_S$ , and  $C_{p,S}$  have been measured or used elsewhere [5, 58, 59, 106, 176–178, 180–183], though some experimental measurements for thermal conductivity suggest values approximately half that in Eq. (12.8b) [178, 179, 181–183]. This discrepancy may be attributable to the assumption that the inner and outer layers have the same properties despite annealing of the inner layer during the silicon carbide deposition process [180, 183].

## 12.9 Silicon Carbide

Monolithic silicon carbide is formed by CVD and is the main integrity layer in TRISO particles. Silicon carbide density, thermal conductivity, and isobaric specific heat capacity are given as

$$\rho_S \text{ (kg/m}^3\text{)} = 3216 , \quad (12.9a)$$

$$k_S \text{ (W/m}\cdot\text{K)} = \begin{cases} \left( -0.0003 + 1.05 \times 10^{-5} T_S \right)^{-1} & \text{Snead model} \\ \frac{17885}{T_S} + 2 & \text{PARFUME model} \end{cases} , \quad (12.9b)$$

$$C_{p,S} \text{ (J/kg}\cdot\text{K)} = 925.65 + 0.3772 T_S - 7.9259 \times 10^{-5} T_S^2 - 3.1946 \times 10^7 T_S^{-2} . \quad (12.9c)$$

Eq. (12.9c) is valid for  $200 \text{ K} \leq T_S \leq 2400 \text{ K}$  [184]. The same or slightly different values for  $\rho_S$  and  $C_{p,S}$  have been measured or used elsewhere [58, 106, 176, 184]. Two thermal conductivity models are available to cover the wider range in measurements observed [58, 59, 177–179, 184].

## 12.10 Stainless Steel 316

Stainless steel 316 density, thermal conductivity, and isobaric specific heat capacity are given as [185]

$$\rho_S \text{ (kg/m}^3\text{)} = 7863 , \quad (12.10a)$$

$$k_S \text{ (W/m}\cdot\text{K)} = 15.17 + 13.3 \frac{T_S - 273}{1000} , \quad (12.10b)$$

$$C_{p,S} \text{ (J/kg}\cdot\text{K)} = \frac{7.8 \times 10^6}{\rho_S} \left( 0.4533 + 0.382 \frac{T_S - 273}{1000} \right) . \quad (12.10c)$$

Eq. (12.10b) is valid for  $173 \text{ K} < T_S < 1023 \text{ K}$  and Eq. (12.10c) is valid for  $T_S < 1473 \text{ K}$ .

## 12.11 Uranium Dioxide

UO<sub>2</sub> density, thermal conductivity, and isobaric specific heat capacity are given as [186]

$$\rho_S \text{ (kg/m}^3\text{)} = 10970 \left( 1.0056 - 1.6324 \times 10^{-5} T_S - 8.3281 \times 10^{-9} T_S^2 + 2.0176 \times 10^{-13} T_S^3 \right) , \quad (12.11a)$$

$$k_S \text{ (W/m}\cdot\text{K)} = \begin{cases} \frac{100}{6.8337 + 1.6693 \times 10^{-2} T_S + 3.1885 \times 10^{-6} T_S^2} + 0.12783 T_S e^{-13475.11144/T_S} & T_S < 2670 \\ 4.1486 - 2.2673 \times 10^{-4} T_S & \text{else} \end{cases} , \quad (12.11b)$$

$$C_{p,S} \text{ (J/kg}\cdot\text{K)} = \begin{cases} C_1 a_1^2 \frac{e^{a_1/T_S}}{\left[ T_S (e^{a_1/T_S} - 1) \right]^2} + 2C_2 T_S + C_3 a_2 e^{-a_3/T_S} \left[ 1 + (T_S - 298.15) \frac{a_3}{T_S^2} \right] & T_S < 2670 \\ 167 & \text{else} \end{cases} , \quad (12.11c)$$

where  $a_1 = 516.11$ ,  $a_2 = 8.6144 \times 10^{-5}$ ,  $a_3 = 1.8815/a_2$ ,  $C_1 = 78.212$ ,  $C_2 = 3.8616 \times 10^{-3}$ , and  $C_3 = 3.3993 \times 10^8$ . Eq. (12.11) is valid for  $298 \text{ K} \leq T_S \leq 3120 \text{ K}$ .

## 13 Heterogeneous Solid Properties

This section describes models available for the mesoscale thermal properties in the HSD method and how properties of multi-layer homogeneous solids are combined together to give pebble-averaged properties. It is assumed that average properties of a mixture or multi-layer solid can be obtained as some combination of the properties of the individual, pure, materials. This simplification neglects differences in microstructure between the pure components and the mixture, which can be significant. For example, pure matrix graphite tends to be highly anisotropic, while the matrix graphite in final manufacture form in pebbles and compacts has a microstructure more conducive to heat transfer. Assuming the matrix graphite in a fabricated pebble has the same properties as the source matrix graphite material may significantly underpredict the average pebble thermal conductivity [187]. A similar example can be found in FCM fuels, where the effective thermal conductivity increases with additional sintering additives, despite the fact that the thermal conductivity of these additives is lower than the material they displace [188]. Hence, manufacturing conditions have as significant an impact on the effective properties as does the mixing method. Experimental measurements of effective thermal properties, if available, are preferred to the closures described in this section. It is also assumed that all of the materials to be mixed are at the same temperature.

Many models have been developed to evaluate average material properties for solid-solid mixtures such as CFPs dispersed in a matrix material. Most of the theoretical basis for these models is based on the notion of transport. While some authors use the same mixing models for all thermal properties [56], most use different models for thermal conductivity than for density and isobaric specific heat capacity.

Fig. 16 shows the ratio of the predicted to measured effective thermal conductivity as a function of the dispersed phase packing fraction for the models available in Pronghorn. The experimental data representing the measured effective thermal conductivity is obtained from Lee et. al for FCM fuels [188]; Gonzo for un-heated composites [162]; and Liu et. al for simulations of unheated fuel compacts [60]. Data points are only shown for the thermal conductivity ratios of less than 70 between the dispersed and continuous phases to reflect ranges expected in nuclear applications. Each line represents a linear fit to the predicted to measured conductivity ratio for the five models.

A predicted to measured ratio of unity indicates perfect prediction of the mixed thermal conductivity. For the range of porosity data shown, the effective thermal conductivity is bounded by series and parallel methods. A parallel mixing provides a much better approximation to experimental data than the series model, though preference for overprediction or underprediction of effective thermal conductivity may also guide mixing rule selection. The more refined models from Maxwell, Lewis and Nielsen, and Chiew and Glandt generally predict the experimental data to within 10%.

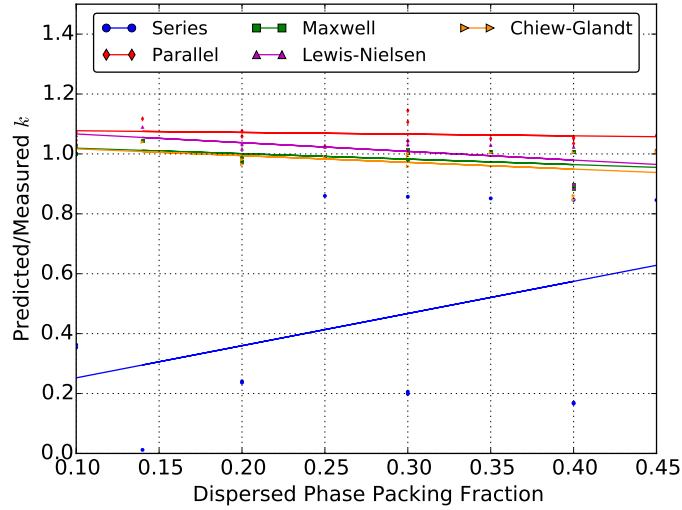


Figure 16: Ratio of predicted to measured effective thermal conductivity data as a function of dispersed phase packing fraction based on the data from Lee et. al, Gonzo, and Liu et. al [60, 162, 188].

In the absence of a heat source, the dependence of effective thermal conductivity on the degree of particle clustering is very weak, with a standard deviation less than 1% [60]. Most mixing models are also developed for unheated composites; strongly nonlinear temperature dependence in material properties will affect effective properties, but are not considered here. The remainder of this section describes models for

Consider a mixture of materials  $i$  for  $i = 1 \dots N$  each with a phase fraction  $\epsilon_i$  and generic property  $x_i$ . These phase fractions sum to unity. The following sections describe a number of different models for mixing these properties to obtain an effective homogenized property for an arbitrary number of mixed materials in Section 13.1 and for binary systems in Section 13.2.

The models described in this section are used to mix a number of pure component materials. If a component itself is heterogeneous, such as the dispersed CFP phase in a binary solid-solid mixing model, properties are averaged on the fine scales before next averaging on the coarser scales. For example, the average thermal conductivity of a fuel pebble would be the average of the homogeneous graphite shell properties and the fuel-matrix properties. The fuel-matrix properties are determined as an average of the CFP properties and the matrix, where the averaged CFP properties are determined as an average over the CFP layers.

## 13.1 Arbitrary Component Numbers

This section describes mixing models applicable to systems with arbitrary  $N$ .

### 13.1.1 Parallel

The parallel combination gives

$$\frac{1}{x} = \sum_{i=1}^N \frac{\epsilon_i}{x_i} . \quad (13.1)$$

### 13.1.2 Series

The series combination gives

$$x = \sum_{i=1}^N \epsilon_i x_i . \quad (13.2)$$

A series combination is the most commonly-used mixing method due to its equivalence to volume weighting [54, 55].

## 13.2 Binary Systems

This section describes mixing models applicable to binary systems, for which  $N = 2$ . Such binary systems consist of a single dispersed phase with phase fraction  $\epsilon_d$  in a single continuous phase with phase fraction  $\epsilon_c \equiv 1 - \epsilon_d$ .

### 13.2.1 Chiew and Glandt

Chiew and Glandt extended Maxwell's formulation in Section 13.2.3 to order  $\epsilon_d^2$ ; with the non-constant fitting coefficients suggested by Gonzo, the Chiew and Glandt formulation can be made correct to order  $\epsilon_d^3$  [162],

$$x = x_c \frac{1 + 2\beta_n \epsilon_d + (2\beta_n^3 - 0.1\beta_n) \epsilon_d^2 + 0.05\epsilon_d^3 \exp(4.5\beta_n)}{1 - \beta_n \epsilon_d} , \quad (13.3)$$

where  $\beta_n$  is defined as

$$\beta_n \equiv \frac{x_d - x_c}{x_d + 2x_c} . \quad (13.4)$$

Eq. (13.3) has shown good agreement with experimental data for prediction of effective thermal conductivity for heated and unheated CFP compacts [56, 60]. Folsom et. al observed the best agreement between the effective thermal conductivity of the fuel-matrix region of CFP fuel compacts with Eq. (13.3) when the dispersed phase thermal conductivity is obtained from a sophisticated twelve-equation model [187].

### 13.2.2 Lewis and Nielsen

Lewis and Nielsen developed an averaging model for thermal conductivity accounting for the shape of the dispersed phase and its packing fraction; for rigid spheres,  $x$  is given as [189, 190]

$$x = x_c \frac{1 + 1.5B_n \epsilon_d}{1 - B_n \epsilon_d \left( 1 + \frac{1 - \epsilon_{\max}}{\epsilon_{\max}^2} \epsilon_d \right)} , \quad (13.5)$$

where  $B_n$  is defined as

$$B_n \equiv \frac{x_d/x_c - 1}{x_d/x_c + 1.5} , \quad (13.6)$$

and  $\epsilon_{\max}$  is the maximum packing density, assumed to be 0.637 corresponding to random close packing of spheres [189, 190]. A comparison of many models against experimental data suggests that Eq. (13.5) provides the best overall agreement with effective thermal conductivity of non-heated solid-solid mixtures [190].

### 13.2.3 Maxwell

From potential theory, Maxwell developed an exact solution for the effective conductivity of randomly-distributed, non-interacting, dispersed spheres as [190]

$$x = x_c \frac{x_d + 2x_c + 2\epsilon_d(x_d - x_c)}{x_d + 2x_c - \epsilon_d(x_d - x_c)} . \quad (13.7)$$

Due to the assumption of non-interacting dispersed phase spheres, Eq. (13.7) should only be used for dispersed phase packing fractions less than approximately 10% [162, 187]. Eq. (13.7) has been used for analysis of FCM fuels and unheated compacts [60, 188], as well as in the PARTicle FUEl ModEl (PARFUME) fuels modeling code with the additional assumption that  $k_d \approx 0$  despite the frequent underprediction of the true effective thermal conductivity [187].

## 14 The Finite Element Method

This section discusses the spatial discretization used for the governing equations described in Section 2. The temporal discretization is discussed in Section 16. A comprehensive description of the Finite Element Method (FEM) is beyond the scope of this manual, but a brief discussion is given here to introduce the more important terminology and concepts associated with weighted residual methods necessary to understand the stabilization methods described in Section 15. Additional information is available in the rich literature on the subject, such as in the cited references [191–193]. A brief discussion on the choice of element size with regards to the porous media method is also given.

### 14.1 Weighted Residual Methods and the Galerkin Method

A weighted residual method seeks an approximate solution to a differential equation with the assumed form

$$u = \sum_{j=1}^N C_j \phi_j , \quad (14.1)$$

where  $u$  is the approximate solution,  $C$  are coefficients,  $\phi$  are functions, and  $N$  is the number of terms in the summation. The functions  $\phi$  are often referred to as “shape” functions. Any differential equation can in general be expressed as

$$K(u_*) = f , \quad (14.2)$$

where  $K$  is an operator that acts on the true solution  $u_*$  and  $f$  is a function that does not contain  $u_*$ . The approximation in Eq. (14.1) is in general not the true solution such that the residual  $R$  is nonzero,

$$R \equiv K(u) - f . \quad (14.3)$$

A weighted residual method can be constructed by minimizing the residual with respect to a particular norm; the choice of this norm determines the particular method. This minimization process can be written as

$$\min_{\{C_j\} \text{ for } j \in N} \int_{\Omega} R^* \zeta d\Omega , \quad (14.4)$$

where  $\zeta$  is a function whose form is determined by the particular norm to be minimized,  $\Omega$  represents the phase space, and a \* superscript indicates the Hermitian complex conjugate. Eq. (14.4) states that the integral is to be minimized with respect to each of the  $N$  coefficients  $C_j$ . Minimization can also be expressed in terms of the zero of the derivative of Eq. (14.4) with respect to each coefficient,

$$\int_{\Omega} \frac{\partial}{\partial C_j} (R^* \zeta) d\Omega = 0 \quad \text{for } j \in N , \quad (14.5)$$

where differentiation was brought inside the integral because the bounds of the domain are assumed fixed and the residual is assumed real. As an example, if minimization is based on the square of the  $L^2$  norm of the residual, Eq. (14.4) becomes

$$\min_{\{C_j\} \text{ for } j \in N} \int_{\Omega} R^* R d\Omega , \quad (14.6)$$

and Eq. (14.5) becomes

$$\int_{\Omega} 2R \frac{\partial R}{\partial C_j} d\Omega = 0 \quad \text{for } j \in N. \quad (14.7)$$

Eq. (14.7) represents  $N$  equations for the  $N$  unknown coefficients; this method is referred to as the “Method of Least Squares” because it is based on minimizing the square of the  $L^2$  norm of the residual. The weighted residual method was first introduced as a minimization in Eq. (14.4) that was rewritten in Eq. (14.5) for a particular choice of  $\zeta$ . All weighted residual methods, including the Method of Least Squares, may be written in general form as

$$\int_{\Omega} R^* \psi d\Omega = 0, \quad (14.8)$$

where  $\psi$  is a weight function, also sometimes called a “test” function, that acts to weight the residual in an integral sense. The Galerkin method chooses  $\psi$  in an attempt to minimize the error  $e$ , defined as

$$e \equiv u_* - u. \quad (14.9)$$

The true solution may not lie in the same space as the numerical approximation in Eq. (14.1), so zero error is generally not achievable. However, the error is minimized when  $e$  is orthogonal to  $u$ , which may be expressed as

$$\int_{\Omega} e^* u d\Omega = 0. \quad (14.10)$$

The error is not known unless the true solution is known, so Eq. (14.10) does not provide a useful condition. However, a good approximation of the error is the residual, since the residual is zero when the error is also zero. The Galerkin method seeks to minimize the residual by requiring that it be orthogonal to the approximate solution  $u$ ,

$$\int_{\Omega} R^* u d\Omega = 0. \quad (14.11)$$

In other words, the weight function  $\psi$  in Eq. (14.8) lies in the same space as the numerical solution  $u$ . Eq. (14.11) represents a single condition; to extend to  $N$  equations for the  $N$  coefficients in  $u$  requires that Eq. (14.11) hold for each linearly independent term  $C_j \phi_j$  in  $u$ ,

$$\int_{\Omega} R^* (C_j \phi_j) d\Omega = 0 \quad \text{for } j \in N. \quad (14.12)$$

## 14.2 The Finite Element Method

The FEM is an application of the Galerkin weighted residual method given in Eq. (14.12) with specific requirements for 1) reduced differentiability requirements on  $\phi$ ; 2) the interpolation functions  $\phi$ ; and 3) BC specification. In addition, as the name implies, the FEM is an application of the Galerkin weighted residual method to a domain discretized into a number of elements. Fig. 17 shows an illustration of a continuous domain that has been discretized into triangular elements. One triangular element is highlighted.

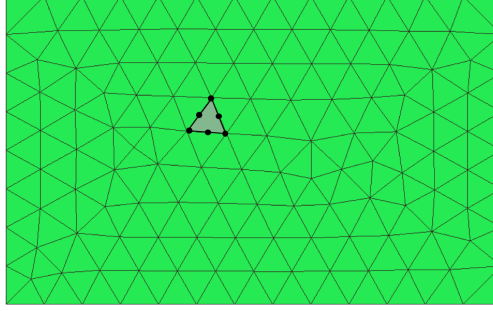


Figure 17: Illustration of a continuous domain discretized into triangular finite elements.

Section 14.2.1 introduces the concept of a weak form that is used to reduce differentiability requirements. Next, Section 14.2.2 describes the selection of  $\phi$  and BCs in terms of the nodes, shown as black dots, in Fig. 17. Section 14.2.3 briefly discusses some numerical implementation considerations. Section 14.2.4 closes with a discussion of the time discretization.

### 14.2.1 The Weak Form

Many solutions to physical problems are not continuously differentiable, such as shock waves in fluid dynamics. When the higher-order derivatives in the operator  $A$  are integrated in the weighted residual statement, infinite or singular values may result. For example, consider the following general differential equation:

$$-\alpha \frac{\partial^2 u_*}{\partial x^2} + \frac{\partial u_*}{\partial x} - f(x) = 0. \quad (14.13)$$

Applying the Galerkin method in Eq. (14.11) with  $u$  understood to be in the same space as  $\psi$  gives

$$\int_{\Omega} \psi \left[ -\alpha \frac{\partial^2 u}{\partial x^2} + \frac{\partial u}{\partial x} - f(x) \right] d\Omega = 0. \quad (14.14)$$

To ensure that Eq. (14.14) remains finite,  $\tilde{u}$  must be second order differentiable or higher. Reduced differentiability requirements can be achieved by integrating Eq. (14.14) by parts,

$$\int_{\Omega} \alpha \frac{\partial u}{\partial x} \frac{\partial \psi}{\partial x} d\Omega - \int_{\Gamma} \alpha \frac{\partial u}{\partial x} \cdot \hat{n} \psi d\Gamma + \int_{\Omega} \psi \frac{\partial u}{\partial x} d\Omega = \int_{\Omega} f(x) \psi d\Omega \quad \forall \psi \quad (14.15)$$

Eq. (14.15) is referred to as a “weak form,” and it must hold for all choices of  $\psi$  to ensure equivalence with Eq. (14.14). The FEM involves solution of Eq. (14.15), rather than Eq. (14.14).

Because  $u$  and  $\psi$  live in the same function space, inserting Eq. (14.1) for both  $u$  and  $\psi$  into Eq. (14.15) (with different coefficients for  $\psi$  than for  $u$ ) more clearly illustrates the system of  $N$  equations for the  $N$  coefficients in  $u$ ,

$$\sum_{i=1}^N \sum_{j=1}^N C_j \left[ \int_{\Omega} \alpha \frac{\partial \phi_j}{\partial x} \frac{\partial \phi_i}{\partial x} d\Omega - \int_{\Gamma} \alpha \frac{\partial \phi_j}{\partial x} \cdot \hat{n} \phi_i d\Gamma + \int_{\Omega} \phi_i \frac{\partial \phi_j}{\partial x} d\Omega \right] = \sum_{i=1}^N \int_{\Omega} f(x) \phi_i d\Omega. \quad (14.16)$$

The coefficients in the expansion for  $\psi$  cancel from every term because  $\psi$  is in each term in Eq. (14.15).

## 14.2.2 Shape and Test Functions

The FEM prescribes specific requirements for the shape functions  $\phi$  related to the boundary integrals in the weak form. The boundary term in Eq. (14.15) is an integral over the entire boundary of the domain. On some portions of this boundary, the flux  $\alpha \nabla u \cdot \hat{n}$  may be unknown — rather, the value of  $u$  might be known. Rather than back-calculating the flux that results in the desired boundary value of  $u$ , it is simpler to require  $\psi$  to be zero on Dirichlet boundaries.

If  $\psi$  and  $\phi$  are nonzero over the entire domain  $\Omega$ , every region of the problem is tightly coupled to all other regions, producing a dense matrix system once discretized. To achieve a sparse matrix system, an additional requirement is placed on the shape functions  $\phi$  — they are selected as a nodal basis,

$$\phi_i(\Omega_j) = \delta_{ij} , \quad (14.17)$$

where  $\Omega_j$  is the coordinate describing the location of the  $j$ -th node. The number of nodes on the element is equal to the number of shape functions used to represent the numerical solution on that element, and hence the number of unknown coefficients corresponding to that element. Therefore, each shape function is unity at a single node and zero at all other nodes such that shape functions are local to an element and its immediate neighbors. A nodal basis also ensures continuity along element edges.

In principle, there are an infinite number of functions that satisfy Eq. (14.17). To ensure finite integrals in the weak form, all shape functions must be sufficiently differentiable. Define the Hilbert-space norm in 1-D for a function  $\chi$  as

$$\|\chi\|_{H^l(\Omega)} \equiv \left[ \sum_{j=0}^l \int_{\Omega} \frac{\partial^j \chi}{\partial x^j} \frac{\partial^j \chi}{\partial x^j} d\Omega \right]^{1/l} , \quad (14.18)$$

where  $l$  is an integer. For a weak form with highest derivative  $l$  on either  $u$  or  $\psi$ , finite integrals are ensured if

$$\|u\|_{H^l(\Omega)} < \infty , \quad (14.19a)$$

$$\|\psi\|_{H^l(\Omega)} < \infty , \quad (14.19b)$$

which may also be expressed as  $u \in H^l(\Omega)$  and  $\psi \in H^l(\Omega)$ . In simpler terms, the highest derivative appearing in the weak form must be finite.

The most common shape functions used in the FEM are the Lagrange, Hermite, and Spline shape functions. Lagrange shape functions, the default in MOOSE, are polynomials that interpolate between nodes. The “order” of a Lagrange basis refers to the order of the polynomial in each element; a linear, or first-order, interpolation is the default.

## 14.2.3 Software Implementation Considerations

The shape functions discussed in Section 14.2.2 are tedious to compute for each element due to their unique locations in space because the node coordinates are interpolated by polynomials. Each element in the physical domain exists over a unique  $x_{1,min} \leq x_1 \leq x_{1,max}$ ,  $x_{2,min} \leq x_2 \leq x_{2,max}$ ,  $x_{3,min} \leq x_3 \leq x_{3,max}$ , where  $x_{i,min/max}$  is the lower or upper bound of the element’s physical span in the  $x_i$  direction. A more efficient implementation defines all shape functions on a “master” element extending over  $-1 \leq \xi_1 \leq 1$ ,  $-1 \leq \xi_2 \leq 1$ ,  $-1 \leq \xi_3 \leq 1$ , with mappings performed to and from the physical domain to relate integrals on the physical domain that appear in the weak form to integrals on the master domain. This mapping is given by

$$d\vec{x} = |\mathcal{J}| d\vec{\xi}, \quad (14.20a)$$

$$dx_i = \frac{\partial x_i}{\partial \xi_j} d\xi_j, \quad (14.20b)$$

where  $\mathcal{J}$  is the deformation gradient. The determinant of  $\mathcal{J}$ , or  $|\mathcal{J}|$ , must be nonzero to obtain a reversible mapping. In a 1-D domain with equal-sized elements,  $|\mathcal{J}| = h_e/2$ , where  $h_e$  is the element size. A general volume integral in the physical domain is transformed to the master domain as

$$\int_{x_{3,min}}^{x_{3,max}} \int_{x_{2,min}}^{x_{2,max}} \int_{x_{1,min}}^{x_{1,max}} f(x_1, x_2, x_3) dx_1 dx_2 dx_3 = \int_{-1}^{+1} \int_{-1}^{+1} \int_{-1}^{+1} f(x_1(\xi_1, \xi_2, \xi_3), x_2(\xi_1, \xi_2, \xi_3), x_3(\xi_1, \xi_2, \xi_3)) |\mathcal{J}| d\xi_1 d\xi_2 d\xi_3. \quad (14.21)$$

Surface integrals transform as

$$dx_1 dx_2 = \left( |\mathcal{J}| \mathcal{J}^{-T} \cdot \hat{n}_x \right) \cdot \hat{n}_\xi d\xi_1 d\xi_2, \quad (14.22)$$

where the boundary is arbitrarily represented as a 2-D integration and  $\hat{n}_x$  and  $\hat{n}_\xi$  are unit vectors to the surfaces in the physical and master domains, respectively. The mapping  $x_i(\xi_1, \xi_2, \xi_3)$  can take a variety of forms, but is generally categorized into three main types —

1. Subparametric - the mapping is of lower order than the shape functions. This mapping is used when the physical data is of lower-order than the desired solution order.
2. Isoparametric - the mapping is of the same order as the shape functions. This mapping, which tends to be the most commonly-used, is usually performed using the shape functions of the numerical solution,

$$x_i(\xi_1, \xi_2, \xi_3) = \sum_{i=1}^N X_i \phi_i(\xi_1, \xi_2, \xi_3), \quad (14.23)$$

where  $X$  are the physical node coordinates and  $\phi$  are the basis functions used in the numerical solution.

3. Superparametric - the mapping is of higher order than the shape functions. This type of mapping is used to capture physically-curved geometries without needing to use high-order shape functions. In other words, linear elements can be used to obtain the solution in curved domains, but the domain is approximated using higher-order mappings.

Quadrature rules are used for approximating the weak form integrals by integrand evaluations at  $n_{qp}$  quadrature points,

$$\int_a^b f(x) dx = \sum_{i=1}^{n_{qp}} w_i f(x_i), \quad (14.24)$$

where  $w$  are weights. Many quadrature rules, such as Simpson's rule and the trapezoid rule, can be derived by first interpolating the integrand as a polynomial, and then integrating that polynomial exactly.

Rather than compute integrals over the entire domain  $\Omega$  as suggested by Eq. (14.15), the weak form is evaluated on each element on the master domain, transformed to the physical domain, and then assembled into a linear system

of equations that can be solved with the techniques described in Section 16. This assembly of local element matrices into a global matrix system is now briefly described. Fig. 18 shows a four-element domain with global node numbers in gray circles. Local element node numbers are shown in red.

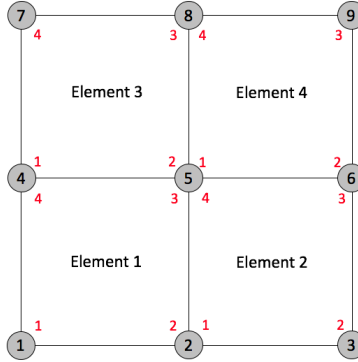


Figure 18: Four-element mesh with nine global nodes shown in gray circles and four local nodes per element shown as red numbers.

The local to global mapping is performed by constructing a data table that relates the element local node numbers to the global node numbers. For the mesh in Fig. 18, this data table is

$$\mathbf{D}_{lg} = \begin{matrix} & 1 & 2 & 4 & 5 \\ \begin{matrix} 1 \\ 2 \\ 5 \\ 4 \end{matrix} & 5 & 6 & 8 & 9 \end{matrix}, \quad (14.25)$$

where the local-to-global map table is referred to as  $\mathbf{D}_{lg}$ . Each column pertains to an element, while each row pertains to the local node numbering scheme. The  $i, e$  entry is the global node number corresponding to the local node number  $i$  for element  $e$ . In a loop over each element (loop in  $e$ ), the weak form is evaluated and the  $i, j$  entry added to the  $\mathbf{D}_{lg}(i, e), \mathbf{D}_{lg}(j, e)$  entry of the global matrix, for  $i = 1 \cdots N$  and  $j = 1 \cdots N$ .

#### 14.2.4 Time Stepping

The MOOSE framework uses separable space-time shape functions; the shape functions are only functions of space, while the expansion coefficients  $C$  in Eq. (14.1) are time-dependent. This approach is often referred to as the Method of Lines (MOL) time discretization. The solution is marched forward in time using the wide variety of Ordinary Differential Equation (ODE) solvers in the Portable, Extensible Toolkit for Scientific Computation (PETSc). The MOL approach is now briefly described for the 1-D time-dependent diffusion equation,

$$\frac{\partial u}{\partial t} - k \frac{\partial^2 u}{\partial x^2} = 0, \quad (14.26)$$

where  $u$  is a generic transported quantity. The weak form is

$$\mathbf{M} \frac{\partial \vec{C}}{\partial t} + \mathbf{K} \vec{C} = 0, \quad (14.27)$$

where  $\vec{C}$  is the vector of expansion coefficients in Eq. (14.1),  $\mathbf{M}$  is the mass matrix with components given by

$$M_{ij} = \int_{\Omega} \phi_i \phi_j dx , \quad (14.28)$$

and  $\mathbf{K}$  is the stiffness matrix with components given by

$$K_{ij} = \int_{\Omega} \frac{\partial \phi_i}{\partial x} k \frac{\partial \phi_j}{\partial x} dx . \quad (14.29)$$

BCs are omitted for simplicity. The MOL discretization replaces  $\dot{\vec{C}}$ , or the time derivative of the expansion coefficients, with a FD approximation of the time derivative. For example, using a Backward Euler (BE) time discretization in Eq. (14.27) gives

$$\mathbf{M} \frac{\vec{C}_{n+1} - \vec{C}_n}{\Delta t} + \mathbf{K} \vec{C}_{n+1} = 0 , \quad (14.30)$$

where  $n$  subscripts indicate the time step. The solution at each successive time step is obtained by solving for  $\vec{C}_{n+1}$  in terms of  $\vec{C}_n$ .



$$(-Pe_{el} - 1)C_{n-1} + 2C_n + (Pe_{el} - 1)C_{n+1} = 0, \quad (15.6)$$

where  $C_n$  is the expansion coefficient corresponding to the  $n$ -th node. Inserting Eq. (15.5) with the Peclet number definition from Eq. (2.132) into Eq. (15.6) gives

$$-\alpha \frac{u_{n+1} - 2u_n + u_{n-1}}{h_e^2} + V \frac{u_{n+1} - u_{n-1}}{h_e} = 0, \quad (15.7)$$

which illustrates that the FEM with linear Lagrange shape functions applies to a constant-coefficient advection-diffusion equation with uniform elements in 1-D is equivalent to central FD on the first and second derivatives.

The continuous FEM is unstable for  $Pe_{el} > 1$ ; above this threshold in  $Pe_{el}$ , Eq. (15.6) gives a purely oscillatory (nonphysical) numerical solution. Assuming the characteristic solution for  $C_j = m^j$ , where  $m$  is an integer, Eq. (15.6) gives two possible values for  $m$ , and hence two possible solutions for  $C_j$  —

$$C_j = 1^j, \quad (15.8a)$$

$$C_j = \left( -\frac{Pe_{el} + 1}{Pe_{el} - 1} \right)^j. \quad (15.8b)$$

If  $Pe_{el} > 1$ , Eq. (15.8b) oscillates due to the alternating powers of  $j$ . While these stability results may appear to be tied to the rather specific 1-D convection diffusion equation selected in Eq. (15.1), the instability can be shown to be related to the observation that convection operators are not self-adjoint, while diffusion operators are self-adjoint [191].

To show that Eq. (15.1) is not self-adjoint, write the weak form of Eq. (15.1) with the divergence rule also applied to the convective term,

$$\int_0^L \left( \alpha \frac{\partial \psi}{\partial x} \frac{\partial u}{\partial x} - V \psi \frac{\partial u}{\partial x} \right) dx + \left( Vu - \alpha \frac{\partial u}{\partial x} \right) \cdot \hat{n} \psi \Big|_0^L = 0. \quad (15.9)$$

Reverse-integrate the first term by parts to write the diffusion term in the same form as the strong form, but with  $u$  and  $\psi$  interchanged relative to Eq. (15.1),

$$-\int_0^L \alpha \frac{\partial^2 \psi}{\partial x^2} u dx = \int_0^L \alpha \frac{\partial \psi}{\partial x} \frac{\partial u}{\partial x} dx - \alpha \frac{\partial \psi}{\partial x} u \cdot \hat{n} \Big|_0^L. \quad (15.10)$$

Substituting Eq. (15.10) into Eq. (15.9) gives

$$\int_0^L \underbrace{\left( -\alpha \frac{\partial^2 \psi}{\partial x^2} - V \frac{\partial \psi}{\partial x} \right)}_{\text{adjoint of original problem}} u dx + \alpha \frac{\partial \psi}{\partial x} u \cdot \hat{n} \Big|_0^L + \left( Vu - \alpha \frac{\partial u}{\partial x} \right) \psi \cdot \hat{n} \Big|_0^L = 0. \quad (15.11)$$

The adjoint of the original problem has the opposite sign on the convective term but the same sign on the diffusive term, relative to the starting strong form in Eq. (15.1). Therefore, convective processes are non-self-adjoint, while diffusive processes are self-adjoint.

Convection-dominated instabilities generally manifest themselves as nodal oscillations. Fig. 19 shows the FE and exact solutions to Eq. (15.1). For  $Pe_{el} > 1$ , the solution is oscillatory, with the oscillation magnitude increasing with  $Pe_{el}$ . The oscillatory behavior in the vicinity of the downstream boundary is partly caused by the selection of the BCs, since steep gradients are restricted to narrower and narrower regions as  $Pe_{el} \rightarrow \infty$ . However, the numerical algorithm should still give stable and accurate results because as long as *some* diffusion is present, it is valid to specify BCs on all boundaries.

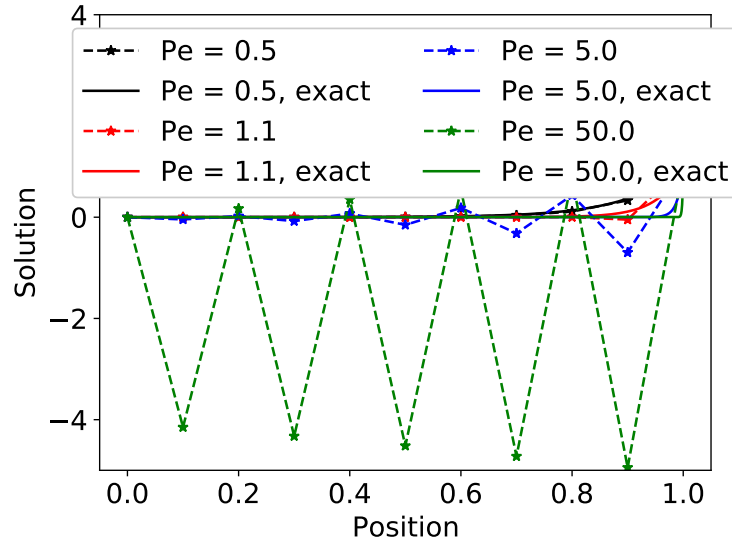


Figure 19: Solution to the the 1-D convection-diffusion problem in Eq. (15.1) with  $h_e = 0.1$  for various  $Pe_{el}$  with BCs of  $u(0) = 0, u(1) = 1$ . The exact solution for these BCs is  $u(x) = [1 - \exp(-Pe_{el}x/L)] / [1 - \exp(-Pe_{el})]$ .

In two dimensions, Fig. 20 shows a FE simulation of helium natural circulation in a closed cavity with a left wall temperature of 320 K and a right wall temperature of 280 K with adiabatic top and bottom boundaries and slip velocity BCs. The mesh used is a uniform  $25 \times 25$  mesh, which clearly illustrates nodal oscillations near the boundaries. These oscillations are nonphysical because the lack of heat sources in the domain should result in all temperatures lying between 280 and 320 K.

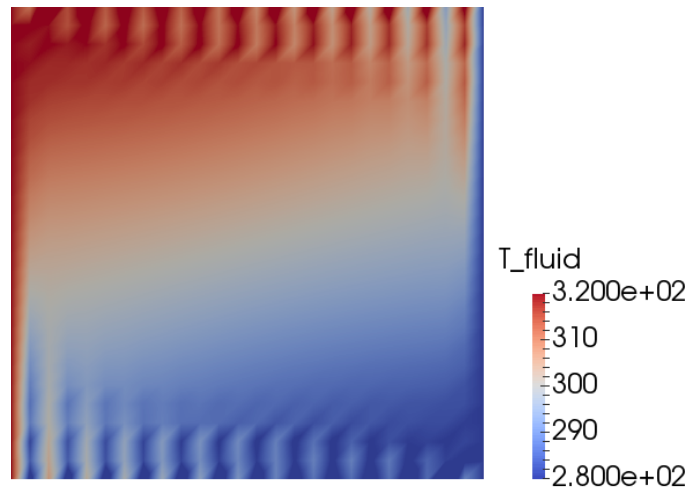


Figure 20: Pronghorn (non-stabilized) fluid temperature predictions for natural convection in an enclosed cavity with left wall temperature of 320 K and right wall temperature of 280 K, with insulated bottom and top boundaries.

As long as some diffusion is present, the mesh can in theory be refined until  $Pe_{el} < 1$ . However, this level of refinement is often prohibitively expensive for most problems.

Fig. 21 illustrates typical convective and diffusive processes transporting in both space and time. While diffusion is a symmetric phenomenon, convective processes translate in the direction of the velocity and are therefore not symmetric. For pure convection, the solution at a point is only dependent on the behavior upstream — a one-sided

phenomenon. The use of a symmetric discretization neglects these important differences between convective and diffusive phenomena, and is the origin of the continuous FEM instability for convection-diffusion equations. A reasonable hypothesis is that a stable discretization can be obtained if a non-symmetric discretization is used for the convective terms that better matches the physical effects of convection. The remainder of this section describes methods to achieve stable continuous FE simulations independent of  $Pe_{el}$ .

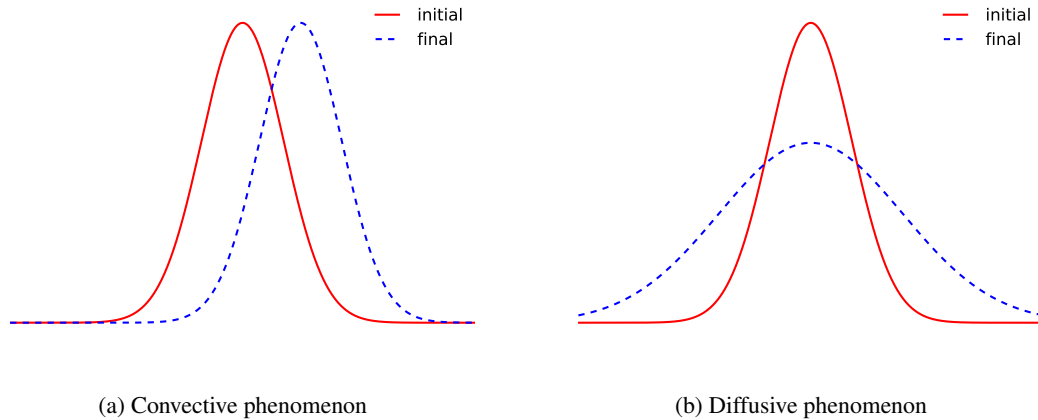


Figure 21: Difference between (a) convective (flow from left to right) and (b) diffusive mechanisms in transporting an initial condition to a new state an arbitrary amount of time later.

## 15.2 Upwinding and Petrov-Galerkin Methods

This section introduces the concept of upwinding, or modifying the discretization to more heavily weight upwind nodes to better capture the directionality of convective processes, and describes how Petrov-Galerkin schemes incorporate upwinding into the context of a weak form. Section 15.3 then discusses generalization of the methods introduced here to multi-dimensional, coupled systems of equations.

In a FD method, upwinding is easily achieved by replacing the central difference approximation to the convective derivative in Eq. (15.7) by a first-order upwind approximation,

$$\frac{\partial u}{\partial x} = \begin{cases} \frac{C_n - C_{n-1}}{h_e} & V > 0 \\ \frac{C_{n+1} - C_n}{h_e} & V < 0 \end{cases}, \quad (15.12)$$

while the symmetric discretization is retained for the diffusive term. Inserting Eq. (15.12) for the convective derivative in the nodal equation in Eq. (15.7) gives

$$(-2Pe_{el} - 1)C_{n-1} + (2Pe_{el} + 2)C_n + (-1)C_{n+1} = 0, \quad (15.13)$$

which has the following two solutions,

$$C_j = 1^j, \quad (15.14a)$$

$$C_j = (2Pe_{el} + 1)^j, \quad (15.14b)$$

neither of which are oscillatory. While upwinding eliminates the instability associated with  $Pe_{el}$ , upwinding does not necessarily give the correct solution. A fully upwind discretization of the convective term only gives nodally exact values for  $Pe_{el} = 0$ , purely diffusive systems, and  $Pe_{el} = \infty$ , purely convective systems. More importantly, an upwind approximation to the convective terms must be incorporated into the context of the weak form.

The shape functions  $\phi$  and weight functions  $\psi$  in the FEM described in Section 14 live in the same function space; this is often referred to as a Bubnov-Galerkin method. Alternatively, a Petrov-Galerkin method selects the shape and weight functions from different function spaces; this idea can be used to achieve upwinding within the context of a weak form.

Modify the weight function to be the sum of the original element-continuous weight functions  $\psi$ , and a discontinuous portion  $\psi^*$ ,

$$\tilde{\psi} = \psi + \alpha_{pg}\psi^* , \quad (15.15)$$

where  $\alpha_{pg}$  is a scaling parameter and  $\tilde{\psi}$  is the Petrov-Galerkin weight function. To show that this modification achieves upwinding in the weak form, insert Eq. (15.15) into the weak form in Eq. (15.9),

$$\int_0^L \left( \alpha \frac{\partial \psi}{\partial x} \frac{\partial u}{\partial x} - Vu \frac{\partial \psi}{\partial x} \right) dx + \left( Vu - \alpha \frac{\partial u}{\partial x} \right) \cdot \hat{n} \psi \Big|_0^L + \underbrace{\int_0^L \alpha_{pg} \left( -\alpha \frac{\partial^2 u}{\partial x^2} + V \frac{\partial u}{\partial x} \right) \psi^* dx}_{\text{new term}} = 0 . \quad (15.16)$$

The last term on the RHS of Eq. (15.16) is new relative to Eq. (15.9). The element discontinuous portion  $\psi^*$  is restricted to element interiors by not integrating by parts; this avoids modifications to BCs or inter-element continuity. There are many choices for  $\psi^*$ ; a common choice is

$$\alpha_{pg}\psi^* = \frac{h_e}{2\|\vec{V}\|} \vec{V} \cdot \nabla \psi . \quad (15.17)$$

For linear Lagrange elements, Eq. (15.17) is equivalent to

$$\alpha_{pg}\psi^* = \begin{cases} \frac{h_e}{2} \left( \pm \frac{1}{2} \right) & V > 0 \\ -\frac{h_e}{2} \left( \pm \frac{1}{2} \right) & V < 0 \end{cases} , \quad (15.18)$$

where the + sign occurs upwind of the node and the - sign occurs downwind of the node. Inserting Eq. (15.17) into the weak form in Eq. (15.16) and assembling the nodal equation for an interior node gives Eq. (15.13). Therefore, the particular choice for  $\psi^*$  in Eq. (15.17) is equivalent to introducing a one-sided FD approximation of the convective derivative in the 1-D convection diffusion equation on equal-sized elements with linear Lagrange basis functions.

Further, by asserting that this problem be self-adjoint, it can be shown that nodally exact values are obtained through a minor modification of  $\alpha_{pg}\psi^*$  from Eq. (15.17) to [191]

$$\alpha_{pg}\psi^* = \frac{h_e}{2\|\vec{V}\|} \left( \coth |Pe_{el}| - \frac{1}{|Pe_{el}|} \right) \vec{V} \frac{\partial \psi}{\partial x} . \quad (15.19)$$

Any arbitrary choice of  $\alpha_{pg}$  in Eq. (15.15) is insufficient, but it can be shown that a threshold value exists in 1-D above which oscillations are eliminated. Fig. 22 shows the Petrov-Galerkin stabilized results for the same problem shown in Fig. 19 with  $\alpha_{pg}\psi^*$  given by Eq. (15.19); oscillations have been entirely removed.

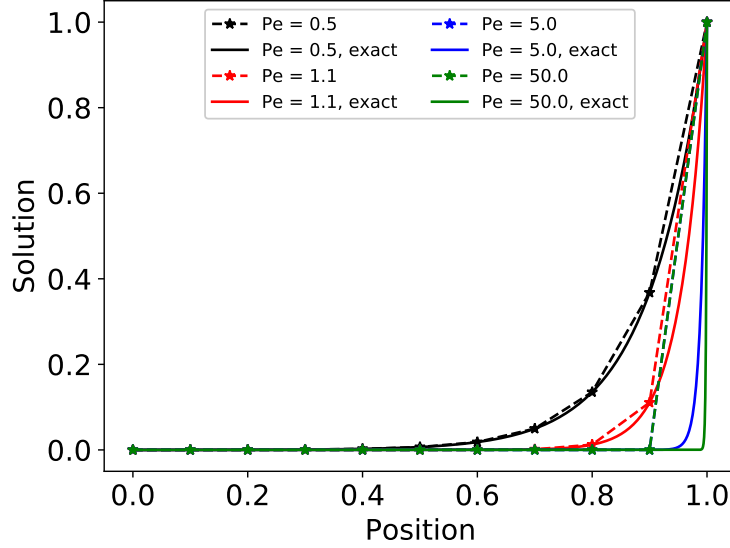


Figure 22: Solution to the 1-D convection-diffusion problem in Eq. (15.1) with  $\alpha_{pg}$  given by Eq. (15.19) and  $h_e = 0.1$  for various  $Pe_{el}$  with  $u(0) = 0, u(1) = 1$ . The exact solution is  $\phi(x) = [1 - \exp(Pe_{el}x/L)] / [1 - \exp(Pe_{el})]$ .

For diagonalizable systems of 1-D equations, the optimal upwinding in Eq. (15.19) may be applied; however, the Navier-Stokes equations are not in general diagonalizable, so Eq. (15.19) has rather limited utility [194].

If the perturbation  $\alpha_{pg}\Psi^*$  is added to each term in the weak form, the Petrov-Galerkin scheme is consistent — that is, the true solution is also a solution to the stabilized equation because the added domain integral is a weighted integral of the strong residual. Consistency requires that the shape functions used in the numerical solution are sufficiently high order to capture derivatives that are no longer integrated by parts in this additional term. For convection-diffusion problems, linear basis functions have a zero second derivative such that consistency cannot be achieved. However, this observation is of little practical consequence because applications for which  $Pe_{el} \gg 1$  are dominated by convection such that neglecting a diffusive strong kernel in the Petrov-Galerkin weak form has only a small impact on the overall accuracy.

Many other methods have been developed based on the notion of upwinding, but that are implemented in an inconsistent manner. For example, it can be shown that amplifying the diffusivity in the 1-D convection diffusion equation in Eq. (15.1) as

$$\alpha = \alpha + \frac{Vh_e}{2} \alpha_{pg} , \quad (15.20)$$

in the absence of other source terms and with a linear Lagrange discretization, is equivalent to a Petrov-Galerkin scheme with (15.17). This interpretation led many early researchers to seek stabilization by amplifying the diffusivity even for problems outside this range of applicability. This method, referred to as isotropic diffusion stabilization, is inconsistent and will result in excessive crosswind diffusion for multidimensional problems and in the presence of source kernels.

Others have attempted upwinding through the use of different quadrature rules and/or different element-continuous weight functions for the convective and diffusive terms. Similar to isotropic diffusion stabilization, these methods are frequently inconsistent [195].

### 15.3 Streamline-Upwind Petrov-Galerkin Stabilization

This section describes how upwinding is generalized to multidimensional systems of coupled equations with the SUPG method [195]. The SUPG method, introduced without motivation in Section 2.8.1, is one of the most commonly-used schemes for stabilizing FE discretizations of convection-diffusion equations.

The SUPG method is a Petrov-Galerkin scheme that is based on adding an element-discontinuous weight function to  $\psi$  to achieve upwinding in directions parallel to the velocity. The weak form for the coupled macroscale equations solved in Pronghorn was provided in Eq. (2.119); the additional integral arising from the SUPG is repeated here for reference,

$$\int_{\Omega} \varepsilon \left\{ \mathbf{A}_i \left[ \tau_{SUPG} \left( \vec{\mathcal{R}} + \vec{\mathcal{Z}}_s \right) \right] \right\} \cdot \frac{\partial \vec{W}}{\partial x_i} d\Omega, \quad (15.21)$$

where this form is generally applicable to all systems of coupled advection-diffusion equations except for the factor of porosity, which arises due to the particular set of equations solved in Pronghorn.  $\mathbf{A}_i$  are the inviscid flux Jacobian matrices defined in Eq. (2.111),  $\vec{W}$  is the vector of weight functions for the coupled equations,  $\tau_{SUPG}$  is a matrix of stabilization parameters similar to  $\alpha_{pg}$ ,  $\vec{\mathcal{R}}$  is the quasi-linear strong residual in Eq. (2.110), and  $\vec{\mathcal{Z}}_s$  is an additional term required for solution in axisymmetric coordinates defined in Eq. (2.120). In index notation, the  $j$ -th component of Eq. (15.21) is

$$\int_{\Omega} \varepsilon \mathbf{A}_{i,jk} \tau_{SUPG,kl} R_l \frac{\partial W_j}{\partial x_i} d\Omega, \quad (15.22)$$

For a 5-equation system in 3 spatial dimensions,  $j, k, l = 1, 2, 3, 4, 5$  and  $i = 1, 2, 3$ . Eq. (15.21) stabilizes each equation in the coupled system against all other equations in the system.

It is important to note that as written in Eq. (15.21), the SUPG method does not preserve monotonicity. In the vicinity of shocks or very sharp gradients in the solution, over/undershoots will result from approximating an infinite-term series with a finite basis, resulting in nonphysical numerical oscillations that can rapidly pollute the entire solution. In the vicinity of shocks, modifications to Eq. (15.21) referred to as “shock-capturing” terms may recover shock-like behavior. These modifications are not yet available in Pronghorn, and accuracy in the vicinity of shocks cannot be expected.

Section 15.3.1 provides an example application of the SUPG method to Eq. (2.100) with the ideal gas EOS to make Eq. (15.21) clearer. A simpler example with the multi-dimensional convection-diffusion equation in Section 15.3.2 explains the underlying stabilizing effect in Eq. (15.21) that is still overly complex in Section 15.3.1. Section 15.3.3 then motivates the selection of the entries in  $\tau_{SUPG}$ . Finally, Section 15.4 discusses small differences in application of SUPG stabilization to the various models in Pronghorn.

#### 15.3.1 An Ideal Gas Example

This section builds a connection between the generic multi-dimensional, coupled equation system, SUPG method shown in Eqs. (15.21) and (15.22) and the Petrov-Galerkin upwinding introduced in Section 15.2. Because the inviscid flux Jacobian matrices depend on the particular fluid EOS, this demonstration is performed assuming the ideal gas EOS for simplicity. Section 19.4 provides the  $\mathbf{A}_i$  matrices for the ideal gas EOS in 3-D. In addition, assume that  $\tau_{SUPG}$  is a diagonal matrix,

$$\tau_{SUPG} = \begin{bmatrix} \tau_c & 0 & 0 & 0 & 0 \\ 0 & \tau_u & 0 & 0 & 0 \\ 0 & 0 & \tau_u & 0 & 0 \\ 0 & 0 & 0 & \tau_u & 0 \\ 0 & 0 & 0 & 0 & \tau_e \end{bmatrix}, \quad (15.23)$$

where the stabilization parameter for the mass, momentum, and energy conservation equations is  $\tau_c$ ,  $\tau_u$ , and  $\tau_e$ , respectively.

Based on the different entries in  $\mathbf{A}_i$  and  $\tau_{SUPG}$ , and comparing the new term in Eq. (15.16) to the SUPG term in Eq. (15.22), the SUPG method is equivalent to the use of different element-discontinuous  $\psi^*$  for each coupled equation. In addition, the quasi-linear strong residual against which the element-discontinuous weight function is multiplied differs for each coupled equation, and in general is a combination of the quasi-linear strong residuals of all coupled equations. These observations can be made clearer by explicitly writing the new SUPG terms added to the weak forms of each of the mass, momentum, and energy conservation equations. Throughout this derivation, terms arising due to the axisymmetric solution vector  $\vec{Z}_s$  are omitted for brevity.

Carrying through the algebra in Eq. (15.22) for  $j = 0$  gives the following additional term for the mass conservation equation,

$$\int_{\Omega} \varepsilon \tau_u \nabla W_0 \cdot \vec{\mathcal{R}}_u \, d\Omega, \quad (15.24)$$

where  $\vec{\mathcal{R}}_u$  is the vector of momentum equation quasi-linear strong residuals. The mass conservation equation is stabilized by a term proportional to the dot product of the gradient of the mass equation weight function with the momentum equation quasi-linear strong residuals.

Carrying through the algebra in Eq. (15.22) for  $j = 1, 2, 3$  gives the following additional term for the  $j$ -th momentum equation,

$$\begin{aligned} \int_{\Omega} \varepsilon \tau_u \left[ (1 - \gamma) \vec{V} \cdot \vec{\mathcal{R}}_u \frac{\partial W_j}{\partial x_j} + \vec{V} \cdot \nabla W_j \mathcal{R}_{uj} + V_j \nabla W_j \cdot \vec{\mathcal{R}}_u \right] d\Omega + \int_{\Omega} \varepsilon \tau_e \mathcal{R}_e (\gamma - 1) \frac{\partial W_j}{\partial x_j} d\Omega + \\ \int_{\Omega} \varepsilon \tau_c \mathcal{R}_c \left[ -V_j \vec{V} \cdot \nabla W_j + \frac{1}{2} (\gamma - 1) \|\vec{V}\|_2^2 \frac{\partial W_j}{\partial x_j} \right] d\Omega \end{aligned} \quad (15.25)$$

where summation over  $j$  is not implied,  $\mathcal{R}_c$  is the continuity equation quasi-linear strong residual, and  $\mathcal{R}_e$  is the energy equation quasi-linear strong residual. The momentum equations are therefore stabilized by terms proportional to the continuity, momentum, and energy equation quasi-linear strong residuals.

Carrying through the algebra in Eq. (15.22) for  $j = 4$  gives the following additional term for the energy conservation equation,

$$\begin{aligned} \int_{\Omega} \varepsilon \tau_u \left[ H_f \nabla W_4 \cdot \vec{\mathcal{R}}_u + (1 - \gamma) (\vec{V} \cdot \vec{\mathcal{R}}_u) (\vec{V} \cdot \nabla W_4) \right] d\Omega + \int_{\Omega} \varepsilon \tau_e \mathcal{R}_e \gamma \vec{V} \cdot \nabla W_4 d\Omega + \\ \int_{\Omega} \varepsilon \tau_c \mathcal{R}_c \left[ \frac{(\gamma - 1)}{2} \|\vec{V}\|_2^2 - H_f \right] \vec{V} \cdot \nabla W_4 d\Omega. \end{aligned} \quad (15.26)$$

The energy equation is therefore stabilized by a term proportional to the continuity, momentum, and energy equation quasi-linear strong residuals.

### 15.3.2 The Stabilizing Effect

Eqs. (15.24)-(15.26) illustrate the cross-stabilization effect characteristic of the SUPG method. However, an intuitive understanding of why the terms in Eqs. (15.24)-(15.26) act to stabilize FE discretizations of convection-diffusion equations may not be readily apparent. Consider the multidimensional form of Eq. (15.1) with time dependence and unity thermal properties,

$$\frac{\partial u}{\partial t} + \nabla \cdot (u\vec{V}) - \nabla^2 u = 0. \quad (15.27)$$

The solution vector, inviscid flux vector, and the inviscid flux Jacobian matrices are

$$\vec{U} = [u], \quad \vec{F}_i = [uV_i], \quad \mathbf{A}_i = [V_i]. \quad (15.28)$$

The combined weak form, with the SUPG term given by Eq. (15.21), becomes

$$\begin{aligned} \int_{\Omega} \left( \frac{\partial u}{\partial t} \psi + \nabla u \cdot \nabla \psi - u\vec{V} \cdot \nabla \psi \right) d\Omega + \int_{\Gamma} \left( -\nabla u + u\vec{V} \right) \cdot \hat{n} \psi d\Gamma + \\ \int_{\Omega} \left[ \frac{\partial u}{\partial t} + \nabla \cdot (u\vec{V}) - \nabla^2 u \right] \tau_{cd} \vec{V} \cdot \nabla \psi = 0, \end{aligned} \quad (15.29)$$

where  $\tau_{cd}$  is the stabilization parameter for this convection-diffusion equation. The weak form of the diffusion kernel is symmetric with regard to the gradients on  $u$  and the weight function  $\psi$ . This symmetry arises due to the self-adjoint properties of diffusive operators. The SUPG method adds a term that is symmetric with respect to gradients of the advective flux  $u\vec{V}$  and the weight function, essentially mimicking the symmetry of the diffusive kernel. This added symmetry to a convective kernel is the underlying stabilizing effect.

Related to this idea, it can be shown that the SUPG method applied to a single multi-dimensional equation is equivalent to a linear combination of the Bubnov-Galerkin FE and Galerkin Least Squares (GLS) methods [191]. The GLS seeks to minimize the square of the residual, and therefore results in symmetric linear equations.

### 15.3.3 Calculation of the Stabilization Parameter $\tau_{SUPG}$

The stabilization parameter  $\tau_{SUPG}$  is an  $N \times N$  matrix of intrinsic time scales associated with the  $N$ -equation system.  $\tau_{SUPG}$  is often approximated as a diagonal matrix as in Eq. (15.23), and this same convention is used in Pronghorn.

The accuracy of the SUPG method is dependent on a good choice for  $\tau_{SUPG}$  that balances accuracy and stability [196]. Optimal values are only available for the simplest of equations, such as the 1-D linear convection-diffusion equation and diagonalizable convection-diffusion systems of equations. For multidimensional and non-diagonalizable systems of equations,  $\tau_{SUPG}$  is a combination of the waves generated by each eigenvalue, the determination of which involves the solution of an eigenvalue problem at each quadrature point. This Central Processing Unit (CPU)-intensive process is frequently substituted with the use of ad-hoc time-scales and extensions of optimal 1-D expressions to higher dimensions [196].

The  $(i, i)$  component in  $\tau_{SUPG}$  represents an intrinsic time scale associated with the  $i$ -th coupled equation. Three different time scales are usually considered — 1) a transient limit,  $\tau_{temporal}$ ; 2) an advective limit,  $\tau_{advective}$ ; and 3) a diffusive limit,  $\tau_{diffusive}$ . The advective limit is in some cases specified in terms of both an incompressible limit  $\tau_{advective, inc}$  and a compressible limit  $\tau_{advective, com}$ . Regardless of how these time scales are defined, there are generally two different methods in which these time scales are combined to give a representative time scale. The “switching method” smoothly transitions between the three time scales as

$$\tau_j = \left[ \left( \frac{1}{\tau_{\text{temporal}}} \right)^\chi + \left( \frac{1}{\tau_{\text{advective}}} \right)^\chi + \left( \frac{1}{\tau_{\text{diffusive}}} \right)^\chi \right]^{-1/\chi} \quad (15.30)$$

where  $j = c, u, e$  and  $\chi$  is an integer typically chosen as 2 [197, 198]. Alternatively,  $\tau_j$  is selected as the minimum of the three different limits [63, 196],

$$\tau_j = \min(\tau_{\text{temporal}}, \tau_{\text{advective}}, \tau_{\text{diffusive}}) . \quad (15.31)$$

Eq. (15.31) is equivalent to Eq. (15.30) with  $\chi = \infty$ . The three time scales can be obtained by non-dimensionalizing the element matrices and vectors that arise directly from the FEM discretization of each of the conservation equations. Each conservation equation is written as if it were stabilized only against itself — that is, the cross-stabilizing effects, shown by example with the ideal gas EOS for Eq. (2.100) in Section 15.3.1, are not considered. Because the objective is purely to provide intuition for the selection of the three time scales for each conservation equation, simplicity mandates the assumption of linear basis functions and all other terms constant.

The advective, temporal, and diffusive time scales are obtained by normalizing the advective, temporal, and diffusive terms in the non-stabilized weak form, respectively, by the advective term in the additional SUPG term [196, 197]. Beginning with the mass equation, the weak form with the SUPG term written in the style of Eq. (15.29) by neglecting cross-stabilization effects, is

$$\int_{\Omega} \left( \frac{\partial \rho}{\partial t} - \rho \vec{V} \cdot \hat{n} \right) \psi d\Omega + \int_{\Gamma} \rho \vec{V} \cdot \hat{n} \psi d\Gamma + \int_{\Omega} \tau_c \vec{V} \cdot \nabla \psi \left[ \frac{\partial \rho}{\partial t} + \nabla \cdot (\rho \vec{V}) \right] d\Omega = 0 . \quad (15.32)$$

The incompressible advective limit for the mass equation is

$$\begin{aligned} \tau_{\text{advective, inc}} &= \frac{\| \int_{\Omega} \rho \vec{V} \cdot \nabla \psi d\Omega \|}{\| \int_{\Omega} (\vec{V} \cdot \nabla \psi) \nabla \cdot (\rho \vec{V}) d\Omega \|} \\ &= \frac{h_e}{2 \| \vec{V} \|} . \end{aligned} \quad (15.33)$$

Eq. (15.33) is considered an incompressible limit because  $\rho$  was assumed constant. A compressible advective limit is formed in an ad hoc manner by replacing  $\| \vec{V} \|$  by  $\| \vec{V} \| + c$ , the largest eigenvalue of the Euler equations,

$$\tau_{\text{advective, com}} = \frac{h_e}{2(\| \vec{V} \| + c)} . \quad (15.34)$$

While incompressible simulations commonly set  $\tau_{\text{advective}}$  as Eq. (15.33) [198], Eq. (15.34) usually gives better performance for the flows typical of Pronghorn's application space. Setting  $\tau_{\text{advective}}$  as the sum of Eqs. (15.33) and (15.34) has been observed elsewhere to give better numerical performance near stagnation points in compressible flows [196].

The temporal limit for the mass equation is

$$\begin{aligned} \tau_{\text{temporal}} &\equiv \frac{\| \int_{\Omega} \rho \vec{V} \cdot \nabla \psi d\Omega \|}{\| \int_{\Omega} \vec{V} \cdot \nabla \psi \frac{\partial \rho}{\partial t} d\Omega \|} \\ &= \frac{\Delta t}{2} . \end{aligned} \quad (15.35)$$

A factor of 2 is used to obtain a Lax-Wendroff method [196, 198, 199]. Finally, there are no diffusive terms in the mass equation such that there is no diffusive time scale. The weak form of the  $i$ -th momentum equation is

$$\int_{\Omega} \frac{\partial(\rho_f V_i)}{\partial t} \psi d\Omega + \int_{\Omega} (\tau : \nabla \psi - \rho_f V_i \vec{V}) \cdot \nabla \psi d\Omega + \int_{\Gamma} (\rho_f V_i \vec{V} \cdot \hat{n} - \tau : \hat{n}) \psi d\Gamma + \int_{\Omega} \tau_{ii} \vec{V} \cdot \nabla \psi \left( \frac{\partial(\rho_f V_i)}{\partial t} + \nabla \cdot (\rho_f V_i \vec{V}) - \nabla \cdot \tau \right) d\Omega = 0, \quad (15.36)$$

where the pressure and gravitational terms are omitted because they are not needed for the normalization process. The time and advective scales are the same as those obtained for the mass equation, except that  $\rho$  is replaced by  $\rho_f V_i$ . A diffusive limit is [196]

$$\begin{aligned} \tau_{\text{diffusive}} &= \frac{\| \int_{\Omega_e} \rho_f V_i \vec{V} \cdot \nabla \psi d\Omega \|}{\| \int_{\Omega_e} \vec{V} \cdot \nabla \psi \nabla \cdot \tau d\Omega \|} \\ &= \frac{\rho_f h_e^2}{4\tilde{\mu}/\varepsilon}. \end{aligned} \quad (15.37)$$

An additional factor is sometimes included in the numerator of Eq. (15.37) that accounts for an inverse estimate of the second derivatives of the shape functions, which is 1/3 for linear basis functions [196].

The energy conservation equation has the same temporal and advective limits as the mass and momentum equations. By analogy with momentum diffusion, the diffusive limit for the energy equation is

$$\begin{aligned} \tau_{\text{diffusive}} &= \frac{\| \int_{\Omega_e} \rho C_p \vec{V} \cdot \nabla T \psi d\Omega \|}{\| \int_{\Omega_e} \vec{V} \cdot \nabla \psi \nabla \cdot (k \nabla T) d\Omega \|} \\ &= \frac{\rho_f C_p h_e^2}{4\kappa_f/\varepsilon}. \end{aligned} \quad (15.38)$$

Other applications differ slightly in these limits through multiplicative factors, so each time scale can be multiplied by a scalar to obtain equivalence [63, 196–198]. The use of  $\tilde{\mu}\varepsilon$  in place of  $\mu_f$  and  $\kappa_f/\varepsilon$  in place of  $k_f$  simply reflects the form of the porous media macroscale equations, since these terms reduce to  $\mu_f$  and  $k_f$  for open flows. In addition, the element lengths for the advective and diffusive length scales are assumed the same, though some authors use a flow-aligned length scale for the advective limits and an average element length scale for the diffusive limit [63, 196].

$\tau_{SUPG}$  is therefore given by Eq. (15.23), with each diagonal entry a combination of the temporal, advective, and diffusive time scales according to either Eq. (15.30) or Eq. (15.31). As a final note, when using the low Mach preconditioner described in Section 2.8.2,  $\tau_{SUPG}$  is left-multiplied by  $\mathbf{M}^{-1}$ , giving a non-diagonal matrix,

$$\tau_{SUPG} = \mathbf{M}^{-1} \tau_{SUPG}, \quad (15.39)$$

where  $\tau_{SUPG}$  on the RHS is the diagonal form in Eq. (15.23). Eq. (15.39) has been observed to result in faster convergence than the diagonal form in Eq. (15.23) [196].

## 15.4 SUPG Stabilization of the Navier-Stokes, Euler, and Friction-Dominated Models

The three models in Pronghorn were summarized in Section 2.10. For the Navier-Stokes and Euler models, the fluid conservation equations can be written in the form of Eq. (2.100) and SUPG stabilization applied as described in Section 2.8.1. Because the fluid energy conservation equation in the friction-dominated model is not written in

conservative form, a slightly different version of the SUPG stabilization described up until this point is applied to the friction-dominated model.

The SUPG stabilization of the friction-dominated model only requires stabilization of the mass and fluid energy equations, since the momentum equation lacks an advective kernel. In Section 15.3.1, SUPG stabilization of the mass conservation equation leads to a term involving the gradient of the mass equation weight function with the vector of momentum residuals. Therefore, the advective term in friction-dominated mass equation is stabilized in the same manner. The fluid energy conservation equation is then stabilized as a single equation similar to Eq. (15.29).

## 16 Solution of Nonlinear Equations

This section describes the solution of the nonlinear systems of equations given in Section 2 with a Newton-Krylov method and Jacobians calculated using AD techniques. These equations are discretized with the FEM in Section 14 and stabilized with the SUPG method in Section 15. The nonlinear system of equations is a root-finding problem; extending Eq. (14.3) to the discretized case, this nonlinear system is

$$\vec{R}(\vec{u}) = 0 , \quad (16.1)$$

where  $\vec{R}$  is the discrete nonlinear residual vector and  $\vec{u}$  is the discrete approximate nonlinear solution. A Newton-Krylov method first linearizes Eq. (16.1) to the form

$$\mathbf{A}\vec{x} = \vec{b} , \quad (16.2)$$

where  $\mathbf{A}$  is a matrix,  $\vec{x}$  is the linear solution vector, and  $\vec{b}$  is the RHS vector. Following this linearization, the Newton-Krylov method involves two main loops — 1) an inner loop with index  $k$  that iteratively solves for  $\vec{x}$  in Eq. (16.2); and 2) an outer loop with index  $i$  that iteratively solves for  $\vec{u}$  in Eq. (16.1).

Linearization is performed with Newton's method by forming a Taylor series approximation about the current nonlinear iterate,

$$\vec{R}(\vec{u}_{i+1}) = \vec{R}(\vec{u}_i) + \frac{\partial \vec{R}(\vec{u}_i)}{\partial \vec{u}} (\vec{u}_{i+1} - \vec{u}_i) + O(\vec{u}_{i+1} - \vec{u}_i)^2 . \quad (16.3)$$

Setting Eq. (16.3) to zero and neglecting quadratic and higher-order terms, a linear form is obtained,

$$\mathbf{J}(\vec{u}_i)\vec{\delta}_i = -\vec{R}(\vec{u}_i) , \quad (16.4)$$

where  $\mathbf{J}(\vec{u}_i)$  is the Jacobian of the  $i$ -th iterate, defined as

$$\mathbf{J}(\vec{u}_i) \equiv \frac{\partial \vec{R}(\vec{u}_i)}{\partial \vec{u}} , \quad (16.5)$$

and  $\vec{\delta}_i$  is the update vector, defined as

$$\vec{\delta}_i \equiv \vec{u}_{i+1} - \vec{u}_i . \quad (16.6)$$

Comparing Eq. (16.4) with the general linear form in Eq. (16.2) shows that  $\mathbf{A}$  represents  $\mathbf{J}$ ,  $\vec{b}$  represents  $-\vec{R}$ , and  $\vec{x}$  represents  $\vec{\delta}_i$ . To match convention used in most linear algebra texts, the notation in Eq. (16.2) is used throughout to describe the linear problem in Eq. (16.4) with the understanding that Eq. (16.4) is the linear problem.

To summarize the Newton-Krylov method, the inner loop iteratively solves for  $\vec{x}_k$  until the norm of the linear residual in the  $k$ -th iteration,  $\vec{r}_k$ , is less than a specified tolerance  $\epsilon_l$ ,

$$\|\vec{r}_k\| \leq \epsilon_l , \quad (16.7)$$

where

$$\vec{r}_k \equiv \mathbf{A}\vec{x}_k - \vec{b}. \quad (16.8)$$

After the linear iterations have converged, the  $(i + 1)$ -th nonlinear iterate is calculated as

$$\vec{u}_{i+1} = \vec{u}_i + \vec{x}_k. \quad (16.9)$$

The matrix  $\mathbf{A}$  and RHS vector  $\vec{b}$  are then updated based on  $\vec{u}_{i+1}$ , and the linear iteration repeated to obtain the next linear iterate  $\vec{x}_{k+1}$ . The nonlinear problem is converged once the norm of the nonlinear residual in the  $i$ -th iteration is less than a specified tolerance  $\epsilon_n$ ,

$$\|\vec{R}(\vec{u}_i)\| \leq \epsilon_n. \quad (16.10)$$

Combining Eqs. (16.2) and (16.8) with the definition of the linear error  $\vec{e}$ ,

$$\vec{e} \equiv \vec{x}_* - \vec{x}, \quad (16.11)$$

where  $\vec{x}_*$  is the true linear solution, the linear error and linear residual are related to one another as

$$\mathbf{A}\vec{e} = -\vec{r}. \quad (16.12)$$

Combined with the condition number for matrix-vector multiplication in Eq. (17.21), the residual is expected to be a good indication of the error provided  $\mathbf{A}$  and  $\mathbf{A}^{-1}$  are well-conditioned.

Finally, for simple roots, or roots that do not also coincide with the root of a derivative of  $\vec{R}$ , provided the initial iterate is sufficiently close to the true solution, Newton's method converges quadratically. That is, the error in the  $i$ -th iteration is less than or equal to the square of the error in the previous iteration,

$$\|\vec{u}_{i+1} - \vec{u}_*\| \leq C\|\vec{u}_i - \vec{u}_*\|^2 \quad (16.13)$$

for a positive constant  $C$ . However, for multiple roots, Newton's method only converges linearly. The damped Newton methods available in MOOSE improve the likelihood of convergence by restricting the step size taken in each iteration so that overshoot past small features of  $\vec{R}$  is reduced.

The remainder of this section describes linear solution methods in Section 16.1 and Jacobian evaluation in Section 16.2. Finally, Section 16.3 describes the preconditioning process used to accelerate convergence.

## 16.1 Iterative Solution of Linear Equations

After linearization of the nonlinear problem to the linear form in Eq. (16.2), any number of linear solution methods can be applied to solve the system of equations. Linear solution techniques can generally be characterized as either direct or iterative methods. Direct methods involve factorization of  $\mathbf{A}$  and forward and/or backward substitution; Gaussian elimination is a direct method. The computational cost of direct methods generally scales as  $N^3$  for a system of  $N$  equations, and the factorization results in substantial fill-in when applied to sparse systems. The large, sparse, and non-constant matrices expected in Pronghorn's application space motivate the use of iterative methods, which are the focus of the remainder of this section. Many direct solvers are available through PETSc interfaces if desired.

Iterative methods involve iteratively updating an approximate solution based on a series of matrix-vector products. The computational cost of iterative methods scales as the cost of a matrix-vector product times the number of iterations;

provided  $\mathbf{A}$  is sparse, repeated matrix-vector calculations may represent substantially lower evaluations than a direct method. The nodal FEM basis functions produce sparse systems, so iterative methods are a natural default choice in MOOSE. The remainder of this section presents a detailed description of some of the most common iterative methods to provide the necessary concepts to understand the Generalized Minimal Residuals (GMRES) algorithm used in MOOSE.

In this section, the true and approximate solutions to Eq. (16.2) are denoted as  $\vec{x}_*$  and  $\vec{x}$ , respectively. All iterative methods begin from some initial guess  $\vec{x}_0$  and successively update this initial guess at each iteration,

$$\begin{aligned}\vec{x}_{k+1} &= \vec{x}_k + \alpha_k \vec{p}_k \\ &= \vec{x}_0 + \sum_{i=0}^k \alpha_i \vec{p}_i,\end{aligned}\tag{16.14}$$

where  $\alpha_k$  is a step length and  $\vec{p}_k$  is the update vector. Recursion has been used to relate the  $(k+1)$ -th iterate to the initial guess. By definition of the error in Eq. (14.9), subtracting  $\vec{x}_*$  from both sides of Eq. (16.14) gives

$$\begin{aligned}\vec{e}_{k+1} &= \vec{e}_k + \alpha_k \vec{p}_k \\ &= \vec{e}_0 + \sum_{i=0}^k \alpha_i \vec{p}_i.\end{aligned}\tag{16.15}$$

From Eq. (16.12), multiplying Eq. (16.14) by  $-\mathbf{A}$  gives

$$\begin{aligned}\vec{r}_{k+1} &= \vec{r}_k - \alpha_k \mathbf{A} \vec{p}_k \\ &= \vec{r}_0 - \mathbf{A} \sum_{i=0}^k \alpha_i \vec{p}_i.\end{aligned}\tag{16.16}$$

For time-dependent systems, the starting vector  $\vec{x}_0$  is often selected as the solution from the most recently computed time step, which generally improves convergence properties with every time step, provided the time steps are not extremely large. The differences in the iterative methods discussed in this section reduce to differences in the selection of the  $\alpha_k$  and  $\vec{p}_k$ . Introduce the following quadratic function  $\mathcal{Y}$  of the approximate solution  $\vec{x}$ ,

$$\mathcal{Y}(\vec{x}) \equiv \frac{1}{2} \vec{x}^* \mathbf{A} \vec{x} - \vec{b}^* \vec{x}.\tag{16.17}$$

The gradient of Eq. (16.17) with respect to  $\vec{x}$  is

$$\frac{\partial \mathcal{Y}(\vec{x})}{\partial \vec{x}} = \begin{cases} \frac{1}{2} (\vec{x}^* \mathbf{A} + \mathbf{A} \vec{x}) - \vec{b} & \text{else} \\ \mathbf{A} \vec{x} - \vec{b} & \text{hermitian } \mathbf{A} \end{cases}.\tag{16.18}$$

If  $\mathbf{A}$  is hermitian, the solution to the linear equation occurs when

$$\nabla \mathcal{Y}(\vec{x}) = 0.\tag{16.19}$$

The  $\vec{x}$  at which  $\nabla \mathcal{Y}(\vec{x}) = 0$  depends on the properties of  $\mathbf{A}$ , which determine the shape of  $\mathcal{Y}(\vec{x})$ . A hermitian matrix can be either definite or indefinite. All matrices considered in Pronghorn are real, and from this point forward “hermitian” will be replaced with the slightly less general “symmetric” nomenclature without loss of generality. If  $\mathbf{A}$  is symmetric

and definite, then the location at which Eq. (16.19) holds either corresponds to minimization of  $\mathcal{Y}$  (for Symmetric Positive Definite (SPD)  $\mathbf{A}$ ) or maximization of  $\mathcal{Y}$  (for Symmetric Negative Definite (SND)  $\mathbf{A}$ ). If  $\mathbf{A}$  is indefinite, the solution is a saddle point, and Eq. (16.19) does not correspond to a minimum or a maximum. If  $\mathbf{A}$  is singular, then there is no unique solution, and the solution is a line or hyperplane along which  $\mathcal{Y} = 0$  has multiple solutions.

In order to determine why a definite matrix corresponds to minimization or maximization of  $\mathcal{Y}(x)$ , evaluate Eq. (16.17) at a point slightly perturbed by an error  $\vec{e}$  from the true solution,

$$\begin{aligned}\mathcal{Y}(\vec{x}_* + \vec{e}) &= \frac{1}{2}(\vec{x}_* + \vec{e})^T \mathbf{A}(\vec{x}_* + \vec{e}) - \vec{b}^T (\vec{x}_* + \vec{e}) \\ &= \mathcal{Y}(\vec{x}_*) + \frac{1}{2} \left( \vec{x}_*^T \mathbf{A} \vec{e} + \vec{e}^T \mathbf{A} \vec{x}_* \right) + \frac{1}{2} \vec{e}^T \mathbf{A} \vec{e} - \vec{b}^T \vec{e} .\end{aligned}\tag{16.20}$$

If  $\mathbf{A}$  is symmetric, Eq. (16.20) simplifies to

$$\mathcal{Y}(\vec{x}_* + \vec{e}) = \mathcal{Y}(\vec{x}_*) + \frac{1}{2} \vec{e}^T \mathbf{A} \vec{e} .\tag{16.21}$$

If  $\mathbf{A}$  is SPD, the second term in Eq. (16.21) is always positive, so the true solution occurs at the minimum of  $\mathcal{Y}$ . If  $\mathbf{A}$  is SND, the second term is always negative, and the true solution occurs at the maximum of  $\mathcal{Y}$ . A SND matrix can always be transformed to a SPD matrix by negating it, so the remainder of this section will refer to the true solution as the *minimum* of  $\mathcal{Y}(x)$ , with the understanding that the nomenclature applies for both SPD and SND matrices. From Eq. (16.21), minimizing the energy norm of the error is equivalent to minimizing  $\mathcal{Y}$ .

The quadratic function construct will be most useful for describing iterative methods for SPD systems. Not all of the numerical methods discussed in this section are of direct relevance to Pronghorn, but are included to provide a complete description of the building blocks needed to fully understand the GMRES method. The remainder of this section is organized as follows. Section 16.1.1 introduces classical matrix-splitting methods and fundamental fixed point iteration concepts. While the linear system of equations in Pronghorn will likely never be SPD unless specifically constructed as such, Sections 16.1.2 and 16.1.3 discuss the Steepest Descent (SD) and Conjugate Gradient (CG) methods for SPD matrices to introduce the concept of Krylov subspace iterative methods and iterative Krylov methods as equivalent to polynomial minimization problems. Section 16.1.4 introduces the Arnoldi iteration, which is a key step in the GMRES algorithm. Readers already familiar with fixed point iteration, Krylov subspaces, and Arnoldi iteration can skip directly to Section 16.1.5.

### 16.1.1 Matrix Splitting Methods

Matrix splitting methods are based on splitting  $\mathbf{A}$  into multiple matrices, at least one of which is easy to invert. Represent  $\mathbf{A}$  as the sum of diagonal, lower triangular, and upper triangular matrices,

$$\mathbf{A} \equiv \mathbf{L} + \mathbf{U} - \mathbf{D} .\tag{16.22}$$

The simplest example of a matrix splitting method is the Jacobi method. The Jacobi method only uses previously-known values to update diagonal entries, so the problem becomes

$$\vec{x}_{k+1} = \mathbf{B} \vec{x}_k + \vec{z} ,\tag{16.23}$$

where  $\mathbf{B}$  and  $\vec{z}$  are given by

$$\mathbf{B} \equiv \mathbf{D}^{-1}(\mathbf{L} + \mathbf{U}) ,\tag{16.24}$$

$$\vec{z} = -\mathbf{D}^{-1}\vec{b} . \quad (16.25)$$

All matrix-splitting methods can be written in the general form in Eq. (16.23), but with different  $\mathbf{B}$  and  $\vec{z}$ . For example, the Gauss-Seidel is a small variation on the Jacobi method that uses information calculated at the  $(k+1)$ -th iterate as soon as it becomes available;  $\mathbf{B}$  and  $\vec{z}$  are then defined as

$$\mathbf{B} = (\mathbf{D} - \mathbf{L})^{-1} \mathbf{U} , \quad (16.26)$$

$$\vec{z} = (\mathbf{D} - \mathbf{L})^{-1} \vec{b} . \quad (16.27)$$

An important interpretation of matrix-splitting methods can be obtained by rewriting Eq. (16.23) by expressing the previous iterate as the true solution plus some error, giving

$$\vec{e}_{k+1} = \mathbf{B}\vec{e}_k . \quad (16.28)$$

For symmetric  $\mathbf{B}$ , each iterate can be expressed as a sum of the  $m$  linearly independent eigenvectors of  $\mathbf{B}$ . Combining this observation with Eq. (17.25), the Jacobi and Gauss-Seidel methods converge the error to zero provided the spectral radius of  $\mathbf{B}$  is less than unity,

$$\begin{aligned} \vec{e}_{k+1} &= \mathbf{B}^{k+1} \sum_{i=1}^m C_i \vec{v}_i \\ &= \sum_{i=1}^m C_i \lambda_i^{k+1} \vec{v}_i . \end{aligned} \quad (16.29)$$

Matrix-splitting methods are referred to as “smoother” methods, since with every iteration all eigenvector error components are decreased.

### 16.1.2 The Steepest Descent Method

The SD method is an iterative method commonly applied to symmetric matrices; for simplicity of discussion, all matrices in this section are assumed symmetric. The SD method selects the next iterate  $\vec{x}_{k+1}$  to lie somewhere along the direction of the steepest decrease in  $\mathcal{Y}(\vec{x}_k)$  [200]. By definition, the gradient corresponds to the direction of steepest increase of  $\mathcal{Y}$ , so the search direction is taken as the negative of the gradient of  $\mathcal{Y}$ . From Eq. (16.18), the negative of the gradient for symmetric matrices is the residual such that  $\vec{p}_k = \vec{r}_k$ . The step size is chosen such that  $\mathcal{Y}$  is minimized, which can equivalently be phrased as  $\nabla \mathcal{Y}(\vec{x}_{k+1}) = 0$  along the line  $\vec{p}_k$ . This gives the following method,

$$\begin{aligned} \frac{\partial \mathcal{Y}(\vec{x}_{k+1})}{\partial \alpha_k} &= \frac{\partial}{\partial \alpha} \left[ \frac{1}{2} (\vec{x}_k + \alpha_k \vec{p}_k)^T \mathbf{A} (\vec{x}_k + \alpha_k \vec{p}_k) - \vec{b}_k^T (\vec{x}_k + \alpha_k \vec{p}_k) \right] \\ &= \vec{p}_k^T \mathbf{A} \vec{x}_k + \alpha_k \vec{p}_k^T \mathbf{A} \vec{p}_k - \vec{b}_k^T \vec{p}_k . \end{aligned} \quad (16.30)$$

Setting Eq. (16.30) equal to zero in order to find the minimum gives

$$\alpha_k = \frac{\vec{p}_k^T \vec{r}_k}{\vec{p}_k^T \mathbf{A} \vec{p}_k} . \quad (16.31)$$

$\alpha_k$  represents the distance moved along  $\vec{p}_k$  until reaching the location where the search direction is orthogonal to the next residual,

$$\vec{p}_k^T \vec{r}_{k+1} = 0. \quad (16.32)$$

For the SD method, the search direction equal to the residual, so Eq. (16.32) can also be written as

$$\vec{r}_k^T \vec{r}_{k+1} = 0, \quad (16.33a)$$

$$\vec{p}_k^T \vec{p}_{k+1} = 0. \quad (16.33b)$$

The directional derivative in Eq. (16.30) can also be written in compact, chain-rule form to provide an important interpretation of the choice of  $\alpha_k$  in Eq. (16.31):

$$\begin{aligned} \frac{\partial \mathcal{Y}(\vec{x}_{k+1})}{\partial \alpha_k} &= \frac{\partial \mathcal{Y}(\vec{x}_{k+1})}{\partial \vec{x}_{k+1}} \frac{\partial \vec{x}_{k+1}}{\partial \alpha_k} \\ &= -\vec{r}_{k+1}^T \vec{p}_k \\ &= (\mathbf{A}\vec{e}_{k+1})^T \vec{p}_k \\ &= \vec{e}_{k+1}^T \mathbf{A}\vec{p}_k, \end{aligned} \quad (16.34)$$

where the last form uses Eq. (16.12). With the choice of  $\alpha_k$  in Eq. (16.31), the next iterate's error is A-orthogonal to the previous search direction. The SD method as written has two important downsides — 1)  $\mathbf{A}$  has to be SPD and 2) the convergence rate of the method is relatively poor. Consider a matrix equation in  $\mathbb{R}^2$ . Eq. (16.33) shows that with each iteration, the residual is orthogonal to the residual of the previous iterate. Unless a fortuitous initial guess is selected, this results in a right-angle zig-zag stepping in  $\mathbb{R}^2$  towards  $\nabla \mathcal{Y}(\vec{x}) = 0$ , which will generally require many iterations to converge. Therefore, the SD is often not a practical method for solving Eq. (16.2). However, an understanding of the method is important for grasping the more complex CG method described in Section 16.1.3.

### 16.1.3 The Conjugate Gradient Method

A major drawback of the SD method is obvious from Eq. (16.33b) — because each search direction is only orthogonal to the previous direction, the same directions are searched over and over again without expanding the space of the search with each iteration. An improvement would be to select the search directions to be A-orthogonal to *all* previous search directions, or

$$\vec{p}_i^T \mathbf{A}\vec{p}_j = 0, \quad i \neq j. \quad (16.35)$$

Choosing orthogonality, rather than A-orthogonality, would be equivalent to the SD method. In infinite precision arithmetic, choosing A-conjugate search directions leads to exact convergence in  $m$  iterations. An even better choice would be to enforce  $\vec{e}_{k+1}^T \vec{p}_k = 0$ , in which case if  $\vec{p}_k$  is selected as the  $k$ -th unit vector, each iteration exactly finds one component of  $\vec{x}$ . But, this option is not possible, since in general the error is unknown.

Because mutually A-orthogonal vectors are linearly independent, express the initial error as a linear combination of search directions with coefficients  $C_j$ ,

$$\vec{e}_0 = \sum_{j=0}^{m-1} C_j \vec{p}_j, \quad (16.36)$$

where indexing begins at zero such that the indexing is consistent with the zero-indexing in Eq. (16.15). Then, by A-conjugacy of the search directions, premultiplying both sides above by  $\vec{p}_k^T \mathbf{A}$  picks out a single term from the summation in Eq. (16.36), which after rearranging gives:

$$\begin{aligned} C_k &= \frac{\vec{p}_k^T \mathbf{A} \vec{e}_0}{\vec{p}_k^T \mathbf{A} \vec{p}_k} \\ &= \frac{\vec{p}_k^T \mathbf{A} \left( \vec{e}_k + \sum_{i=0}^{k-1} \alpha_i \vec{p}_i \right)}{\vec{p}_k^T \mathbf{A} \vec{p}_k} \\ &= \frac{\vec{p}_k^T \mathbf{A} \vec{e}_k}{\vec{p}_k^T \mathbf{A} \vec{p}_k} \\ &= -\alpha_k, \end{aligned} \quad (16.37)$$

where Eq. (16.15) was used to rewrite  $\vec{e}_0$  and A-conjugacy was again applied to eliminate the sum. The step length  $\alpha_k$  is identical to the length of the error in the  $\vec{p}_k$  direction — because this term is successively subtracted from the error, the Conjugate Directions (CD) method is exact in  $m$  iterations.

A Gram-Schmidt process, described in Section 17, is used to generate the set of A-orthogonal search directions by subtracting from an initial set of linearly independent vectors the components that are in the A-conjugate direction of the previously-generated A-orthogonal vectors. If an arbitrary selection is made for the starting linearly independent vectors, the method presented thus far is known as the CD method; the search directions from all previous iterations would need to be stored to perform the Gram-Schmidt conjugation each iteration, which is memory-intensive and expensive, negating the benefits of iterative methods. Instead, the CG method makes a more intelligent and computationally efficient choice for the starting search directions.

By A-conjugacy of the search directions, all of the search directions are linearly independent, and therefore form a space  $\mathcal{K}_k$ , also referred to as a Krylov subspace,

$$\begin{aligned} \mathcal{K}_k &\equiv \text{span}\{\vec{p}_0, \vec{p}_1, \dots, \vec{p}_k\} \\ &= \text{span}\{\vec{x}_0, \vec{x}_1, \dots, \vec{x}_k\}, \end{aligned} \quad (16.38)$$

which from Eq. (16.14) is the same space spanned by the  $\vec{x}_i$ . With each iteration, the energy norm of the error is minimized in the space  $\vec{e}_0 + \mathcal{K}_k$  such that  $\vec{e}_{k+1} \in \vec{e}_0 + \mathcal{K}_k$ . To show that the energy norm is minimized in this space, express the energy norm in terms of linear combinations of the search directions, where  $e_{k+1}$  is given by Eq. (16.15) with the initial error expressed as in Eq. (16.36), with Eq. (16.37) allowing the replacement of  $\alpha_k$  by  $-C_k$  —

$$\vec{e}_{k+1} = \sum_{j=0}^{m-1} C_j \vec{p}_j - \sum_{j=0}^k C_j \vec{p}_j, \quad (16.39a)$$

$$\|\vec{e}_{k+1}\|_A^2 = \sum_{j=k+1}^{m-1} C_j^2 \vec{p}_j^T \mathbf{A} \vec{p}_j. \quad (16.39b)$$

Eq. (16.39b) then uses A-conjugacy of the search directions. Each term in Eq. (16.39b) represents a search direction that has not yet been traversed, and by increasing the size of the space, the error can only be minimized (or stay the same). While this optimality of the error term seems very advantageous, the high cost of the Gram-Schmidt conjugation makes selecting arbitrary vectors to A-conjugate impractical. The CG method is a very slight tweak to the CD method that selects the search directions by conjugation of the residuals.

$\vec{r}_{k+1}$  is orthogonal to  $\vec{p}_k$  according to Eq. (16.32), and because all of the search directions are mutually A-orthogonal, the residual is guaranteed to provide a new, linearly independent search direction. Therefore, all of the residuals are mutually orthogonal. The search directions are built from the residuals, so the residuals and search directions share the same space given in Eq. (16.38), giving

$$\mathcal{K}_k = \text{span}\{\vec{r}_0, \vec{r}_1, \dots, \vec{r}_k\}, \quad (16.40a)$$

$$\mathcal{K}_k = \text{span}\{\vec{p}_0, \mathbf{A}\vec{p}_0, \dots, \mathbf{A}^{k-1}\vec{p}_0\}, \quad (16.40b)$$

$$\mathcal{K}_k = \text{span}\{\vec{r}_0, \mathbf{A}\vec{r}_0, \dots, \mathbf{A}^{k-1}\vec{r}_0\}, \quad (16.40c)$$

$$\mathcal{K}_k = \text{span}\{\mathbf{A}\vec{e}_0, \mathbf{A}^2\vec{e}_0, \dots, \mathbf{A}^k\vec{e}_0\}, \quad (16.40d)$$

$$\mathcal{K}_k = \text{span}\{\vec{b}, \mathbf{A}\vec{b}, \dots, \mathbf{A}^{k-1}\vec{b}\}. \quad (16.40e)$$

From Eq. (16.16), the newest residual is the sum of the previous residual and  $\mathbf{A}\vec{p}_k$ , giving Eq. (16.40b). From Eq. (16.38) and Eq. (16.40b), the newest residual space represents the union of  $\mathcal{K}_k$  and  $\mathbf{A}\mathcal{K}_k$ , giving Eq. (16.40c). Eq. (16.12) gives Eq. (16.40d), and assuming  $\vec{x}_0 = \vec{0}$  gives Eq. (16.40e). Eq. (16.40) is a Krylov space, formed by repeatedly applying a matrix to a vector. Hence, the CG method is a Krylov subspace iterative method. Because the residual is A-orthogonal to all of the previous search directions, the Gram-Schmidt conjugation becomes nearly trivial, significantly reducing the cost and memory storage required of the CD method. The CG method is also characterized by better convergence properties than the SD method.

#### 16.1.4 The Arnoldi Iteration

A matrix can be transformed into an upper Hessenberg matrix through unitary similarity transformations,

$$\mathbf{A} = \mathbf{QHQ}^*, \quad (16.41a)$$

$$\mathbf{AQ} = \mathbf{QH}, \quad (16.41b)$$

where  $\mathbf{Q}$  is a unitary matrix, defined in Eq. (17.6). Similar to the difference between the full and reduced QR factorizations discussed in Section 17, we can find only the first  $n$  columns of  $\mathbf{AQ} = \mathbf{QH}$  in an iterative procedure,

$$\mathbf{A}\hat{\mathbf{Q}}_n = \hat{\mathbf{Q}}_{n+1}\tilde{\mathbf{H}}_n, \quad (16.42)$$

where  $\hat{\mathbf{Q}}_n$  is of size  $m \times n$ ,  $\hat{\mathbf{Q}}_{n+1}$  is of size  $m \times (n+1)$  and  $\tilde{\mathbf{H}}_n$  is of size  $(n+1) \times n$ . This iterative procedure is known as the Arnoldi iteration, an important step in the GMRES algorithm discussed in Section 16.1.5.

A Gram-Schmidt procedure, described in Section 17, is used to successively subtract from the  $i$ -th column of  $\mathbf{A}\hat{\mathbf{Q}}_n$  the components parallel to the first  $i$  columns of  $\hat{\mathbf{Q}}_n$  in order to find the new rightmost column in  $\hat{\mathbf{Q}}_{n+1}$ :

$$\vec{q}_{i+1} = \mathbf{A}\vec{q}_i \quad (16.43a)$$

$$\vec{q}_{i+1} = \vec{q}_{i+1} - \vec{q}_j^* \vec{q}_{i+1} \vec{q}_j \quad \text{repeat for } j = 1, \dots, i \quad (16.43b)$$

$$\vec{q}_{i+1} = \frac{\vec{q}_{i+1}}{\|\vec{q}_{i+1}\|_2} \quad (16.43c)$$

In other words, an orthonormal basis for  $\mathbf{A}\hat{\mathbf{Q}}_n$  is found using the basis vectors in  $\hat{\mathbf{Q}}_n$  plus one new flexible vector  $\vec{q}_{n+1}$  (because we could not guarantee that  $\hat{\mathbf{Q}}_n$  would lie in the column space of  $\mathbf{A}$ ). Thus, the Arnoldi iteration increases

the dimension of  $\hat{\mathbf{Q}}$  by 1 each iteration. For the very first iteration,  $\hat{\mathbf{Q}}_n$  is a column vector of length  $m$ , and can be determined starting from any arbitrary vector  $\vec{b}$ , which the GMRES method selects as the initial residual assuming  $\vec{x}_0 = \vec{0}$ , in which case  $\vec{b}$  is the same vector in Eq. (16.2). If the Arnoldi iteration is performed  $m$  times, then the full factorization in Eq. (16.41) will be obtained.

From Eq. (16.43a), each new vector  $\vec{q}_{i+1}$  is obtained by finding an orthonormal basis for  $\langle \vec{q}_0, \mathbf{A}\vec{q}_1, \dots, \mathbf{A}\vec{q}_i \rangle$ . Hence,  $\hat{\mathbf{Q}}_{n+1}$  represents an orthonormal basis for the Krylov space  $\mathcal{K}_{n+1}$ ,

$$\mathcal{K}_{n+1} = \text{span}\{\vec{b}, \mathbf{A}\vec{b}, \dots, \mathbf{A}^n \vec{b}\}. \quad (16.44)$$

The most important interpretation of the Arnoldi iteration is that it is a method by which to construct orthonormal bases for successive Krylov subspaces. In other words, the Arnoldi iteration finds the reduced QR factorization of the matrix whose columns are the vectors in the Krylov subspace in Eq. (16.44). Defining the Krylov matrix  $\mathbf{K}_n$  with columns corresponding to the vectors in the Krylov space  $\mathcal{K}_n$ , the Arnoldi iteration generates

$$\mathbf{K}_n = \hat{\mathbf{Q}}_n \hat{\mathbf{R}}_n. \quad (16.45)$$

However, neither  $\mathbf{K}_n$  or  $\hat{\mathbf{R}}_n$  are explicitly formed — doing so would result in the columns of  $\mathbf{K}_n$  being nearly linearly dependent, since the explicit construction of a Krylov space is equivalent to a form of power iteration.

### 16.1.5 The GMRES Method

The GMRES algorithm is one of the most widely used iterative algorithms that alleviates the SPD requirement of the SD and CG methods discussed in Sections 16.1.2 and 16.1.3. Like the SD and CG methods, the GMRES method is a Krylov subspace iterative method. However, this method does not rely on the concepts of a step length and search direction. Instead, the  $k$ -th iterate is obtained by finding the vector  $\vec{x}_k$  restricted to the Krylov space  $\mathcal{K}_k$  defined in Eq. (16.44) that minimizes the  $L^2$  norm of the residual, or

$$\min_{\vec{x}_k \in \mathcal{K}_k} \|\mathbf{A}\vec{x}_k - \vec{b}\|_2. \quad (16.46)$$

$\vec{x}_k$  can be ensured to be in  $\mathcal{K}_k$  by requiring that  $\vec{x}_k$  be in the column space of the Krylov matrix  $\mathbf{K}_k$ . This can be ensured by replacing  $\vec{x}_k$  by  $\mathbf{K}_k \vec{c}$  for some vector  $\vec{c}$ , since matrix-vector multiplication is equivalent to a linear combination of the columns of the matrix,

$$\min_{\vec{x}_k \in \mathcal{K}_k} \|\mathbf{A}\mathbf{K}_k \vec{c} - \vec{b}\|_2. \quad (16.47)$$

However, as-written, Eq. (16.47) is numerically unstable, since explicit formation of  $\mathbf{K}_k$  is equivalent to power iteration, and the columns of  $\mathbf{K}_k$  become very nearly linearly independent. Instead of forming  $\mathbf{K}_k$ , the Arnoldi iteration discussed in Section 16.1.4 is used to require  $\vec{x}_k$  be in the column space of  $\hat{\mathbf{Q}}_k$  (which is the same as the column space of  $\mathbf{K}_k$ , but much better conditioned). This involves the same trick used in Eq. (16.47) by replacing  $\vec{x}_k$  by  $\hat{\mathbf{Q}}_k \vec{y}$  for some other vector  $\vec{y}$ . Eq. (16.45) is used to construct a QR factorization of  $\mathbf{K}_k$ , so Eq. (16.47) can equivalently be written as:

$$\min \left\| \mathbf{A} \hat{\mathbf{Q}}_k \vec{y} - \vec{b} \right\|_2, \quad (16.48a)$$

$$\min \left\| \hat{\mathbf{Q}}_{k+1} \tilde{\mathbf{H}}_k \vec{y} - \vec{b} \right\|_2, \quad (16.48b)$$

$$\min \left\| \tilde{\mathbf{H}}_k \vec{y} - \hat{\mathbf{Q}}_{k+1}^* \vec{b} \right\|_2, \quad (16.48c)$$

$$\min \left\| \tilde{\mathbf{H}}_k \vec{y} - \|\vec{b}\|_2 \vec{e}_1 \right\|_2. \quad (16.48d)$$

From Eq. (16.42), Eq. (16.48a) can be written as Eq. (16.48b), while invariance of unitary multiplication in the  $L^2$  norm is used to obtain Eq. (16.48c). Because  $\vec{b}/\|\vec{b}\|$  was the selection made for  $\vec{q}_1$ , and because the columns in  $\mathbf{Q}$  are orthonormal, Eq. (16.48c) simplifies to Eq. (16.48d), the form most commonly shown. In the  $k$ -th iteration, Eq. (16.48d) is solved for  $\vec{y}$ , then  $\vec{x}_k$  is obtained by

$$\vec{x}_k = \hat{\mathbf{Q}}_k \vec{y}. \quad (16.49)$$

In other words, for each GMRES iteration, one Arnoldi iteration is performed to compute the orthonormal basis for  $\mathcal{K}_k$ , then a least squares problem is solved to find the  $\vec{x}_k$  that minimizes the  $L^2$  norm of the residual in this space, using the orthonormal basis instead of  $\mathbf{K}_k$  directly. The least-square problem is of size  $(n+1) \times n$ , i.e. there are  $n+1$  conditions but only  $n$  unknowns.

The objective of solving a least-squares problem is to minimize the residual for an over-determined problem, i.e.  $\mathbf{A}$  has more rows than columns. In solving a least-squares problem of the general form  $\mathbf{A}\vec{x} = \vec{b}$ , the RHS vector is in general not in the column space of  $\mathbf{A}$ , so the object is to find  $\vec{x}$  such that  $\vec{b}$  is as close to the column space of  $\mathbf{A}$  as possible. This can be achieved by selecting the point  $\vec{x}$  such that  $\vec{b} - \mathbf{A}\vec{x}$  is orthogonal to the column space of  $\mathbf{A}$ . Therefore, least squares problems solving  $\mathbf{A}\vec{x} = \vec{b}$  solve

$$\mathbf{A}^* (\vec{b} - \mathbf{A}\vec{x}) = 0. \quad (16.50)$$

The GMRES method converges monotonically because with each iteration, the space over which the norm of the residual is minimized increases in dimension, so the norm of the residual always decreases (or stays the same) from one iteration to the next. Similar to the CG method, the GMRES method is a direct method if applied  $m$  times in infinite precision arithmetic, since then the basis for  $\mathcal{K}_m$  includes all of  $\mathbb{R}^m$ . A more specific convergence statement can be obtained by expressing the residual minimization process as a polynomial optimization. The iterate  $\vec{x}_k$  can be written as a linear sum of the vectors in  $\mathcal{K}_k$ ,

$$\vec{x}_k = \sum_{i=1}^k C_i \mathbf{A}^{i-1} \vec{b}. \quad (16.51)$$

Then, Eq. (16.46) can be written as a polynomial  $\mathcal{P}_k$  of  $\mathbf{A}$  acting on  $\vec{b}$ ,

$$\min \|\mathcal{P}_k(\mathbf{A})\vec{b}\|_2 \quad (16.52)$$

Select a normalization  $\mathcal{P}_k(0) = 1$ . From the triangle inequality, and because  $\vec{r}_k \equiv \mathcal{P}_k(\mathbf{A})\vec{b}$ , Eq. (16.52) gives

$$\|\vec{r}_k\| \leq \|\mathcal{P}_k(\mathbf{A})\| \|\vec{b}\| \quad (16.53a)$$

$$\frac{\|\vec{r}_k\|}{\|\vec{b}\|} \leq \min_{p \in \mathcal{P}_k} \|p(\mathbf{A})\|. \quad (16.53b)$$

Unless  $\vec{b}$  has a very special structure,  $\|\mathcal{P}_k(\mathbf{A})\|$  will dictate the convergence, giving Eq. (16.53).  $\mathbf{A}$  is nondefective if the algebraic multiplicity of its eigenvalues (number of a repeated eigenvalue) does not exceed the geometric multiplicity of its eigenvalues (dimensions of eigenspace corresponding to eigenvector), then  $\mathbf{A}$  is diagonalizable as  $\mathbf{A} = \mathbf{X}\mathbf{\Lambda}\mathbf{X}^{-1}$ , where  $\mathbf{\Lambda}$  is a diagonal matrix with the eigenvalues of  $\mathbf{A}$  on its diagonal. Then,

$$\mathcal{P}_k(\mathbf{A}) = \mathbf{X}\mathcal{P}_k(\mathbf{\Lambda})\mathbf{X}^{-1}, \quad (16.54)$$

and Eq. (16.53b) can be written equivalently as follows, again using the triangle inequality,

$$\frac{\|\vec{r}_k\|}{\|\vec{b}\|} \leq \kappa(\mathbf{X}) \min_{p \in \mathcal{P}_k} \max_{\lambda} \|p(\lambda)\|, \quad (16.55)$$

where the condition number definition  $\kappa(\mathbf{X}) \equiv \|\mathbf{X}\|\|\mathbf{X}^{-1}\|$  has been used. The GMRES method will converge quickly if the eigenvalues of  $\mathbf{A}$  are clustered and located relatively far from the origin and  $\mathbf{X}$  is well-conditioned. These conditions may not necessarily be obtained, in which case an effective preconditioner must be used to obtain convergence in a practical number of iterations. Preconditioners are discussed in Section 16.3.

## 16.2 Jacobian Calculations

The MOOSE framework was originally based on the Jacobian-Free Newton Krylov (JFNK) method, which calculates the Jacobian in Eq. (16.5) as a FD approximation of the derivative of the residual. Rather than use a JFNK method, Pronghorn uses the relatively new AD features in MOOSE to calculate the Jacobian [201]. Operator overloads are defined for all of the fundamental arithmetic operators, such as addition, subtraction, multiplication, and division, as well as for elementary functions such as exponentials and logarithms. These overloads then systematically apply the chain rule to the sequence of arithmetic operations used to construct the residual  $\vec{R}$  to compute a working precision accurate estimate of the derivatives of  $\vec{R}$  with respect to  $\vec{u}$ . The use of AD enables faster application development by avoiding the by-hand derivation of nonlinear residual derivatives and in many cases decreases the number of linear and nonlinear iterations due to the more accurate Jacobian evaluation. Specifically within Pronghorn, the use of AD allows seamless interchange between different sets of solution variables without any modifications to the kernel and BC classes.

## 16.3 Preconditioning

The convergence of most iterative linear solution schemes depends on the condition number of  $\mathbf{A}$  and the location and clustering of eigenvalues. A preconditioner is a matrix  $\mathbf{M}$  that when applied to Eq. (16.2) reduces the condition number and/or shifts the eigenvalue spectrum to conditions more ideal for convergence. Preconditioning is essential to the successful use of most iterative methods. A general-purpose preconditioner for all types of problems is unlikely to exist, and the selection of an appropriate preconditioner requires an understanding of the problem and possible scoping investigations.

There are three general types of preconditioning processes — left preconditioning as in Eq. (16.56a), right preconditioning as in Eq. (16.56b), and split preconditioning as in Eq. (16.56c), where the preconditioner itself is factored into  $\mathbf{M} = \mathbf{M}_1\mathbf{M}_2$ :

$$\mathbf{M}^{-1}\mathbf{A}\vec{x} = \mathbf{M}^{-1}\vec{b}, \quad (16.56a)$$

$$\mathbf{A}\mathbf{M}^{-1}(\mathbf{M}\vec{x}) = \vec{b}, \quad (16.56b)$$

$$\mathbf{M}_1^{-1}\mathbf{A}\mathbf{M}_2^{-1}(\mathbf{M}_2\vec{x}) = \mathbf{M}_1^{-1}\vec{b}. \quad (16.56c)$$

Methods based on minimizing residuals, such as the GMRES method, are typically combined with right preconditioning so that the residual is unchanged. A good choice for preconditioner has as similar structure to  $\mathbf{A}$  as possible, but with a simple solution to  $\mathbf{M}\vec{c} = \vec{d}$ . Any of the preconditioners available in PETSc can be used in Pronghorn; refer to the PETSc documentation to learn more about these options [202].

## 17 Mathematical Definitions and Concepts

This section discusses some mathematical definitions and concepts that appear throughout this manual.

### The Material Derivative

A material derivative represents the total derivative of a quantity from the Eulerian perspective, and hence accounts for both local changes ( $\partial/\partial t$ ) and changes as the fluid particle moves about ( $\vec{V} \cdot \nabla$ ). The material derivative is defined as

$$\frac{d(\cdot)}{dt} \equiv \frac{\partial(\cdot)}{\partial t} + \vec{V} \cdot \nabla(\cdot). \quad (17.1)$$

### Important Classes of Matrices and Other Definitions

A matrix is Hermitian if

$$A^* = A, \quad (17.2)$$

where a \* superscript denotes the Hermitian complex conjugate transpose, i.e. the transpose of  $A$  with all imaginary components negated. For real matrices, there are no imaginary components, and Eq. (17.2) becomes

$$A^T = A. \quad (17.3)$$

In other words, a Hermitian matrix is the complex equivalent of a symmetric matrix. A matrix is normal if

$$\mathbf{A}^* \mathbf{A} = \mathbf{A} \mathbf{A}^*. \quad (17.4)$$

Hermitian matrices are therefore normal matrices. A matrix can be indefinite, positive definite, or negative definite,

$$\vec{x}^* \mathbf{A} \vec{x} \text{ is } \begin{cases} 0 & \text{indefinite} \\ > 0 & \text{positive definite} \\ < 0 & \text{negative definite} \end{cases}, \quad (17.5)$$

for some nonzero vector  $\vec{x}$ . A matrix is singular if any of the following equivalent statements are true — 1)  $\mathbf{A} \vec{x} = \vec{0}$  for some nonzero vector  $\vec{x}$ , i.e. the nullspace of  $\mathbf{A}$  contains more than just the zero vector such that a system  $\mathbf{A} \vec{x} = \vec{b}$  does not have a unique solution; 2)  $\mathbf{A}^{-1}$  is not defined; 3)  $\det(\mathbf{A}) = 0$ ; or 4)  $\mathbf{A}$  has a zero eigenvalue.

A unitary matrix  $\mathbf{Q}$  is a square matrix in  $\mathbb{C}^{m \times m}$  that satisfies:

$$\mathbf{Q}^* = \mathbf{Q}^{-1}. \quad (17.6)$$

In other words,  $\mathbf{Q}^* \mathbf{Q} = \mathbf{I}$ . Therefore, the columns of a unitary matrix represent an orthonormal basis for  $\mathbb{C}^m$ . Multiplication by a unitary matrix does not change the magnitude of the  $L^2$  vector norm, and instead represents a rigid rotation or reflection based on the sign of the determinant of  $\mathbf{Q}$ ,

$$\begin{aligned}\|\vec{x}\|_2 &\equiv \vec{x}^* \vec{x} \\ \|\mathbf{Q}\vec{x}\|_2 &\equiv \vec{x}^* \underbrace{\mathbf{Q}^* \mathbf{Q}}_{\mathbf{I}} \vec{x}.\end{aligned}\tag{17.7}$$

A Hessenberg matrix  $\mathbf{H}$  is a diagonal matrix with one nonzero sub-diagonal (upper Hessenberg) or one nonzero super-diagonal (lower Hessenberg). For example, an upper Hessenberg matrix of size  $4 \times 4$  has the form

$$\mathbf{H} = \begin{bmatrix} \times & \times & \times & \times \\ \times & \times & \times & \times \\ & \times & \times & \times \\ & & \times & \times \end{bmatrix}.\tag{17.8}$$

## Norms

A vector norm is a measure of the “size” of a vector. The  $p$ -norm, also written as the  $L^p$  norm, of a vector  $\vec{x} \in \mathbb{C}^n$  is defined as

$$\|\vec{x}\|_p \equiv \left( \sum_{i=1}^n |x_i|^p \right)^{1/p}.\tag{17.9}$$

A matrix norm may be defined based on norms induced by vectors. The  $(m, n)$   $p$ -norm of a matrix  $\mathbf{A} \in \mathbb{C}^{m \times n}$  is defined as the maximum factor by which  $\mathbf{A}$  can stretch a unit vector,

$$\|\mathbf{A}\|_{(m,n)} \equiv \sup_{\vec{x} \in \mathbb{C}^n, \|\vec{x}\|=1} \|\mathbf{A}\vec{x}\|_{(m)}.\tag{17.10}$$

## Suffix Notation

Suffix notation, sometimes referred to as “Einsteinian” notation, is commonly used in mechanics fields to shorten summation notation. Suffix notation obeys the following rules —

1. A single appearance of a suffix in a term does not get summed.
2. Two appearances of a suffix in a term indicates summation (usually up to 3, the typical number of spatial dimensions used).
3. No more than two appearances of the same suffix can appear in a single term.

For example, a dot product between a vector  $\vec{a}$  and  $\vec{b}$  is represented in suffix notation as:

$$\vec{a} \cdot \vec{b} \equiv a_i b_i.\tag{17.11}$$

A cross product can be represented in suffix notation as

$$(\vec{a} \times \vec{b})_i \equiv \epsilon_{ijk} a_j b_k,\tag{17.12}$$

where  $\epsilon_{ijk}$  is the permutation, defined as

$$\epsilon_{ijk} = \begin{cases} +1 & \text{cyclic permutation of } 1, 2, 3 \\ -1 & \text{anti-cyclic permutation of } 1, 2, 3 \\ 0 & \text{otherwise} \end{cases} . \quad (17.13)$$

Another useful term that appears when using suffix notation is the Kronecker delta, defined as

$$\delta_{ij} = \begin{cases} +1 & i = j \\ 0 & i \neq j \end{cases} . \quad (17.14)$$

## Vectors and Tensors

A vector is an ordered triplet (for 3-D) of numbers, together with a rule defining how the vector transforms under a change of coordinate axes. This rule can be easily obtained by considering two different sets of axes, each composed of three mutually orthogonal axes. Denoting one of these axes with primes and the other without, a vector can be expressed equivalently in either frame,

$$\vec{r} = x_k \vec{e}_k = x_{k'} \vec{e}_{k'} . \quad (17.15)$$

Dotting this expression with either  $\vec{e}_{i'}$  or  $\vec{e}_i$ ,

$$x_{i'} = \vec{e}_k \cdot \vec{e}_{i'} x_k = a_{ik} x_k , \quad (17.16a)$$

$$x_i = \vec{e}_{k'} \cdot \vec{e}_i x_{k'} = a_{ki} x_{k'} , \quad (17.16b)$$

where  $a_{ik}$  is the transformation rule. As long as a matrix satisfies the transformation rule in Eq. (17.16), the matrix is a vector. Because the transformation matrices are independent of time, they can be differentiated with respect to time (or multiplied by constants) to show that physical quantities such as velocities and forces are also vectors, so long as position is a vector.

Tensors  $t$  are defined in a similar manner. A tensor is essentially a matrix that transforms one vector to another vector with the following transformation rule, where  $a$  is defined as in Eq. (17.16). Tensors therefore transform vectors into new vector spaces,

$$t_{ik'} = a_{ij} a_{kl} t_{jl} . \quad (17.17)$$

A symmetric tensor  $S_{ij}$  satisfies the relation  $S_{ij} = S_{ji}$ , while an antisymmetric tensor  $A_{ij}$  satisfies the relation  $A_{ij} = -A_{ji}$ . The product of a symmetric tensor with an asymmetric tensor must equal zero,

$$S_{ij} A_{ij} \rightarrow S_{ji} A_{ij} \rightarrow -S_{ji} A_{ji} \rightarrow -S_{ij} A_{ij} , \quad (17.18)$$

where the dummy indices were swapped on the last term.

## Conditioning

The convergence behavior of many iterative solution methods depends strongly on the “conditioning” of the problem to be solved. Consider a generic function  $f$  that maps some input data  $x \in X$  to some output space  $Y$ . This function is well-conditioned if a relatively small change in the input data produces a correspondingly small change in the output data. This behavior can be captured with the definition of a condition number  $\kappa$

$$\begin{aligned}\kappa &\equiv \sup_{\delta x} \frac{\|f(x + \delta x) - f(x)\| / \|\delta x\|}{\|f(x)\| / \|x\|} \\ &= \sup_{\delta x} \frac{\|\partial f(x) / \partial x\|}{\|f(x)\| / \|x\|} .\end{aligned}\tag{17.19}$$

A large condition number indicates that the problem is very sensitive to the input. By forming a first-order accurate FD approximation to  $f(x + \delta x) - f(x)$ , the condition number can also be written in terms of the Jacobian of the problem,  $\partial f(x) / \partial x$ . Eq. (17.19) normalizes the derivative of  $f$  to as to represent a relative change (rather than an absolute change), which is usually of more important in floating point arithmetic where the introduced errors are relative, rather than absolute. Of most interest to the present application is the condition number of the solution of a linear system such as in Eq. (16.2). The relative condition number for matrix-vector multiplication is

$$\begin{aligned}\kappa &= \sup_{\delta \vec{x}} \frac{\|\mathbf{A}(\vec{x} + \delta \vec{x}) - \mathbf{A}\vec{x}\| / \|\vec{x}\|}{\|\mathbf{A}\vec{x}\| / \|\delta \vec{x}\|} \\ &= \frac{\|\mathbf{A}\|}{\|\mathbf{A}\vec{x}\| / \|\vec{x}\|} ,\end{aligned}\tag{17.20}$$

where linearity of Eq. (16.2) and the definition of a matrix norm induced by a vector norm in Eq. (17.10) were used. Because  $\|\vec{x}\| / \|\mathbf{A}\vec{x}\| \leq \|\mathbf{A}^{-1}\|$ , the condition number for matrix-vector multiplication simplifies to an inequality independent of the input  $\vec{x}$ ,

$$\kappa \leq \|\mathbf{A}\| \|\mathbf{A}^{-1}\| .\tag{17.21}$$

Matrix-vector multiplication of the form  $\mathbf{A}\vec{x}$  is of similar form to linear system solution of the form  $\mathbf{A}^{-1}\vec{b}$ , and because Eq. (17.21) is symmetric with respect to  $\mathbf{A}$  and its inverse, Eq. (17.21) is also the condition number for the solution of linear systems. A large condition number indicates that the problem (solving a linear system) is extremely sensitive to the input  $\vec{b}$ , which illustrates that a large condition number makes numerical solution more difficult when the solution occurs on a finite precision computer.

## Eigenvalues and Eigenvectors

The eigenvectors of  $\mathbf{A}$  are nonzero vectors  $\vec{v}$  that do not rotate (but may change magnitude) when  $\mathbf{A}$  is applied to them,

$$\mathbf{A}\vec{v} = \lambda\vec{v} ,\tag{17.22}$$

where  $\lambda$  is the eigenvalue corresponding to the eigenvector  $\vec{v}$ . The eigenvalue represents the scaling of  $\vec{v}$  when  $\mathbf{A}$  is applied to it. Provided a matrix is nondefective, a concise representation of all the eigenvalues and eigenvectors is formed in an eigenvalue decomposition,

$$\mathbf{A} = \mathbf{X}\mathbf{\Lambda}\mathbf{X}^{-1} ,\tag{17.23}$$

where  $\mathbf{X}$  is a matrix with columns equal to the eigenvectors of  $\mathbf{A}$  and  $\Lambda$  is a diagonal matrix with entries equal to the eigenvalues of  $\mathbf{A}$ . A Hermitian matrix has real eigenvalues. And not only are the eigenvalues of SPD matrices all real, they are positive.

A Hermitian matrix also has a full set of orthonormal eigenvectors, and are unitarily diagonalizable. Other matrices are also unitarily diagonalizable; the most general statement is that all *normal* matrices are unitarily diagonalizable. Any vector  $\vec{x}$  can be expressed as a linear combination of the orthonormal eigenvectors of a normal matrix,

$$\vec{x} = \sum_{j=1}^n C_j v_j, \quad (17.24)$$

where  $C_j$  are the coefficients in the linear sum. So, applying  $\mathbf{A}$  to an arbitrary vector  $\vec{x}$  is equivalent to applying  $\mathbf{A}$  to a linear combination of eigenvectors,

$$\mathbf{A}^i \vec{x} = \sum_{j=1}^n C_j \lambda_j^i \vec{x}_j. \quad (17.25)$$

Repeated application of  $\mathbf{A}$  will stretch  $\vec{x}$  in the direction of the eigenvector with the largest eigenvalue. If all of the eigenvalues of  $\mathbf{A}$  have magnitude less than unity, then the above result diminishes to zero as  $i \rightarrow \infty$ . Otherwise, the components with  $|\lambda_j| > 1$  will diverge. The spectral radius  $\rho(\mathbf{A})$  is a useful measure of the eigenvalues,

$$\rho(\mathbf{A}) \equiv \max_j |\lambda_j|. \quad (17.26)$$

Because eigenvectors are non-zero vectors,  $\lambda \mathbf{I} - \mathbf{A}$  must be singular,

$$\begin{aligned} \mathbf{A} \vec{v} &= \lambda \mathbf{I} \vec{v} \\ (\mathbf{A} - \lambda \mathbf{I}) \vec{v} &= 0. \end{aligned} \quad (17.27)$$

## The QR Factorization

A QR factorization forms an orthonormal basis for the spaces spanned by the successive columns of  $\mathbf{A}$ . In other words, a QR factorization generates orthonormal vectors  $\langle \vec{q}_1, \vec{q}_2, \dots, \vec{q}_n \rangle$  than span the space defined by the first  $i$  columns of  $\mathbf{A}$ . These orthonormal vectors are the columns of a unitary matrix  $\hat{\mathbf{Q}}$ , whose first  $i$  columns span the same space as the first  $i$  columns of  $\mathbf{A}$ . The QR factorization of a matrix  $\mathbf{A} \in \mathbb{C}^{m \times n}$ , with  $m \geq n$ , is

$$\mathbf{A} = \hat{\mathbf{Q}} \hat{\mathbf{R}}, \quad (17.28a)$$

$$\mathbf{A} \hat{\mathbf{R}}^{-1} = \hat{\mathbf{Q}}, \quad (17.28b)$$

where  $\hat{\mathbf{Q}}$  is a unitary matrix of size  $m \times n$  and  $\hat{\mathbf{R}}$  is an upper-triangular matrix of size  $n \times n$ . Eq. (17.28) is known as a “reduced” QR factorization of  $\mathbf{A}$ . An additional  $m - n$  orthonormal columns can be appended to  $\hat{\mathbf{Q}}$ , with additional zero rows appended to  $\hat{\mathbf{R}}$ , to form the full QR factorization, in which case the hat overbars in Eq. (17.28) are dropped and  $\mathbf{Q}$  is of size  $m \times m$  and  $\mathbf{R}$  of size  $m \times n$ . As evident in Eq. (17.28b), a QR factorization is equivalent to a triangular orthogonalization of  $\mathbf{A}$ , since the inverse of an upper triangular matrix is still upper triangular.

There are several common methods for computing the QR factorization of a matrix [203], but because only a conceptual understanding is required here, the classical Gram-Schmidt process is used for illustration. In this process,

the  $i$ -th column of  $\mathbf{Q}$  is obtained by subtracting from the  $i$ -th column of  $\mathbf{A}$  the components parallel to the  $i - 1$  previous columns of  $\mathbf{Q}$ , and then normalizing to a unit vector,

$$\vec{q}_i = \vec{a}_i - \sum_{j=1}^{i-1} \vec{q}_j^* \vec{a}_i \vec{q}_j, \quad (17.29a)$$

$$\vec{q}_i = \frac{\vec{q}_i}{\|\vec{q}_i\|_2}, \quad (17.29b)$$

where  $\vec{q}_i$  is the  $i$ -th column of  $\mathbf{Q}$  and  $\vec{a}_i$  is the  $i$ -th column of  $\mathbf{A}$ .

## 18 Notation

This section defines the symbols and mathematical notation used throughout this manual. The third column lists units for the term and the fourth column provides an equation number where the symbol is defined, if not conventional notation. In some cases, the same symbol has multiple interpretations that should be clear from context. For brevity, symbols introduced strictly for placeholder illustration purposes that are not re-used are omitted from these tables; their context should be clear from the discussion immediately surrounding their introduction.

### Greek Symbols

$\alpha$	Interphase convective heat transfer coefficient, <i>or</i> Diffusivity, <i>or</i> Hsu correlation parameter (Section 9 only), <i>or</i> Linear update step size (Section 16 only)	$\text{W/m}^3 \cdot \text{K}$ $\text{m}^2/\text{s}$ 1 1	Eq. (2.76) — Eqs. (9.48) and (9.47) —
$\alpha_{pg}$	Petrov-Galerkin scaling parameter	1	Eq. (15.15)
$\alpha_T$	Compressibility	Pa	Eq. (2.123)
$\alpha_w$	Within-bed fluid-to-wall convective coefficient	W/m	—
$\alpha_1$	Hsu correlation parameter	1	Eq. (9.46)
$\beta$	Expansivity	1/K	Eq. (2.65)
$\beta_n$	Chiew and Glandt correlation parameter	1	Eq. (13.4)
$\chi$	General function, <i>or</i> Switching method parameter	many 1	— Eq. (15.30)
$\tilde{\chi}$	Percentage reduction in porosity	1	—
$\delta$	Kronecker delta, <i>or</i> A differential change independent of end states	1 1	Eq. (17.14) —
$\tilde{\delta}_i$	Newton update for iteration $i$	many	Eq. (16.6)
$\tilde{\delta}_{ij}$	$1 - \delta_{ij}$	1	—
$\tilde{\delta}r$	Incremental distance vector	m	—
$\delta q$	Heat addition per unit mass	J/kg	—
$\delta w$	Work performed per unit mass	J/kg	—
$\varepsilon$	Porosity	1	Eq. (19.15)
$\varepsilon_{\min}$	Minimum porosity	1	—
$\varepsilon_{\text{pipe}}$	Pipe roughness	m	—
$\varepsilon_r$	Emissivity	1	—
$\varepsilon'_{r,s}$	Vortmeyer correlation parameter	1	Eq. (9.27)
$\varepsilon_{\text{wall}}$	Wall porosity	1	—
$\varepsilon_{\infty}$	Infinite-bed porosity	1	—
$\gamma$	Specific heat ratio	1	Eq. (4.19)
$\gamma_a$	Hsu 2-D correlation parameter, <i>or</i> Hsu 3-D correlation parameter	1 1	Eq. (9.50) Eq. (9.52)
$\Gamma$	Boundary	$\text{m}^2$	—
$\kappa$	Condition number	1	—
$\kappa_f$	Effective fluid thermal conductivity	W/m·K	Eq. (2.81)
$\tilde{\kappa}_f$	Thermal dispersion thermal conductivity	W/m·K	Eq. (2.80)
$\kappa_{\text{fluid conduction}}$	Solid-to-fluid-to-solid conduction component of $\kappa_s$	W/m·K	—
$\kappa_{\text{radiation}}$	Solid-to-solid radiation component of $\kappa_s$	W/m·K	—
$\kappa_s$	Effective solid thermal conductivity	W/m·K	Eq. (2.87)
$\kappa_{\text{solid conduction}}$	Solid-to-solid contact conduction component of $\kappa_s$	W/m·K	—
$\lambda$	Second coefficient of viscosity, <i>or</i> Solid-to-fluid thermal conductivity ratio, <i>or</i> Eigenvalue, <i>or</i>	Pa·s 1 many	— Eq. (9.4) Eq. (17.22)

	Wavelength (Section 19.3 only)	m	—
$\lambda_{mfp}$	Momentum exchange mean free path	m	—
$\tilde{\lambda}_{mfp}$	Modified mean free path	m	—
$\Lambda$	Normalized radiation thermal conductivity, <i>or</i> Diagonal matrix of eigenvalues	1 many	Eq. (9.14) Eq. (17.23)
$\mu$	Dynamic viscosity	Pa·s	—
$\tilde{\mu}$	Brinkman viscosity	Pa·s	—
$\nu$	Specific volume	m <sup>3</sup> /kg	Eq. (2.47)
$\nu_p$	Poisson ratio	1	—
$\omega$	Wave pulsation	1/s	Eq. (19.67)
$\tilde{\omega}$	Vorticity	1/s	Eq. (2.18)
$\Omega$	Domain	m <sup>3</sup>	—
$\rho$	Density	kg/m <sup>3</sup>	—
$\phi$	Finite element shape function	1	—
$\phi_{g,f}$	Gravitational potential	1/s <sup>2</sup>	Eq. (19.38)
$\Phi$	Generic field	many	—
$\Psi$	Weight function	1	—
$\tilde{\Psi}$	Petrov-Galerkin shape function	1	Eq. (15.15)
$\Psi^*$	Element-discontinuous weight function	1	—
$\Psi_I$	Kunii and Smith correlation parameter	1	Eq. (9.18)
$\Psi_V$	Vortmeyer correlation parameter	1	Eq. (9.24)
$\sigma$	Stress tensor, <i>or</i> Stefan-Boltzmann constant	N/m <sup>2</sup> W/m <sup>4</sup> ·K	Eq. (2.9) —
$\tau$	Deviatoric stress tensor	N/m <sup>2</sup>	Eq. (2.26)
$\tau_{\text{advective}}$	Advection-dominated component of $\tau_{SUPG}$	s	—
$\tau_{\text{advective, com}}$	Advection-dominated compressible component of $\tau_{SUPG}$	s	—
$\tau_{\text{advective, inc}}$	Advection-dominated incompressible component of $\tau_{SUPG}$	s	—
$\tau_c$	Continuity equation $\tau_{SUPG}$ component	s	Eq. (15.23)
$\tau_{cd}$	Convection-diffusion stabilization parameter	s	—
$\tau_{\text{diffusive}}$	Diffusion-dominated component of $\tau_{SUPG}$	s	—
$\tau_e$	Energy equation $\tau_{SUPG}$ component	s	Eq. (15.23)
$\tau_{SUPG}$	SUPG stabilization parameter matrix	s	—
$\tau_{\text{temporal}}$	Transient-dominated component of $\tau_{SUPG}$	s	—
$\tau_u$	Momentum equation $\tau_{SUPG}$ component	s	Eq. (15.23)
$\tau_v$	Vortmeyer correlation parameter	1	Eq. (9.25)
$\theta$	Azimuthal coordinate	1	—
$\Upsilon$	Constant multiplier on $\tilde{\mu}$	1	Eq. (7.1)
$\varepsilon$	Permutation tensor	1	Eq. (17.13)
$\varepsilon_l$	Linear solution absolute tolerance	1	—
$\varepsilon_n$	Nonlinear solution absolute tolerance	1	—
$\phi$	Contact area fraction, deformation ratio	1	—
$\varsigma$	Function in weighted residual	many	Eq. (14.4)
$\xi$	Antisymmetric stress tensor	N/m <sup>2</sup>	Eq. (2.16)
$\xi_i$	Position vector in master finite element	1	—
$\zeta$	Bulk viscosity	Pa·s	Eq. (2.27)

## English Symbols

$a$	$\kappa_s$ correlation parameter, <i>or</i> Tensor transformation matrix (Section 17 only) Wave speed (Section 19.3 only), <i>or</i>	1 many m/s	Eq. (9.8) Eq. (17.16) Eq. (19.68)
$a_w$	Wetted area per unit length	m	Eq. (2.77)
$A$	Linear friction pressure drop coefficient	1	Eq. (6.3)

$A_c$	Churchill correlation parameter	1	Eq. (6.15)
$A_w$	Eisfeld correlation parameter	1	Eq. (6.13a)
$\mathbf{A}$	Matrix in linear system	many	Eq. (16.2)
$\mathbf{A}_i$	$i$ -th inviscid flux Jacobian matrix	many	Eq. (2.111)
$\mathcal{A}$	Second-order viscous stress approximation tensor	$1/\text{m}^2$	Eq. (19.43)
$\vec{b}$	Body force vector, i.e. $\vec{g}$ if only gravitational, <i>or</i> Linear RHS vector	$\text{m}/\text{s}^2$ many	— Eq. (16.2)
$B$	Quadratic friction pressure drop coefficient, <i>or</i> Geometric shape factor, <i>or</i> Hsu correlation parameter (Section 9.3.2 only), <i>or</i>	1 1 1	Eq. (6.3) Eq. (9.7) Eqs. (9.47) and (9.48)
$B_c$	Churchill correlation parameter	1	Eq. (6.16)
$B_n$	Lewis and Nielsen correlation parameter	1	Eq. (13.6)
$B_w$	Eisfeld correlation parameter	1	Eq. (6.13b)
$B_r$	Radiation transmission number	1	Eq. (9.29)
$\mathbf{B}$	Matrix splitting application matrix	many	Eq. (16.23)
$\mathcal{B}$	Third-order viscous stress approximation tensor	$\text{s}/\text{m}^3$	Eq. (19.43)
$Br$	Brinkman number	1	Eq. (2.135)
$c$	Fourth-order Newtonian closure tensor, <i>or</i> Speed of sound	$\text{N}\cdot\text{s}/\text{m}^2$ $\text{m}/\text{s}$	Eq. (2.23) —
$\vec{c}$	Generic vector	many	—
$C$	Approximate solution expansion coefficients	many	Eq. (14.1)
$C_p$	Isobaric specific heat	$\text{J}/\text{kg}$	Eq. (2.62)
$C_v$	Isochoric specific heat	$\text{J}/\text{kg}$	Eq. (2.63)
$C_0$	Kunii and Smith correlation parameter, <i>or</i> Linear Peclet coefficient	1 1	Eq. (9.17) Eq. (10.2)
$\mathcal{C}$	Third-order fluctuating velocity approximation tensor	$\text{m}/\text{s}$	Eq. (19.44)
$\mathbb{C}^n$	Space of complex numbers of dimension $n$	1	—
$d$	Distance from a wall	$\text{m}$	Eq. (5.3)
$d_{\text{bed}}$	Cylindrical bed diameter	$\text{m}$	—
$d_c$	Diameter of pebble-pebble contact area	$\text{m}$	—
$d_p$	Pebble diameter	$\text{m}$	—
$D$	Hydraulic diameter	$\text{m}$	Eq. (5.18)
$\mathbf{D}$	Generic diagonal matrix	many	—
$\mathbf{D}_{lg}$	Local-to-global element mapping	1	—
$\mathbb{D}$	Packed bed diffusivity	$\text{m}^2/\text{s}$	—
$\mathbb{D}_f$	Fluid diffusivity	$\text{m}^2/\text{s}$	—
$e$	Symmetric stress tensor, <i>or</i> Internal energy per unit mass, <i>or</i> Nonlinear error (Section 14 only)	$\text{N}/\text{m}^2$ $\text{J}/\text{kg}$ many	Eq. (2.15) — Eq. (14.9)
$\vec{e}_i$	Mutually orthogonal basis vectors, $i = 1, 2, 3$	1	—
$E$	Total energy per unit mass, <i>or</i> Young's modulus	$\text{J}/\text{kg}$ $\text{Pa}$	Eq. (2.40) —
$Ec$	Eckert number	1	Eq. (2.134)
$\mathcal{E}$	Second-order pressure approximation tensor	1	Eq. (19.45)
$\vec{\epsilon}$	Linear error vector	many	Eq. (16.11)
$f$	Phase function, <i>or</i> Forcing term, <i>or</i> Wave frequency (Section 19.3 only)	1 many $1/\text{s}$	Eq. (19.3) — —
$\vec{f}$	Stress vector	$\text{N}/\text{m}^2$	Eq. (2.9)
$\vec{f}_s$	Surface tension force vector	$\text{N}$	—
$F$	Collinear force	$\text{N}$	Eq. (9.11)
$F_E$	Radiation exchange factor	1	—
$\vec{F}_i$	Inviscid flux vector in the $i$ -th dimension	many	Eq. (2.102)

$\vec{g}$	Gravitational acceleration vector	$\text{m/s}^2$	—
$\vec{G}_i$	Diffusive flux vector in the $i$ -th dimension	many	Eq. (2.104)
$h$	Enthalpy per unit mass	J/kg	Eq. (2.45)
$h_c$	Convective heat transfer coefficient	$\text{W/m}^2$	—
$h_e$	Element size	m	—
$h_{rs}$	Radiation heat transfer coefficient between solid surfaces	$\text{W}\cdot\text{K}^2/\text{m}^3$	Eq. (9.19)
$h_{rv}$	Radiation heat transfer coefficient in voids	$\text{W}\cdot\text{K}^2/\text{m}^3$	Eq. (9.20)
$h_v$	Vortmeyer correlation parameter	1	Eq. (9.26)
$H$	Total enthalpy per unit mass,	J/kg	Eq. (2.46)
$H^l(\Omega)$	Hilbert-Sobolev space	1	—
$\hat{H}$	Radial or axial extent of bed	m	—
$\mathbf{H}$	Hessenberg matrix	many	—
$\hat{\mathbf{H}}$	Portion of Hessenberg matrix	many	—
$\tilde{\mathbf{H}}$	Arnoldi iteration Hessenberg matrix	many	—
$i$	Nonlinear loop iteration index, <i>or</i>	1	—
	Generic index	1	—
$\mathbf{I}$	identity matrix	1	—
$\mathbf{J}$	Jacobian matrix of the Newton solve	many	Eq. (16.5)
$\mathcal{J}$	Jacobian matrix of physical-to-master transformation	m	Eq. (14.20)
$k$	Thermal conductivity, <i>or</i>	$\text{W/m}\cdot\text{K}$	—
	Linear loop iteration index (Section 16 only), <i>or</i>	1	—
	Wave number (Section 19.3 only)	1/m	Eq. (19.66)
$\vec{k}$	Wave number vector	$\text{W/m}\cdot\text{K}$	—
$K$	Form loss coefficient, <i>or</i>	1	—
	Generic operator	many	Eq. (14.2)
$K_T$	Isothermal bulk modulus	Pa	Eq. (2.70)
$Kn$	Knudsen number	1	Eq. (2.1)
$\mathbf{K}$	Stiffness matrix	many	Eq. (14.29)
$\mathbf{K}_k$	Krylov matrix of dimension $k$	many	—
$\mathbf{K}_{ij}$	Diffusive flux Jacobian matrix	many	Eq. (2.112)
$\mathcal{K}$	Permeability tensor	$1/\text{m}^2$	Eq. (19.52)
$\mathcal{K}_D$	Normalized gas diffusion thermal conductivity	1	Eq. (9.5)
$\mathcal{K}_k$	Krylov space of dimension $k$	many	Eq. (16.44)
$\mathcal{K}_R$	Normalized radiation thermal conductivity	1	Eq. (9.13)
$\mathcal{K}_{SF}$	Normalized radiation-conduction conductivity	1	—
$l$	Pore flow length scale	m	—
$\ell$	Length scale	m	—
$L$	Engineering flow length scale, <i>or</i>	m	—
$\mathbf{L}$	Generic lower triangular matrix	many	—
$\mathcal{L}$	Fourth-order fluctuating velocity approximation tensor	1	Eq. (19.44)
$M$	Molar mass	kg/mol	—
$\mathbf{M}$	Chain rule differentiation matrix, <i>or</i>	many	Eq. (2.121)
	Mass matrix	many	Eq. (14.28)
	Preconditioner matrix (Section 16 only)	many	—
$\mathcal{M}$	Third-order pressure approximation tensor	m/Pa	Eq. (19.45)
$n_{el}$	Number of elements	1	—
$n_p$	Number of particles	1	—
$n_{sd}$	Number of spatial dimensions	1	—
$n_{qp}$	Number of quadrature points	1	—
$\hat{n}$	Unit outward normal vector	m	—
$N$	Constant in Eq. (5.5), <i>or</i>	1	—
	Number of materials to be mixed, <i>or</i>	1	—
	Number of shape functions in approximation	1	—
$N_c$	Coordination number	1	—

$N_A$	Number of spheres per unit area	$1/m^2$	Table 4
$N_L$	Number of spheres per unit length	$1/m$	Table 4
$Nu$	Nusselt number	1	Eq. (2.79a)
$Nu_h$	Nusselt number	1	Eq. (2.79b)
$Nu_{lam}$	Gnielinski correlation parameter	1	Eq. (8.5)
$Nu_{turb}$	Gnielinski correlation parameter	1	Eq. (8.6)
$\mathcal{O}$	Of order	1	—
$\vec{p}$	Linear update vector	many	—
$P$	Thermodynamic pressure, <i>or</i> Contact pressure (Section 9 only)	Pa Pa	— —
$P'$	Reduced pressure	Pa	Eq. (2.35)
$Pe$	Peclet number	1	Eq. (2.132)
$Pe_{el}$	Element Peclet number	1	Eq. (15.5)
$Pr$	Prandtl number	1	Eq. (2.133)
$\mathcal{P}_k$	Polynomial of degree less than or equal to $k$	1	—
$\dot{q}$	Volumetric heat source	$W/m^3$	—
$\vec{q}$	Heat flux vector, <i>or</i> Columns of $\mathbf{Q}$ (Section 16 only)	$W/m^2$ many	— Eq. (16.43)
$\bar{q}$	Known heat flux	$W/m^2$	—
$\mathbf{Q}$	Unitary matrix	many	Eq. (17.6)
$\hat{\mathbf{Q}}$	Portion of unitary matrix	many	—
$\mathbf{Q}_k$	Orthonormal basis for $\mathcal{K}_k$	many	Eq. (16.43)
$r$	Radial coordinate	m	—
$r_{th}$	Thermal resistance	K/W	—
$\vec{r}$	Linear residual	many	Eq. (16.8)
$R$	Nonlinear residual	many	Eq. (14.3)
$\vec{R}$	Nonlinear residual vector	many	Eq. (16.1)
$\vec{\mathcal{R}}$	Quasi-linear strong residual vector	many	Eq. (2.110)
$R_i$	Cylindrical bed inner radius	m	—
$R_o$	Cylindrical bed outer radius	m	—
$R_r$	Radiation reflection number	1	Eq. (9.28)
$\vec{R}$	Residual vector	many	Eq. (14.3)
$\mathcal{R}_c$	Quasi-linear mass strong residual	$kg/m^3 \cdot s$	—
$\mathcal{R}_e$	Quasi-linear fluid energy strong residual	$W/m^3$	—
$\vec{\mathcal{R}}_u$	Vector of momentum equation quasi-linear strong residuals	$kg/m^2 \cdot s^2$	—
$\mathbf{R}$	Generic upper triangular matrix	1	—
$Re$	Reynolds number	1	Eq. (2.129a)
$Re_h$	Reynolds number	1	Eq. (2.129b)
$Re_i$	Reynolds number	1	Eq. (2.129c)
$\mathbb{R}^n$	Space of real numbers of dimension $n$	1	—
$s$	Entropy, <i>or</i> Arc length	J/kg·K m	— —
$S$	Surface	$m^2$	—
$\vec{S}$	Source term vector	many	Eq. (2.105)
$S_e$	Non-interface portion of a surface	$m^2$	—
$S_i$	Phase-interface portion of a surface	$m^2$	—
$S_F$	Component of collinear force that is aligned with gravity	1	Table 4
$t$	Time	s	—
$t$	Generic tensor	many	Eq. (17.17)
$T$	Temperature	K	—
$\bar{T}$	Specified temperature, <i>or</i> Bed-averaged temperature (Section 9 only)	K K	— —
$\mathcal{T}$	Tortuosity	1	—

$\bar{u}$	Approximate solution	many	Eq. (14.1)
$\vec{\bar{u}}$	Approximate solution vector	many	—
$u_*$	True solution	many	—
$\vec{U}$	Vector of conserved quantities	many	Eq. (2.101)
$\vec{\bar{U}}$	Vector of arbitrary solution fields	many	—
$\mathbf{U}$	Generic upper triangular matrix	many	—
$\bar{v}$	Extrinsic, superficial, or Darcy velocity, <i>or</i> Eigenvector	m/s many	— Eq. (17.22)
$\vec{V}$	Intrinsic velocity	m/s	—
$\vec{V}'$	Relative velocity of fluid with respect to interface	m/s	Eq. (4.1)
$\mathcal{V}$	Velocity of material interface	m/s	Eq. (4.2)
$\mathcal{V}$	Volume	m <sup>3</sup>	—
$w$	Quadrature weight	1	—
$\vec{w}$	Velocity of the surface	m/s	—
$W$	Interphase friction factor	1/s	Eq. (6.9)
$\vec{W}$	Vector of weight functions	1	—
$\vec{x}$	Position vector, <i>or</i> Linear solution vector	m many	— Eq. (16.2)
$\vec{x}_*$	True linear solution vector	many	—
$X$	Physical coordinate	m	—
$\mathbf{X}$	Eigenvalue decomposition matrix	many	Eq. (17.23)
$\vec{y}$	Generic vector	many	—
$\mathcal{Y}$	Potential function	many	Eq. (16.17)
$z$	Height	m	—
$z_0$	Minimum coordinate of bed	m	—
$\vec{z}$	Matrix splitting vector	1	Eq. (16.23)
$Z_i$	Cylindrical bed bottom boundary	m	—
$Z_o$	Cylindrical bed top boundary	m	—
$\vec{Z}_s$	Quasi-linear strong form axisymmetric contribution	many	Eq. (2.120)
$\vec{Z}_w$	Weak form axisymmetric contribution	Pa/m	Eq. (2.109)

## Math Symbols

Some of the math symbols are described using dummy variables  $x$  and  $y$  for clarity.

$dx/dt$	Material derivative of $x$	Eq. (17.1)
$\otimes$	Outer product	—
$\partial x/\partial y$	Partial derivative of $x$ with respect to $y$	—
$\text{Tr}(x)$	Trace of $x$	—
$\parallel$	Parallel to	—
$\diamond$	Placeholder	—
$x_k$	Value of $x$ in the $k$ phase, <i>or</i> $k$ -th component of $\vec{x}$	Eq. (19.5) —
$\langle x \rangle$	Spatial average of $x$	Eq. (19.2)
$\langle x_k \rangle$	Spatial phase (extrinsic) average of $x$	Eq. (19.6)
$\langle x_k \rangle^k$	Spatial phase (intrinsic) average of $x$	Eq. (19.7)
$\ x\ _i$	$L^i$ norm of $x$	Eq. (17.9)
$\ x\ _{H^l(\Omega)}$	Hilbert-space norm of $x$	Eq. (14.18)
$ x $	Absolute value of $x$ (if $x$ is a scalar), <i>or</i> Determinant of $x$ (if $x$ is a matrix)	— —
$\in$	In the set	—
$\forall$	For all	—

## Subscripts

$c$	Continuous phase
$d$	Dispersed phase
$e$	Pertaining to a finite element, <i>or</i> Effective value
$f$	Intrinsic fluid phase average
$h$	Pertaining to a finite element (of size $h_e$ )
$i$	Imposed
$k$	Generic phase $k$
$max$	Maximum
meso	Mesoscale
micro	Microscale
$min$	Minimum
$o$	Reference value
$p$	Pebble
$S$	Internal solid phase
$s$	Intrinsic solid phase average
stag	Stagnation value
$x, y, z$	$x, y, z$ components of Cartesian space
0	An initial value
$\infty$	The adjacent or far-field region

## 18.1 Superscripts and Overbars

Some of the overbars are described using a dummy variable  $x$  for clarity.

$-1$	Inverse
$\bar{x}$	Area average of $x$
$\hat{x}$	Spatial fluctuating component of $x$ , <i>or</i> Reduced version of $x$
$\tilde{x}$	Marginal PDF of $x$
+	Nondimensional
*	Hermitian complex conjugate
T	transpose

## 19 Appendix

### 19.1 Mathematical Properties of Averages

This section presents definitions and theorems for relating a generic field  $\Phi$  in a multi-phase domain to various mathematical operations on its spatial average. Similar to the RANS derivation,  $\Phi$  is represented as the sum of its average  $\langle \Phi \rangle$  and a fluctuating component  $\hat{\Phi}$  with zero average,

$$\Phi = \langle \Phi \rangle + \hat{\Phi} , \quad (19.1)$$

where  $\langle \Phi \rangle$  is defined as

$$\langle \Phi \rangle \equiv \frac{1}{V} \int_V \Phi dV . \quad (19.2)$$

In order to characterize the distribution of phases in the REV, a phase function  $f_k$  is defined as

$$f_k = \begin{cases} 1 & \text{in phase } k \\ 0 & \text{not in phase } k \end{cases} . \quad (19.3)$$

The porosity for phase  $k$  is defined as the fraction of the total volume that is made up by phase  $k$ ,

$$\begin{aligned} \varepsilon_k &\equiv \frac{1}{V} \int_V f_k dV \\ &= \frac{V_k}{V} . \end{aligned} \quad (19.4)$$

$\Phi_k$  represents the value of  $\Phi$  in the  $k$  phase,

$$\Phi_k \equiv \Phi f_k , \quad (19.5)$$

while  $\langle \Phi_k \rangle$  indicates an average of  $\Phi_k$  over all phases,

$$\langle \Phi_k \rangle \equiv \frac{1}{V} \int_V \Phi f_k dV , \quad (19.6)$$

and  $\langle \Phi_k \rangle^k$  indicates an average of  $\Phi_k$  over the  $k$  phase,

$$\langle \Phi_k \rangle^k \equiv \frac{1}{V_k} \int_{V_k} \Phi f_k dV . \quad (19.7)$$

$\langle \Phi_k \rangle$  is referred to as the “extrinsic” average, while  $\langle \Phi_k \rangle^k$  is referred to as the “intrinsic” average. Combining Eqs. (19.7), (19.6), and (19.4) provides the relationship between intrinsic and extrinsic averages,

$$\langle \Phi_k \rangle = \varepsilon_k \langle \Phi_k \rangle^k . \quad (19.8)$$

The foundational requirement for the use of the identities derived in this section is that an average be independent of the volume over which it is averaged; this statement is equivalent to the requirement that the average of the average equals the average, or

$$\langle\langle\Phi\rangle\rangle \equiv \langle\Phi\rangle. \quad (19.9)$$

Eq. (19.9) also implies that

$$\langle\langle\Phi_k\rangle^k\rangle = \langle\Phi_k\rangle^k. \quad (19.10)$$

Eqs. (19.9) and (19.10) require that the averaging volume be much larger than the volume over which the microscopic solution varies appreciably. In other words,

$$l \ll L, \quad (19.11)$$

where  $l$  is the length scale characterizing the microscopic scale and  $L$  is the REV averaging scale. Applying a Taylor series to  $\langle\Phi\rangle$  and  $\langle\langle\Phi\rangle\rangle$  shows that Eq. (19.9) is accurate to  $\mathcal{O}(l/L)^2$ . Further, expressing volume averages in terms of a one-dimensional integral of a spatially-dependent surface average shows that volume averages are equivalent to area averages with accuracy  $\mathcal{O}(l/L)^2$ .

Combining Eqs. (19.1), (19.9), and (19.10) gives

$$\Phi_k f_k = \langle\Phi_k\rangle + \hat{\Phi}_k f_k \quad (19.12a)$$

$$\Phi_k f_k = \langle\Phi_k\rangle^k + \hat{\Phi}_k f_k. \quad (19.12b)$$

The presence of the phase function  $f_k$  indicates that  $\Phi_k$  and  $\hat{\Phi}_k$  both are zero in the non- $k$  phases, which is why Eq. (19.12b) is also valid.

Taking the average of the Taylor series expansion of  $\langle\Phi\rangle$  about the centroid of the averaging volume can be used to estimate the order of accuracy of the assumption made in Eq. (19.9). Denoting the centroid with a subscript “c”, this Taylor series expansion is:

$$\langle\Phi\rangle = \langle\Phi\rangle_c + x_i \left( \frac{\partial\langle\Phi\rangle}{\partial x_i} \right)_c + \frac{x_i x_j}{2} \left( \frac{\partial^2\langle\Phi\rangle}{\partial x_i \partial x_j} \right)_c + \mathcal{O}(x_i x_j x_k) \quad (19.13)$$

Taking the average gives:

$$\langle\langle\Phi\rangle\rangle = \langle\Phi\rangle_c + \underbrace{\left( \frac{\partial\langle\Phi\rangle}{\partial x_i} \right)_c}_{\mathcal{O}(1/L^2)} \frac{1}{V} \int_V dV x_i + \frac{1}{2} \underbrace{\left( \frac{\partial^2\langle\Phi\rangle}{\partial x_i \partial x_j} \right)_c}_{\mathcal{O}(1/L^2)} \frac{1}{V} \int_V dV x_i x_j + \mathcal{O}(x_i x_j x_k) \quad (19.14)$$

where all terms that have been subscripted with “c” are independent of the averaging volume, and hence can be brought outside the integrals. The second term on the RHS is zero because the coordinate  $x_i$  is measured from the centroid of the averaging volume, so the integration represents an integral of an odd function. So, Eq. (19.9) is valid provided  $l^2/L^2 \ll 1$ , which is the same requirement in Eq. (19.11).

The notational convention used here is that  $\varepsilon_f \rightarrow \varepsilon$  represents the porosity of the fluid, while  $\varepsilon_s \rightarrow 1 - \varepsilon$  represents the porosity of the solid. All voids are assumed connected such that Eq. (19.4) becomes

$$\varepsilon \equiv \frac{\text{void volume}}{\text{total volume}}. \quad (19.15)$$

The extrinsic average of an intrinsic average simply equals the intrinsic average,

$$\begin{aligned} \langle\langle \Phi_k \rangle^k \rangle &\equiv \frac{1}{\mathcal{V}} \int_{\mathcal{V}} \langle \Phi_k \rangle^k d\mathcal{V} \\ &= \frac{1}{\mathcal{V}} \int_{\mathcal{V}} \left( \frac{1}{\mathcal{V}_k} \int_{\mathcal{V}_k} d\mathcal{V} \Phi f_k \right) d\mathcal{V} \\ &= \frac{1}{\mathcal{V}_k} \int_{\mathcal{V}_k} \left( \frac{1}{\mathcal{V}} \int_{\mathcal{V}} d\mathcal{V} \Phi f_k \right) d\mathcal{V} \\ &= \langle \Phi_k \rangle^k. \end{aligned} \quad (19.16)$$

A similar process of swapping orders of integration shows that the intrinsic average of an extrinsic average simply equals the extrinsic average,

$$\langle\langle \Phi_k \rangle \rangle^k = \langle \Phi_k \rangle. \quad (19.17)$$

Several additional identities are needed to derive the porous media equations; applying the general transport theorem in Eq. (2.3) to a material volume gives

$$\int_{\mathcal{V}} \nabla \Phi_k d\mathcal{V} = \nabla \int_{\mathcal{V}} \Phi_k d\mathcal{V} + \int_{S_i} \Phi_k \hat{n}_k dS, \quad (19.18)$$

where  $S_i$  is the phase interface portion of the surface enclosing  $\mathcal{V}$  [204]. Then, dividing each term by  $\mathcal{V}$ , Eq. (19.18) gives Eq. (19.19),

$$\langle \nabla \Phi_k \rangle = \nabla \langle \Phi_k \rangle + \frac{1}{\mathcal{V}} \int_{S_i} \Phi_k \hat{n}_k dS \quad (19.19a)$$

$$\langle \nabla \Phi_k \rangle = \varepsilon_k \nabla \langle \Phi_k \rangle^k + \frac{1}{\mathcal{V}} \int_{S_i} \hat{\Phi}_k \hat{n}_k dS. \quad (19.19b)$$

In other words, equality between the average of a gradient and the gradient of an average is offset by the integral of the field over the phase interfacial area [131]. Extensions of Eq. (19.19) to vectors convert gradients to divergences.

To derive Eq. (19.18), consider a point in the porous media located on a curve with an arc length  $s$ . At each point on this curve, we can define an averaging volume  $\mathcal{V}(s)$  and the surface bounding that volume  $S(s)$ . By assuming that there is a continuous and invertible mapping between time  $t$  and arc length,  $t$  in Eq. (2.3) can be replaced by  $s$ :

$$\frac{d}{ds} \int_{\mathcal{V}(s)} \Phi d\mathcal{V} = \int_{\mathcal{V}(s)} \frac{\partial \Phi}{\partial s} d\mathcal{V} + \int_{S(s)} \Phi \frac{d\vec{x}}{ds} \cdot \hat{n} dS \quad (19.20)$$

where the velocity of the surface  $\vec{V} = \partial \vec{x} / \partial t$  also substituted arc length for time.  $\Phi$  only depends on arc length *implicitly* through its dependence on the spatial coordinate, so the first term on the RHS is zero. Due to the no-penetration condition, which requires that the normal component of velocity at a boundary must be zero, the nonzero component of  $\partial \vec{x} / \partial s$  is perpendicular to the unit normal vector at the solid-fluid interfaces (giving a zero dot product). Hence, the area  $S(s)$  that appears above can be simplified to the total area minus any

solid-fluid interface area  $S_i(s)$ . For simplicity, this non-interface area is denoted as  $S_e(s) \equiv S(s) - S_i(s)$ :

$$\frac{d}{ds} \int_{\mathcal{V}(s)} \Phi d\mathcal{V} = \int_{S_e(s)} \Phi \frac{d\vec{x}}{ds} \cdot \hat{n} dS \quad (19.21)$$

Finally, each point along the curve is described by a position vector  $\vec{x}_0(s)$  relative to some arbitrary origin. Let the vector  $\vec{p}(s)$  represent the location of the points on the enclosing surface relative to a point on the curve. The vector representing points on the surface is then the sum of the vector to a point on the curve plus the vector to the point on the surface:

$$\vec{x}(s) = \vec{x}_0(s) + \vec{p}(s) \quad (19.22)$$

By the chain rule, the directional derivative with respect to the arc length is given as:

$$\begin{aligned} \frac{d}{ds} &= \frac{d}{dx_i} \frac{dx_i}{ds} \\ &= \nabla \cdot \frac{d\vec{x}}{ds} \end{aligned} \quad (19.23)$$

Using Eq. (19.22) and (19.23) in the transport theorem gives:

$$\frac{d\vec{x}_0}{ds} \cdot \left( \nabla \int_{\mathcal{V}(s)} \Phi d\mathcal{V} - \int_{S_e(s)} \Phi \hat{n} dS \right) = \int_{S_e(s)} \Phi \frac{d\vec{p}}{ds} \cdot \hat{n} dS \quad (19.24)$$

where  $d\vec{x}_0/ds$  was removed from the integration because it is independent of the area integration variable for a fixed value of  $s$ . As long as  $\mathcal{V}(s)$  is translated along the curve without rotation, then any differential change in  $\vec{p}$  is parallel to the surface, and hence the RHS term above is zero. Then, because the vector  $\vec{x}_0$  was arbitrary, the expression must hold for any vector  $\vec{x}_0$ , which means that the remaining multiplied term must be zero:

$$\nabla \int_{\mathcal{V}(s)} \Phi d\mathcal{V} - \int_{S_e(s)} \Phi \hat{n} dS = 0 \quad (19.25)$$

By the divergence theorem, a volume integral can be related to surface integrals:

$$\int_{\mathcal{V}(s)} \nabla \Phi d\mathcal{V} = \int_{S_e(s)} \Phi \hat{n} dS + \int_{S_i(s)} \Phi \hat{n} dS \quad (19.26)$$

Substituting Eq. (19.26) into Eq. (19.25) for the surface integral over the non-phase interface  $S_e(s)$  gives Eq. (19.19a).

Taking the average of the nonlinear advective operator will require taking the average of a product. From Eq. (19.4), an average over  $\mathcal{V}$  can be related to an average over the phase volume  $\mathcal{V}_k$ , giving

$$\begin{aligned} \langle \vec{V}_k \Phi_k \rangle &= \varepsilon_k \langle \vec{V}_k \Phi_k \rangle^k \\ &= \varepsilon_k \langle \vec{V}_k \rangle^k \langle \Phi_k \rangle^k + \langle \hat{\vec{V}}_k \hat{\Phi}_k \rangle, \end{aligned} \quad (19.27)$$

where Eq. (19.12) was substituted for both  $\vec{V}_k$  and  $\Phi_k$  and Eq. (19.4) was used to rewrite  $\varepsilon_k \langle \hat{\vec{V}}_k \hat{\Phi}_k \rangle^k$ . For some advective terms, an average of three terms will be needed. In this case, Eq. (19.27) becomes:

$$\begin{aligned} \langle a_k b_k c_k \rangle &= \varepsilon_k \langle a_k b_k c_k \rangle^f \\ &= \langle \hat{a}_k \hat{b}_k \hat{c}_k \rangle + \langle \hat{a}_k \hat{b}_k \rangle \langle c_k \rangle^k + \langle \hat{a}_k \hat{c}_k \rangle \langle b_k \rangle^k + \langle \hat{c}_k \hat{b}_k \rangle \langle a_k \rangle^k + \varepsilon_k \langle a_k \rangle^k \langle b_k \rangle^k \langle c_k \rangle^k. \end{aligned} \quad (19.28)$$

According to Eq. (19.8), two different velocities can be defined for a porous media.  $\vec{v}$  represents the fluid velocity averaged over  $\mathcal{V}$ . This velocity is often referred to as the Darcy velocity, the extrinsic phase velocity, or the superficial

velocity.  $\vec{V}$  represents the fluid velocity averaged over  $\mathcal{V}_f$ , and is referred to as the intrinsic phase velocity. Neither of these velocities are the actual local fluid velocity. The intrinsic and extrinsic velocities are related to one other by Eq. (19.8),

$$\vec{v} = \varepsilon \vec{V} . \quad (19.29)$$

Adding Eqs. (19.19a) and (19.19b) and using Eq. (19.12) gives

$$\frac{1}{\mathcal{V}} \int_{S_i} \langle \Phi_k \rangle^k \hat{n}_k dS = - \langle \Phi_k \rangle^k \nabla \varepsilon_k . \quad (19.30)$$

Finally, in order to express averages of time derivatives, divide each term in the general transport theorem in Eq. (2.3) by  $\mathcal{V}$  and use the identities derived in this section, giving

$$\frac{d}{dt} \frac{1}{\mathcal{V}} \int_{\mathcal{V}} \Phi_k d\mathcal{V} = \frac{1}{\mathcal{V}} \int_{\mathcal{V}} \frac{\partial \Phi_k}{\partial t} d\mathcal{V} + \frac{1}{\mathcal{V}} \int_{S_i} \Phi_k \vec{w}_k \cdot \hat{n}_k dS \quad (19.31a)$$

$$\frac{d \langle \Phi_k \rangle}{dt} = \left\langle \frac{\partial \Phi_k}{\partial t} \right\rangle + \frac{1}{\mathcal{V}} \int_{S_i} \Phi_k \vec{w}_k \cdot \hat{n}_k dS , \quad (19.31b)$$

where  $\vec{w}_k$  is the velocity of the phase interface [204].

## 19.2 Spatial Homogenization of the Conservation Equations

This section presents spatial homogenization of the conservation of mass, momentum, and energy equations. In the sections that follow, it is assumed that thermal and pressure gradients are not very large such that density, thermal conductivity, and isobaric specific heat capacity fluctuations are much smaller than velocity fluctuations and can hence be assumed zero [204]. It is also assumed that the solid-fluid interface is stationary such that  $\vec{V}_f = \vec{w}_f$  and  $\vec{w}_f = 0$ .

### 19.2.1 The Mass Equation

This section presents the derivation of the porous media version of Eq. (2.5) using the averaging identities defined in Section 19.1. The time derivative term is averaged with Eq. (19.31b) and the advective term is averaged using Eq. (19.19a) with Eq. (19.27), giving

$$\frac{\partial \langle \varepsilon \langle \rho_f \rangle^f \rangle}{\partial t} + \frac{\partial \langle \hat{\rho}_f \rangle}{\partial t} + \nabla \cdot \langle \varepsilon \langle \rho_f \rangle^f \langle \vec{V}_f \rangle^f \rangle + \nabla \cdot \langle \hat{\rho}_f \hat{\vec{V}}_f \rangle + \frac{1}{\mathcal{V}} \int_{S_i} \rho_f (\vec{V}_f - \vec{w}_f) \hat{n}_f dS = 0 , \quad (19.32)$$

where Eq. (19.8) has been used. With the assumptions listed at the end of Section 19.2, Eq. (19.32) becomes the spatially homogenized mass conservation equation,

$$\frac{\partial \langle \varepsilon \langle \rho_f \rangle^f \rangle}{\partial t} + \nabla \cdot \langle \varepsilon \langle \rho_f \rangle^f \langle \vec{V}_f \rangle^f \rangle = 0 . \quad (19.33)$$

### 19.2.2 The Momentum Equation

This section presents the derivation of the porous media version of Eq. (2.29) using the averaging identities defined in Section 19.1. The time derivative term is rewritten using Eqs. (19.31b) and (19.27),

$$\left\langle \frac{\partial(\rho_f \vec{V}_f)}{\partial t} \right\rangle = \frac{\partial(\varepsilon \langle \rho_f \rangle^f \langle \vec{V}_f \rangle^f)}{\partial t} + \frac{\partial \langle \hat{\rho}_f \hat{V}_f \rangle}{\partial t} - \frac{1}{V} \int_{S_i} \rho_f \vec{V}_f \vec{w}_f \cdot \hat{n}_f dS. \quad (19.34)$$

The advective term is averaged using Eq. (19.19a) and Eq. (19.28),

$$\begin{aligned} \langle \nabla \cdot (\rho_f \vec{V}_f \vec{V}_f) \rangle &= \nabla \cdot \left[ \varepsilon \langle \rho_f \rangle^f \langle \vec{V}_f \rangle^f \langle \vec{V}_f \rangle^f + 2 \langle \hat{\rho}_f \hat{V}_f \rangle \langle \vec{V}_f \rangle^f \right] + \\ &\nabla \cdot \left[ \langle \rho_f \rangle^f \langle \hat{V}_f \hat{V}_f \rangle + \langle \hat{\rho}_f \hat{V}_f \hat{V}_f \rangle \right] + \frac{1}{V} \int_{S_i} \rho_f \vec{V}_f \vec{V}_f \cdot \hat{n}_f dS. \end{aligned} \quad (19.35)$$

The normal stress term is averaged using Eq. (19.19b),

$$\langle \nabla P_f \rangle = \varepsilon \nabla \langle P_f \rangle^f + \frac{1}{V} \int_{S_i} \hat{P}_f \hat{n}_f dS. \quad (19.36)$$

Eq. (19.19b), rather than Eq. (19.19a), is required to obtain the correct zero-velocity physics using the porous media closure relations readily available in the literature [38]. If Eq. (19.19a) were used instead, then for a zero-velocity, non-constant porosity system, the gradient in porosity would induce a nonphysical flow.

The deviatoric stress term is averaged using Eq. (19.19a),

$$\langle \nabla \cdot \tau_f \rangle = \nabla \cdot \langle \tau_f \rangle + \frac{1}{V} \int_{S_i} \tau_f \hat{n}_f dS. \quad (19.37)$$

Finally, the source term is  $-\rho_f \nabla \phi_{g,f}$ , where it has been assumed that  $\vec{b} = \vec{g}$  and  $\phi_{g,f}$  is the gravitational potential function,

$$\nabla \phi_{g,f} \equiv -g \vec{e}_z. \quad (19.38)$$

Using Eqs. (19.19b) and (19.27) gives

$$\begin{aligned} \langle S_f \rangle &= -\langle \rho_f \nabla \phi_{g,f} \rangle \\ &= -\langle \rho_f \rangle^f \langle \nabla \phi_{g,f} \rangle - \langle \hat{\rho}_f \nabla \hat{\phi}_{g,f} \rangle \\ &= -\varepsilon \langle \rho_f \rangle^f \nabla \langle \phi_{g,f} \rangle^f - \frac{\langle \rho_f \rangle^f}{V} \int_{S_i} \hat{\phi}_{g,f} \hat{n}_f dS \\ &= -\varepsilon \langle \rho_f \rangle^f \nabla \langle \phi_{g,f} \rangle^f, \end{aligned} \quad (19.39)$$

where the terms containing the fluctuation of  $\vec{g}$  are zero because the gravitational acceleration vector is constant. Combining all of these terms gives

$$\begin{aligned}
& \frac{\partial(\varepsilon\langle\rho_f\rangle^f\langle\vec{V}_f\rangle^f)}{\partial t} + \frac{\partial\langle\hat{\rho}_f\hat{V}_f\rangle}{\partial t} + \nabla \cdot \left[ \varepsilon\langle\rho_f\rangle^f\langle\vec{V}_f\rangle^f\langle\vec{V}_f\rangle^f + 2\langle\hat{\rho}_f\hat{V}_f\rangle\langle\vec{V}_f\rangle^f \right] \\
& \quad \frac{1}{\mathcal{V}} \int_{S_i} \rho_f \vec{V}_f (\vec{V}_f - \vec{w}_f) \cdot \hat{n}_f dS + \nabla \cdot \left[ \langle\rho_f\rangle^f\langle\hat{V}_f\hat{V}_f\rangle + \langle\hat{\rho}_f\hat{V}_f\hat{V}_f\rangle \right] = \\
& \nabla \cdot \langle\tau_f\rangle + \frac{1}{\mathcal{V}} \int_{S_i} \tau_f \hat{n}_f dS - \varepsilon\nabla\langle P_f\rangle^f - \frac{1}{\mathcal{V}} \int_{S_i} \left( \hat{P}_f - \langle\rho_f\rangle^f\hat{\Phi}_{g,f} \right) \hat{n}_f dS - \varepsilon\langle\rho_f\rangle^f\nabla\langle\phi_{g,f}\rangle^f,
\end{aligned} \tag{19.40}$$

where  $\langle\rho_f\rangle^f$  has been moved inside the surface integral of the gravitational force for later illustration. With the assumptions listed at the end of Section 19.2, Eq. (19.40) becomes

$$\begin{aligned}
& \frac{\partial(\varepsilon\langle\rho_f\rangle^f\langle\vec{V}_f\rangle^f)}{\partial t} + \nabla \cdot \left[ \varepsilon\langle\rho_f\rangle^f\langle\vec{V}_f\rangle^f\langle\vec{V}_f\rangle^f + \langle\rho_f\rangle^f\langle\hat{V}_f\hat{V}_f\rangle \right] = \\
& \nabla \cdot \langle\tau_f\rangle + \frac{1}{\mathcal{V}} \int_{S_i} \tau_f \hat{n}_f dS - \varepsilon\nabla\langle P_f\rangle^f - \frac{1}{\mathcal{V}} \int_{S_i} \left( \hat{P}_f - \langle\rho_f\rangle^f\hat{\Phi}_{g,f} \right) \hat{n}_f dS - \varepsilon\langle\rho_f\rangle^f\nabla\langle\phi_{g,f}\rangle^f.
\end{aligned} \tag{19.41}$$

Assuming a Newtonian fluid such that  $\tau$  is given by Eq. (2.26),  $\nabla \cdot \langle\tau_f\rangle$  becomes

$$\nabla \cdot \langle\tau_f\rangle = \nabla \cdot \left\{ \langle\mu_f\rangle \left[ \nabla\langle\vec{V}_f\rangle + (\nabla\langle\vec{V}_f\rangle)^T - \frac{2}{3}\nabla \cdot \langle\vec{V}_f\rangle\mathbf{I} \right] \right\}, \tag{19.42}$$

where the surface integrals arising from Eq. (19.19) are zero, and hence not shown, because the no-slip condition is satisfied at phase interfaces and the medium does not deform.

The  $\tau_f \hat{n}_f$  integral in Eq. (19.41) represents the average viscous drag of the solid on the fluid. This average viscous stress can be expressed in terms of the difference in intrinsic velocities between the phases, since the viscous stress should be zero if neither phase is moving. Expressing the dependence as a second-order expansion in the phase velocity difference,

$$\frac{1}{\mathcal{V}} \int_{S_i} \tau_f \cdot \hat{n}_f dS = \langle\mu_f\rangle \varepsilon \mathcal{A} \left( \langle\vec{V}_s\rangle^s - \langle\vec{V}_f\rangle^f \right) + \langle\mu_f\rangle \varepsilon \mathcal{B} : \left( \langle\vec{V}_s\rangle^s - \langle\vec{V}_f\rangle^f \right) \cdot \left( \langle\vec{V}_s\rangle^s - \langle\vec{V}_f\rangle^f \right), \tag{19.43}$$

where  $\mathcal{A}$  is a second-order tensor and  $\mathcal{B}$  a third-order tensor [204]. The  $\langle\hat{V}_f\hat{V}_f\rangle$  term in Eq. (19.41) will only be zero if the fluid moves at the same velocity as the fluid-solid interface. This requirement can also be expressed as a two-term expansion, where Eq. (19.8) is first used to obtain an intrinsic phase average,

$$\begin{aligned}
\langle\hat{V}_f\hat{V}_f\rangle &= \varepsilon\langle\hat{V}_f\hat{V}_f\rangle^f \\
&= \varepsilon\mathcal{C} \cdot \left( \langle\vec{V}_s\rangle^s - \langle\vec{V}_f\rangle^f \right) + \varepsilon\mathcal{L} : \left( \langle\vec{V}_s\rangle^s - \langle\vec{V}_f\rangle^f \right) \left( \langle\vec{V}_s\rangle^s - \langle\vec{V}_f\rangle^f \right),
\end{aligned} \tag{19.44}$$

where  $\mathcal{C}$  is a third-order tensor and  $\mathcal{L}$  is a fourth-order tensor. Because  $\langle\hat{V}_f\hat{V}_f\rangle^f$  is symmetric, both of these tensors must be symmetric in their first two indices, and  $\mathcal{L}$  also in the last two indices. Only one more constitutive relationship is required to fully express the momentum equation. This can be reasoned by showing that the fluctuating pressure and gravitational field are nonzero perturbations that can still satisfy  $\nabla\langle P_f\rangle^f + \langle\rho_f\rangle^f\nabla\langle\phi_{g,f}\rangle^f = 0$ , such as in cases where the fluid is hydrostatic. Therefore, using a second-order expansion,

$$\begin{aligned}
\frac{1}{\mathcal{V}} \int_{S_i} \left( \hat{P}_f + \langle\rho_f\rangle^f\hat{\Phi}_{g,f} \right) \hat{n}_f dS &= \varepsilon\mathcal{E} \cdot \left( \nabla\langle P_f\rangle^f + \langle\rho_f\rangle^f\nabla\langle\phi_{g,f}\rangle^f \right) + \\
&\varepsilon\mathcal{M} : \left( \nabla\langle P_f\rangle^f + \langle\rho_f\rangle^f\nabla\langle\phi_{g,f}\rangle^f \right) \left( \nabla\langle P_f\rangle^f + \langle\rho_f\rangle^f\nabla\langle\phi_{g,f}\rangle^f \right),
\end{aligned} \tag{19.45}$$

where  $\mathcal{E}$  is a second-order tensor and  $\mathcal{M}$  is a third-order tensor that is symmetric in its second and third indices. A factor of  $\varepsilon$  arbitrarily appears for later convenience. Inserting Eqs. (19.42)-(19.45) into Eq. (19.41) gives the porous media momentum equation for a Newtonian fluid,

$$\begin{aligned}
& \frac{\partial(\varepsilon\langle\rho_f\rangle^f\langle\vec{V}_f\rangle^f)}{\partial t} + \nabla \cdot \left[ \varepsilon\langle\rho_f\rangle^f\langle\vec{V}_f\rangle^f\langle\vec{V}_f\rangle^f \right] + \nabla \cdot \left[ \varepsilon\langle\rho_f\rangle^f\mathcal{C} \cdot \left( \langle\vec{V}_s\rangle^s - \langle\vec{V}_f\rangle^f \right) \right] + \\
& \quad \nabla \cdot \left[ \varepsilon\langle\rho_f\rangle^f\mathcal{L} : \left( \langle\vec{V}_s\rangle^s - \langle\vec{V}_f\rangle^f \right) \left( \langle\vec{V}_s\rangle^s - \langle\vec{V}_f\rangle^f \right) \right] = \\
& \quad \nabla \cdot \left\{ \langle\mu_f\rangle \left[ \nabla\langle\vec{V}_f\rangle + (\nabla\langle\vec{V}_f\rangle)^T - \frac{2}{3}\nabla \cdot \langle\vec{V}_f\rangle\mathbf{I} \right] \right\} + \\
& \quad \langle\mu_f\rangle\varepsilon\mathcal{A} \left( \langle\vec{V}_s\rangle^s - \langle\vec{V}_f\rangle^f \right) + \langle\mu_f\rangle\varepsilon\mathcal{B} : \left( \langle\vec{V}_s\rangle^s - \langle\vec{V}_f\rangle^f \right) \cdot \left( \langle\vec{V}_s\rangle^s - \langle\vec{V}_f\rangle^f \right) \\
& \quad \quad - \varepsilon(\mathbf{I} + \mathcal{E}) \cdot \left( \nabla\langle P_f\rangle^f + \langle\rho_f\rangle^f\nabla\langle\phi_{g,f}\rangle^f \right) \\
& \quad - \mathcal{M} : \left( \nabla\langle P_f\rangle^f + \langle\rho_f\rangle^f\nabla\langle\phi_{g,f}\rangle^f \right) \left( \nabla\langle P_f\rangle^f + \langle\rho_f\rangle^f\nabla\langle\phi_{g,f}\rangle^f \right) .
\end{aligned} \tag{19.46}$$

Experimentally-determined values for all of the tensors that appear in Eq. (19.46) do not exist. But, simplifications can be made for isotropic flows or slow flows such that advection and the time rate of change of momentum can be neglected [204].

$\mathcal{M}$ ,  $\mathcal{C}$ , and  $\mathcal{B}$  are third-order tensors that are symmetric in two of their indices. There are no isotropic symmetric third-order tensors, so all three of these tensors must be zero for isotropic media [204]. The only symmetric second-order tensor is a multiple of the identity matrix, such that  $\mathcal{A} = A\mathbf{I}$ , where  $A$  is a constant. Likewise,  $\varepsilon(\mathbf{I} + \mathcal{E}) = E\mathbf{I}$ . Therefore, Eq. (19.46) becomes for isotropic flows

$$\begin{aligned}
& \frac{\partial(\varepsilon\langle\rho_f\rangle^f\langle\vec{V}_f\rangle^f)}{\partial t} + \nabla \cdot \left[ \varepsilon\langle\rho_f\rangle^f\langle\vec{V}_f\rangle^f\langle\vec{V}_f\rangle^f \right] + \\
& \quad \nabla \cdot \left[ \varepsilon\langle\rho_f\rangle^f\mathcal{L} : \left( \langle\vec{V}_s\rangle^s - \langle\vec{V}_f\rangle^f \right) \left( \langle\vec{V}_s\rangle^s - \langle\vec{V}_f\rangle^f \right) \right] = \\
& \quad \nabla \cdot \left( \mu_f\nabla\langle\vec{V}_f\rangle \right) + \nabla \cdot \left( \mu\nabla\langle\vec{V}_f\rangle \right)^T - \frac{2}{3}\nabla \left( \mu\nabla \cdot \langle\vec{V}\rangle \right) + \\
& \quad \mu\varepsilon\mathcal{A} \left( \langle\vec{V}_s\rangle^s - \langle\vec{V}_f\rangle^f \right) - E \cdot \left( \nabla\langle P_f\rangle^f + \langle\rho_f\rangle^f\nabla\langle\phi_{g,f}\rangle^f \right) .
\end{aligned} \tag{19.47}$$

A generic fourth-order isotropic tensor can be written in component form as

$$\mathcal{L}_{ijkl} = L\delta_{ij}\delta_{kl} + \frac{l}{2}(\delta_{ik}\delta_{jl} + \delta_{il}\delta_{jk}) + q(\delta_{ik}\delta_{jl} - \delta_{il}\delta_{jk}) , \tag{19.48}$$

where  $L$ ,  $l$ , and  $q$  are constants. Because  $\mathcal{L}$  is symmetric in its first two indices, as well as in its last two indices, the last term above is zero. This only requires the definition of the constants  $L$ ,  $l$ , and  $A$ . So, the momentum equation for an isotropic porous media is

$$\begin{aligned}
& \frac{\partial(\varepsilon\langle\rho_f\rangle^f\langle\vec{V}_f\rangle^f)}{\partial t} + \nabla \cdot \left[ \varepsilon\langle\rho_f\rangle^f\langle\vec{V}_f\rangle^f\langle\vec{V}_f\rangle^f \right] + \\
& \nabla \cdot \left[ \varepsilon\langle\rho_f\rangle^f L \left( \langle\vec{V}_s\rangle^s - \langle\vec{V}_f\rangle^f \right) \cdot \left( \langle\vec{V}_s\rangle^s - \langle\vec{V}_f\rangle^f \right) \right] + \\
& \nabla \cdot \left[ \varepsilon\langle\rho_f\rangle^f l \left( \langle\vec{V}_s\rangle^s - \langle\vec{V}_f\rangle^f \right) \left( \langle\vec{V}_s\rangle^s - \langle\vec{V}_f\rangle^f \right) \right] = \\
& \nabla \cdot \left( \mu_f \nabla \langle\vec{V}_f\rangle \right) + \nabla \cdot \left( \mu \nabla \langle\vec{V}_f\rangle \right)^T - \frac{2}{3} \nabla \left( \mu \nabla \cdot \langle\vec{V}\rangle \right) + \\
& \mu \varepsilon \mathcal{A} \left( \langle\vec{V}_s\rangle^s - \langle\vec{V}_f\rangle^f \right) - E \cdot \left( \nabla \langle P_f \rangle^f + \langle \rho_f \rangle^f \nabla \langle \phi_{g,f} \rangle^f \right) .
\end{aligned} \tag{19.49}$$

For slow flows where the advection and time rate of change of momentum is negligible, Eq. (19.46) instead simplifies to

$$\begin{aligned}
& \nabla \cdot \left( \mu_f \nabla \langle\vec{V}_f\rangle \right) + \nabla \cdot \left( \mu \nabla \langle\vec{V}_f\rangle \right)^T - \frac{2}{3} \nabla \left( \mu \nabla \cdot \langle\vec{V}\rangle \right) + \mu \varepsilon \mathcal{A} \left( \langle\vec{V}_s\rangle^s - \langle\vec{V}_f\rangle^f \right) + \\
& \mu \varepsilon \mathcal{B} : \left( \langle\vec{V}_s\rangle^s - \langle\vec{V}_f\rangle^f \right) \cdot \left( \langle\vec{V}_s\rangle^s - \langle\vec{V}_f\rangle^f \right) - \varepsilon \left( \mathbf{I} + \mathcal{E} \right) \cdot \left( \nabla \langle P_f \rangle^f + \langle \rho_f \rangle^f \nabla \langle \phi_{g,f} \rangle^f \right) \\
& - \mathcal{M} : \left( \nabla \langle P_f \rangle^f + \langle \rho_f \rangle^f \nabla \langle \phi_{g,f} \rangle^f \right) \left( \nabla \langle P_f \rangle^f + \langle \rho_f \rangle^f \nabla \langle \phi_{g,f} \rangle^f \right) = 0 .
\end{aligned} \tag{19.50}$$

The second-order Taylor series terms and the viscous stress terms are also negligible for slow flows [204]. Eq. (19.50) then reduces to Darcy's law

$$\mathcal{K} \left( \nabla \langle P_f \rangle^f + \langle \rho_f \rangle^f \nabla \langle \phi_{g,f} \rangle^f \right) = \mu \varepsilon \left( \langle\vec{V}_s\rangle^s - \langle\vec{V}_f\rangle^f \right) , \tag{19.51}$$

where the second-order permeability tensor  $\mathcal{K}$  is defined as

$$\mathcal{K} \equiv \varepsilon \left( \mathbf{I} + \mathcal{E} \right) \mathcal{A}^{-1} . \tag{19.52}$$

Mechanical effects of the solid on the fluid are neglected such that  $\mathcal{C} = \mathbf{0}$  and  $\mathcal{L} = \mathbf{0}$ . Second-order effects of the pressure and gravitational forces are also neglected such that  $\mathcal{M} = \mathbf{0}$ . Both of these approximations are valid for relatively slow flows [204]. Finally, the solid phase is assumed stationary and the gradient of the gravitational potential is replaced by  $\vec{b}$ , reintroducing the possibility of other conservative body forces for generality.

### 19.2.3 The Energy Equation

This section presents the derivation of the porous media versions of Eqs. (2.51) and (2.73) using the averaging identities defined in Section 19.1.

The time derivative in Eq. (2.51) is averaged using Eqs. (19.31b) and (19.27), giving

$$\left\langle \frac{\partial(\rho_f E_f)}{\partial t} \right\rangle = \frac{\partial(\varepsilon\langle\rho_f\rangle^f\langle E_f\rangle^f)}{\partial t} + \frac{\partial\langle\hat{\rho}_f\hat{E}_f\rangle}{\partial t} - \frac{1}{\mathcal{V}} \int_{S_i} \rho_f E_f \vec{w}_f \cdot \hat{n}_f dS . \tag{19.53}$$

The time derivative term in Eq. (2.73) is averaged using Eqs. (19.31b) and (19.28) to give

$$\begin{aligned} \left\langle \rho_f C_{p,f} \frac{\partial T_f}{\partial t} \right\rangle &= \left\langle \hat{\rho}_f \hat{C}_{p,f} \frac{\partial \hat{T}_f}{\partial t} \right\rangle + \left\langle \hat{\rho}_f \frac{\partial \hat{T}_f}{\partial t} \right\rangle \langle C_{p,f} \rangle^f + \left\langle \hat{C}_{p,f} \frac{\partial \hat{T}_f}{\partial t} \right\rangle \langle \rho_f \rangle^f + \\ &\quad \left[ \varepsilon \langle \rho_f \rangle^f \langle C_{p,f} \rangle^f + \langle \hat{\rho}_f \hat{C}_{p,f} \rangle \right] \left[ \frac{\partial \langle T_f \rangle^f}{\partial t} - \frac{1}{V} \int_{S_i} T_f \vec{w}_f \cdot \vec{n}_f dS \right]. \end{aligned} \quad (19.54)$$

The advective term in Eq. (2.51) is first averaged using Eqs. (19.19a) and (19.28), giving

$$\begin{aligned} \langle \nabla \cdot (\rho_f H_f \vec{V}_f) \rangle &= \nabla \cdot \left[ \varepsilon \langle \rho_f \rangle^f \langle H_f \rangle^f \langle \vec{V}_f \rangle^f + \langle \hat{\rho}_f \hat{H}_f \hat{V}_f \rangle + \langle \rho_f \rangle^f \langle \hat{H}_f \hat{V}_f \rangle \right] + \\ &\quad \nabla \cdot \left[ \langle H_f \rangle^f \langle \hat{\rho}_f \hat{V}_f \rangle + \langle \vec{V}_f \rangle^f \langle \hat{\rho}_f \hat{H}_f \rangle \right] + \frac{1}{V} \int_{S_i} \rho_f H_f \vec{V}_f \cdot \hat{n}_f dS. \end{aligned} \quad (19.55)$$

The advective term in Eq. (2.73) is rewritten using (19.28), giving

$$\begin{aligned} \langle \rho_f C_{p,f} \vec{V}_f \cdot \nabla T_f \rangle &= \langle \hat{\rho}_f \hat{C}_{p,f} \hat{V}_f \cdot \nabla \hat{T}_f \rangle + \langle \hat{\rho}_f \hat{C}_{p,f} \nabla \hat{T}_f \rangle \cdot \langle \vec{V}_f \rangle^f + \langle \hat{\rho}_f \hat{V}_f \cdot \nabla \hat{T}_f \rangle \langle C_{p,f} \rangle^f + \\ &\quad \langle \hat{C}_{p,f} \hat{V}_f \cdot \nabla \hat{T}_f \rangle \langle \rho_f \rangle^f + \langle \rho_f \rangle^f \langle C_{p,f} \rangle^f \langle \hat{V}_f \cdot \nabla \hat{T}_f \rangle + \langle \vec{V}_f \rangle^f \langle C_{p,f} \rangle^f \langle \hat{\rho}_f \cdot \nabla \hat{T}_f \rangle + \\ &\quad \langle \rho_f \rangle^f \langle \vec{V}_f \rangle^f \cdot \langle \hat{C}_{p,f} \nabla \hat{T}_f \rangle + \left( \langle \hat{\rho}_f \hat{C}_{p,f} \rangle \langle \vec{V}_f \rangle^f + \langle \hat{\rho}_f \hat{V}_f \rangle \langle C_{p,f} \rangle^f \right) \cdot \langle \nabla T_f \rangle^f + \\ &\quad \left( \langle \hat{V}_f \hat{C}_{p,f} \rangle \langle \rho_f \rangle^f + \varepsilon \langle \rho_f \rangle^f \langle C_{p,f} \rangle^f \langle \vec{V}_f \rangle^f + \langle \hat{\rho}_f \hat{C}_{p,f} \hat{V}_f \rangle \right) \cdot \langle \nabla T_f \rangle^f. \end{aligned} \quad (19.56)$$

Then, neglecting fluctuations in density and specific heat and applying Eq. (19.19b) to the gradient term gives

$$\langle \rho_f C_{p,f} \vec{V}_f \cdot \nabla T_f \rangle = \langle \rho_f \rangle^f \langle C_{p,f} \rangle^f \langle \hat{V}_f \cdot \nabla \hat{T}_f \rangle + \varepsilon \langle \rho_f \rangle^f \langle C_{p,f} \rangle^f \langle \vec{V}_f \rangle^f \cdot \left( \nabla \langle T_f \rangle^f + \frac{1}{V} \int_{S_i} \hat{T}_f \hat{n}_f dS \right). \quad (19.57)$$

The surface integral in Eq. (19.57) represents the tortuosity advective flux, or the increase in advection caused by mechanical effects of the solid on the fluid. It is neglected here.

Averaging the heat conduction term using Eq. (19.19b) and then applying Eq. (19.27) and Eq. (19.19b) gives

$$\langle \nabla \cdot (k_f \nabla T_f) \rangle = \nabla \cdot \langle k_f \rangle^f \left( \varepsilon \nabla \langle T_f \rangle^f + \frac{1}{V} \int_{S_i} \hat{T}_f \hat{n}_f dS \right) + \nabla \cdot \langle \hat{k}_f \nabla \hat{T}_f \rangle + \frac{1}{V} \int_{S_i} k_f \nabla T_f \hat{n}_f dS, \quad (19.58)$$

The first integral in Eq. (19.58) is often represented as the tortuosity heat flux (though some authors define the tortuosity heat flux based on the use of Eq. (19.19a), rather than Eq. (19.19b)) [44]. This tortuosity heat flux is often very small because convection dominates conduction, and hence is neglected [44]. The second integral in Eq. (19.58) represents the average heat flux from the fluid to the solid at the fluid-solid boundary. This can be expressed using Newton's law of cooling as

$$\frac{1}{V} \int_{S_i} k_f \nabla T_f \hat{n}_f dS = \alpha \left( \langle T_s \rangle^s - \langle T_f \rangle^f \right), \quad (19.59)$$

where  $\alpha$  is the convective heat transfer coefficient between the two intrinsic phase averaged temperatures that is discussed at greater length in the main body of the text in the vicinity of Eq. (2.76).

Finally, the source term is  $S_f = -\rho_f \vec{V}_f \cdot \vec{g} - \dot{q}$  for Eq. (2.51). For Eq. (2.67), the gravitational acceleration term was subtracted out earlier in the formation of the internal energy equation. Eq. (19.27) is used to rewrite the product term, giving

$$\begin{aligned} \langle S_f \rangle &= -\langle \rho_f \vec{V}_f \cdot \vec{b} \rangle - \langle \dot{q}_f \rangle \\ &= -\varepsilon \langle \rho_f \rangle^f \langle \vec{V}_f \rangle^f \cdot \langle \vec{b} \rangle^f - \varepsilon \langle \hat{\rho}_f \hat{V}_f \rangle \cdot \langle \vec{b} \rangle^f - \langle \dot{q}_f \rangle . \end{aligned} \quad (19.60)$$

Combining all terms together, with the assumptions listed at the end of Section 19.2, the spatially homogenized total energy equation becomes

$$\begin{aligned} \frac{\partial(\varepsilon \langle \rho_f \rangle^f \langle E_f \rangle^f)}{\partial t} + \nabla \cdot \left[ \varepsilon \langle \rho_f \rangle^f \langle H_f \rangle^f \langle \vec{V}_f \rangle^f + \langle \rho_f \rangle^f \langle \hat{H}_f \hat{V}_f \rangle \right] - \\ \nabla \cdot \varepsilon \langle k_f \rangle^f \nabla \langle T_f \rangle^f - \alpha \left( \langle T_s \rangle^s - \langle T_f \rangle^f \right) - \varepsilon \langle \rho_f \rangle^f \langle \vec{V}_f \rangle^f \cdot \langle \vec{b} \rangle^f - \langle \dot{q}_f \rangle = 0 , \end{aligned} \quad (19.61)$$

and the spatially homogenized internal energy equation becomes

$$\begin{aligned} \varepsilon \langle \rho_f \rangle^f \langle C_{p,f} \rangle^f \frac{\partial \langle T_f \rangle^f}{\partial t} + \varepsilon \langle \rho_f \rangle^f \langle C_{p,f} \rangle^f \langle \vec{V}_f \rangle^f \cdot \nabla \langle T_f \rangle^f + \langle \rho_f \rangle^f \langle C_{p,f} \rangle^f \langle \hat{V}_f \cdot \nabla \hat{T}_f \rangle - \\ \nabla \cdot \varepsilon \langle k_f \rangle^f \nabla \langle T_f \rangle^f - \alpha \left( \langle T_s \rangle^s - \langle T_f \rangle^f \right) - \langle \dot{q}_f \rangle = 0 . \end{aligned} \quad (19.62)$$

### 19.3 Mathematical Structure of Advection and Diffusion Equations

In order to motivate the discussion regarding “well-posedness,” the mathematical structure of generic advection and diffusion equations is described. For purposes of illustration, consider the 1-D linear convection equation,

$$\frac{\partial u}{\partial t} + a \frac{\partial u}{\partial x} = 0, \quad (19.63)$$

where  $u$  is the convected quantity and  $a$  is the convection velocity. If  $a$  is assumed constant, then an initial condition  $u_0$  is simply translated in space,

$$u(x, t) = u_0(x - at). \quad (19.64)$$

This is a wave solution, which can be expressed as some amplitude  $\hat{u}$  multiplied by a complex exponential,

$$\begin{aligned} u &= \hat{u} e^{\frac{2\pi i}{\lambda}(x-at)} \\ &= \hat{u} e^{i(kx - \omega t)}, \end{aligned} \quad (19.65)$$

where  $\lambda$  is the wavelength of the wave,  $k$  is the wavenumber, defined as

$$k \equiv \frac{2\pi}{\lambda}; \quad (19.66)$$

$\omega$  is the pulsation, defined as

$$\omega \equiv 2\pi f; \quad (19.67)$$

$f$  is the frequency; and  $a$  is the speed of the wave, defined as

$$a \equiv \lambda f. \quad (19.68)$$

Therefore, pure convection is a wave phenomenon, and as such can be described using properties of waves. Now, consider the 1-D linear diffusion equation,

$$\frac{\partial u}{\partial t} = \alpha \frac{\partial^2 u}{\partial x^2}, \quad (19.69)$$

where  $\alpha$  is the diffusivity and  $u$  is the diffused quantity. Physical intuition can be obtained by assuming a wave-like solution given by Eq. (19.65) and inserting into Eq. (19.69), giving an imaginary wave speed

$$a = \alpha \frac{2\pi}{i\lambda} \quad (19.70)$$

and wave solution

$$u = \hat{u} e^{\frac{2\pi i}{\lambda}x} e^{-\frac{4\pi^2}{\lambda^2}\alpha t}. \quad (19.71)$$

While convection is a wave phenomenon with real wave speed, diffusion is a wave phenomenon with imaginary wave speed that is exponentially damped in time. The different wave-like solutions for convective and diffusive kernels are responsible for the difference in well-posed BCs. This will be shown first for time-independent equations and then extended to the generic case of time-dependent equations.

A system of time-independent equations is characterized based on whether its homogeneous part permits wave solutions. The classification of hyperbolic, parabolic, and elliptic equations based on such conditions is —

- Hyperbolic permits wave-like solutions;
- Parabolic permits damped wave solutions; and
- Elliptic does not permit wave-like solutions .

Consider the time-independent, inviscid, form of Eq. (2.100), with porosity omitted for simplicity —

$$\mathbf{A}_i \frac{\partial \vec{U}}{\partial x_i} + \vec{S} = \vec{0} . \quad (19.72)$$

Any second-order system can be written as a system of first-order equations (though this transformation is not necessarily unique and could lead to an artificially degenerate system), so consideration of this equation is quite general. Assume a wave-like solution for all components of the solution vector  $\vec{U}$ ,

$$\vec{U} = \vec{\hat{U}} e^{i\vec{k} \cdot \vec{x}} , \quad (19.73)$$

where  $\vec{x}$  is the spatial position and  $\vec{k}$  is a normal at that position. Each component of  $\vec{k}$  is the wave number in that direction (proportional to the number of wavelengths in that direction); the one-dimensional  $kx$  has been generalized to multiple dimensions as  $\vec{k} \cdot \vec{x}$ . Insert Eq. (19.73) into Eq. (19.72),

$$\mathbf{A}_i \frac{\partial}{\partial x_i} \left( \vec{\hat{U}} e^{i\vec{k} \cdot \vec{x}} \right) = 0 , \quad (19.74a)$$

$$\mathbf{A}_i k_i \vec{\hat{U}} = 0 . \quad (19.74b)$$

The mathematical character is based on the components of  $\vec{k}$  —

- Hyperbolic has all real  $k_i$  with linearly independent solutions;
- Parabolic has all real  $k_i$  with some linearly dependent solutions; and
- Elliptic has all complex  $k_i$  .

Parabolic equations usually arise when there is a combination of convection and diffusion, while elliptic equations generally correspond to purely diffusive systems and hyperbolic equations to purely convective systems.

The characteristic normal  $\vec{k}$  corresponds to a characteristic surface  $S$ ; because  $\vec{k}$  is not a unit normal,  $\vec{k} = \nabla S$ .  $S$  is also known as a “wavefront surface” because it separates the space domain that has already influenced  $\vec{U}$  from the points not yet reached by the wave. Substituting this form for  $\vec{k}$  into the generic wave solution in Eq. (19.73) gives:

$$U = \hat{U} e^{i\nabla S \cdot \vec{x}} . \quad (19.75)$$

The solution is constant along constant values of  $\nabla S \cdot \vec{x}$ . Propagation at constant values is only permitted in directions with real normals. For a problem in  $n_s$  space dimensions, at each point there are  $n_s$  characteristic surfaces, defined by the components of the normals at those locations. These normals are obtained by setting the determinant of Eq. (19.74b) equal to zero and solving for  $\vec{k}$ .

At any point in space, the solution can be obtained from the characteristics that have propagated from the boundary to that location. This allows the definition of the region of dependence of a point consisting of all of the points in space that can physically influence that point's value. Likewise, the zone of influence is the region of points in space that can be physically influenced by that point's value.

To generalize to the case of time-dependent problems, adding a time derivative to Eq. (19.72) gives

$$\frac{\partial \vec{U}}{\partial t} + \mathbf{A}_j \frac{\partial \vec{U}}{\partial x_j} + \vec{S} = \vec{0}. \quad (19.76)$$

The time-independent analysis performed earlier can be repurposed to include time dependence by introducing an additional component into  $\vec{x}$  such that  $\vec{x} = [\vec{x} \ t]^T$ . The assumed wave solution now includes an additional component in the exponent in Eq. (19.73),

$$\vec{U} = \vec{U} e^{i(\nabla S \cdot \vec{x} + \frac{\partial S}{\partial t} t)}, \quad (19.77)$$

where  $\partial S / \partial t = -\omega$ .  $\nabla S$  is now the normal to the characteristic surface at the intersection point with surfaces of constant  $t$ . Plugging this assumed solution into Eq. (19.76) gives

$$\left( \mathbf{A}_j \frac{\partial S}{\partial x_j} - \omega \mathbf{I} \right) \vec{U} = 0, \quad (19.78a)$$

$$\left( \frac{1}{\|\vec{k}\|} \mathbf{A}_j \frac{\partial S}{\partial x_j} - a \mathbf{I} \right) \vec{U} = 0. \quad (19.78b)$$

Solution to Eq. (19.78) requires the determinant of the matrix term in parentheses to equal zero. The wave pulsations are the eigenvalues of  $\mathbf{A}_j k_j$ . Dividing both sides by the norm of the wave number vector so that  $\omega$  then represents the wave speeds  $a$  gives Eq. (19.78b). Therefore, the eigenvalues of Eq. (19.78b) are the wave speeds. For systems of equations, mathematical character is again based on the eigenvalues of the homogeneous portion of the equation —

- Hyperbolic has all real eigenvalues;
- Parabolic has all imaginary eigenvalues; and
- Elliptic has all complex eigenvalues.

## 19.4 Ideal Gas Inviscid Flux Jacobian Matrices

The inviscid flux Jacobian matrices defined in Eq. (2.111) with the ideal gas EOS are

$$\mathbf{A}_1 = \begin{bmatrix} 0 & 1 & 0 & 0 & 0 \\ \frac{\gamma-1}{2} \|\vec{V}\|_2^2 - V_1^2 & (3-\gamma)V_1 & (1-\gamma)V_2 & (1-\gamma)V_3 & \gamma-1 \\ -V_2V_1 & V_2 & V_1 & 0 & 0 \\ -V_3V_1 & V_3 & 0 & V_1 & 0 \\ V_1 \left[ \frac{\gamma-1}{2} \|\vec{V}\|_2^2 - H_f \right] & (1-\gamma)V_1^2 + H_f & (1-\gamma)V_1V_2 & (1-\gamma)V_1V_3 & V_1\gamma \end{bmatrix}, \quad (19.79)$$

$$\mathbf{A}_2 = \begin{bmatrix} 0 & 0 & 1 & 0 & 0 \\ -V_1V_2 & V_2 & V_1 & 0 & 0 \\ \frac{\gamma-1}{2} \|\vec{V}\|_2^2 - V_2^2 & (1-\gamma)V_1 & (3-\gamma)V_2 & (1-\gamma)V_3 & \gamma-1 \\ -V_3V_2 & 0 & V_3 & V_2 & 0 \\ V_2 \left[ \frac{\gamma-1}{2} \|\vec{V}\|_2^2 - H_f \right] & (1-\gamma)V_1V_2 & (1-\gamma)V_2^2 + H_f & (1-\gamma)V_2V_3 & V_2\gamma \end{bmatrix}, \quad (19.80)$$

$$\mathbf{A}_3 = \begin{bmatrix} 0 & 0 & 0 & 1 & 0 \\ -V_1V_3 & V_3 & 0 & V_1 & 0 \\ -V_2V_3 & 0 & V_3 & V_2 & 0 \\ \frac{\gamma-1}{2} \|\vec{V}\|_2^2 - V_3^2 & (1-\gamma)V_1 & (1-\gamma)V_2 & (3-\gamma)V_3 & \gamma-1 \\ V_3 \left[ \frac{\gamma-1}{2} \|\vec{V}\|_2^2 - H_f \right] & (1-\gamma)V_1V_3 & (1-\gamma)V_2V_3 & (1-\gamma)V_3^2 + H_f & V_3\gamma \end{bmatrix}. \quad (19.81)$$

## References

- [1] M. Auferio and M. Fratoni. Development of Multiphysics Tools for Fluoride-Cooled High-Temperature Reactors. In *Proceedings of PHYSOR*, 2016.
- [2] <https://tinyurl.com/wkctmvs>.
- [3] <https://tinyurl.com/sht98ro>.
- [4] <https://tinyurl.com/ucque9l>.
- [5] J.D. Hales, R.L. Williamson, S.R. Novascone, D.M. Perez, B.W. Spencer, and G. Pastore. Multidimensional Multiphysics Simulation of TRISO Particle Fuel. *Journal of Nuclear Materials*, 443:531–543, 2013.
- [6] H.S. Mickley, K.A. Smith, and E.I. Korchak. Fluid Flow in Packed Beds. *Chemical Engineering Science*, 20:237–246, 1965.
- [7] H. Darcy. *Les Fontaines Publiques de la Ville de Dijon: Exposition et Application*. 1856.
- [8] H.G. Diersch. *Finite Element Modeling of Flow, Mass and Heat Transport in Porous and Fractured Media*. 2014.
- [9] J. Ge, W. Tian, S. Qiu, and G.H. Su. CFD Investigation on Thermal Hydraulics of the Passive Residual Heat Removal Heat Exchanger (PRHR HX). *Nuclear Engineering and Design*, 327:139–149, 2018.
- [10] D. Magallon. Characteristics of Corium Debris Bed Generated in Large-Scale Fuel-Coolant Interaction Experiments. *Nuclear Engineering and Design*, 236:1998–2009, 2006.
- [11] B. Raverdy, R. Meignen, L. Piar, S. Picchi, and T. Janin. Capabilities of MC3D to Investigate the Coolability of Corium Debris Beds. *Nuclear Engineering and Design*, 319:48–60, 2017.
- [12] K. Xu, M. Ye, Y. Song, B. Xu, S. Wang, M. Lei, X. Liu, and S. Mao. Parameter Study on Helium Cooled Ceramic Breeder Blanket Neutronics with CFETR Integration Design Platform. *Fusion Engineering and Design*, 124:757–761, 2017.
- [13] H. Zhang, Z. Li, H. Guo, M. Ye, and H. Huang. DEM-CFD Simulation of Purge Gas Flow in a Solid Breeder Pebble Bed. *Fusion Engineering and Design*, 113:288–292, 2016.
- [14] W. Guo, A. Ying, M. Ni, and M. Abdou. Influence of 2D and 3D Convection-Diffusion Flow on Tritium Permeation in Helium Cooled Solid Breeder Blanket Units. *Fusion Engineering and Design*, 81:1465–1470, 2006.
- [15] E. Zarifi, G. Jahanfarnia, and F. Veysi. Thermal-Hydraulic Modeling of Nanofluids as the Coolant in VVER-1000 Reactor Core by the Porous Media Approach. *Annals of Nuclear Energy*, 51:203–212, 2013.
- [16] C.Y. Wu, Y.M. Ferng, C.C. Chieng, and C.C. Liu. Investigating the Advantages and Disadvantages of Realistic Approach and Porous Approach for Closely Packed Pebbles in CFD Simulation. *Nuclear Engineering and Design*, 240:1151–1159, 2010.
- [17] A.G. Dixon, M. Nijemeisland, and E. Hugh Stitt. Systematic Mesh Development for 3D CFD Simulation of Fixed Beds: Contact Points Study. *Computers and Chemical Engineering*, 48:135–153, 2013.
- [18] M. Nijemeisland and A.G. Dixon. CFD Study of Fluid Flow and Wall Heat Transfer in a Fixed Bed of Spheres. *American Institute of Chemical Engineers Journal*, 50, 2004.
- [19] Y. Bai, N. Gui, X. Yang, J. Tu, and S. Jiang. Computational Fluid Dynamics Investigation of Thermal-Hydraulic Characteristics in a Simplified Pebbled Bed Modular Reactor Core Using Different Arrangements of Fuel Elements. *Journal of Computational Multiphase Flows*, 0:1–9, 2017.

- [20] J. Ge, C. Wang, Y. Xiao, W. Tian, S. Qiu, G. Su, D. Zhang, and Y. Wu. Thermal-Hydraulic Analysis of a Fluoride-Salt-Cooled Pebble-Bed Reactor with CFD Methodology. *Progress in Nuclear Energy*, 91:83–96, 2016.
- [21] J. Lee, S. Yoon, G. Park, and W. Jee. Turbulence-Induced Heat Transfer in PBMR Core Using LES and RANS. *Nuclear Science and Technology*, 44:985–996, 2007.
- [22] H. Li, S. Qiu, Y. Zhang, G. Su, and W. Tian. Thermal Hydraulic Investigations with Different Fuel Diameters of Pebble Bed Water Cooled Reactor in CFD Simulation. *Annals of Nuclear Energy*, 42:135–147, 2012.
- [23] S. Song, X. Cai, Y. Liu, Q. Wei, and W. Guo. Pore Scale Thermal Hydraulics Investigations of Molten Salt Cooled Pebble Bed High Temperature Reactor with BCC and FCC Configurations. *Science and Technology of Nuclear Installations*, 2014, 2014.
- [24] J. Lee and S. Lee. Flow Visualization in the Scaled Up Pebble Bed of High Temperature Gas-Cooled Reactor Using Particle Image Velocimetry Method. *Journal of Engineering for Gas Turbines and Power*, 131, 2009.
- [25] Y. Hassan and E. Dominguez-Ontiveros. Flow Visualization in a Pebble Bed Reactor Experiment Using PIV and Refractive Index Matching Techniques. *Nuclear Engineering and Design*, 238:3080–3085, 2008.
- [26] S. King, E. Kappes, D.T. Nguyen, Y.A. Hassan, and V. Ugaz. Probability Analysis of Velocity Distribution in a Facility of Randomly Packed Spheres Featuring Matching-Refractive-Index and Time-Resolved PIV Techniques. In *Proceedings of ANS Winter*, 2018.
- [27] Y. Ferng and K. Lin. Investigating Effects of BCC and FCC Arrangements on Flow and Heat Transfer Characteristics in Pebbles Through CFD Methodology. *Nuclear Engineering and Design*, 258:66–75, 2013.
- [28] Y. Hassan. Thermal-hydraulic experiments for advanced reactor modeling and simulation. MeV School, 2018.
- [29] S. Zhang, X. Zhao, and Z. Yang. Flow Simulations in a Pebble Bed Reactor by a Combined DEM-CFD Approach. *Nuclear Science and Engineering*, 189:135–151, 2018.
- [30] V. Rintala, H. Suikkanen, J. Leppanen, and R. Kyrki-Rajamaki. Modeling of Realistic Pebble Bed Reactor Geometries Using the Serpent Monte Carlo Code. *Annals of Nuclear Energy*, 77:223–230, 2015.
- [31] S. Becker and E. Laurien. Three-Dimensional Numerical Simulation of Flow and Heat Transport in High-Temperature Nuclear Reactors. In *High Performance Computing in Science and Engineering*, 2002.
- [32] A. Amiri and K. Vafai. Analysis of Dispersion Effects and Non-Thermal Equilibrium, Non-Darcian, Variable Porosity Incompressible Flow Through Porous Media. *International Journal of Heat and Mass Transfer*, 37:939–954, 1994.
- [33] L. Zou, A.J. Novak, R.C. Martineau, and H.D. Gougar. Validation of Pronghorn with the SANA Experiments, INL/EXT-17-44085. Technical report, Idaho National Laboratory, 2017.
- [34] Fluent 6.3 Documentation. Technical report, ANSYS, 2017.
- [35] M. Elmo and O. Cioni. Low Mach Number Model for Compressible Flows and Application to HTR. *Nuclear Engineering and Design*, 222:117–124, 2003.
- [36] C. Hirsch. *Numerical Computation of Internal and External Flows*. Butterworth-Heinemann, 2007.
- [37] G.K. Batchelor. *An Introduction to Fluid Dynamics*. Cambridge University Press, 2000.
- [38] I. Kececiloglu and Y. Jiang. Flow Through Porous Media of Packed Spheres Saturated With Water. *Transactions of the ASME*, 116:164–170, 1994.
- [39] D.A. Nield and A. Bejan. *Convection in Porous Media*. Springer, 2013.
- [40] G.J. Auwerda, Y. Zheng, D. Lathouwers, and J.L. Kloosterman. Effect of Non-Uniform Porosity Distribution on Thermal Hydraulics in a Pebble Bed Reactor. In *Proceedings of NURETH-14*, 2011.

- [41] Heat Transport and Afterheat Removal for Gas Cooled Reactors Under Accident Conditions. Technical Report IAEA-TECDOC-1163, IAEA, 2000.
- [42] D. Vortmeyer and J. Schuster. Evaluation of Steady Flow Profiles in Rectangular and Circular Packed Beds By a Variational Method. *Chemical Engineering Science*, 38:1691–1699, 1983.
- [43] G.J. Hwang, C.C. Wu, and C.H. Chao. Investigation of Non-Darcian Forced Convection in an Asymmetrically Heated Sintered Porous Channel. *Journal of Heat Transfer*, 117:725–732, 1995.
- [44] A. Nakayama, F. Kuwahara, and Y. Kodama. An Equation for Thermal Dispersion Flux Transport and its Mathematical Modelling for Heat and Fluid Flow in a Porous Medium. *Journal of Fluid Mechanics*, 5:81–96, 2006.
- [45] K. Hossain, M. Buck, N. Ben Said, W. Bernnat, and G. Lohnert. Development of a Fast 3D Thermal-Hydraulic Tool for Design and Safety Studies for HTRs. *Nuclear Engineering and Design*, 238:2976–2984, 2008.
- [46] A. Nouri-Borujerdi and S.I.T. Ghomsheh. An Improved Porous Media Approach to Thermal-Hydraulic Analysis of High-Temperature Gas-Cooled Reactors. *Annals of Nuclear Energy*, 76:485–492, 2015.
- [47] C.G. Morrison and W. Ji. Improving Prompt Temperature Feedback by Stimulating Doppler Broadening in Heterogeneous Composite Nuclear Fuel Forms. *Annals of Nuclear Energy*, 112:486–506, 2018.
- [48] B. Stocker and H. Niessen. Data Sets of the SANA Experiment 1994–1996. Technical Report JUEL-3409, Forschungszentrum Julich, 1996.
- [49] X. Cai, S. Qiu, W. Tian, and G. Su. Development of a Thermal-Hydraulic Analysis Code for the Pebble Bed Water-Cooled Reactor. *Nuclear Engineering and Design*, 241:4978–4988, 2011.
- [50] C. Lu, B.D. Hiscox, K.A. Terrani, and N.R. Brown. Fully Ceramic Microencapsulated Fuel in Prismatic High Temperature Gas-Cooled Reactors: Analysis of Reactor Performance and Safety Characteristics. *Annals of Nuclear Energy*, 114:277–287, 2018.
- [51] L.L. Snead, F. Venneri, Y. Kim, K.A. Terrani, J.E. Tulenko, C.W. Forsberg, P.F. Peterson, and E.J. Lahoda. Fully Ceramic Microencapsulated Fuels: A Transformational Technology for Present and Next Generation Reactors. In *Proceedings of ICONE24*, 2011.
- [52] Q.M. Mistarihi, J.T. Hwang, and H.J. Ryu. The Modeling and Simulation of the Thermal Conductivity of Irradiation U-Mo Dispersion Fuel: Estimation of the Thermal Conductivity of the Interaction Layer. *Journal of Nuclear Materials*, 510:199–209, 2018.
- [53] G.Y. Jeong, Y.S. Kim, and D. Sohn. Mechanical Analysis of UMo/Al Dispersion Fuel. *Journal of Nuclear Materials*, 466:509–521, 2015.
- [54] A. Abou Jaoude, C. Thomas, and A. Erickson. Neutronic and Thermal Analysis of Composite Fuel for Potential Deployment in Fast Reactors. *Nuclear Engineering and Design*, 303:50–57, 2016.
- [55] N.R. Brown, H. Ludewig, A. Aronson, G. Raitses, and M. Todosow. Neutronic Evaluation of a PWR with Fully Ceramic Microencapsulated Fuel. Part II: Nodal Core Calculations and Preliminary Study of Thermal Hydraulic Feedback. *Annals of Nuclear Energy*, 62:548–557, 2013.
- [56] S. Kamalpour, A.A. Salehi, H. Khalafi, N. Mataji-Kojouri, and G. Jahanfarnia. The Potential Impact of Fully Ceramic Microencapsulated (FCM) Fuel on Thermal Hydraulic Performance of SMART Reactor. *Nuclear Engineering and Design*, 339:39–52, 2018.
- [57] Y. Xiao, L. Hu, S. Qiu, D. Zhang, G. Su, and W. Tian. Development of a Thermal-Hydraulic Analysis Code and Transient Analysis for a FHTR. In *Proceedings of the International Conference on Nuclear Engineering*, 2014.
- [58] X. Wang. *Coupled Neutronics and Thermal-Hydraulics Modeling for Pebble-Bed Fluoride-Salt-Cooled High-Temperature Reactor*. PhD thesis, University of California, Berkeley, 2018.

- [59] R. Stainsby, A. Grief, M. Worsley, and F. Dawson. Investigation of Local Heat Transfer Phenomena in a Pebble Bed HTGR Core. Technical Report NR001/RP/002 R01, AMEC Nuclear, 2009.
- [60] M. Liu, Y. Lee, and D.V. Rao. Development of Effective Thermal Conductivity Model for Particle-Type Nuclear Fuels Randomly Distributed in a Matrix. *Journal of Nuclear Materials*, 508:168–180, 2018.
- [61] J. Richard, D. Wang, G. Yoder, J. Carbajo, D. Williams, B. Forget, and C. Forsberg. Implementation of Liquid Salt Working Fluids Into TRACE. In *Proceedings of ICAPP 2014*, 2014.
- [62] Y. Li and W. Ji. Thermal Analysis of Pebble-Bed Reactors Based on a Tightly Coupled Mechanical-Thermal Model. In *Proceedings of NURETH*, 2016.
- [63] G. Hauke and T.J.R. Hughes. A Comparative Study of Different Sets of Variables for Solving Compressible and Incompressible Flows. *Computational Methods in Applied Mechanical Engineering*, 153:1–44, 1998.
- [64] G. Hauke and T.J.R. Hughes. A Unified Approach to Compressible and Incompressible Flows. *Computational Methods in Applied Mechanical Engineering*, 113:389–395, 1994.
- [65] T.J.R. Hughes, L.P. Franca, and M. Mallet. A New Finite Element Formulation for Computational Fluid Dynamics: I. Symmetric Forms of the Compressible Euler and Navier-Stokes Equations and the Second Law of Thermodynamics. *Computer Methods in Applied Mechanics and Engineering*, 54:223–234, 1986.
- [66] M.M. Wakil. *Nuclear Heat Transport*. American Nuclear Society, 1978.
- [67] A. Glaser and M.V. Ramana. Weapon-Grade Plutonium Production Potential in the Indian Prototype Fast Breeder Reactor. Technical report, Princeton University, 2007.
- [68] D.G. Roychowdhury et. al. Thermal Hydraulic Design of PFBR Core. Technical report, Indira Ghandi Centre for Atomic Research.
- [69] R. Baumer, I. Kalinowski, E. Rohler, J. Schoning, and W. Wachholz. Construction and Operating Experience with the 300-MW THTR Nuclear Power Plant. *Nuclear Engineering and Design*, 121:155–166, 1990.
- [70] C. Andreades, A. Cisneros, J. Choi, A. Chong, M. Fratoni, S. Hong, L. Huddar, K. Huff, D. Krumwiede, M. Laufer, M. Munk, R. Scarlat, N. Zweibaum, E. Greenspan, and P. Peterson. Technical Description of the “Mark 1” Pebble-Bed Fluoride-Salt-Cooled High-Temperature Reactor (PB-FHR) Power Plant. Technical Report UCBTH-14-002, University of California, Berkeley, 2014.
- [71] B. Sutharshan, M. Mutyala, R.P. Vijuk, and A. Mishra. The AP1000 Reactor: Passive Safety and Modular Design. *Energy Procedia*, 7:293–302, 2011.
- [72] Westinghouse. AP1000 Design Control Document. Technical report.
- [73] E. Nonbøl. Description of the Advanced Gas Cooled Type of Reactor (AGR). Technical Report NKS/RAK2(96)TR-C2, Risø National Laboratory.
- [74] A. Rohde. Eigenvalues and Eigenvectors of the Euler Equations in General Geometries. *American Institute of Aeronautics and Astronautics*, 1999.
- [75] S.J. Kim and D. Kim. Thermal Interaction at the Interface Between a Porous Medium and an Impermeable Wall. *Journal of Heat Transfer*, 123:527–533, 2001.
- [76] B. Alazmi and K. Vafai. Constant Wall Heat Flux Boundary Conditions in Porous Media Under Local Thermal Non-Equilibrium Conditions. *International Journal of Heat and Mass Transfer*, 45:3071–3087, 2002.
- [77] A. Amiri, K. Vafai, and T.M. Kuzay. Effects of Boundary Conditions on Non-Darcian Heat Transfer Through Porous Media and Experimental Comparisons. *Numerical Heat Transfer, Part A: Applications*, 27:651–664, 1995.
- [78] M. Giese, K. Rottschäfer, and D. Vortmeyer. Measured and Modeled Superficial Flow Profiles in Packed Beds with Liquid Flow. *American Institute of Chemical Engineers Journal*, 44:484–490, 1998.

- [79] L.H.S. Roblee, R.M. Baird, and J.W. Tierney. Radial Porosity Variations in Packed Beds. *American Institute of Chemical Engineers*, pages 460–464, 1958.
- [80] J.S. Goodling, R.I. Vachon, W.S. Stelpflug, and S.J. Ying. Radial Porosity Distribution in Cylindrical Beds Packed with Spheres. *Powder Technology*, 35:23–29, 1983.
- [81] R. Hecker, W. Rausch, and R. Schulten. Development of High Temperature Thermal Reactors in Germany. Technical Report 003-63-1, KFA, 1967.
- [82] R.Y. Yang, R.P. Zou, and A.B. Yu. Computer Simulation of the Packing of Fine Particles. *Physical Review E*, 62:3900–3908, 2000.
- [83] C.H. Rycroft, G.S. Grest, J.W. Landry, and M.Z. Bazant. Analysis of Granular Flow in a Pebble-Bed Nuclear Reactor. *Physical Review*, 74, 2006.
- [84] Z.P. Zhang, L.F. Liu, Y.D. Yuan, and A.B. Yu. A Simulation Study of the Effects of Dynamic Variables on the Packing of Spheres. *Powder Technology*, 116:23–32, 2001.
- [85] Y. Li and W. Ji. Effects of Fluid-Pebble Interactions on Mechanics in Large-Scale Pebble-Bed Reactor Cores. *International Journal of Multiphase Flow*, 73:118–129, 2015.
- [86] R. Mardus-Hall, M. Ho, G. Yeoh, and V. Timchenko. Coupled CFD-DEM Analysis of Molten Salt-Cooled Pebble-Bed Reactor Experiment. In *Transactions of the American Nuclear Society*, 2017.
- [87] H. Suikkanen, V. Rintala, and R. Kyrki-Rajamaki. Development of a Coupled Multi-Physics Code System for Pebble Bed Reactor Core Modeling. In *Proceedings of the HTR 2014*, 2014.
- [88] C.G. du Toit. Radial Variation in Porosity in Annular Packed Beds. *Nuclear Engineering and Design*, 238:3073–3079, 2008.
- [89] G.J. Auwerda, J.Kloosterman, D.Lathouwers, and T. Van Der Hagen. Macroscopic and Microscopic Packing Properties of Experimental and Computational Pebble Beds. *Nuclear Technology*, 183:272–286, 2013.
- [90] R.F. Benenati and C.B. Brosilow. Void Fraction Distribution in Beds of Spheres. *American Institute of Chemical Engineers*, 8:359–361, 1962.
- [91] J.S. Goodling and M.S. Khader. Co-ordination Number Distribution of Spherical Particles in a Packed Cylindrical Bed. *Powder Technology*, 44:53–55, 1985.
- [92] G. Mueller. Radial Void Fraction Distribution in Randomly Packed Fixed Beds of Uniformly Sized Spheres in Cylindrical Containers. *Powder Technology*, 72:269–275, 1992.
- [93] A. de Klerk. Voidage Variation in Packed Beds at Small Column to Particle Diameter Ratio. *American Institute of Chemical Engineers*, 49:2022–2029, 2003.
- [94] R.P. Zou and A.B. Yu. The Packing of Spheres in a Cylindrical Container: The Thickness Effect. *Chemical Engineering Science*, 50:1504–1507, 1995.
- [95] G.D. Scott. Packing of Spheres. *Nature*, 188:908–909, 1960.
- [96] Y. Cohen and A.B. Metzner. Wall Effects in Laminar Flow of Fluids Through Packed Beds. *American Institute of Chemical Engineers*, 27:705–715, 1981.
- [97] H. Martin. Low Peclet Number Particle-to-Fluid Heat and Mass Transfer in Packed Beds. *Chemical Engineering Science*, 33:913–919, 1978.
- [98] G. Peter. Numerical Simulation of Accident Scenario in HTGR (Pebble Bed Reactor) Using COMSOL Code. In *Proceedings of ICONE*, 2013.
- [99] R. Abdulmohsin. *Gas Dynamics and Heat Transfer in a Packed Pebble-Bed Reactor for the 4th Generation Nuclear Energy*. PhD thesis, Missouri University of Science and Technology, 2013.

- [100] S. Becker and E. Laurien. Three-Dimensional Numerical Simulation of Flow and Heat Transport in High-Temperature Nuclear Reactors. *Nuclear Engineering and Design*, 222:189–201, 2003.
- [101] N. Amini and Y.A. Hassan. Experimental Study of Bypass Flow in Near Wall Gaps of a Pebble Bed Reactor Using Hot Wire Anemometry Technique. *Annals of Nuclear Energy*, 65:60–71, 2014.
- [102] S.M. White and C.L. Tien. Analysis of Flow Channeling Near the Wall in Packed Beds. *Wärme-und Stoffübertragung*, 21:291–296, 1987.
- [103] J.J. Lerou and G.F. Froment. Velocity, Temperature and Conversion Profiles in Fixed Bed Catalytic Reactors. *Chemical Engineering Science*, 32:853–861, 1977.
- [104] E. Tsotsas and E. Schlünder. Some Remarks on Channeling and on Radial Dispersion in Packed Beds. *Chemical Engineering Science*, 43:1200–1203, 1988.
- [105] G. Zhao, P. Ye, and T. Obala. Variant Porosity Pebble Bed Reactor Core Thermal Hydraulic Simulation. In *Proceedings of ICONE*, May 2010.
- [106] K. Sun, J. Wilson, S. Hauptman, R. Ji, A.J. Dave, Y. Zou, and L. Hu. Neutronics Modeling and Analysis of the TMSR-SF1 Fuel Lattice and Full Core with Explicit Fuel Particle Distribution and Random Pebble Loadings. *Progress in Nuclear Energy*, 109:171–179, 2018.
- [107] W.O. Smith, P.D. Foote, and P.F. Busang. Packing of Homogeneous Spheres. *Physical Review*, 34:1271–1274, 1929.
- [108] G.J. Auwerda, J.L. Kloosterman, D. Lathouwers, and T.H.J.J. van der Hagen. Effects of Random Pebble Distribution on the Multiplication Factor in HTR Pebble Bed Reactors. *Annals of Nuclear Energy*, 37:1056–1066, 2010.
- [109] W.K. Terry, A.M. Ougouag, F. Rahnama, and M.S. McKinley. Effects of Spatial Variations in Packing Fraction of Reactor Physics Parameters in Pebble-Bed Reactors. In *Nuclear Mathematical and Computational Sciences: A Century in Review, A Century Anew*, 2003.
- [110] F.J. Keil. *Modeling of Process Intensification*. Wiley-VCH, 2007.
- [111] W. Van Antwerpen, C.G. du Toit, and P.G. Rousseau. A Review of Correlations to Model the Packing Structure and Effective Thermal Conductivity in Packed Beds of Mono-Sized Spherical Particles. *Nuclear Engineering and Design*, 240:1803–1818, 2010.
- [112] C.J. Visser. Modelling Heat and Mass Flow Through Packed Pebble Beds: A Heterogeneous Volume-Averaged Approach. Master’s thesis, University of Pretoria, 2007.
- [113] W. Schertz and K. Bischoff. Thermal and Material Transport in Nonisothermal Packed Beds. *American Institute of Chemical Engineers Journal*, 15:597–604, 1969.
- [114] H.P. Meissner, A.S. Michaels, and R. Kaiser. Crushing Strength of Zinc Oxide Agglomerates. *I&EC Process Design and Development*, 3:202–205, 1964.
- [115] E. You, X. Sun, F. Chen, L. Shi, and Z. Zhang. An Improved Prediction Model for the Effective Thermal Conductivity of Compact Pebble Bed Reactors. *Nuclear Engineering and Design*, 323:95–102, 2017.
- [116] M. Nakagaki and H. Sunada. Theoretical Studies on Structures of the Sedimentation Bed of Spherical Particles. *Yakugaku Zasshi*, 88:651–655, 1968.
- [117] I.F. Macdonald, M.S. El-Sayed, K. Mow, and F.A.L. Dullien. Flow Through Porous Media - the Ergun Equation Revisited. *Ind. Eng. Chem. Fundam.*, 18:199–207, 1979.
- [118] S. Ergun. Fluid Flow Through Packed Columns. *Chem. Eng. Prog.*, 48, 1952.
- [119] B. Einfeld and K. Schnitzlein. The Influence of Confining Walls on the Pressure Drop in Packed Beds. *Chemical Engineering Science*, 56:4321–4329, 2001.

- [120] E. Achenbach. Heat and Flow Characteristics of Packed Beds. *Experimental Thermal and Fluid Sciences*, 10:17–27, 1995.
- [121] R.D. Barree and M.W. Conway. Beyond Beta Factors: A Complete Model for Darcy, Forchheimer, and Trans-Forchheimer Flow in Porous Media. *Society of Petroleum Engineers*, pages 1–8, 2004.
- [122] H. Huang and J. Ayoub. Applicability of the Forchheimer Equation for Non-Darcy Flow in Porous Media. *Society of Petroleum Engineers*, pages 1–14, 2006.
- [123] X. Wang, F. Thauvin, and K.K. Mohanty. Non-Darcy Flow Through Anisotropic Porous Media. *Chemical Engineering Science*, 54:1859–1869, 1998.
- [124] J.H. Yang and S.L. Lee. Effect of Anisotropy on Transport Phenomena in Anisotropic Porous Media. *International Journal of Heat and Mass Transfer*, 42:2673–2681, 1999.
- [125] S.L. Lee and J.H. Yang. Modeling of Darcy-Forchheimer Drag for Fluid Flow Across a Bank of Circular Cylinders. *International Journal of Heat and Mass Transfer*, 40:3149–3155, 1997.
- [126] D. van Batenburg and D. Milton-Taylor. Discussion of SPE 89325, "Beyond Beta Factors: A Complete Model for Darcy, Forchheimer, and Trans-Forchheimer Flow in Porous Media". *Journal of Petroleum Technology*, pages 72–73, 2005.
- [127] R.M. Fand, B.Y.K. Kim, A.C.C. Lam, and R.T. Phan. Resistance to the Flow of Fluids Through Simple and Complex Porous Media Whose Matrices are Composed of Randomly Packed Spheres. *Transactions of the ASME*, 109:268–273, 1987.
- [128] J.L. Lage, B.V. Antohe, and D.A. Nield. Two Types of Nonlinear Pressure-Drop Versus Flow-Rate Relation Observed for Saturated Porous Media. *Transactions of the ASME*, pages 700–706, 1997.
- [129] KTA. Reactor Core Design of High-Temperature Gas-Cooled Reactors Part 3: Loss of Pressure through Friction in Pebble Bed Cores. Technical Report KTA 3102.3, Nuclear Safety Standards Commission, 1981.
- [130] D.A. Nield. Resolution of a Paradox Involving Viscous Dissipation and Nonlinear Drag in a Porous Medium. *Transport in Porous Media*, 41:349–357, 2000.
- [131] M. Kaviany. *Principles of Heat Transfer in Porous Media*. Springer-Verlag, 1991.
- [132] K. Vafai and C.L. Tien. Boundary and Inertia Effects on Flow and Heat Transfer in Porous Media. *International Journal of Heat and Mass Transfer*, 37:195–203, 1980.
- [133] A.A. Avdeev, B.F. Balunov, R.A. Rybin, R.I. Soziev, and G.A. Filippov. Hydrodynamic Drag Under Conditions of Flow of a Two-Phase Mixture in a Pebble Bed. *High Temperature*, 41:377–383, 2003.
- [134] P. Avigni, A.J. Wysocki, and G.L. Yoder. Liquid Salt Test Loop Modeling Using TRACE. *Annals of Nuclear Energy*, 106:170–184, 2017.
- [135] R.O. Scarlat. *Design of Complex Systems to Achieve Passive Safety: Natural Circulation Cooling of Liquid Salt Pebble Bed Reactors*. PhD thesis, University of California, Berkeley, 2012.
- [136] M.S. Latifi and S. Setayeshi. Effects of Porosity on Thermal-Fluid Phenomena in PBMR Core. *Journal of Thermal Engineering*, 2:853–860, 2016.
- [137] Z. Gao and L. Shi. Thermal Hydraulic Calculation of the HTR-10 for the Initial and Equilibrium Core. *Nuclear Engineering and Design*, 218:51–64, 2002.
- [138] S.W. Churchill. Friction-Factor Equation Spans All Fluid-Flow Regimes. *Chemical Engineering*, 84:91–92, 1977.
- [139] L.J. Petrovic and G. Thodos. Mass Transfer in the Flow of Gases Through Packed Beds. *Industrial & Engineering Chemistry Fundamentals*, 46, 1968.

- [140] D.J. Gunn. Transfer of Heat or Mass to Particles in Fixed and Fluidised Beds. *International Journal of Heat and Mass Transfer*, 21:467–476, 1978.
- [141] A.S. Gupta and G. Thodos. Mass and Heat Transfer in the Flow of Fluids Through Fixed and Fluidized Beds of Spherical Particles. *A.I.Ch.E. Journal*, 8:608–610, 1962.
- [142] J.T.L. McConnachie and G. Thodos. Transfer Processes in the Flow of Gases Through Packed and Distended Beds. *A.I.Ch.E. Journal*, 9:60–64, 1963.
- [143] G.S. Wilkins and G. Thodos. Mass Transfer Driving Forces in Packed and Fluidized Beds. *A.I.Ch.E. Journal*, 15:47–50, 1969.
- [144] KTA. Reactor Core Design of High-Temperature Gas-Cooled Reactors Part 2: Heat Transfer in Spherical Fuel Elements. Technical Report KTA 3102.2, Nuclear Safety Standards Commission, 1983.
- [145] A.S. Gupta and G. Thodos. Transitional Behavior for the Simultaneous Mass and Heat Transfer of Gases Flowing Through Packed and Distended Beds of Spheres. *Industrial & Engineering Chemistry Fundamentals*, 9:218–220, 1963.
- [146] H. Littman, R.G. Barile, and A.H. Pulsifer. Gas-Particle Heat Transfer Coefficients in Packed Beds at Low Reynolds Numbers. *I & EC Technology*, 7:554–561, 1968.
- [147] Jr. G.L. Yoder. Examination of Liquid Fluoride Salt Heat Transfer. In *Proceedings of ICAPP*, 2014.
- [148] N. Wakao, S. Kagueli, and T. Funazkri. Effect of Fluid Dispersion Coefficients on Particle-to-Fluid Heat Transfer Coefficients in Packed Beds: Correlation of Nusselt Number. *Chemical Engineering Science*, 34:325–336, 1979.
- [149] S. Yagi and N. Wakao. Heat and Mass Transfer from Wall to Fluid in Packed Beds. *American Institute of Chemical Engineers Journal*, 5:79–85, 1959.
- [150] H.T. Aichlmayr and F.A. Kulacki. On the Effective Thermal Conductivity of Saturated Porous Media. In *ASME Summer Heat Transfer Conference*, 2005.
- [151] D.L. Swift. The Thermal Conductivity of Spherical Metal Powders Including the Effect of an Oxide Coating. *International Journal of Heat and Mass Transfer*, 9:1061–1074, 1966.
- [152] I. Nozad, R.G. Carbonell, and S. Whitaker. Heat Conduction in Multiphase Systems - II: Experimental Method and Results for Three-Phase Systems. *Chemical Engineering Science*, 40:857–863, 1985.
- [153] C. T. Hsu, P. Cheng, and K. W. Wong. Modified Zehner-Schlünder Models for Stagnant Thermal Conductivity of Porous Media. *International Journal of Heat and Mass Transfer*, 37:2751–2759, 1994.
- [154] E. Tsotsas and H. Martin. Thermal Conductivity of Packed Beds: A Review. *Chemical Engineering Processes*, 22:19–37, 1987.
- [155] R.G. Deissler and C.S. Eian. Investigation of Effective Thermal Conductivities of Powders. In *National Advisory Committee for Aeronautics*, 1952.
- [156] A.J. Novak, J.W. Peterson, L. Zou, D. Andrš, R.N. Slaybaugh, and R.C. Martineau. Validation of Pronghorn Friction-Dominated Porous Media Thermal-Hydraulics Model with the SANA Experiments. *Nuclear Engineering and Design*, 350:182–194, 2019.
- [157] B.P. Singh and M. Kaviany. Effect of Solid Conductivity on Radiative Heat Transfer in Packed Beds. *International Journal of Heat and Mass Transfer*, 37:2579–2583, 1994.
- [158] D. Kunii and J.M. Smith. Heat Transfer Characteristics of Porous Rocks. *AIChE Journal*, 6:71–78, 1960.
- [159] N. Wakao and K. Kato. Effective Thermal Conductivity of Packed Beds. *Journal of Chemical Engineering of Japan*, 2:24–33, 1968.

- [160] G. Breitbach and H. Barthels. Radiant Heat Transfer in the HTR Core After Failure of the Afterheat Removal Systems. *Transactions of the American Nuclear Society*, 31:421–422, 1979.
- [161] K. Ofuchi and D. Kunii. Heat Transfer Characteristics of Packed Beds with Stagnant Fluids. *International Journal of Heat and Mass Transfer*, 8:749–757, 1965.
- [162] E.E. Gonzo. Estimating Correlations for the Effective Thermal Conductivity of Granular Materials. *Chemical Engineering Journal*, 90:299–302, 2002.
- [163] V. Prasad, N. Kladas, A. Bandyopadhaya, and Q. Tian. Evaluation of Correlations for Stagnant Thermal Conductivity of Liquid-Saturated Porous Beds of Spheres. *International Journal of Heat and Mass Transfer*, 32(9):1783–1796, 1989.
- [164] W.R. Fundamenski and P.J. Gierszewski. Comparison of Correlations for Heat Transfer in Sphere-Pac Beds. Technical Report CFFTP G-9181, Canadian Fusion Fuels Technology Project, 1991.
- [165] M. Kandula. On the Effective Thermal Conductivity of Porous Packed Beds with Uniform Spherical Particles. *Journal of Porous Media*, 14(10):919–926, 2011.
- [166] C.T. Hsu, P. Cheng, and K.W. Wong. A Lumped-Parameter Model for Stagnant Thermal Conductivity of Spatially Periodic Porous Media. *Transactions of the ASME*, 117:264–269, 1995.
- [167] C. K. Chan and C. L. Tien. Conductance of Packed Spheres in Vacuum. *Transactions of the ASME*, pages 302–308, 1973.
- [168] S. Yagi and D. Kunii. Studies on Effective Thermal Conductivities in Packed Beds. *American Institute of Chemical Engineers Journal*, 3:373–381, 1957.
- [169] D. Gunn. Axial and Radial Dispersion in Fixed Beds. *Chemical Engineering Science*, 42:363–373, 1987.
- [170] J. Delgado. Longitudinal and Transverse Dispersion in Porous Media. *Chemical Engineering Research and Design*, 85:1245–1252, 2007.
- [171] *MOOSE Fluid Properties Module*.
- [172] Accuratus Corporation. Aluminum oxide ceramic properties, 2013.
- [173] Inc. BNZ Materials. Insulating Fire Brick C-22Z Properties, 2013.
- [174] The Engineering Toolbox. Specific Heat of Solids, 2003.
- [175] A. T. D. Butland and R. J. Maddison. The Specific Heat of Graphite: An Evaluation of Measurements. *Journal of Nuclear Materials*, 49:45–56, 1973.
- [176] IAEA. Evaluation of High Temperature Gas Cooled Reactor Performance: Benchmark Analysis Related to the PBMR-400, PBMM, GT-MHR, HTR-10, and the ASTRA Critical Facility. Technical Report IAEA-TECDOC-1694, IAEA, 2013.
- [177] G. K. Miller, D. A. Petti, J. T. Maki, and D. L. Knudson. PARFUME Theory and Model Basis Report. Technical Report INL/EXT-08-14497, Idaho National Laboratory, 2009.
- [178] D. Rochais, G. Le Meur, V. Basini, and G. Domingues. Microscopic Thermal Characterization of HTR Particle Layers. *Nuclear Engineering and Design*, 238:3047–3059, 2008.
- [179] E. L’opez-Honorato, C. Chiritescu, P. Xiao, D. G. Cahill, G. Marsh, and T. J. Abram. Thermal Conductivity Mapping of Pyrolytic Carbon and Silicon Carbide Coatings on Simulated Fuel Particles by Time-Domain Thermorefectance. *Journal of Nuclear Materials*, 378:35–39, 2008.
- [180] F. Cao, B. Liu, X. Wang, X. Zhao, F. Guo, and P. Xiao. Evaluation of Thermal Conductivity of the Constituent Layers in TRISO Particles Using Raman Spectroscopy. *Journal of the European Ceramic Society*, 37:4457–4465, 2017.

- [181] G. A. Slack. Anisotropic Thermal Conductivity of Pyrolytic Graphite. *Physical Review*, 127:694–701, 1962.
- [182] J. C. Bokros, R. J. Price, and K. Koyama. Neutron-induced Changes in Crystallinity and Thermal Conductivity of Pyrolytic Carbons. *Carbon*, 4:293–295, 1966.
- [183] V. Basini, F. Charollais, D. Rochais, D. Helary, M. Perez, and P. Guillermier. New techniques dedicated to the characterization of innovative fuels, 2005.
- [184] L. L. Snead, T. Nozawa, Y. Katoh, T. Byun, S. Kondo, and D. A. Petti. Handbook of SiC Properties for Fuel Performance Modeling. *Journal of Nuclear Materials*, 371:329–377, 2007.
- [185] H. Gerwin, W. Scherer, A. Lauer, and G. Strydom. TINTE – A Two-Dimensional Code for Reactor Dynamics. Technical Report JUL-4294, Institute for Energy Research, 2009.
- [186] J. K. Fink, M. G. Chasanov, and L. Leibowitz. Thermophysical Properties of Uranium Dioxide. *Journal of Nuclear Materials*, 102:17–25, 1981.
- [187] C. Folsom, C. Xing, C. Jensen, H. Ban, and D.W. Marshall. Experimental Measurement and Numerical Modeling of the Effective Thermal Conductivity of TRISO Fuel Compacts. *Journal of Nuclear Materials*, 458:198–205, 2015.
- [188] H. Lee, D. Kim, S.J. Lee, J.Y. Park, and W. Kim. Thermal Conductivity Analysis of SiC Ceramics and Fully Ceramic Microencapsulated Fuel Composites. *Nuclear Engineering and Design*, 311:9–15, 2017.
- [189] L.E. Nielsen. Thermal Conductivity of Particulate-Filled Polymers. *Journal of Applied Polymer Science*, 17:3819–3820, 1973.
- [190] R.C. Progelhof, J.L. Throne, and R.R. Ruetsch. Methods for Predicting the Thermal Conductivity of Composite Systems: A Review. *Polymer Engineering and Science*, 16:615–625, 1976.
- [191] O.C. Zienkiewicz, R.L. Taylor, and P. Nithiarasu. *The Finite Element Method for Fluid Dynamics, 7th edition*. Butterworth-Heinemann, 2000.
- [192] J.N. Reddy. *An Introduction to the Finite Element Method*. McGraw-Hill, 3 edition, 2005.
- [193] D.L. Logan. *A First Course in the Finite Element Method*. CL Engineering, 5 edition, 2011.
- [194] S.R. Idelsohn and E. Oñate. Finite Volumes and Finite Elements: Two 'Good Friends'. *International Journal for Numerical Methods in Engineering*, 37:3323–3341, 1994.
- [195] A.N. Brooks. *A Petrov-Galerkin Finite Element Formulation for Convection Dominated Flows*. PhD thesis, California Institute of Technology, 1981.
- [196] G. Hauke. Simple Stabilizing Matrices for the Computation of Compressible Flows in Primitive Variables. *Computational Methods of Applied Mechanical Engineering*, 190:6881–6893, 2001.
- [197] T.E. Tezduyar and Y. Osawa. Finite Element Stabilization Parameters Computed from Element Matrices and Vectors. *Computer Methods in Applied Mechanics and Engineering*, 190:411–430, 2000.
- [198] B.S. Kirk. *Adaptive Finite Element Simulation of Flow and Transport Applications on Parallel Computers*. PhD thesis, The University of Texas at Austin, 2007.
- [199] T.E. Tezduyar and T.J.R. Hughes. Finite Element Formulations for Convection Dominated Flows with Particular Emphasis on the Compressible Euler Equations. *21st Aerospace Sciences Meeting*, 1983.
- [200] J. Shewchuk. An Introduction to the Conjugate Gradient Method Without the Agonizing Pain. Technical Report 1.25, Carnegie Mellon University, 1994.
- [201] A. Griewank and A. Walther. *Evaluating Derivatives: Principles and Techniques of Algorithmic Differentiation*. Society for Industrial and Applied Math, 2 edition, 2008.

- [202] PETSc Users Manual. Technical Report ANL-95/11, Argonne National Laboratory, 2020.
- [203] L.N. Trefethen and D. Bau III. *Numerical Linear Algebra*. SIAM, 1997.
- [204] W. Gray and K. O'Neill. On the General Equations for Flow in Porous Media and Their Reduction to Darcy's Law. *Water Resources Research*, 12:148–154, 1976.



